IMPERIAL COLLEGE LONDON

DOCTORAL THESIS

Understanding the impact of an expanded neutral current pion production model on long-baseline oscillation analyses at T2K

Author:	*Supervisor:*
Charlie Naseby	Dr. Mark Scott

A thesis submitted in fulfilment of the requirements
for the degree of Doctor of Philosophy

in the

High Energy Physics
Department of Physics

May 18, 2023

IMPERIAL COLLEGE LONDON

Abstract

Faculty of Natural Sciences
Department of Physics

Doctor of Philosophy

Understanding the impact of an expanded neutral current pion production model on long-baseline oscillation analyses at T2K

by Charlie Naseby

As long-baseline neutrino oscillation experiments continue to collect data, systematic uncertainties will play a more significant role in limiting measurement precision. The work presented here examines one such source of systematic uncertainty in the T2K (Tokai to Kamioka) experiment, neutral current neutrino interactions producing pions.

The process of expanding the oscillation analysis with an expanded cross-section treatment is described, in conjunction with the addition of SK neutral current π^0 control samples. The analysis makes use of a Markov Chain Monte Carlo method to investigate the impact of these additions on both the oscillation parameter measurement and other parameters of the fit.

Finally, an investigation of future systematic uncertainties of relevance to the next-generation long-baseline neutrino experiment Hyper-Kamiokande is made. This focuses on the potential provided by a proposed new near-detector to constrain the leading systematic uncertainty in HK's measurement of the neutrino CP violating phase δ_{CP}.

Declaration of Authorship

I, Charlie Naseby, declare that the work presented in this thesis is my own and any figures or studies from external sources are appropriately referenced.

Sections of work presented here that are my own are described below:

In Chapter 6 I added the NCπ^0 samples into MaCh3, ran the simulated data studies and added the additional NC parameters, additionally I chose the prior uncertainty on these parameters. I validated the data against the MC and chose the sample binning in addition to the detector systematics binning. I investigated the leading SK detector systematic components and ran the data fits.

In Chapter 7 I validated the MC and weighted it to the 750m detector design. I optimised the event selections and chose the 1Re sample binning, additionally I added antineutrino samples into the fit and expanded the flux treatment to include this. Additionally I investigated the impact of NC1π separation in the fit.

Copyright Notice

“The story so far: In the beginning, the Universe was created. This has made a lot of people very angry and been widely regarded as a bad move.”

Douglas Adams — The Restaurant At The End Of The Universe

Acknowledgements

I would like to thank my supervisor, Mark Scott, I have been very fortunate to have such an engaged and approachable supervisor to assist me throughout. He has made it both educational and enjoyable, I could not have asked for anyone better.

I am indebted to Ed Atkin for all of his help on MaCh3 and on the T2K oscillation analysis. He was always free to discuss the intricacies of a parameter, or try to imagine how any part of the analysis might affect another, usually while also bouncing a tennis ball between us. Special thanks must go to Dan Martin and Lauren Anthony for their work and experience making NCπ^0 selections at SK, upon which the work of this thesis is based. Working closely with both on the details of the sample has been informative to the analysis approach and useful for understanding its limitations.

A Ph.D. without great co-workers would scarcely be worth doing at all. I would therefore like to thank my friends in T2K and the Imperial LBL group for all of the discussion and fun we had, both in and outside of work. I simultaneously enjoyed myself and learned a surprising proportion of my T2K knowledge from this.

Finally I must thank all of my partner, my parents and sister and my close friends for being such constants and for all of the support they have provided throughout my life.

Contents

List of Figures

List of Tables

List of Abbreviations

CC	**C**harged **C**urrent
CCQE	**C**harged **C**urrent **Q**uasi-**E**lastic
DIS	**D**eep **I**nelastic **S**cattering
ECAL	**E**lectromagnetic **CAL**orimiter
FGD	**F**ine **G**rained **D**etector
FHC	**F**orward **H**orn **C**urrent
FSI	**F**inal **S**tate **I**nteractions
HK	**H**yper-**K**amiokande
INGRID	**IN**teractive neutrino **GRID**
IWCD	**I**ntermediate **W**ater **C**herenkov **D**etector
J-PARC	**J**apan-**P**roton **A**ccelerator **R**esearch **C**omplex
LBL	**L**ong-**B**ase**l**ine
MaCh3	**Ma**rkov **Ch**ain **3** flavour
MBL	**M**edium-**B**ase**l**ine
MCMC	**M**arkov **C**hain **M**onte **C**arlo
NC	**N**eutral **C**urrent
ND280	**N**ear **D**etector at **280** meters
PID	**P**article **ID**entification
PMT	**P**hoto **M**ultiplier **T**ube
PN	**P**hoto **N**uclear
POT	**P**rotons **O**n **T**arget
RHC	**R**everse **H**orn **C**urrent
SI	**S**econdary **I**nteractions
SK	**S**uper-**K**amiokande
TPC	**T**ime **P**rojection **C**hamber
WLS	**W**ave**L**ength **S**hifting

WS	**W**rong-**S**ign
1Re	**1 R**ing **e**lectron
1Rμ	**1 R**ing **m**uon
2p-2h	**2 p**articles-**2 h**oles

Chapter 1

Neutrino Properties

This chapter will discuss discovery and the interpretation of neutrinos within the Standard Model, including their oscillations and interactions with matter. As relevant to accelerator based long baseline neutrino oscillation experiments.

1.1 Standard Model Neutrinos

1.1.1 Discovery

First Hints

The first evidence for the existence of neutrinos came from radioactive beta decay experiments. In 1914, James Chadwick discovered that electrons produced in β decay had a continuous energy distribution [1]. This was in stark contrast to α and γ decays which yielded monoenergetic decay products.

A two-body decay process conserving energy and momentum would require that the electrons produced from the decay all have the same energy. It was therefore impossible to explain the observed spectrum using the two decay products without abandoning energy conservation.

The continuous spectrum could however be explained through the inclusion of a third, unobserved particle, able to carry some of the decay energy away. This was the solution proposed by Pauli in 1930 [2]. His proposal included a new, neutral, weakly interacting particle termed the neutron (later renamed to the neutrino). Such a particle would allow for the removal of some energy from the decay and would not itself be readily detectable. While the mass of this particle was not predicted, Pauli believed it would have to be comparable to, or smaller than the mass of the electron.

This neutrino was included in Fermi's 1934 theory for weak interactions [3], which was extremely successful in describing the lifetimes and energy spectra for β decay processes. Fermi theory was later expanded by Gamow and Teller in 1936 [4] to include axial-vector currents. The precise form of weak interactions, that of the V-A structure was not yet known.

Direct Detection

The first experiment to directly detect a neutrino was that of Cowan and Reines in 1956 [5]. At this point, several of the properties of the neutrino had been inferred, including an upper limit on its mass, being below 250eV/c^2 [6].

This experiment consisted of a layer of water target, with liquid scintillator on either side, placed close to an active nuclear reactor. The reactor would provide an intense flux of anti electron neutrinos while the hydrogen nuclei in the water would act as a proton target for the inverse beta decay process:

$$\bar{\nu}_e + p^+ \rightarrow e^+ + n^0 \tag{1.1}$$

The positron produced would rapidly collide with an atomic electron, producing two photons of characteristic 0.511MeV energy.

The neutron would thermalise over several microseconds and then be captured on a cadmium nucleus dissolved in the water. This cadmium nucleus would then emit several photons. These photons would pass into the liquid scintillator layer, convert and be detected by a number of photomultiplier tubes.

An inverse beta decay reaction would produce a distinctive signal consisting of two prompt photons, one in each scintillator layer from the positron. This would be followed a number of microseconds later by a larger, delayed signal in the scintillator from the neutron capture.

Using this setup, Cowan and Reins were able to detect approximately three neutrino interaction events per hour associated with the reactor operation, in agreement with the predicted flux and theoretical cross-section for the process in Fermi theory.

This demonstrated the existence of neutrinos as well as the efficacy of Fermi theory to describe their interactions.

1.1.2 Three Generations

Muon Neutrinos

While the existence of a new particle had been shown, it was not yet known that there was more than one generation. The muon had been discovered in 1937 [7] and the available limits for $\mu \to e + \gamma$ decay indicated that lepton flavour was a conserved quantity, similarly to the conservation of lepton number.

This principle of the conservation of lepton flavour would imply that the neutrinos produced in $\pi^+ \to \mu^+ \nu_\mu$ decay are unable to interact with matter to produce electrons. This hypothesis was tested by Lederman, Schwartz and Steinberger using one of the first accelerator based neutrino experiments [8].

This experiment utilised a 15GeV proton beam striking a stationary target to produce charged pions, both π^+ and π^-. These pions would decay in flight, producing muon neutrinos see Fig 1.1. A 13.5m thick iron shield was used to stop the majority of the muons produced by these decays, permitting only the neutrinos to reach the detection region.

The detector used was a 10ton aluminium spark chamber. The expected behaviour, if muon neutrinos were different to electron neutrinos, would be an excess of events in the detector producing muons relative to electrons. In the detector muons would be seen as single spark tracks passing through numerous aluminium plates. Electrons would however cause showers of sparks and pass through fewer layers of the spark chamber.

In total, subtracting the cosmic background, 29 muon events were detected, as compared to just six shower events. Accounting for detector efficiency, 20 such showers would be expected if there were only one neutrino flavour. This was therefore conclusive evidence that the neutrinos produced by pion decay were indeed different from those produced in radioactive decay.

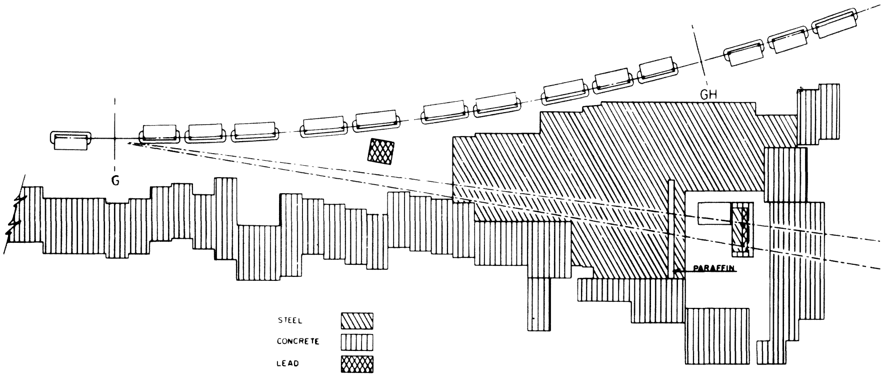

FIGURE 1.1: The experimental setup of the Lederman, Schwartz and Steinberger experiment. Protons strike a target at point G, producing charged pions. These decay to muon neutrinos and pass through the steel shielding. A small fraction interact in the Aluminium spark chamber detector and are identified as electron or muon flavour. Reproduced from [8].

Tau Neutrinos

The 1975 observation of interactions consistent with the production of a new heavy, charged lepton (τ) at the $e^+ e^-$ collider at SLAC [9] provided the first evidence of the theorised third generation of leptons. Subsequent experiments [10] [11] in 1976-77 provided additional evidence for the existence of this generation.

The detection method used for the tau lepton discovery, that of observing missing energy in a collider was consistent with a tau neutrino. However it would not be until 2000 that the first direct detection of a tau neutrino interaction would be made.

The DONUT experiment was constructed with the express purpose of detecting ν_τ. An 800GeV proton beam from the TeVatron was sent to a beam dump. The D_s mesons produced by this decayed into τ and $\bar{\nu}_\tau$, these τ's would then further decay into ν_τ [12].

An emulsion detector consisting of layers of nuclear emulsion, some with interleaved steel sheets was located behind a thick shield, 36m downstream of the target. A ν_τ interaction would be associated with a short τ track in the developed emulsion. This would originate in the steel or the emulsion and show a distinct kink at the τ decay point, followed by a subsequent track from a single charged daughter.

In total, four events were found to meet the requirements for the τ selection against an expected 0.34 ± 0.05 events without ν_τ interactions. This thus provided final confirmation of the existence of the third neutrino generation.

Further Generations

Searches for fourth or higher generation fermions have not yet yielded any conclusive evidence for their existence. A fourth generation of neutrinos are strongly limited by the combined results obtained by ALEPH, DELPHI, L3, OPAL at CERN and SLD at SLC [13]. These experiments looked for the decay width of Z^0 bosons to invisible i.e. $Z^0 \rightarrow \nu\bar{\nu}$, this width is directly related to the number of light neutrino generations ($M_\nu < M_Z/2$). These results showed a strong preference for three light neutrino generations see Fig 1.2.

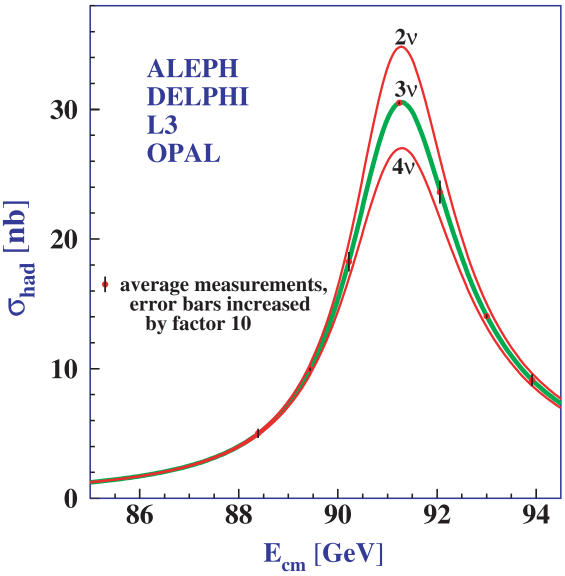

FIGURE 1.2: The cross-section for hadron production around the Z mass peak for the combined ALEPH, DELPHI, L3, OPAL and SLD dataset. The data is in agreement with the SM prediction with three light neutrino generations and strongly disfavours the two or four neutrino prediction overlaid. Reproduced from [13].

A fit to these data yields $N_\nu = 2.9840 \pm 0.0082$ in agreement with the known three generations and strongly excluding further generations.

As a result, any fourth generation of neutrino must either have a mass greater than approximately $M_Z/2$ or not couple to the Z. This is the subject of ongoing investigation into heavy neutral leptons and sterile neutrinos respectively.

1.1.3 Modern View

In the modern interpretation of the Standard Model (SM), there are known to be three generations of charged lepton, each associated with a single, separate neutrino as seen in Fig 1.3.

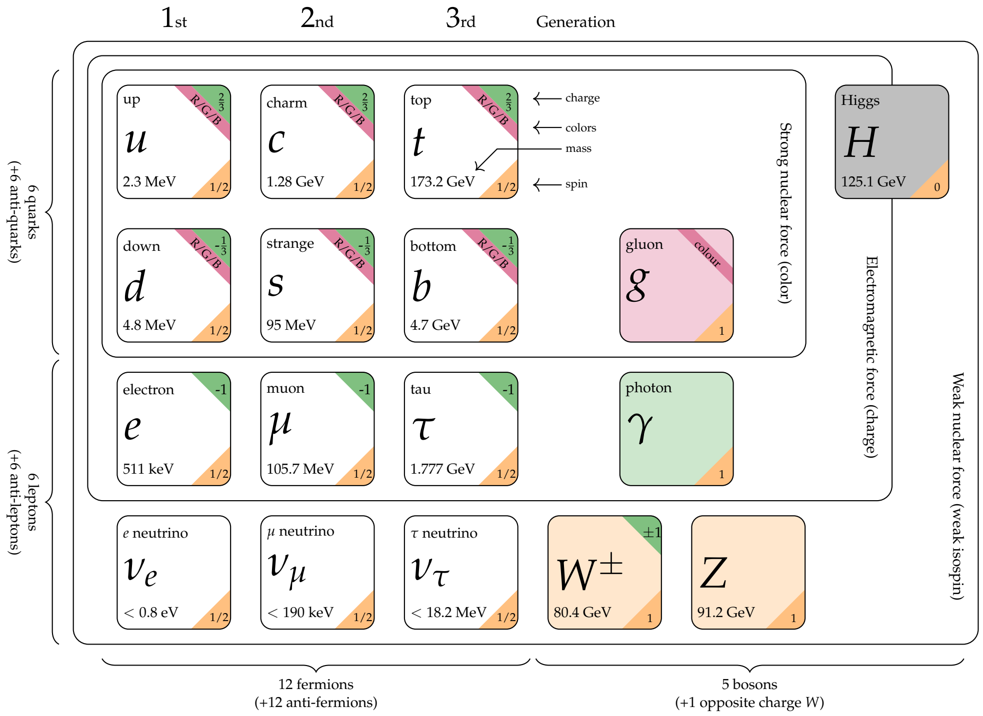

FIGURE 1.3: The fundamental particles in the Standard Model. Adapted from [14]. Values taken from [15] and [16].

Neutrinos have no electric or colour charge and therefore do not interact via the electromagnetic or strong forces. Interactions via the weak force are possible and are the only way neutrinos can be produced or detected in the SM.

The large masses of the $W^{\pm}$ and Z^{0} bosons (80.4 and 91.2GeV respectively) are the cause of the observed low interaction probability for neutrinos with energy on the GeV scale. As there is insufficient centre-of-mass energy to produce an on-shell boson, the interaction cross-section is suppressed by a factor G_F^2 ($1.36 \times 10^{-10}\,\mathrm{GeV}^2/c^4$) compared to an EM mediated interaction.

One consequence of neutrinos only interacting via the weak force is that (anti) neutrinos are always produced in left (right) handed chiral states. In the Standard Model, neutrinos are massless, and helicity and chiral states coincide. This implies a left (right) handed helicity state which does not evolve with time. Thus there are no right (left) handed (anti)neutrinos. This is in contrast with all other fermions in the Standard Model which can take on both states.

With the observation of neutrino oscillations, §1.2 neutrinos are known to be massive, however their absolute masses are unknown. The best direct limits on neutrino mass come from the KATRIN experiment, which provides an upper limit on the mass of electron neutrinos at 0.8eV (90% confidence) [16]. The mechanism for this mass generation is currently unknown.

The inclusion of a Higgs mass term for neutrinos requires an extremely small coupling constant to yield the observed limits on neutrino masses and requires the introduction of a right-handed neutrino field [17].

One other possibility is that of a Majorana mass term [18]. In this scheme neutrinos and antineutrinos are considered as equivalent but with different chirality i.e. 'antineutrinos' are simply right-handed neutrinos. This possibility is currently an active area of research for neutrinoless double beta decay ($0\nu\beta\beta$) experiments such as CUORE [19] and KamLAND-Zen [20]. The presence of the Majorana mass term allows for the existence of the 'see-saw' mechanism [21] which is capable of naturally explaining the small mass of neutrinos through the inclusion of an extremely massive right-handed neutrino.

The neutrino flavours are associated with the charged leptons via the requirement of lepton flavour conservation, hence the only allowable interaction vertex between a charged lepton and its associated neutrino in the standard model is:

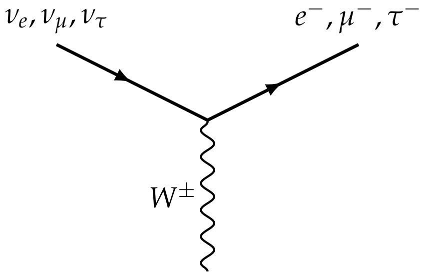

1.2 Neutrino Oscillation

While no direct measurement has yet placed a lower bound on the mass of neutrinos, it is known that neutrino mass is non-zero. Evidence of this derives from the observation of neutrino oscillation.

Neutrino oscillation describes the change in flavour of a neutrino as it propagates through space. A neutrino originally produced as a muon neutrino, has variable probability of being observed as a muon flavour as a function of distance travelled.

Such a neutrino would start as pure muon flavour, becoming almost entirely tau flavour after a certain distance, then at double this distance becoming almost entirely muon flavour again.

This behaviour is only possible if the neutrino states have different masses, resulting in the states propagating through space differently and interfering. Observation of neutrino oscillation therefore necessitates non-zero neutrino masses.

The first experimental evidence of this effect was made at the Homestake experiment in 1968 [22]. This experiment used the reaction of ν_e ^{8}B solar neutrinos with chlorine:

$$^{37}Cl + \nu_e \rightarrow {}^{37}Ar^+ + e^- \tag{1.2}$$

The resulting unstable isotope of argon was extracted and counted using its decays. Compared to the contemporary prediction for the ν_e ^{8}B flux [23] this experiment reported approximately 1/3rd the flux of the prediction. Similar results were later observed by SAGE [24], GALLEX [25] and Kamiokande [26].

In the neutrino oscillation paradigm, this can be explained as the effect of oscillation from ν_e to ν_μ and ν_τ. Due to the large distance to the sun and wide energy spread of the ^{8}B neutrinos, the flux at earth averages out to approximately equal quantities of each neutrino flavour. With experiments sensitive to only electron neutrinos this manifests as an observation of only 1/3rd the expected event rate without oscillations.

Proof that this effect was a result of neutrino oscillation would wait until the joint observations at SK (Super-Kamiokande) [27] and SNO (Sudbury Neutrino Observatory) [28][29]. SK detected oscillation of atmospheric neutrinos and SNO detected the presence of a ν_μ and ν_τ component of solar flux.

SK used the flux of neutrinos produced by cosmic ray interactions in the atmosphere. The angle at which such a neutrino reaches SK is dependant on its production point. A directly downward going neutrino would have been produced directly above SK with a travel distance of approximately 15km, while a vertically upwards going neutrino would have travelled 13 000km from the other side of the earth. As neutrino production was expected to be approximately homogeneous around the world, the angle of the incident neutrino could be used as a measure of the distance travelled by the neutrino and therefore the baseline for potential oscillation.

SK observed a significant deficit of upwards going muon neutrino interactions relative to the unoscillated prediction and well described by a fitted oscillation model. Muon neutrinos travelling a greater distance being more likely to have oscillated to an unobserved tau neutrino than those being produced closer to SK, as seen in Fig 1.4.

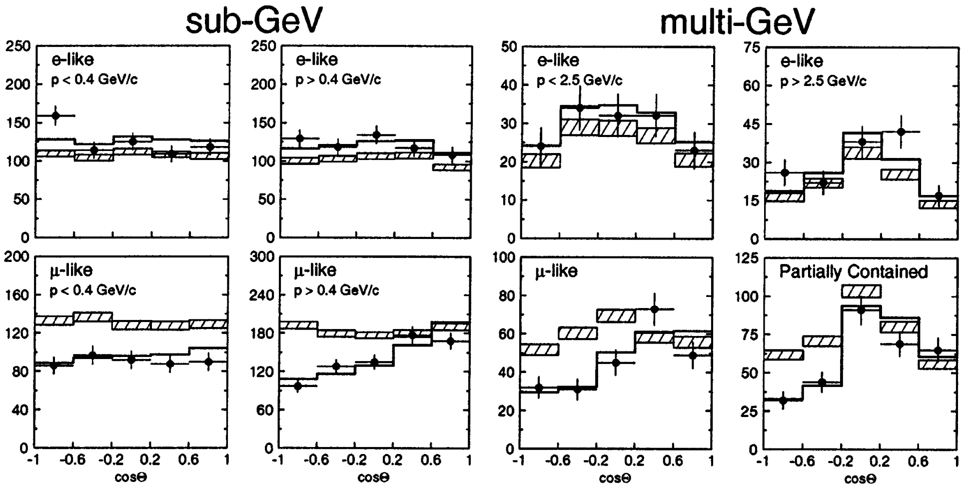

FIGURE 1.4: The predicted unoscillated event rate (hatched) compared to the observed data and a fit with oscillation (black) for the eight samples used in the SK neutrino oscillation discovery. Little change is observed in the electron-like samples relative to the prediction, however all of the muon-like samples show a significant difference relative to the prediction. Additionally a dependence on zenith angle is seen, indicating a relationship between distance travelled and probability of being observed as ν_μ. Reproduced from [27].

While this observation was strong evidence for neutrino oscillation from ν_μ to ν_τ or other unobserved neutrino, this was not in and of itself, evidence for an explanation of the observed solar neutrino ν_e deficit.

The SNO experiment's solar neutrino measurements were able to resolve this. ^{8}B neutrinos produced in the sun have insufficient kinetic energy to generate muons or taus during a charged-current interaction. Thus in previous experiments relying solely on CC (charged-current) interactions, the flux of ν_μ and ν_τ were not observable. SNO was also sensitive to ν_μ and ν_τ flux, making use of elastic scattering off atomic electrons and through the use of a heavy water target, observation of neutral-current interactions were also possible.

NC (neutral current) interactions were detectable via tagging of the neutron emitted during an NC interaction on deuterium. As no massive, charged lepton is produced in NC interactions, the energy threshold of this reaction is the deuterium binding energy of 2.2MeV and is the same for all neutrino flavours. This therefore allows a measurement of total ^{8}B neutrino flux to be made in addition to the ν_e only CC interaction. Elastic scattering of a neutrino off an atomic electron has an NC component for all three neutrino flavours in addition to a CC component for ν_e alone, hence the total event rate in this channel provides some sensitivity to the NC contribution from ν_μ and ν_τ.

The resultant constraint on ν_e and $\nu_\mu + \nu_\tau$ flux can be seen in Fig 1.5, there is good agreement between all three samples, showing approximately 1/3$^{\text{rd}}$ of the total neutrino flux being ν_e with the remaining 2/3$^{\text{rds}}$ being ν_μ and ν_τ. This result definitively showed that the disappearance of solar ν_e's was associated with a corresponding increase in ν_μ and ν_τ, consistent with the effects of neutrino oscillation.

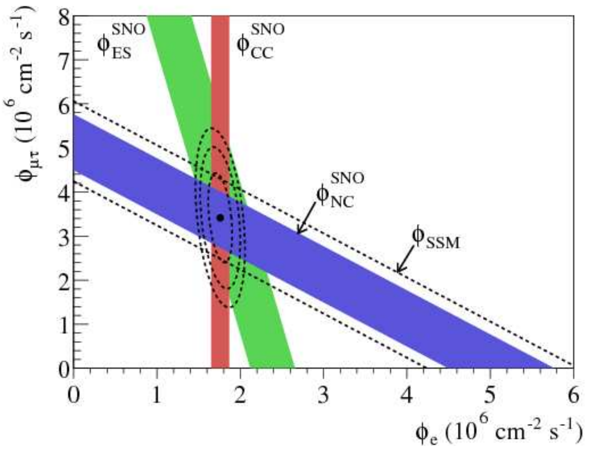

FIGURE 1.5: The flux of ^{8}B solar neutrinos measured by SNO from its three interaction channels, each providing differing sensitivity to ν_e and total neutrino flux. The three constraints overlap well in a region predicted by the standard solar model with oscillation. Reproduced from [28].

The combination of observations at SK and SNO therefore provided definitive experimental evidence for both ν_μ and ν_e oscillation. This explained the solar neutrino deficit observed in experiments since Homestake and proved that neutrinos must have mass.

1.2.1 Oscillation Probability

The observation of neutrino oscillation implies that neutrinos have non-zero mass. In addition, it is necessary for the flavour eigenstates to differ from the mass eigenstates.

The PMNS (Pontecorvo–Maki–Nakagawa–Sakata) formalism describes the relationship between neutrino flavour and mass eigenstates. Neutrinos are produced and interact as neutrino flavour eigenstates; ν_e, ν_μ and ν_τ, these are eigenstates of the weak interaction. The eigenstates of the vacuum Hamiltonian are given by the mass states ν_1, ν_2 and ν_3. These states individually can propagate freely as a plane wave through space.

The relationship (mixing) between these flavour and mass eigenstates is given by:

$$|\nu_i\rangle = \sum_\alpha U_{\alpha i}|\nu_\alpha\rangle \tag{1.3}$$

Where $|\nu_i\rangle$ denotes mass eigenstate $i \in \{1,2,3\}$ and $|\nu_\alpha\rangle$ denotes flavour eigenstate $\alpha \in \{e,\mu,\tau\}$. The orthogonal basis $|\nu_i\rangle$ is composed of a linear combination of the flavour basis $|\nu_\alpha\rangle$.

The propagation of these mass eigenstates is governed by the time-dependant Schrodinger equation:

$$i\frac{d}{dt}|\nu_i\rangle = \mathcal{H}|\nu_i(t)\rangle \tag{1.4}$$

Hence a neutrino mass eigenstate propagating in vacuum has the plane wave solution:

$$|\nu_i(x)\rangle = e^{-ip^\mu x_\mu}|\nu_i(0)\rangle \tag{1.5}$$

Here p is the four-momentum of the neutrino and x is the four-position. In the ultra-relativistic limit where $m_j \ll |\vec{p}|$ the energy of the neutrino mass eigenstate is given by:

$$E = \sqrt{m_i^2 + |\vec{p}|^2} \approx |\vec{p}| + \frac{m_i^2}{2|\vec{p}|} \tag{1.6}$$

In addition, as the neutrino is ultra-relativistic $|\vec{p}| \approx E$, its distance from the initial point as a function of time is given by $L \approx t$ thus:

$$P^{\mu} x_{\mu} = Et - |\vec{p}|L \approx \left(|\vec{p}| + \frac{m_i^2}{2|\vec{p}|} \right) L - |\vec{p}|L = \frac{Lm_i^2}{2E} \tag{1.7}$$

Substituting this into eqn 1.5 yields the wavefunction at the position L:

$$|\nu_i(L)\rangle = e^{-i\frac{L}{2E}m_i^2} |\nu_i(0)\rangle \tag{1.8}$$

The probability of a neutrino starting in flavour eigenstate α oscillating to flavour eigenstate β after travelling a distance L is given by:

$$p(\nu_\alpha \to \nu_\beta) = |\langle \nu_\beta | \nu_\alpha(L) \rangle|^2 \tag{1.9}$$

Using equations 1.3, 1.8 and 1.9 this oscillation probability can be expressed as:

$$p(\nu_\alpha \to \nu_\beta) = \left| \sum_i U_{\alpha i}^{*} e^{-i\frac{L}{2E}m_i^2} \langle \nu_\beta | \nu_i \rangle \right|^2 = \left| \sum_i \sum_\gamma U_{\alpha i}^{*} U_{\gamma i} e^{-i\frac{L}{2E}m_i^2} \langle \nu_\beta | \nu_\gamma \rangle \right|^2 \tag{1.10}$$

Using orthogonality $\langle \nu_\beta | \nu_\gamma \rangle = \delta_{\beta\gamma}$, this can be simplified to:

$$P(\nu_\alpha \to \nu_\beta) = \left| \sum_i U_{\alpha i}^{*} U_{\beta i} e^{-i\frac{L}{2E}m_i^2} \right|^2 \tag{1.11}$$

Expanding this out:

$$P(\nu_\alpha \to \nu_\beta) = \sum_i \sum_j U_{\alpha i}^{*} U_{\beta i} U_{\alpha j} U_{\beta j}^{*} e^{-i\frac{L}{2E}\Delta m_{ij}^2} \tag{1.12}$$

where $\Delta m_{ij}^2 \equiv m_i^2 - m_j^2$. Using the unitarity property of the PMNS matrix, this is most often written as [17]:

$$\begin{aligned} P\left(\overset{(-)}{\nu}_\alpha \to \overset{(-)}{\nu}_\beta \right) = \delta_{\alpha\beta} - 4 \sum_{i>j} \Re\{U_{\alpha i}^{*} U_{\beta i} U_{\alpha j} U_{\beta j}^{*}\} \sin^2 \left(\frac{\Delta m_{ij}^2 L}{4E} \right) \\ + (-)2 \sum_{i>j} \Im\{U_{\alpha i}^{*} U_{\beta i} U_{\alpha j} U_{\beta j}^{*}\} \sin \left(\frac{\Delta m_{ij}^2 L}{2E} \right) \end{aligned} \tag{1.13}$$

the sign of the final term being negative for antineutrino oscillation.

The probability of oscillation therefore depends on the magnitude and phases of the PMNS matrix elements. The oscillation length depends on the squared mass differences between the neutrino mass states Δm^2_{ij} and the energy of the neutrino.

There are a number of points that are illustrated by eqn. 1.13:

- For oscillations to occur Δm^2_{ij} must be non-zero. Hence the observation of atmospheric and solar neutrino oscillation implies that the three mass states have different masses with at least two being non-zero.

- The absolute mass of the neutrinos cannot be determined by oscillation experiments alone, only the mass squared differences $(m^2_i - m^2_j)$ can be measured.

- In vacuum, the sign of Δm^2_{ij} only affects the final term of eqn 1.13. Hence the sign of Δm^2_{ij} cannot be determined by vacuum oscillation experiments without additional knowledge of the complex component of the PMNS matrix. This results in an ambiguity in the ordering of the mass states. Normal Ordering (NO): $m_1 < m_2 < m_3$ or Inverted Ordering (IO): $m_3 < m_1 < m_2$.

- If the PMNS matrix has complex components then the oscillation probability $P(\nu_\alpha \rightarrow \nu_\beta) \neq P(\bar{\nu}_\alpha \rightarrow \bar{\nu}_\beta)$ i.e. neutrino oscillations can violate CP symmetry.

1.2.2 PMNS Matrix

The PMNS matrix, describing the relationship between the mass and flavour states eqn. 1.3 can be described by a unitary 3×3 matrix with nine free parameters. Neglecting non-observable degrees of freedom, and neglecting the Majorana phases, this can be composed of three rotation matrices and one complex phase [17]. One of the most common such parameterisations and that used throughout this thesis is [30]:

Parameter	Normal Ordering	Inverted Ordering
$\sin^2\theta_{12}$	$0.304^{+0.012}_{-0.012}$	$0.304^{+0.013}_{-0.012}$
$\sin^2\theta_{13}$	$0.02246^{+0.00062}_{-0.00062}$	$0.02241^{+0.00074}_{0.00062}$
$\sin^2\theta_{23}$	$0.450^{+0.019}_{-0.016}$	$0.570^{+0.016}_{-0.022}$
δ_{CP}/Rad	$-2.27^{+0.63}_{-0.44}$	$-1.43^{+0.38}_{-0.52}$
$\delta m^2_{21}(\times 10^{-5} eV^2)$	$7.42^{+0.21}_{-0.20}$	$7.42^{+0.21}_{-0.20}$
$\delta m^2_{32}(\times 10^{-3} eV^2)$	$2.510^{+0.027}_{-0.027}$	$-2.490^{+0.026}_{-0.28}$

TABLE 1.1: The current NuFIT [31][32] global best-fit values for the neutrino oscillation parameters and their ±1σ ranges.

$$
\begin{aligned}
U_{PMNS} &= \begin{pmatrix} 1 & 0 & 0 \\ 0 & c_{23} & s_{23} \\ 0 & -s_{23} & c_{23} \end{pmatrix} \begin{pmatrix} c_{13} & 0 & s_{13}e^{-i\delta_{CP}} \\ 0 & 1 & 0 \\ -s_{13}e^{i\delta_{CP}} & 0 & c_{13} \end{pmatrix} \begin{pmatrix} c_{12} & s_{12} & 0 \\ -s_{12} & c_{12} & 0 \\ 0 & 0 & 1 \end{pmatrix} \\
&= \begin{pmatrix} c_{12}c_{13} & s_{12}c_{13} & s_{13}e^{-i\delta_{CP}} \\ -s_{12}c_{23} - c_{12}s_{23}s_{13}e^{i\delta_{CP}} & c_{12}c_{23} - s_{12}s_{23}s_{13}e^{i\delta_{CP}} & s_{23}c_{13} \\ s_{12}s_{23} - c_{12}c_{23}s_{13}e^{i\delta_{CP}} & -c_{12}s_{23} - s_{12}c_{23}s_{13}e^{i\delta_{CP}} & c_{23}c_{13} \end{pmatrix}
\end{aligned}
\tag{1.14}
$$

where $s_{ij} = \sin(\theta_{ij})$ and $c_{ij} = \cos(\theta_{ij})$. This is unitary by construction and has four independent parameters: θ_{12}, θ_{13}, θ_{23} and δ_{CP}. The current global best-fit values of these parameters is shown in Table 1.1.

1.2.3 Matter Effects

One additional factor must be considered for terrestrial experiments; the impact of the medium in which the neutrinos propagate. While hard neutrino scatters on matter are rare, neutrinos do experience a different effective potential in matter to that of the vacuum.

This is caused by two coherent forward scattering processes between neutrinos and matter, shown in Fig 1.6. In these interactions, a weak boson is exchanged between the neutrino and an atomic electron or nucleus in the matter.

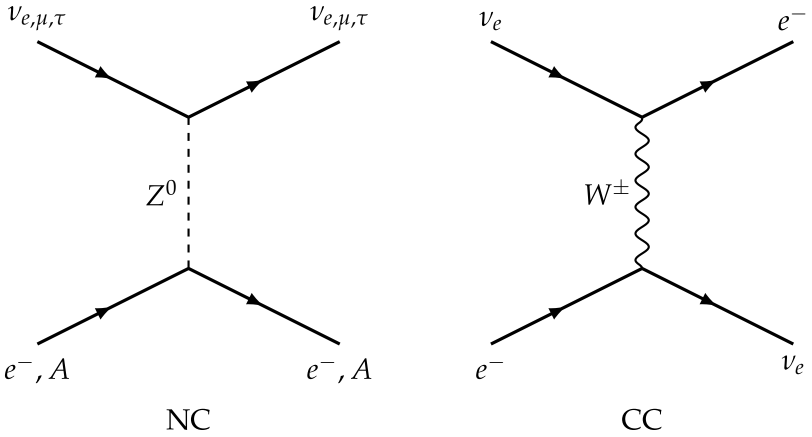

FIGURE 1.6: Tree level Feynman diagrams for the coherent forward scattering process. All neutrino flavours undergo neutral-current scattering off atomic electrons or nuclei while only ν_e can undergo a charged-current interaction with atomic electrons.

As the neutral current Z interaction is flavour agnostic, each neutrino flavour experiences the same effective potential V_{NC}. The $W^\pm$ interaction however is only possible for ν_e and $\bar{\nu}_e$, hence only electron flavour neutrinos experience the effective potential V_{CC}. These potentials can be added to the vacuum Hamiltonian to obtain the effective propagation Hamiltonian for neutrinos in matter.

Here in the flavour basis (ν_e, ν_μ, ν_τ) the effective Hamiltonian can be written as:

$$\mathcal{H}_{Eff} = \mathcal{H}_{Vac} + V_{Matter} = \mathcal{H}_{Vac} + \begin{pmatrix} V_{NC} + V_{CC} & 0 & 0 \\ 0 & V_{NC} & 0 \\ 0 & 0 & V_{NC} \end{pmatrix} \tag{1.15}$$

As the NC component is proportional to the identity matrix, this has no effect on the relative phase of the neutrino mass eigenstates and therefore does not impact neutrino flavour oscillation [15][33]. The CC interaction does however contribute, changing the effective propagation eigenstates and mass splittings.

The matter potential V_{CC} is given by [34]:

$$V_{CC} = \pm\sqrt{2}G_F n_e \tag{1.16}$$

Here G_F is the Fermi constant and n_e is the number density of electrons in the medium, the term is positive for ν_e and negative for $\bar{\nu}_e$. The impact of matter effects is therefore opposite for neutrino and antineutrino propagation.

1.2.4 Phenomenology

No current single experiment is able to measure all of the oscillation parameters of the PMNS matrix eqn. 1.3 and the mass splittings. A combination of measurements from different experiments is therefore used to constrain these parameters. The sensitivity of different experiment types is summarised in Table 1.2.

Experiment	Sensitivity
Solar Experiments	θ_{12}, θ_{13}, Δm^2_{21}
Reactor LBL	θ_{12}, θ_{13}, Δm^2_{21}
Reactor MBL	θ_{13}, $\lvert\Delta m^2_{31}\rvert$, $\lvert\Delta m^2_{32}\rvert$
Atmospheric Experiments	θ_{13}, θ_{23}, δ_{CP}, $\lvert\Delta m^2_{31}\rvert$, $\lvert\Delta m^2_{32}\rvert$
Accelerator LBL $\nu_\mu \to \nu_\mu$	θ_{23}, $\lvert\Delta m^2_{31}\rvert$, $\lvert\Delta m^2_{32}\rvert$
Accelerator LBL $\nu_\mu \to \nu_e$	θ_{13}, θ_{23}, δ_{CP}

TABLE 1.2: The ability of different experiment types to provide measurements of different PMNS parameters. Reproduced from [15].

Accelerator based LBL (long baseline) experiments offer leading sensitivity for the atmospheric mass splitting, θ_{23} and δ_{CP}, in addition these experiments have some sensitivity to θ_{13} and the neutrino mass ordering [35].

These LBL experiments have a number of advantages over atmospheric only experiments for precision measurement: the beam is produced at a known distance to the detector, with a predictable and measurable flux and using the off-axis principle §2.2.3 can be made to target their peak flux around a maximum of oscillation probability.

Currently the best method for generating a high intensity neutrino beam is through the decay of boosted, charged pions, see §2.2.2. Such beams are dominated by muon flavour neutrinos and antineutrinos, due to the high branching ratio for pion decay to muons. As such, LBL experiments are typically able to observe the $\nu_\mu \to \nu_\mu$ 'disappearance' channel or the $\nu_\mu \to \nu_e$ 'appearance' channel at a detector some distance away.

The probability of observing a muon neutrino some distance L from the ν_μ production point is given by [36]:

$$
\begin{aligned}
P\left(\overset{(-)}{\nu}_\mu \to \overset{(-)}{\nu}_\mu\right) &\approx 1 - 4\left((s_{23}^2 c_{13}^2)(1 - s_{23}^2 c_{13}^2)\right)\sin^2\left(\Delta_{32} + \Delta_{21}\frac{s_{12}^2 c_{23}^2}{1 - s_{23}^2 c_{13}^2}\right) \\
&\quad + \mathcal{O}\left(a^2, \Delta_{21}\right) \\
&\approx 1 - \sin^2 2\theta_{23}\sin^2\left(\Delta_{32}\right)
\end{aligned}
\tag{1.17}
$$

Where $\Delta_{ij} = \frac{\Delta m_{ij}^2 L}{4E}$ and the matter effect contribution $a = G_F n_e L/\sqrt{2}$.

For many LBL experiments, such as Tokai to Kamioka (T2K) and Hyper-Kamiokande (HK), L is chosen such that $\Delta_{31} \approx \pi/2$ for the peak of the ν_μ flux distribution.

Due to the much smaller mass splitting $\Delta m_{21}^2 \ll \Delta m_{32}^2$ for these LBL experiment baselines $\sin\Delta_{21} \ll 1$, hence terms of order Δm_{21}^2 are omitted. In addition, over these baselines matter effects in ν_μ disappearance are small $a^2 \approx 0.01$, hence these may be ignored. From reactor neutrino experiments θ_{13} is known to be small [37], hence c_{13}^2 is taken to be unity.

From this probability, it can be seen that the disappearance channel is heavily affected by θ_{23} and the mass splitting Δm_{32}^2.

As the neutrino beams used in LBL experiments have a broad energy distribution, Δ_{32} will vary significantly across this energy distribution, hence so will the oscillation probability, as seen in Fig 1.7. LBL experiments are sensitive to θ_{23} through the amplitude of this disappearance probability. The neutrino energy corresponding to the minimum in the oscillation probability is sensitive to Δm_{32}^2.

Including matter effects, the probability for ν_μ to ν_e oscillation is given by [33]:

$$
\begin{aligned}
P\left(\overset{(-)}{\nu}_\mu \to \overset{(-)}{\nu}_e\right) \approx{}& \sin^2\theta_{23}\sin^2 2\theta_{13}\frac{\sin^2\left(\Delta_{31} \mp a\right)}{(\Delta_{31} \mp a)^2}\Delta_{31}^2 \\
&+ \sin 2\theta_{23}\sin 2\theta_{13}\sin 2\theta_{12}\cos\theta_{12}\frac{\sin\left(\Delta_{31} \mp a\right)}{\Delta_{31} \mp a}\Delta_{31}\frac{\sin a}{a}\Delta_{21}\cos\Delta_{31}\cos\delta_{CP} \\
&\mp \sin 2\theta_{23}\sin 2\theta_{13}\sin 2\theta_{12}\cos\theta_{12}\frac{\sin\left(\Delta_{31} \mp a\right)}{\Delta_{31} \mp a}\Delta_{31}\frac{\sin a}{a}\Delta_{21}\sin\Delta_{31}\sin\delta_{CP} \\
&+ \cos^2\theta_{13}\cos^2\theta_{23}\sin^2 2\theta_{12}\frac{\sin^2 a}{a^2}\Delta_{21}^2
\end{aligned}
\tag{1.18}
$$

Where the symbols have the same meaning as in eqn. 1.17. Here again, around the ν_μ oscillation maximum $\Delta_{32} \approx \pi/2$ and $\Delta_{21} \ll \Delta_{32}$ hence the first term is the leading contribution. Unlike ν_μ disappearance however, due to the small value of θ_{13} the second and third terms are important.

Notably the term proportional to $\sin\delta_{\mathrm{CP}}$ has opposite sign for ν_e and $\bar{\nu}_e$, non-zero values of $\sin\delta_{\mathrm{CP}}$ therefore result in different behaviour for neutrinos and antineutrinos. Discovery and subsequent measurement of this matter-antimatter asymmetry (CP symmetry violation) is of particular interest to LBL experiments owing to its potential importance to baryon asymmetry.

At LBL experiments, measurement of this can be performed by observing ν_e and $\bar{\nu}_e$ event rates. Taking the difference in ν_e and $\bar{\nu}_e$ appearance probability cancels most of the contribution from the leading terms and isolates the $\sin\delta_{\mathrm{CP}}$ term. This allows for a more sensitive measurement of δ_{CP} with less reliance on the precise determination of the other oscillation parameters.

The appearance oscillation probability depends strongly on θ_{13} and δ_{CP}. Changes in θ_{13} and δ_{CP} both affect the normalisation of the ν_e and $\bar{\nu}_e$, an increase in θ_{13} increasing the event rate in both, however δ_{CP} can increase the event rate for neutrino and decrease for antineutrino and vice a versa.

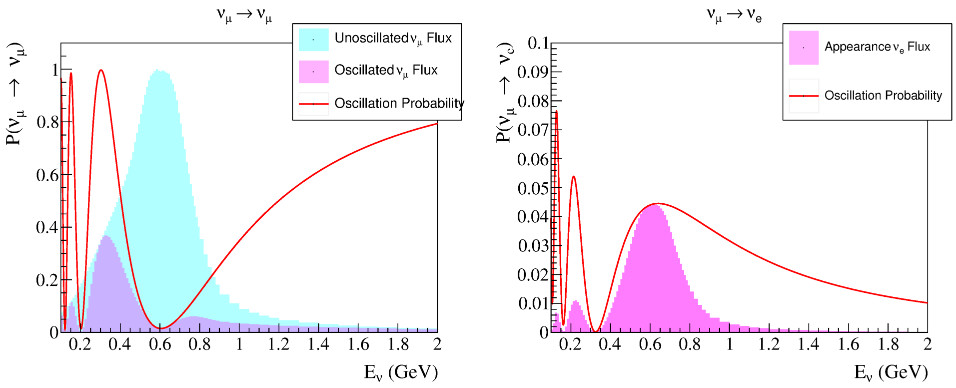

FIGURE 1.7: The oscillation probability and expected T2K fluxes for $\nu_\mu \to \nu_\mu$ oscillation (left) and $\nu_\mu \to \nu_e$ (right). The oscillation parameters are those of the NuFIT best point as in Table 1.1.

1.2.5 Mass Ordering

As discussed in §1.2.1 the masses of the states ν_1, ν_2, ν_3 are not observable in oscillation experiments, only their mass squared differences can be measured. In addition, the sign of the mass squared difference Δm^2_{32} is unknown. As such, the ordering of these mass states have two possibilities: Normal Ordering $m_1 < m_2 < m_3$ which would mirror the behaviour seen in charged leptons and quarks or Inverted Ordering $m_3 < m_1 < m_2$ as shown in Fig 1.8.

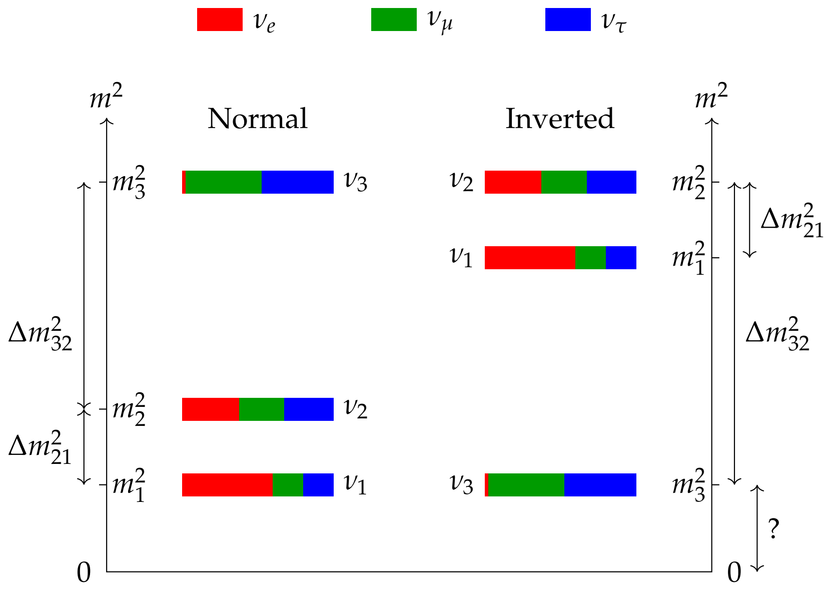

FIGURE 1.8: A diagram of the neutrino masses and the approximate composition of each neutrino mass state in terms of the flavour states for the two possible mass orderings.

While this ordering ambiguity cannot be resolved by oscillation experiments in vacuum, the addition of matter effects has the ability to break this degeneracy. As seen in eqn 1.18 the magnitude of the leading terms depend on the sign of Δm_{31}^2, with a larger effect as $a \rightarrow \Delta_{31}$ where $a = G_F n_e L/\sqrt{2}$. Therefore, for LBL experiments investigating mass ordering, the higher energy region with lower Δ_{31} increases the impact of the mass ordering on the observed oscillation probability.

1.3 Neutrino Interactions

In LBL neutrino oscillation experiments, the observation of neutrinos is dependant on a neutrino interacting with a target nucleus. The complexity of the strongly bound nucleus coupled with the neutrino energy range in use by LBL experiments (0.3 — 5GeV) means that numerous interactions are possible. The cross-sections for these interactions are not precisely known, hence the uncertainty on these can be a dominant systematic uncertainty in LBL experiments [38].

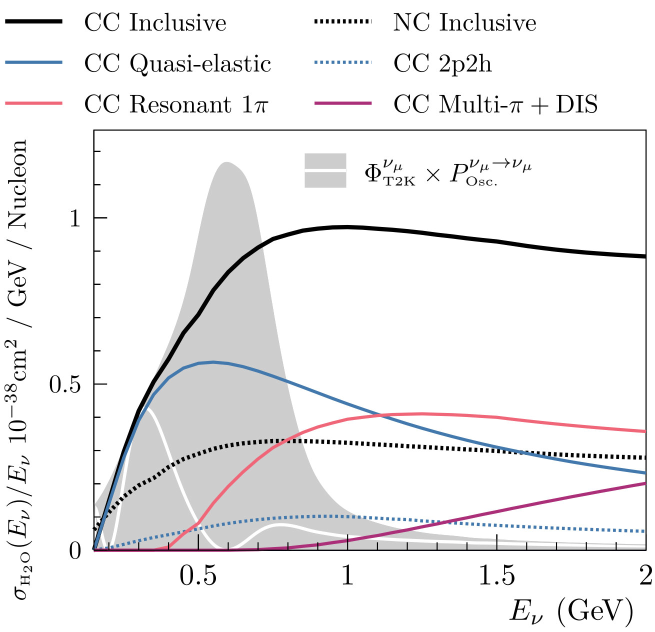

FIGURE 1.9: The interaction cross-section for ν_μ on water broken down by interaction type. Superimposed with the unoscillated T2K ν_μ flux (grey) and a typical oscillated flux (white). At T2K energies, CCQE is the leading interaction type, however NC and CC1π contribute significantly at higher energies. Reproduced from [39].

1.3.1 Interaction Types

Neutrino interactions with nuclei can be separated into two groups, charged current (CC) and neutral current (NC) interactions, corresponding to the exchange of a W and Z boson respectively. At the GeV scale, interactions are possible across the entire nucleus coherently, with a single nucleon and even with individual quarks, the most common of these being a single nucleon interaction.

These CC and NC interactions can be further broken down by the interactions of the struck nucleon or quark within the nucleus. Due to the complexity of nuclear modelling, the number of possible interactions is high, hence for analysis purposes, many of these are grouped according to the number and types of observable particles escaping the nucleus.

The cross-section of some of these interactions in the energy range of relevance for T2K can be seen in Fig 1.9. Several interaction types are possible in this energy range, each requiring consideration for a full understanding of T2K data.

CC0π

The dominant interactions in the low to medium energy region of the T2K and HK flux (0—1GeV) are CC0π interactions. These are charged-current neutrino interactions which produce no pions escaping the nucleus, there may however be other escaping hadrons.

This work focuses on water Cherenkov detectors at single GeV energy scale, hence distinction is not made by number of outgoing hadrons. Such low-energy hadrons will lack sufficient energy to be detectable via Cherenkov emission.

There are multiple possible in-nucleus interactions that contribute to this overall interaction type, including charged-current quasi-elastic (CCQE) and the interaction with a pair of nucleons (2p-2h), schematic diagrams of these can be seen in Fig 1.10.

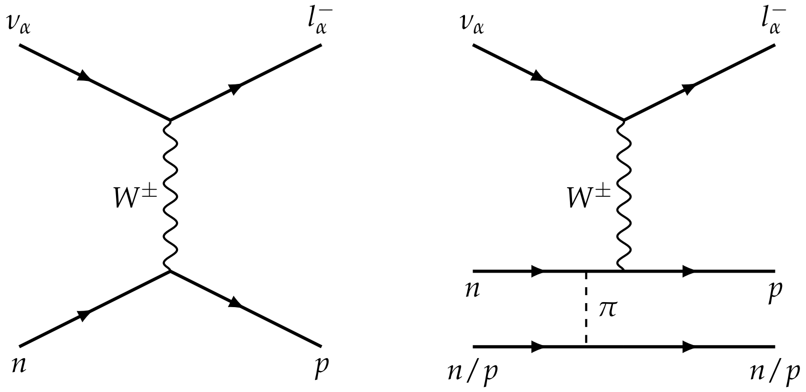

FIGURE 1.10: Schematic diagrams of a CCQE (left) and 2p-2h (right) interaction.

As can be seen in Fig 1.9 CCQE has a larger cross-section than 2p-2h however the 2p-2h contribution to CC0π is more significant at higher energies.

CC1π

At higher incident neutrino energies, a charged-current interaction producing a pion in the final state becomes the dominant interaction mode, see Fig 1.9.

In the Rein-Sehgal model for resonant pion production [40], the struck nucleon is excited into a resonant state, this then decays into a nucleon and a pion as seen in Fig 1.11.

Depending on the struck nucleon, the outgoing pion may be π^+ or π^0. The reaction producing π^- is less easily experimentally observed as such a π^- is readily absorbed in the nucleus.

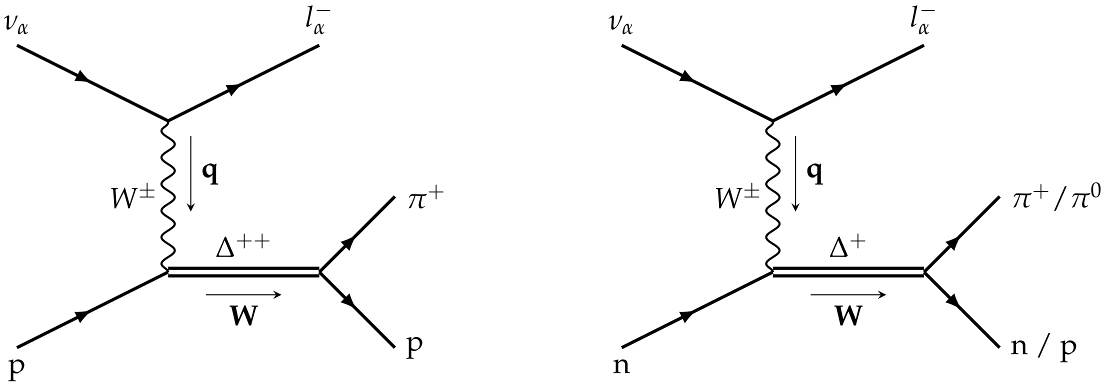

FIGURE 1.11: Resonant CC1π production via a Δ intermediate. **W** is the four-momentum of the intermediate. The four-momentum transfer from the neutrino to the nucleon is **q**.

CC1π events are also possible via non-resonant processes. The MC used by T2K and HK makes use of a simplified Rein-Sehgal model, including many of the possible resonant intermediates and their interference along with a non-resonant background.

NC1π

Neutral current interactions with a single pion in the final state are the most common, readily detectable NC events in T2K. These proceed via a similar resonant process to CC1π as in Fig 1.12.

NCπ^0 events are of significant interest as these are a major background to selecting electron neutrino events at water Cherenkov detectors. In addition, unlike other CC backgrounds to the electron neutrino samples, NC events are flavour agnostic and so their contribution is not decreased due to neutrino oscillation.

NC Coherent

Neutral current coherent interactions involve an interaction between a neutrino and the whole nucleus. This interaction does not excite or break apart the nucleus nor change its constituent nucleons as shown in Fig 1.13.

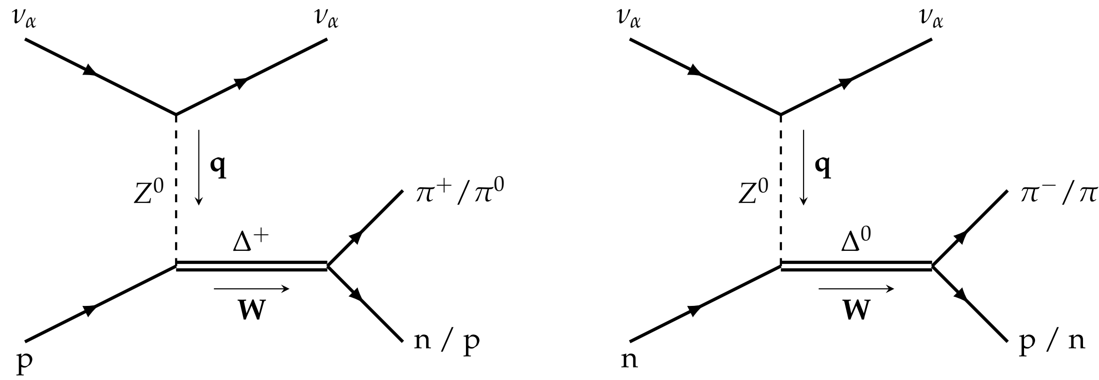

FIGURE 1.12: Resonant NC1π production via a Δ intermediate. **W** is the four-momentum of the intermediate. The four-momentum transfer from the neutrino to the nucleon is **q**.

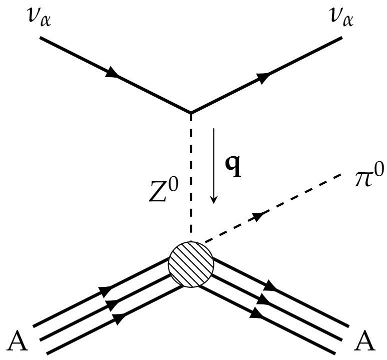

FIGURE 1.13: Coherent NC1π production on a whole nucleus, leaving the nucleus unchanged other than recoiling.

The experimental signature of such an interaction is extremely similar to that of NC1π interactions. The requirement of coherence across the whole nucleus and that the nucleus remains intact limits the available momentum transfer to the nucleus. As a result the outgoing pions are produced at a low angle relative to the incident neutrino.

Chapter 2

T2K

2.1 Introduction

The Tokai to Kamioka (T2K) experiment [41] is a current generation long baseline neutrino oscillation experiment.

T2K produces a beam of muon neutrinos using decay in-flight of charged pions created by the J-PARC facility. The energy distribution and flavour composition of this beam before oscillation is measured with a series of near detectors placed close to the neutrino production point as seen in Fig 2.1. These neutrinos are then allowed to propagate through 295km of rock before reaching the far-detector (SK). During travel these neutrinos oscillate as described in §1.2.4, changing the flavour composition of the beam, in addition to the energy distribution of each flavour component as seen in Fig 1.7.

Comparing the flavour and energy distributions of neutrinos detected in SK to those from the near detector, the impact of of neutrino oscillation can be observed.

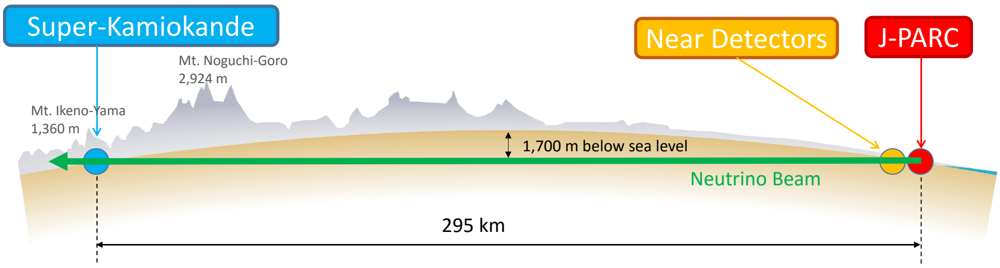

FIGURE 2.1: Schematic view of T2K, neutrinos are produced at J-PARC and are measured with the near detectors, these neutrinos then oscillate in flight before being detected at SK.

2.2 Accelerator Beamline

The T2K neutrino beam is produced at the J-PARC accelerator complex. A 30GeV beam of protons is generated and accelerated in three stages; first, H^- ions are accelerated in a linear accelerator up to an energy of 400MeV, these pass through a charge stripping foil to produce H^+ before being further accelerated in the RCS (rapid-cycling synchrotron) up to 3GeV.

Finally these bunches are injected into the MR (main ring), this is a triangular synchrotron with a 1567m long beam path that is responsible for the final acceleration of the protons. Each beam bunch from the RCS is injected into the MR until a total of eight bunches are present in the MR, once this is achieved the bunches are accelerated from 3GeV to 30GeV.

Once this energy has been reached, kicker magnets deflect the beam bunches into a separate beamline. This allows the entire stored energy in the beam to be sent towards neutrino production in a window of just 5μsec. At current beam power this is a total of 2.6×10^{14} protons, carrying a kinetic energy of 1.28MJ. This procedure is repeated every 2.48s [41].

The short window for proton extraction has a number of engineering advantages, particularly in the magnetic focusing horns in §2.2.2 which would not be able to operate continuously due to power and heating constraints. The primary physics benefit is in the reduction of external backgrounds to neutrino detection; by only accepting events coincident with the known beam timing, background interactions occurring in the remaining $\approx$2.48s of the cycle can be rejected.

2.2.1 Primary Beamline

The neutrino beamline Fig 2.2 takes these proton bunches and, through the use of both normal and superconducting magnets, redirects the beam to point West, towards SK.

The protons then pass into the final focusing section, this is a series of ten normal conducting magnets that focus and direct the beam slightly downwards, so that the beam is directed 2.5° below the straight-line direction of SK. To aid this aiming, several SSEMs (segmented secondary emission beam monitors) can be inserted into the proton beam path, these record the position and spread of the beam during this deflection and focusing process.

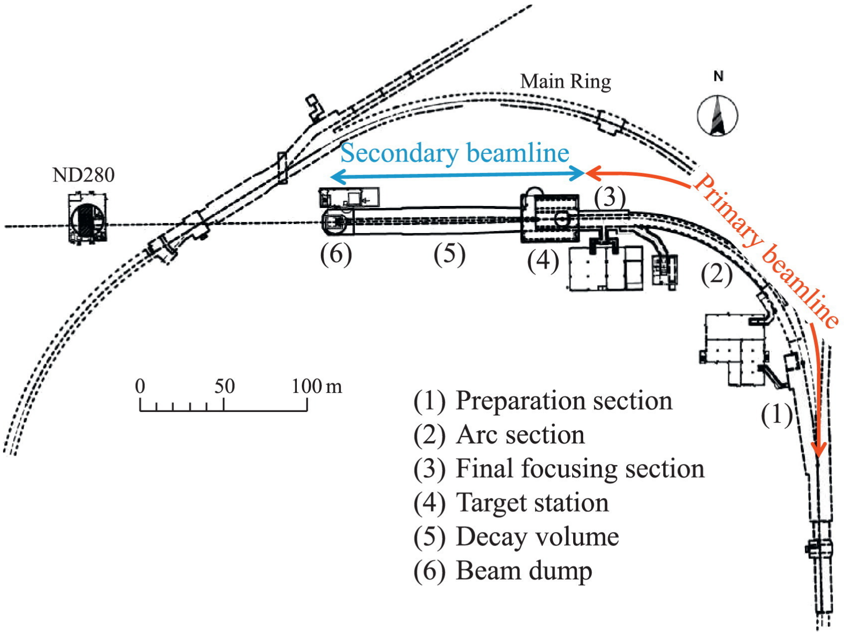

FIGURE 2.2: A schematic diagram of the neutrino beamline at J-PARC. Protons are focused from the main ring in the preparation section (1), redirected by superconducting magnets in the arc section (2) and then focused and directed downwards by the final focusing section (3). Reproduced from [41].

2.2.2 Secondary Beamline

This aimed and focused beam from the primary beamline then passes through a titanium beam window into the helium vessel. Due to the large size of the helium vessel it is prohibitively difficult to maintain this volume at vacuum during beam operation. In order to limit the absorption of the produced pions and prevent the production of nitrogen oxides, helium at 1atm of pressure is used.

The beam then passes through the final beam monitor, the OTR (optical transition radiation monitor), this measures the proton beam position just upstream of the target. During normal operation, this position data is used in conjunction with data from a single SSEM further upstream to determine the direction and position with which the proton beam strikes the target.

Uncertainty on the proton beam direction, position and size play a significant role in the uncertainty on the final neutrino beam as can be seen in Fig 2.5. As discussed in §2.2.3, the precise angle at which T2K's detectors are located relative to the direction of the neutrino beam affects the mean energy of the neutrino flux.

After passing through the OTR beam monitor, the proton beam is then allowed to impinge on a graphite target in the target station. This is a 91.4cm long, 2.6cm diameter graphite rod placed within a 250kA magnetic horn, see Fig 2.3. Protons colliding within this rod produce charged pions and kaons of both positive and negative charge. These escape the graphite rod and are deflected by the magnetic field produced by the first focusing horn. Depending upon the current passing through the horn, either positively or negatively charged particles will be focused in the forward direction. Oppositely charged particles will be deflected away from this direction.

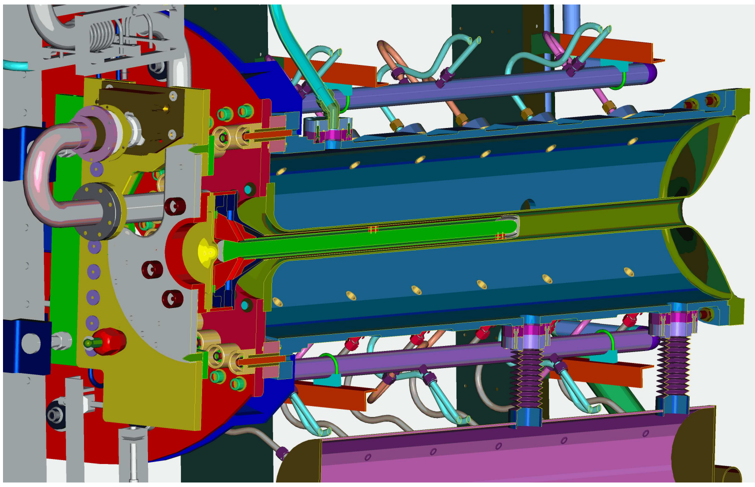

FIGURE 2.3: A cross-section diagram of the first magnetic focusing horn (blue) and the graphite target (green) within the horn's inner conductor. Reproduced from [41].

Two further magnetic horns focus these charged mesons and defocus oppositely charged mesons. The selected charged mesons are then allowed to decay in flight down a 96m long decay volume Fig 2.4. At the end of this decay volume is a graphite and iron beam-dump which blocks any surviving hadrons and muons with momenta lower than 5GeV/c [41].

Beyond this beam-dump, 117.5m from the target, lies MUMON (muon monitor)[42]. This detector uses ionisation chambers with downstream silicon PIN photodiodes to detect penetrating high-momentum muons and reconstruct the profile of the muon beam in two dimensions. From this it is capable of measuring the beam direction to a precision of 0.28mrad (0.016°) on a bunch-by-bunch basis [43].

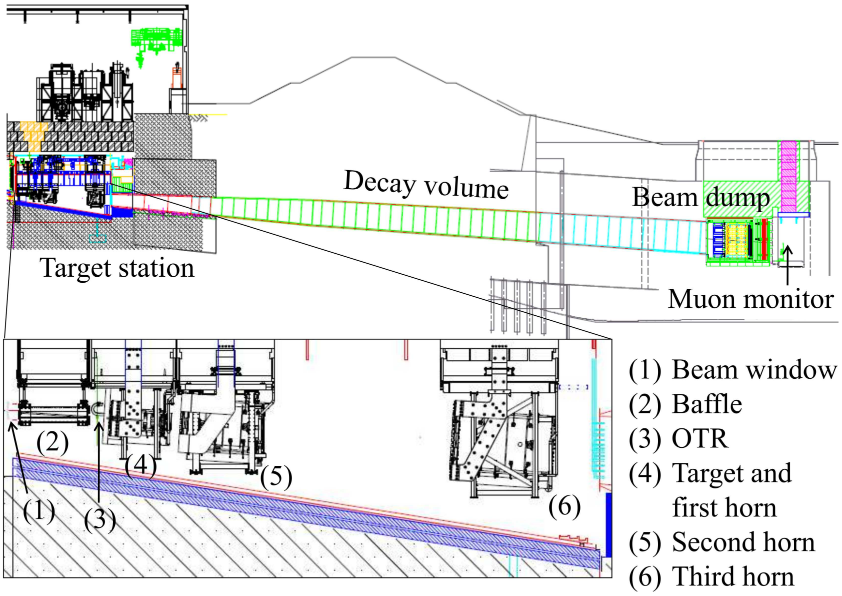

FIGURE 2.4: A cross-section diagram of the secondary beamline showing the three magnetic focusing horns, the decay volume, the beam dump and the muon beam monitor (MUMON). Reproduced from [41].

2.2.3 Neutrino Beam Properties

The mesons escaping the target are primarily composed of $\pi^{\pm}$, $K^{\pm}$ and K^0_L. The magnetic focusing horns charge select and focus these mesons along the direction of the incident proton beam. In neutrino mode operation, the horns select and focus positively charged mesons while defocusing negatively charged mesons, this is Forward Horn Current (FHC) while antineutrino mode reverses the direction of the current in the horns (Reverse Horn Current) to select negatively charged mesons.

In FHC there are four parent particles that dominate the neutrino flux, Table 2.1 shows the decay modes of these parents that produce neutrinos and their branching ratios.

$\pi^+ \rightarrow$	BR	$K^+ \rightarrow$	BR	$K^0_L \rightarrow$	BR	$\mu^+ \rightarrow$	BR
$\mu^+ + \nu_\mu$	99.99%	$\mu^+ + \nu_\mu$ $\pi^+ + \pi^0$ $\pi^+ + \pi^+ + \pi^-$ $\pi^0 + e^+ + \nu_e$ $\pi^0 + \mu^+ + \nu_\mu$	63.6% 20.7% 5.6% 5.1% 3.4%	$\pi^{\pm} + e^{\mp}$ $\pi^{\pm} + \mu^{\mp} + \nu_\mu$ $\pi^+ + \pi^- + \pi^0$	40.6% 27.0% 12.5%	$e^+ + \bar{\nu}_\mu + \nu_e$	100%

TABLE 2.1: The decay modes producing neutrinos for the four major neutrino parent particles [15]. Note, some decay chains are possible such as $\pi^+ \rightarrow \mu^+ \rightarrow e^+$.

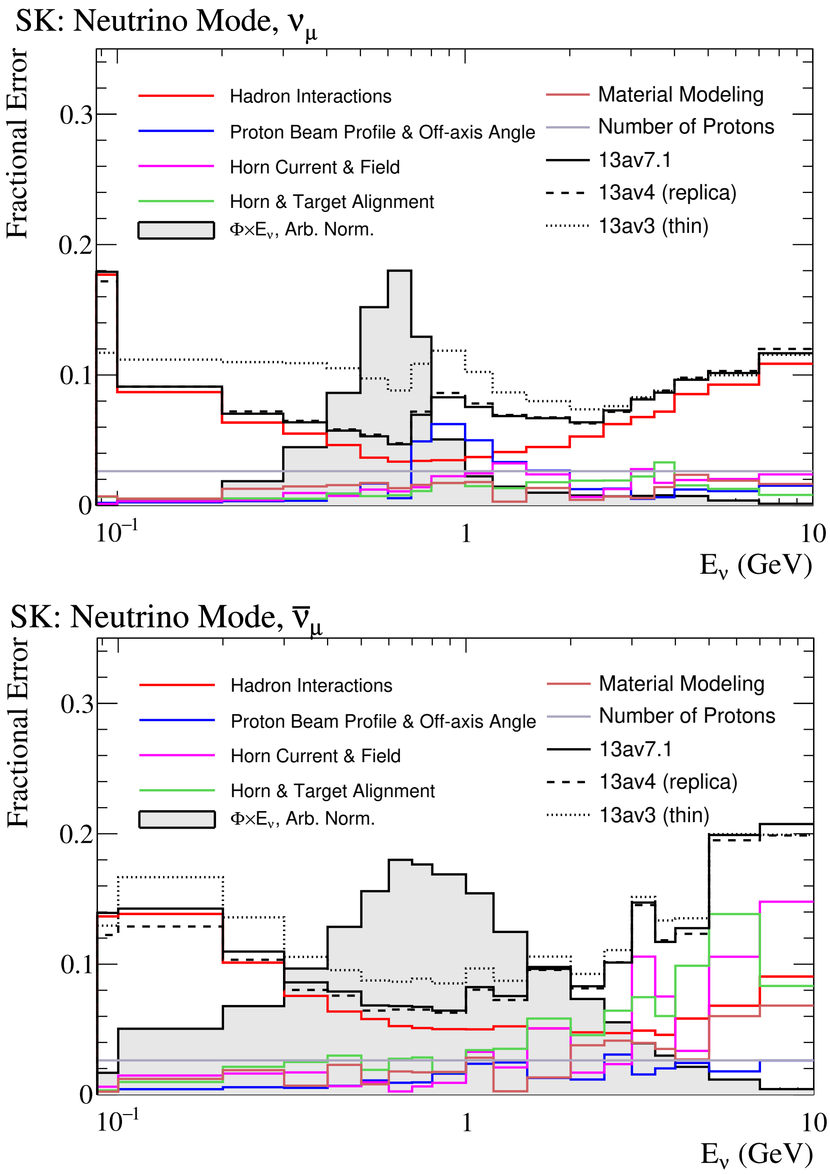

FIGURE 2.5: The sources of systematic uncertainty on the T2K flux prediction. Uncertainties in hadron production are dominant for much of the energy range, however around 1GeV proton beam properties become significant. The major change from 13av3 to 13av4+ is the use of hadron production data from a replica of the T2K graphite target made by the NA61/SHINE experiment [44], drastically reducing hadron interaction uncertainty. Reproduced from [45].

Off-axis Principle

By far the most dominant decay is $\pi^+ \rightarrow \mu^+ + \nu_\mu$ which results in a final neutrino beam primarily composed of ν_μ with contamination of $\bar{\nu}_\mu$ (wrong sign) from scattered π^- and μ^+ decays.

While these charged pions can be focused into a tight beam by the magnetic focusing horns, the momentum imparted by its decay on the resulting neutrino cannot be eliminated. The neutrino beam will therefore have a significantly broader angular distribution than the pion beam, along with a different energy distribution.

From two-body decay kinematics, the energy of a neutrino emitted by a decaying boosted π^+ depends on the angle of emission according to:

$$E_\nu = \frac{m_\pi^2 - m_\mu^2}{2(\sqrt{p_\pi^2 + m_\pi^2} - p_\pi \cos(\theta_{lab}))} \tag{2.1}$$

Here E_ν is the neutrino energy in the lab frame, p_π is the pion momentum in the lab frame and θ_{lab} is the angle of the outgoing neutrino with respect to the pion direction, the ‘off-axis angle’.

For $\theta_{lab} = 0$ and $p_\pi \gg m_\pi$ the neutrino energy is proportional to pion momentum. The pions produced by the proton beam striking the target are produced with a broad range of momenta, hence the neutrinos produced directly on-axis have a similarly broad energy distribution.

For non-zero values of θ_{lab} the denominator does not cancel to first order in p_π, thus higher momenta pions may produce lower energy neutrinos for a given off-axis angle, as seen in Fig 2.6. A broad range of pion momenta can therefore produce neutrinos of similar energy, this has the effect of compressing the neutrino energy spectrum and reducing the peak energy compared to an on-axis beam.

For T2K this is useful as the direction of the beam can be adjusted to align the neutrino energy peak with the first oscillation maximum as seen in Fig 2.7. This maximises the proportion of muon neutrinos that oscillate into other flavours by the far detector [41].

Not all of the neutrino flux arises from pion decay, both muon and kaon decays contribute, these have decay modes via a three-body process and do not exhibit the same off-axis energy dependence as the pion decay kinematics. Figs 2.8 and 2.9 show

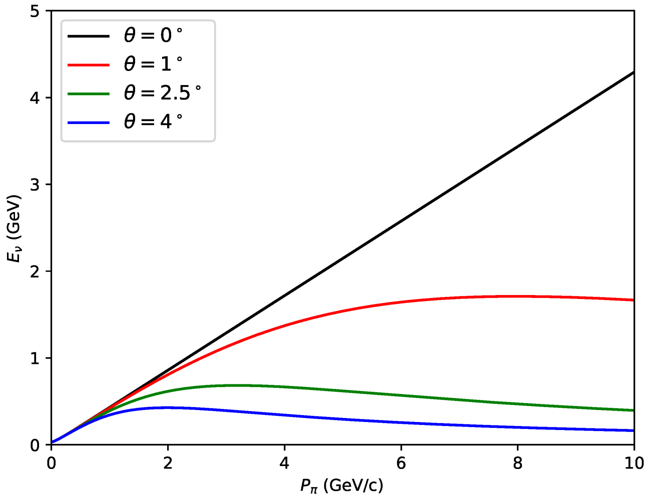

FIGURE 2.6: The energy of a neutrino produced by a $\pi^\pm$ decay as a function of the decaying pion momentum and off-axis angle of the outgoing neutrino. At 2.5° off-axis, a wide range of pion momenta centred around 3GeV/c yield a neutrino with energy 0.6GeV.

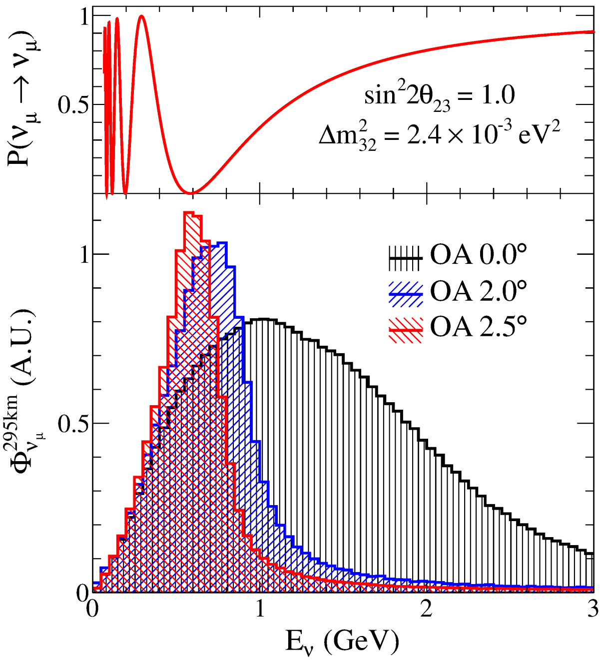

FIGURE 2.7: The survival probability of muon neutrinos at 295km as a function of neutrino energy (top). The unoscillated ν_μ fluxes for three different off-axis angles from the neutrino beam (bottom). T2K uses an off-axis angle that maximises the impact of oscillation on ν_μ event rate. Reproduced from [46].

the contribution of each decay parent to the resulting neutrino flux for neutrino and antineutrino operation respectively.

In neutrino (antineutino) mode, the ν_μ ($\bar{\nu}_\mu$) flux peak at 600MeV and is composed of neutrinos from charged pion decays as discussed above, the high energy tail comes from the more massive charged kaon decay. The ν_e ($\bar{\nu}_e$) contamination of the flux primarily comes from muon decays that in turn are a result of charged pion decays, however there is a significant secondary contribution from kaons. Due to the reduced production rate of π^- relative to π^+, the total flux in antineutrino mode is slightly lower than neutrino mode, with a larger wrong sign component.

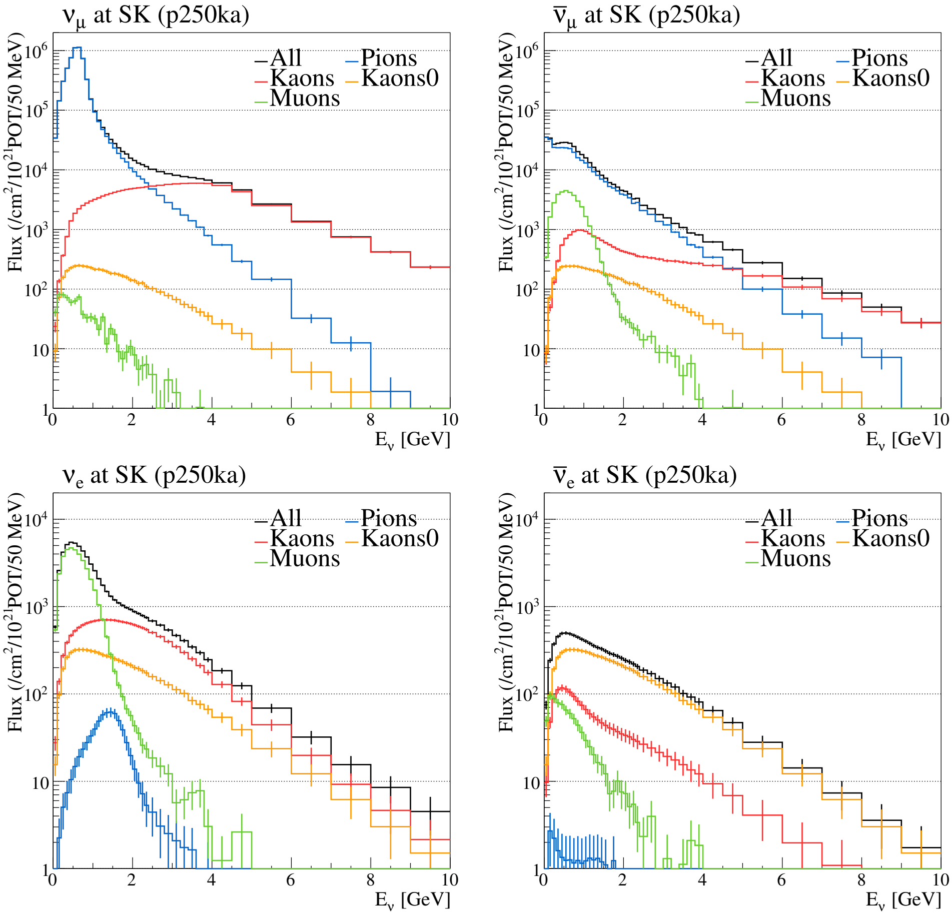

FIGURE 2.8: Beam MC showing the unoscillated neutrino flux at SK in neutrino beam operation along with the parent particle of those (anti)neutrinos. Reproduced from [45].

2.2.4 Simulation

The flux simulation uses FLUKA 2011.2c.6 [45][47] to simulate the proton beam interaction in the baffle and graphite target. Hadrons escaping the graphite are passed

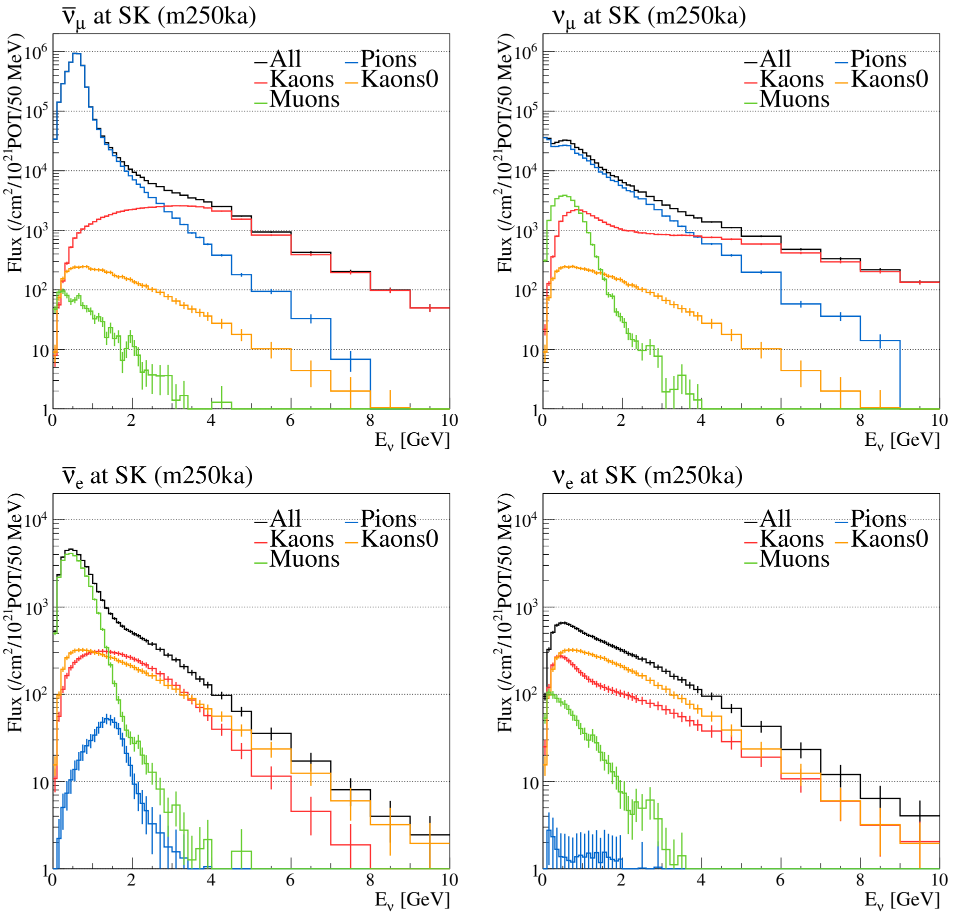

FIGURE 2.9: Beam MC showing the unoscillated neutrino flux at SK in antineutrino beam operation along with the parent particle of those (anti)neutrinos. Reproduced from [45].

to JNUBEAM, a GEANT3[48] based simulation package which propagates the particles through the field created by the magnetic horns. Hadronic interactions outside of the target, e.g. with the magnetic horns and structure are modelled with GCALOR 1.05/04 [49] within JNUBEAM.

The hadronic interactions are then tuned using data from the NA61/SHINE experiment [44].

2.3 The Near-Detector complex

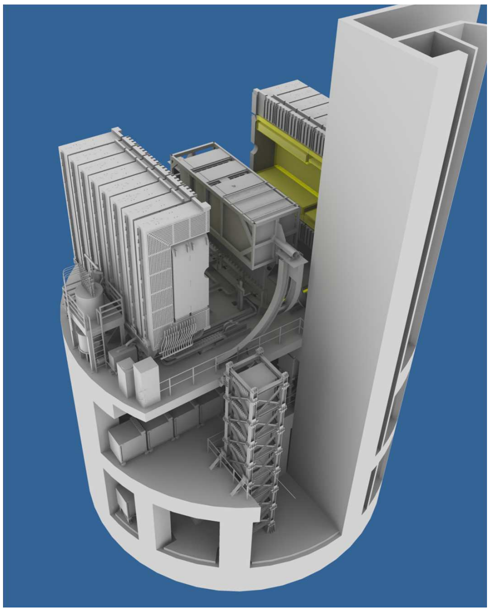

FIGURE 2.10: The T2K near-detector complex, ND280 sits on the highest level, here shown with the magnet open. INGRID lies below ND280 with the vertical and horizontal arms offset along the beam direction. Additional detectors such as WAGASCI/Baby-MIND are present but not shown. Reproduced from [41].

In order to make precision measurements of neutrino oscillations it is necessary to precisely measure both the properties of the neutrino beam and of neutrino-nucleus interactions. T2K makes use of its near-detector complex to achieve these goals as seen in Fig 2.10. The complex includes several neutrino experiments such as WAGACI/Baby-MIND [50][51] and NINJA [52] however the two T2K detectors are INGRID (interactive neutrino grid) [53] and ND280 (near detector at 280m) [41].

2.3.1 INGRID

The INGRID detector is an on-axis neutrino beam monitor used to measure both the position of the centre of the neutrino beam and its width. This serves as an additional check on the off-axis angle of ND280 and SK and is able to provide daily measurements of the direction of the beam to a precision of 0.4mrad (0.02°) [41]. The detector is composed of 16 identical modules arranged in a cross shape in a direction perpendicular to the neutrino beam axis as shown in Fig 2.11 and located 280m downstream of the pion production target. The arms of the cross have a length of 10m and cover angles of ± 18mrad (1.0°) in both the vertical and horizontal axes of the beam. The two additional modules located above the main horizontal arm are used to investigate the axial symmetry of the beam.

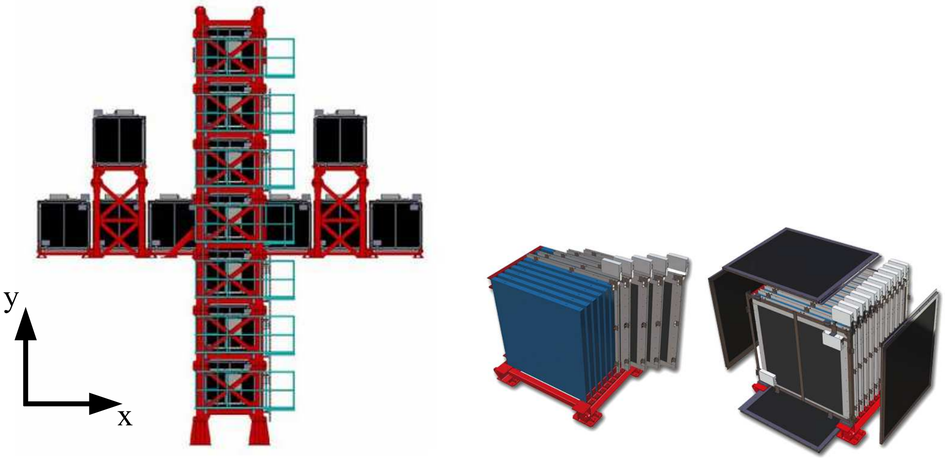

FIGURE 2.11: The full INGRID detector (left) is composed of 16 iron and scintillator modules (right). The centre of the neutrino beam passes through the centre of the INGRID cross and can be monitored for width, position and symmetry. Reproduced from [41].

Each module is composed of alternating layers of iron target and polystyrene scintillator. In total 11 layers of scintillator with nine layers of iron are used, giving a target mass of 7.1tons per module (4.4tons fiducial) [54]. Each scintillator layer is composed of two sets of scintillator bars, one set oriented vertically and the other horizontally to allow for 2d reconstruction of the particle track. Each bar is 1cm thick in the beam-direction and 5cm wide with a wavelength shifting fibre passing down the full length of the bar. This fibre is read out by an MPPC (multi pixel photon counter) attached at one end.

Surrounding each module on the sides are a series of veto planes composed of polystyrene scintillator as seen in Fig 2.11, these act to identify and exclude backgrounds entering the module from the sides.

With these, INGRID fits a Gaussian profile to the beam in order to to determine the beam centre, width and intensity as shown in Fig 2.12.

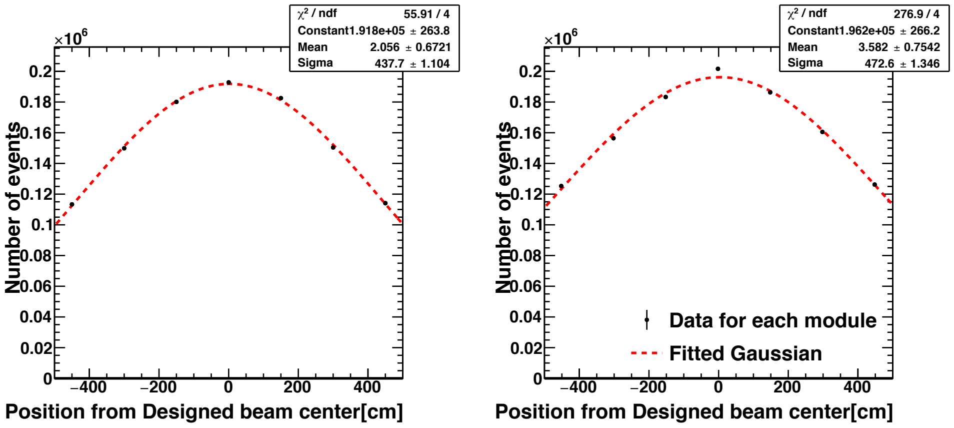

FIGURE 2.12: A Gaussian fit to determine the centre of the neutrino beam used by T2K. Each data point corresponds to the event rate in an INGRID module, horizontal (left) and vertical (right). Reproduced from [55].

2.3.2 ND280

Having created a high intensity neutrino beam and measured its direction, it is possible to measure the oscillated flux with a far-detector and extract a constraint on oscillation parameters. Such a constraint would rely heavily on models of neutrino flux and interaction cross-section which would quickly become limiting to the overall sensitivity. A detector capable of measuring the flux and interaction cross-section, before oscillation, could allow for a stronger constraint on these systematic uncertainties, allowing the overall experiment to recover tighter constraint on oscillation parameters.

ND280 fulfils this role in T2K, being responsible for the measurement of cross-section for the different possible interaction types, along with properties of the flux such as the relative ν_μ to $\bar{\nu}_\mu$ contribution.

In order to achieve these goals ND280 is a significantly different detector design than the far-detector SK. This choice is designed to allow ND280 to investigate, in detail, the properties of neutrino interactions, in a way that would not be possible with a water-Cherenkov based near-detector.

ND280 is located 280m downstream from the pion production target directly above INGRID as in Fig 2.10. This places ND280 at an off-axis angle of 2.5° relative to the neutrino beam, the same as the far-detector, to ensure both detectors experience the same incident flux.

The detector itself is a magnetised tracking detector composed of six main parts as shown in Fig 2.13. The central core contains the target mass and trackers, the polystyrene-based FGDs (fine grained detectors) act as the target mass as well as providing tracking. These are sandwiched between TPCs (time projection chambers), these provide charged particle momentum reconstruction and particle identification.

These FGDs and TPCs are contained within ECALs (electromagnetic calorimeters) used to measure the energy of escaping particles. All of this is contained within a magnetic field to provide track curvature for charge identification as well as TPC momentum reconstruction.

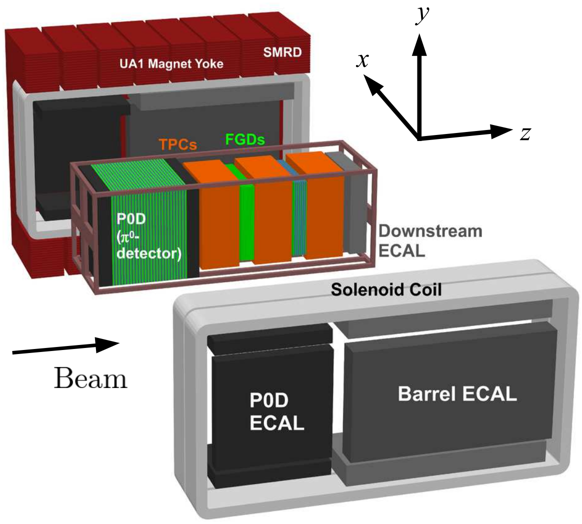

FIGURE 2.13: An exploded diagram of ND280. The main basket contains the PØD, three TPCs, two FGDs and a downstream ECAL. These are used as the target masses and for tracking. This basket is surrounded by ECALs and a magnet system utilising the UA1 magnet. Reproduced from [41].

FGDs

The target mass for ND280 comes from two FGDs (fine grained detectors) [56], these are composed of square bars of extruded polystyrene scintillator of dimensions 9.6mm × 9.6mm × 1864mm which have a white reflective TiO_2 coating and a single WLS (wavelength shifting) fibre passing through a hole along the full length of the bar. These bars are arranged in planes, containing 192 bars each. Two such planes are arranged into a single 'XY' module with one plane of bars oriented horizontally and one oriented vertically.

FGD1 (the upstream FGD) is composed of 15 such modules while FGD2 (the downstream FGD) uses seven modules with six 2.5cm thick water fillable reservoirs between the layers, both have a target mass of approximately 1.1 tons [56]. By comparing the event distributions in both FGDs, the interaction cross-section on oxygen can be determined, allowing for measurements of interactions on the same target nucleus as used in SK. Each of the scintillator bars are readout using an MPPC attached to one end of each of the WLS fibres. This layer structure coupled with the fine segmentation allows for 3D tracking of charged particles as they travel through the FGDs.

For particles that stop before reaching the TPCs, such as pions or protons at high angles relative to the incident neutrino beam, the energy deposition and track length within the FGD can be used to determine particle energy and PID. Using this, it is possible to distinguish protons from minimally ionising particles such as muons or pions, as can be seen in Fig 2.14. This is particularly important for analyses investigating the hadronic properties of an interaction [57].

TPCs

Three TPCs (time projection chambers) are used in ND280, arranged with an FGD between each TPC as seen in Fig 2.13. The first TPC acts to veto charged particles entering the first FGD from neutrino interactions upstream, either from the PØD or interactions in the magnet yoke. Subsequent TPCs are used to determine particle momentum from the curvature of the track in the magnetic field, in addition to PID (particle identification) from the energy deposition along the track, as can be seen in

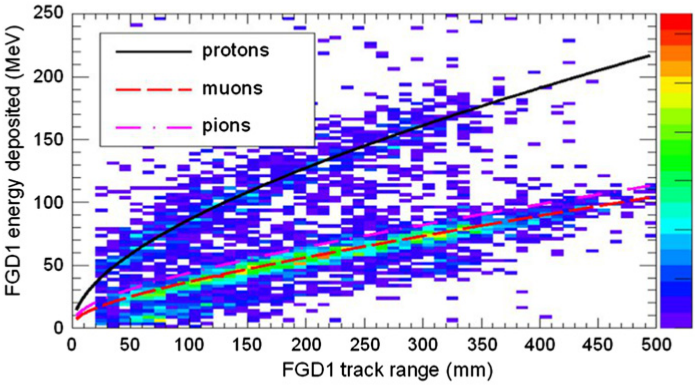

FIGURE 2.14: The relationship between track length and energy deposition for stopping particles in FGD1. The curves show MC expectation for protons, muons and pions while the histogram shows observed neutrino data. This can be used to determine PID and energy of particles not entering a TPC. Reproduced from [56].

Fig 2.15. Using this energy deposition method, the probability of mis-identifying an electron as a muon is 0.2% for particles of momenta below 1GeV/c. The resolution on muon momentum as a function of transverse muon momentum can be seen in Fig 2.16, the resolution is best for particles with lower momenta and therefore higher track curvature.

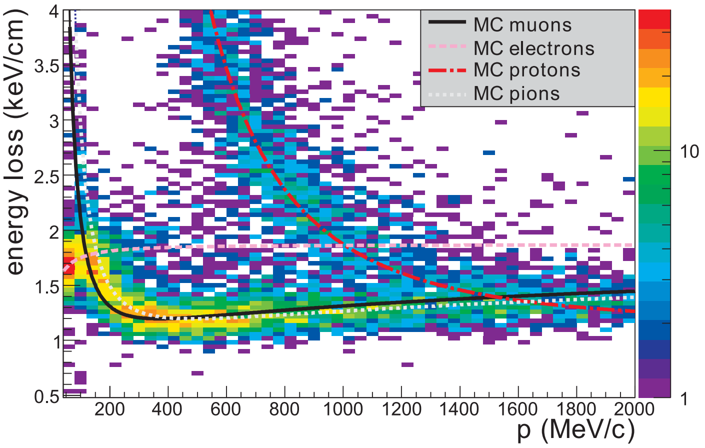

FIGURE 2.15: The distribution of energy loss against particle momentum in the TPCs for positively charged particles in FHC operation. The curves show the expected energy deposition while the histogram shows neutrino interaction data. Clear separation between protons and MIPs can be seen at momenta below 1GeV/c. Reproduced from [58].

The TPCs are composed of an outer and inner box, the inner box contains an argon, tetrafluoromethane, isobutane drift gas mix [58]. In the centre of the TPC is a cathode plane as can be seen in Fig 2.17. Charged particles passing through the gas ionise the gas ejecting electrons, these electrons drift in the field created by

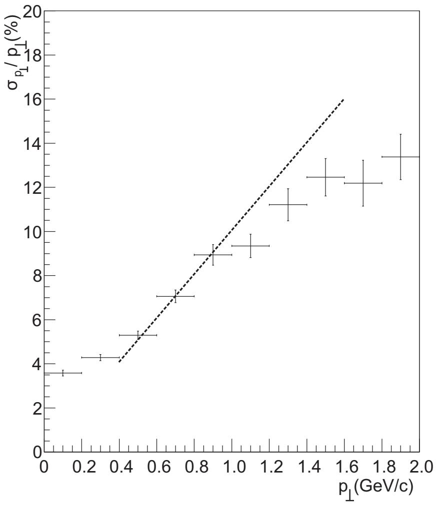

FIGURE 2.16: The fractional error on the reconstructed muon momentum perpendicular to the applied magnetic field for a muon passing through a single TPC. The measurement is based on track curvature in the magnetic field, hence higher momentum muons are less precisely measured. The dashed line corresponds to the design goal of the TPCs. Reproduced from [58].

the cathode towards the sides of the TPC, here they are amplified and detected by a micromegas detector [59] [60]. The reconstruction ability of ND280 is enhanced when particles traverse multiple TPCs as is the case for high-momentum muons such as that seen in Fig 2.18.

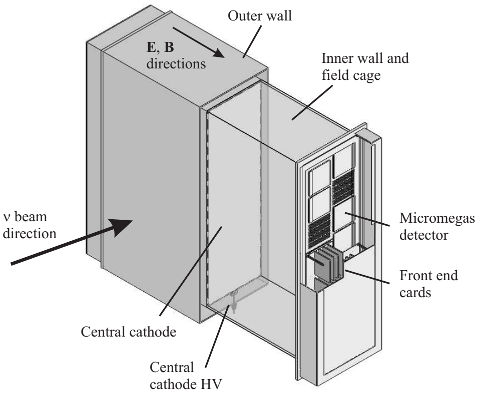

FIGURE 2.17: The gaseous argon TPCs used at ND280. The TPC has two sections separated by a central cathode. Transiting charged particles ionise the gas, the resulting electrons drift to the Micromegas detectors and the particle track reconstructed. Reproduced from [41].

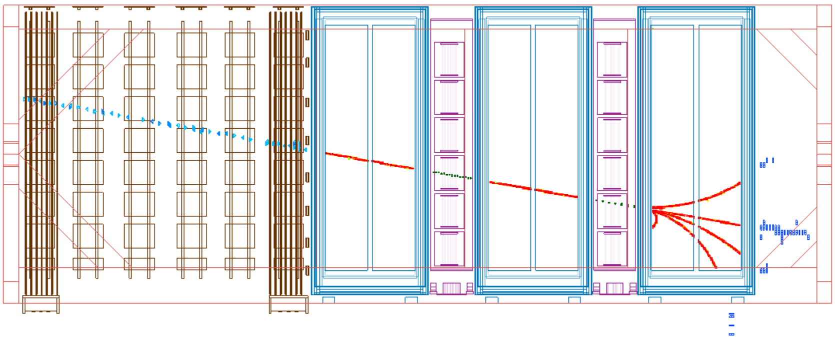

FIGURE 2.18: An example event in ND280 here an entering muon passes through the PØD, the first two TPCs and the first FGD before interacting in the second FGD. The resulting secondary particles are tracked by the final TPC and are stopped by the ECALs. Reproduced from [41].

PØD

The π^0 detector (PØD) is the most upstream component of ND280 and is intended to measure NCπ^0 neutrino interactions on water. The PØD uses alternating 'XY' layers of triangular scintillator bar interleaved with layers of brass and water fillable bags as in Fig 2.19. At the upstream and downstream ends of the PØD these brass and water layers are replaced with lead in order to act as an ECAL and improve the containment of electromagnetic showers from the π^0 decay photons [41].

Each scintillator bar is a triangular prism, the outer edges are impregnated with white reflective TiO_2 to reduce light leakage to adjacent bars and to increase the amount of light entering the WLS fibre that passes through a central hole in the bar. This WLS fibre is readout via MPPC at one end with the other end being covered in a reflective coating to increase light yield.

Each XY scintillator layer is composed of 134 vertical and 126 horizontal scintillator bars giving a total layer size of 2340mm × 2200mm × 34mm (width × height × length). The PØD contains 40 such XY layers with 25 layers of water and brass, of thickness 28mm and 1.5mm respectively [61].

The ECAL sections of the PØD are composed of seven 'XY' layers with a 4mm thick stainless steel and lead sandwich between each layer. The total mass of the PØD is 13.3 tons and 16.1 tons with the water layers filled, the fiducial mass of water in the detector being 1900kg.

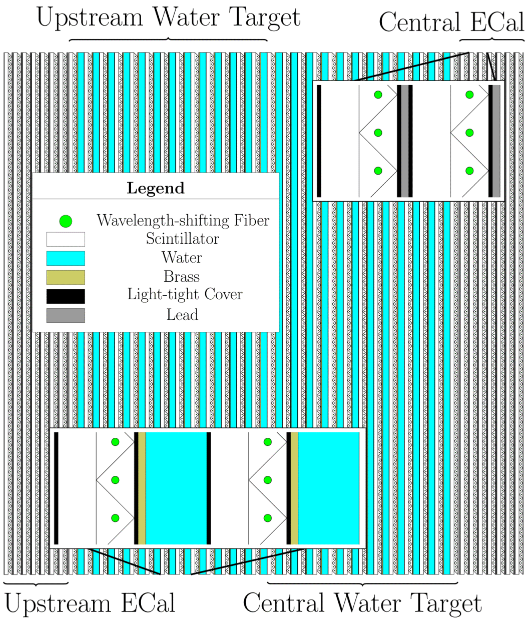

FIGURE 2.19: A cross-section of the PØD, showing the scintillator, brass and fillable water layers. Reproduced from [41].

ECAL

The central detector core of ND280 is surrounded by ECALs as seen in Fig 2.13, these act to contain and measure the energy of any charged particles escaping the central core. There are three main groups, the PØD ECAL, the barrel ECAL and the downstream ECAL.

All three ECALs are of similar construction, consisting of alternating sheets of lead and bars of PPO doped polystyrene scintillator. All of these bars have a TiO_2 coating to improve light containment in the bar and a thickness of 10mm, width of 40mm and varying lengths depending on application [41]. Readout is provided by a WLS fibre passing through a hole in the scintillator bar with an MPPC attached to one or both ends of the fibre.

The thickness and number of lead sheets is different in each ECAL. Both the barrel and downstream ECAL use 1.75mm thick sheets with 31 and 34 layers respectively, providing in excess of $9X_0$ to ensure containment of electrons and photons. While the six PØD ECALs are each composed of five layers of 4mm thick lead sheets interleaved within six layers of scintillator bars, giving a total radiation length of $4.3X_0$.

Magnet

This central assembly (basket) of detectors are contained within a 0.2T magnetic field. This allows for reconstruction of charged particle momentum from track curvature and identification of the sign of their charge. This is particularly important for the discrimination between neutrino and antineutrino interaction events.

The magnet consists of four water-cooled aluminium solenoid coils and an iron return yolk, both reused from the UA1/NOMAD experiments. The four aluminium coils surround the central basket, as seen in Fig 2.13. A DC current of 2900A passes through each of the coils, generating a dipole field. This field was mapped with a series of Hall effect probes yielding a final uncertainty on each orthogonal component of the field of 2 Gauss (2×10^{-4}T) in the 0.2T field. [41]

The return yolk acts to confine the stray magnetic field outside of the detector region and reduce the power requirement for the solenoid coils. This yolk is composed of 16 ‘C’ shaped sections that encloses the detector and solenoids arranged in pairs of two. When the magnet is closed these sections combine to surround all four sides of the basket. Each section is composed of 16 layers of steel plates, with a thickness of 4.8cm, between each plate is a 1.7cm thick air gap.

SMRD

The Side Muon Range Detector (SMRD) are a series of 440 scintillator modules placed in the air gaps between the steel plates that make up the magnet return yolk. These are used to identify incoming cosmic ray muons that penetrate the detector in addition to detecting muons exiting the detector at high angles relative to the beam and muons from neutrino interactions outside of the detector volume.

2.4 Super-Kamiokande

As a far-detector, T2K makes use of the SK detector. This is a water-Cherenkov detector located 295km west of the J-PARC facility, underneath Mt. Ikenoyama.

2.4.1 Water Cherenkov Principles

A water Cherenkov detector consists of a volume of water that acts as a target mass. When a charged particle passes through this water faster than the local phase velocity of light, optical photons are emitted in a cone around the direction of travel of the particle. This light may then be detected by photon detectors instrumenting the water volume, most commonly PMTs (photomultiplier tubes). This phenomenon allows for detection of charged particles travelling faster than 0.75c, the velocity of light in water.

2.4.2 Super-K Construction

The detector consists of a cylindrical cavern lined with stainless steel and backfilled with concrete, resulting in a vertical cylindrical volume of height 42m and diameter 39m and able to hold 50kton of pure water [62]. Within this volume a stainless steel scaffold cylinder divides the volume into the ID (inner detector) and OD (outer detector) regions as seen in Fig 2.20. The OD region has a thickness of approximately 2.7m on the sides (barrel) and 2.6m at the top and bottom on the cylinder (end caps). The ID volume has a diameter of 33.8m and height 36.2m.

The ID volume is instrumented by 11,129 PMTs arranged on the inner surface of the support scaffold, in a 70cm square grid. Each PMT has a diameter of 50cm with a peak quantum efficiency of 21% for 380nm light. This gives a total of 40% photocathode coverage on the ID surface.

In order to reduce the impact of the earth's magnetic field on the PMT performance, a set of 26 vertically and horizontally aligned Helmholtz coils are arranged around the inner surface of the tank. These act to reduce the average field felt by the PMTs from 450mGauss to approximately 50mGauss [62]. The inner surface of the support structure is covered in a black plastic sheet in order to limit light reflections within the ID as well as optically isolate the OD and ID volumes.

The OD is instrumented with 1,885 smaller 20cm PMTs, the light collection capacity of these is augmented with a wavelength shifting plate attached to each PMT. These plates are square acrylic panels with width 60cm and thickness 1.3cm. These act to capture UV photons and convert them to optical frequencies to which the PMT

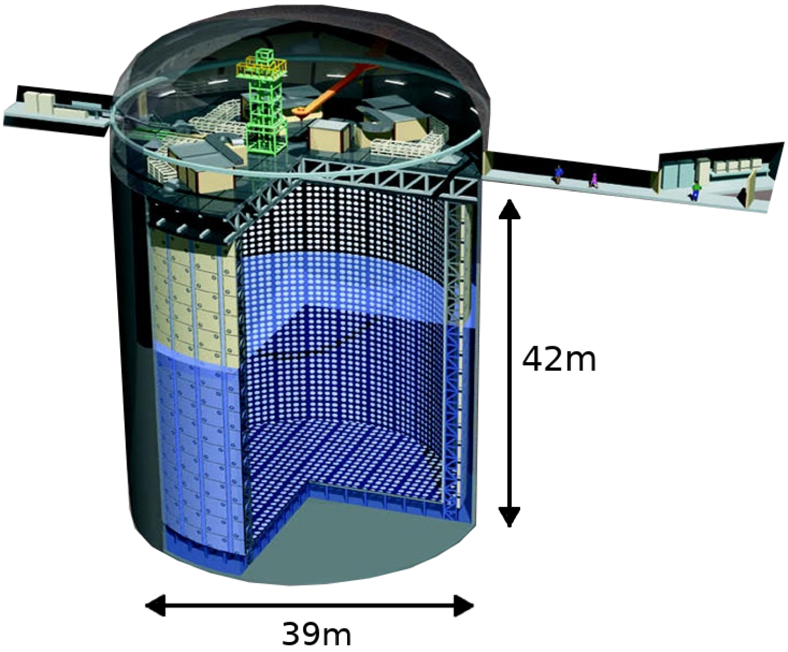

FIGURE 2.20: A cutaway diagram of SK showing the central ID region surrounded by PMTs.

is more sensitive. This improves the sensitivity of each PMT by a factor of 1.5. In addition, both surfaces of the OD region are covered in a white reflective Tyvec® to increase the probability of photons reflecting onto the PMTs [62].

The OD acts as a veto for cosmic ray muons as well as for interactions occurring outside of the ID volume or escaping from the ID. To reduce backgrounds from radioactive decays in the support structure and the surrounding rock, a variable veto region from the wall of the ID is used, this ranges from 50cm to 80cm depending on sample. In total, the available fiducial mass is approximately 28kton.

2.4.3 Particle Identification

For T2K it is necessary to identify the neutrino flavour in order to extract oscillation properties, in particular, separating ν_e and ν_μ events is critical to measurement of δ_{CP}. This can be achieved for charged-current interactions by identifying the charged lepton produced.

Due to their high mass, muons travelling through the water volume are not scattered significantly as they propagate. The Cherenkov light therefore forms a sharp edged ring, this then propagates to the ID wall where the PMT response shows a sharp ring Fig 2.21(a). Electrons by contrast have a much lower mass and scatter as they propagate, the light they produce is therefore a combination of many faint overlapping rings. The resulting pattern on the ID wall is therefore of a ‘fuzzy’ ring Fig 2.21(b).

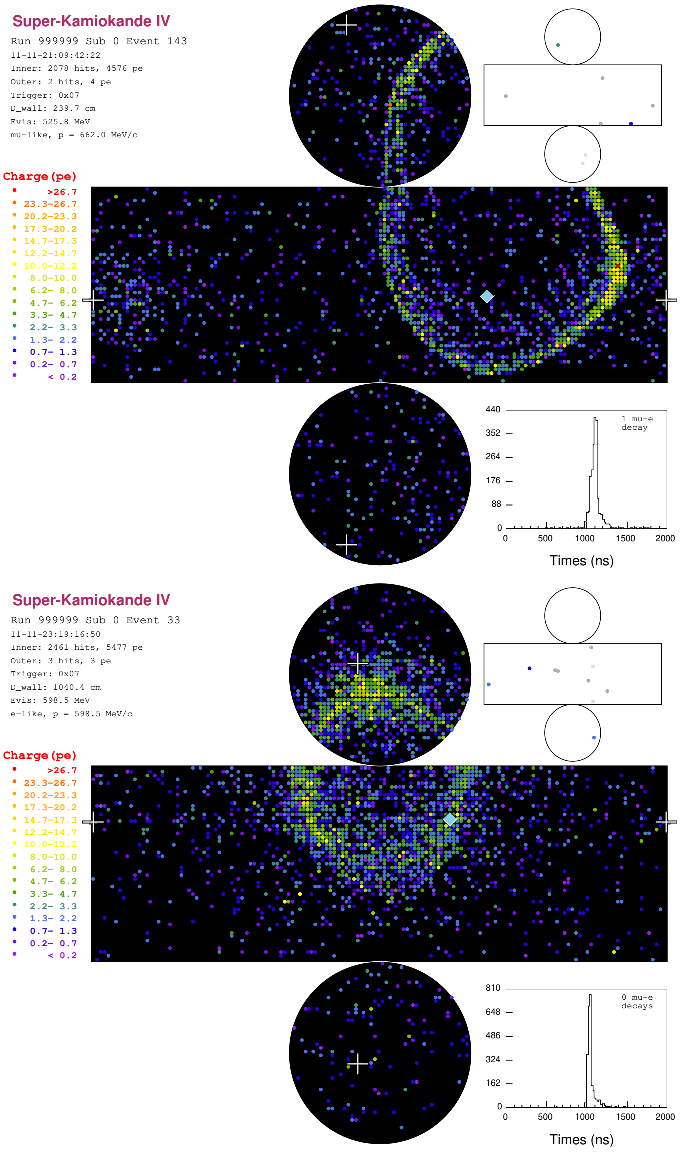

FIGURE 2.21: Event displays of two T2K neutrino interaction events in SK. A muon candidate (top) results in a sharply defined Cherenkov ring on the ID PMTs while an electron (bottom) produces a diffuse ring.

T2K uses a maximum likelihood based reconstruction method fiTQun [63][64]. This takes the PMT hit times and charges then maximises a likelihood of observing the measured distributions under several different particle hypotheses, for freely varying particle momenta and positions. In this way, a best-fit likelihood for each combination of particles is obtained in addition to the best-fit kinematic properties of those particles.

The likelihood used for this fitting is given by:

$$L(\mathbf{x}) = \prod_{i \in unhit} P_i(unhit|\mathbf{x}) \times \prod_{j \in hit} P_j(hit|\mathbf{x}) f_q(q_i|\mathbf{x}) f_t(t_i|\mathbf{x})$$

Where **x** is a parameter vector describing the properties of the particles involved in the production of the event, momentum, position etc. The products run over all hit and unhit PMTs, $P_i(hit|\mathbf{x})$ is the probability of the 'i'th PMT being hit given the track parameters **x**. The $f_q(q_i|\mathbf{x})$ and $f_t(t_i|\mathbf{x})$ denote the probability that the 'i'th PMT observes a total charge of q_i and is hit at time t_i respectively, given track parameters **x**. The MC simulation used for these probabilities is a custom Geant3 [48] based simulation package SKDETSIM [62].

This likelihood is maximised with respect to **x** in order to obtain the best-fit track properties. A cut can be placed on the likelihood value of the best-fit hypotheses for the creation of analysis samples.

2.4.4 Energy Reconstruction

As the oscillation probability depends strongly on neutrino energy, it is advantageous to reconstruct the energy of the incident neutrino from the properties of the outgoing particles observed in the detector. For this, SK assumes interactions are CCQE as in Fig 1.10(a) and uses the outgoing charged lepton kinematics to infer the original neutrino energy.

$$E^{rec}_{CCQE} = \frac{2M_{N,i}E_l - M_l^2 + M_{N,f}^2 - M_{N,i}^2}{2(M_{N,i} - E_l + p_l \cos\theta_l)} \tag{2.2}$$

Here $M_{N,i}$ and $M_{N,f}$ are the mass of the initial and final nucleon respectively. M_l, E_l, p_l and θ_l are the outgoing charged leptons mass, energy, momentum and angle relative to the incident neutrino respectively.

While this reconstruction works well for true CCQE interactions, events with outgoing undetected particles or those with different interaction kinematics will reconstruct with biased energy relative to the true incident neutrino energy.

Chapter 3

Hyper-Kamiokande

3.1 Introduction

The HK experiment is a next-generation neutrino observatory and proton decay experiment currently in the construction phase. The major component of this is the HK detector, a new water-Cherenkov detector of similar construction to SK but with more than eight times the fiducial mass.

Using this large instrumented mass, HK will expand on the success of SK, with physics aims including world-leading sensitivity to proton decay [65], atmospheric neutrino oscillation and solar neutrino observation [66].

HK includes a long-baseline neutrino oscillation component, the successor to T2K. This reuses many components from the T2K experiment but with a number of upgrades to the beam and near-detectors along with a new detector the IWCD (Intermediate Water Cherenkov Detector), see Fig 3.1.

The principle of operation is identical to T2K; muon neutrinos produced at J-PARC are measured by a near detector suite, then allowed to oscillate in-flight before reaching the far detector HK, here the energy and flavour distribution can be measured. The use of HK as the far-detector will allow for the collection of an unprecedented number of neutrino events in the far detector, which will allow for world-leading physics sensitivity [66].

3.2 Beamline

HK will make use of the same J-PARC beamline currently used by T2K (see section 2.2) but with a number of upgrades scheduled to increase neutrino beam flux.

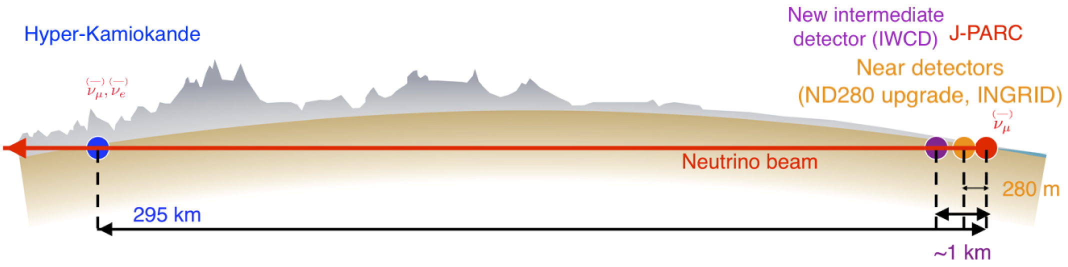

FIGURE 3.1: A schematic diagram of the LBL component of HK, muon neutrinos produced at J-PARC are detected by the near-detector suite, the IWCD and the HK detector.

The overall goal of the beamline for HK is to deliver a proton beam with equivalent continuous power of greater than 1.3MW [66] [67]. This will be achieved through an upgrade to the beamline power supplies and RF cavities. The goal of this is to allow for an increase in the repetition rate of the beam, from the current T2K 2.48s to a goal of 1.16s. Along with this, the number of protons per pulse is set to increase from 2.5×10^{14} to 3.2×10^{14} protons per pulse as seen in Fig 3.2 [67].

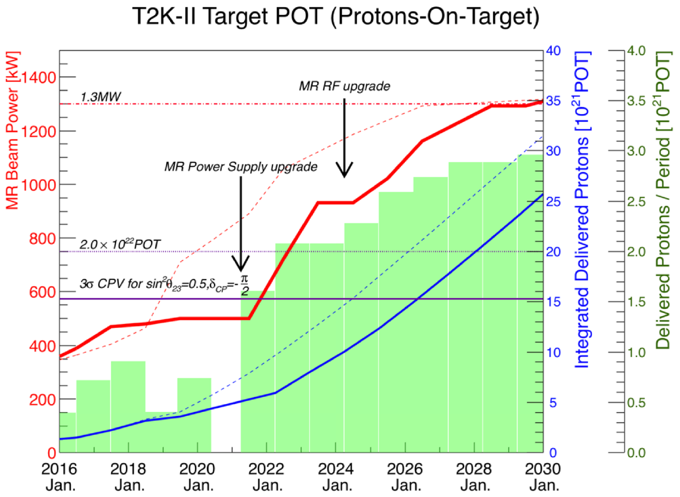

FIGURE 3.2: The J-PARC beam power upgrade road map. The solid red line shows the beam power while the green histogram shows the deliverable POT (protons on target) per year, assuming 6 months of running with 90% uptime. The beam power is expected to reach 1.3MW at the start of HK running. Reproduced from [67].

In order to reduce the wrong-sign component, the three magnetic focusing horns will have their current increased from the 250kA used by T2K to 320kA.

3.3 Near-Detector Complex

HK intends reuse the existing near-detector suite of INGRID and ND280. As part of T2K-II, ND280 will undergo an upgrade to include a new sFGD (super fine grained detector) detector component [68]. This will consist of over 2 million 1cm × 1cm ×1cm doped polystyrene scintillator cubes, arranged in a grid. Each cube has three WLS fibres passing through in the X, Y & Z axes, these are readout by MPPCs (multi pixel photon counters) at the ends of each fibre and allow for 3D tracking of charged particles in the sFGD.

This sFGD is sandwiched between two TPCs arranged vertically above and below the sFGD, this allows for the tracking and momentum measurement of charged particles exiting sFGD at high angles relative to the incident neutrino beam, see Fig 3.3.

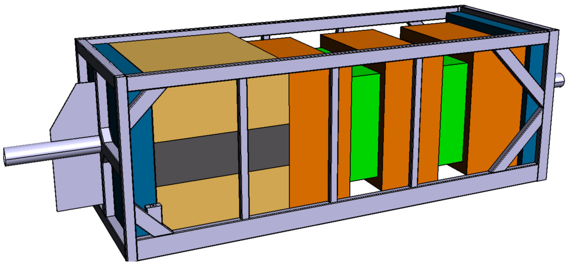

FIGURE 3.3: The ND280 upgrade proposal includes a new Super-FGD (grey) placed within two 'high-angle' TPCs (brown). This arrangement will enable ND280 to perform measurements of neutrino interaction with outgoing particles travelling transverse to the beam direction. Reproduced from [68].

With finer granularity than the existing FGDs and coverage of a greater angular range for outgoing particles, ND280 upgrade will be able to make improved measurements on 2p-2h cross-section, the Q^2 dependence of CCQE and pion absorption [68]. It will however still be limited by its relatively low 2.2t mass for measurement of ν_e and $\bar{\nu}_e$ cross-section in the sub-GeV energy range.

3.4 Intermediate Water Cherenkov Detector

In addition to the upgraded near-detector, HK includes an entirely new detector, the IWCD (Intermediate Water Cherenkov Detector). This is a half-kiloton scale water Cherenkov detector, located approximately 1km from the neutrino production point.

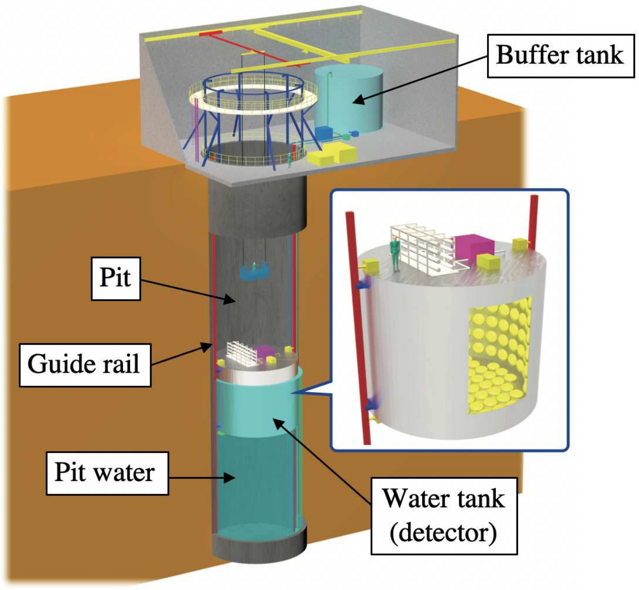

FIGURE 3.4: A diagram of the IWCD showing the detector located inside the water filled pit. By raising and lowering the detector, the angle relative to the centre of the beam can be varied.

The IWCD is composed of an approximately 8m diameter, 6m tall cylinder, filled with pure water and instrumented with PMTs on its inner surface. The detector sits within a 11m diameter, 50m deep cylindrical pit as seen in Fig 3.4. The purpose of this shaft is to allow the detector to move vertically relative to the central axis of the neutrino beam. This allows for the detector to measure the beam at different off-axis angles, due to the decay kinematics discussed in §2.2.3 the neutrino flux has a strong dependence on this off-axis angle. The IWCD can therefore make measurements of regions of the beam with different energies and neutrino compositions.

Construction

The design process of the IWCD is still ongoing, hence some details of the construction discussed here will not match the final detector design.

The IWCD is planned to consist of two stainless steel cylinders, the larger cylinder of diameter 10m and height 8m will sit within the 11m diameter pit. This acts to isolate the detector volume from external light and includes flotation spaces to allow the IWCD to be only slightly negatively buoyant in the water in the shaft. Within this outer cylinder is a 8m diameter 6m tall stainless steel scaffold which divides the volume into the OD region and the ID region. Similarly to SK, the IWCD's ID surface will be covered by a black, light absorbent plastic sheet to limit reflections and to optically isolate the ID from the OD.

Instrumentation

Due to the small scale of the IWCD, traditional large PMTs such as the 50cm PMTs used by SK [62] will not provide sufficient granularity to accurately reconstruct neutrino interaction events. The IWCD will therefore use new mPMT (multi-photomultiplier tubes) modules for ID instrumentation.

The mPMTs are structures composed of 19 small 8cm PMTs arranged within an acrylic dome as seen in Fig 3.5. This design allows for a larger number of PMTs to be contained in the same 50cm footprint of the SK PMTs.

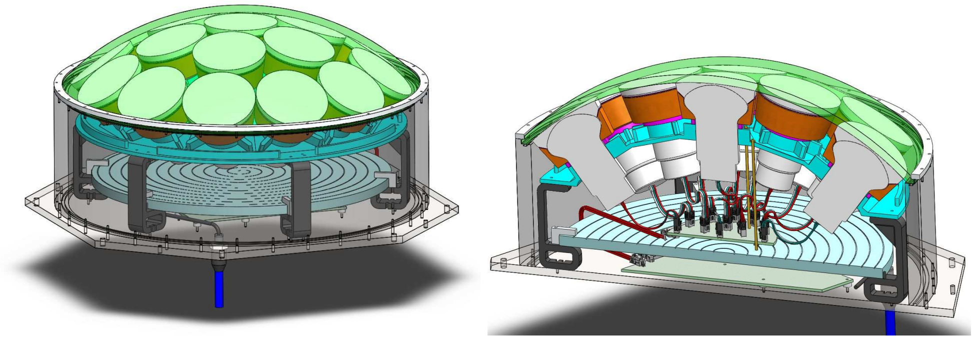

FIGURE 3.5: A model of the 'multiPMT' modules that will be used by the IWCD, 19 small 8cm PMTs are arranged into a single module allowing for higher granularity and more precise timing response than possible with the 50cm PMTs used by the far-detector of HK.

In addition, the mPMT modules include a scintillator plate at the rear of the module. This will be used to identify entering backgrounds from upstream neutrino interactions and provide a measurement of detector pile-up.

Off-Axis Principle

A major feature of the IWCD is its ability to be moved within the vertical shaft it resides in. This movement changes the off-axis angle of the beam being measured. Due to the decay kinematics of pions from §2.2.3 these different off-axis regions experience different neutrino fluxes. Notably, muon neutrinos, primarily produced by pion decay have a strong dependence on off-axis angle, with higher angles having a lower energy flux peak and overall lower integrated flux, electron neutrinos by contrast are primarily produced via the three-body decay of muons, the off-axis effect is therefore less significant as can be seen in Fig 3.6.

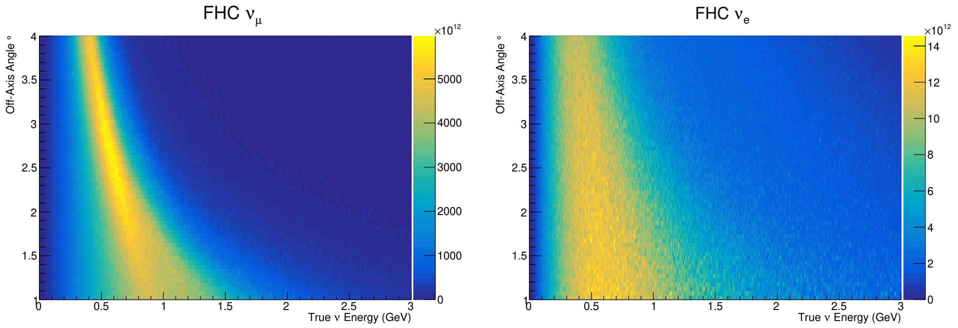

FIGURE 3.6: The dependence on off-axis angle on the ν_μ flux (left) and the ν_e flux (right) for FHC operation. The ν_μ flux shows a strong dependence on off-axis angle, with higher angles having a lower energy. The ν_e flux shows a significantly smaller dependence on this angle.

This will in principle allow for better decoupling of flux and cross-section effects, by taking samples from different off-axis angles, different energy fluxes can be observed, allowing for inference of different interaction cross-sections as a function of neutrino energy. This reduces the reliance on accurate kinematic reconstruction of events necessary to infer cross-section as a function of energy with a fixed detector. Additionally, as the ν_e flux does not drop off as rapidly with off-axis angle as the ν_μ flux, the flavour composition of the beam varies with this angle, the highest purity ν_e region being at the most off-axis angle.

Goals

The IWCD aims to provide a precise measurement of ν_e and $\bar{\nu}_e$ charged-current cross-section in kinematic regions relevant to the HK ν_e appearance channel. Present measurements of this cross-section are hampered either by low statistics [69][70][71] or large systematic uncertainties in the energy range relevant to HK [72].

The 300t ID mass of the IWCD and proximity to the source of the neutrino beam will allow for tens of thousands of ν_e events events to occur within the detector. If a sufficiently pure sample of these events can be constructed, a fit to this data could be performed to directly measure the ν_e cross-section in the energy range of relevance to HK.

As the IWCD can be located at the same 2.5° off-axis angle as HK, it can be used to directly measure the intrinsic ν_e and $\bar{\nu}_e$ contamination of the beam. This intrinsic contamination is an irreducible background at HK to the electron neutrino appearance channel.

The IWCD will also be able to provide a sample of approximately 200 000 neutral current π^0 events, allowing for a precise determination of the interaction cross-section for this process. NC backgrounds, in particular NCπ^0 events are the largest background to the electron-like samples at HK [66][73] and so will also impact CP sensitivity.

Finally it may be possible to perform a more model-independent neutrino oscillation analysis; through addition and subtraction of different off-axis slices, it is possible to obtain an event distribution corresponding to that of an oscillated neutrino flux. By varying the relative weights of the slices, fluxes corresponding to a chosen set of oscillation contours can be produced, this sample can then be used in an oscillation fitter [74].

3.5 Hyper-Kamiokande Detector

The major component of the HK project is the HK detector itself Fig 3.7. This is a water Cherenkov detector of similar design and construction to SK in §2.4.

HK will be considerably larger than SK, with total water mass of 258kton and a fiducial mass of 187kton [75]. This is equivalent to 8.3× the fiducial mass of SK.

Construction

The HK detector will consist of a vertically aligned cylinder of diameter 68m and height 71m. Similarly to SK, a stainless steel scaffold will divide the volume into the ID region, with diameter 64m and height 66m and the OD region with a thickness of approximately 1m in the barrel section and 2m in the end caps.

Instrumentation

The ID surface of HK will be instrumented with 50cm PMTs. The present plan calls for a minimum of 20,000 PMTs, giving 20% photo-coverage [75]. These PMTs will

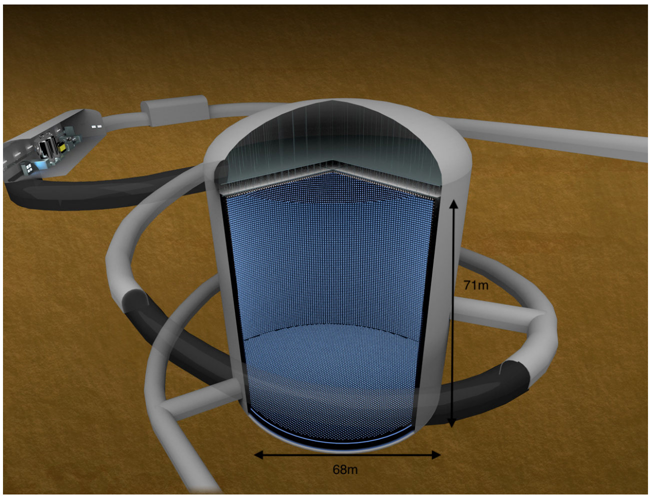

FIGURE 3.7: A cutaway of the HK detector showing the cylindrical construction and inner and outer detector regions.

however have significantly higher quantum efficiency than those used in SK resulting in a similar effective light collection to the 40% photocoverage in SK.

These 50cm PMTs will be augmented with mPMTs [76] of a similar design as the IWCD mPMTs described in §3.4. The OD region will consist of 7600 small 8cm PMTs with an attached WLS plate to increase the light collection efficiency [77] [66].

3.5.1 δ_{CP} Measurement

The scale of HK and the increased beam power will allow for the selection of over 3000 signal oscillated ν_e and $\bar{\nu}_e$ CC events [66]. This represents a greater than 30× increase over the data collected by T2K at present [73].

The impact of different values of δ_{CP} on these 1Re (1 Ring electron) samples can be seen in Fig 3.8, maximal CP violating values of δ_{CP} (-90°, 90°) yield changes to the overall event rate in both samples. With opposite behaviour for the FHC and RHC samples. The CP conserving value of δ_{CP} =180° results in a change in the shape of the distribution with little change in the overall event rate.

This large dataset will provide the necessary statistical power to differentiate such changes as in Fig 3.8. However systematic uncertainties on the ν_e and $\bar{\nu}_e$ event rates can become limiting over statistical uncertainty. This becomes a significant problem in the case of a non-maximal value of δ_{CP}, here systematic uncertainty may prevent HK from making a discovery statement with the expected exposure. Controlling systematic uncertainty is therefore key for the greatest CP sensitivity.

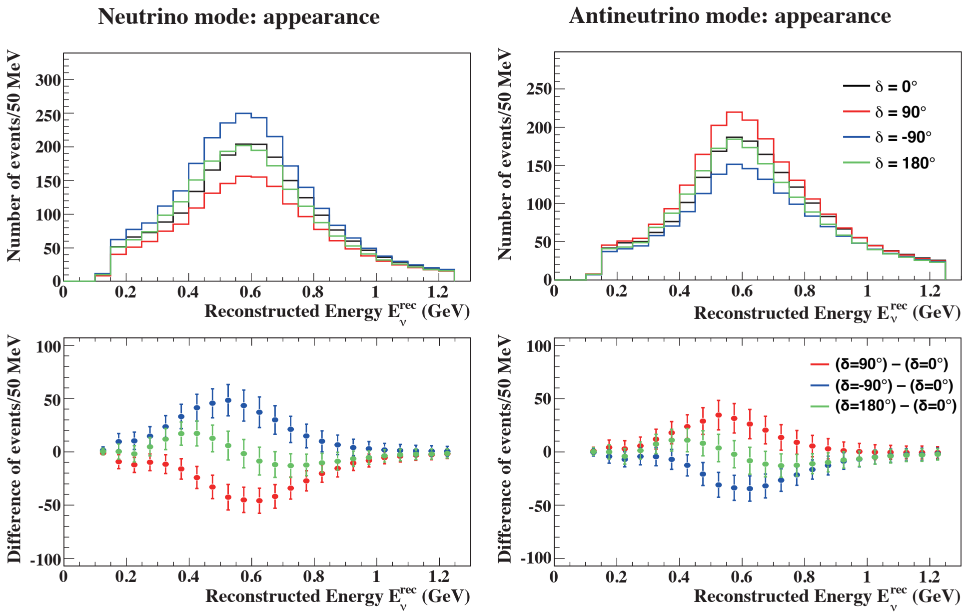

FIGURE 3.8: Top: the expected 1Re event distributions of the full HK beam dataset, the effect of different δ_{CP} values is shown. Bottom: the difference from the δ_{CP} =0 distribution, error bars correspond to statistical uncertainty alone. $\sin^2\theta_{13}$ = 0.026 and normal hierarchy assumed. Reproduced from [66].

Chapter 4

Bayesian Methods

In the T2K analysis, MC is weighted according to a model with 772 free parameters, in order to fit to binned data from the experiment. Such a high-dimensional model is challenging to fit with conventional methods. In addition, some parameters are expected to exhibit non-Gaussian behaviour, further complicating the analysis. Finally, T2K does not exist on its own, and a number of constraints (priors) on many of these parameters are available from external data and should be included where possible to improve the sensitivity of the experiment. Bayesian methods and MCMC (Markov chain Monte Carlo) offer the ability to efficiently handle each of these requirements, in order to obtain measurements of the desired physics parameters of interest.

As Bayesian and the more common frequentist analysis methods differ in a number of regards, it is useful to describe here the techniques used and their interpretation. First the general principle of inclusion of prior information is discussed in §4.1. Markov chain techniques are discussed in §4.2 — 4.5 and finally the use of Markov chains to extract information about model parameters is described in §4.6 — 4.7. Much of this chapter is derived from [78] [79] [80] [81].

4.1 Posterior Probability

Central to the Bayesian analysis paradigm is the posterior probability density. This is composed of two parts, a prior probability density $P(\mathbf{x})$, which describes the probability of a given set of model parameters ($\mathbf{x}$). The second component is the conditional probability for the data, given a set of model parameters $P(D|\mathbf{x})$, this can be obtained through comparison of MC generated with parameters $\mathbf{x}$ to the data.

These respectively represent any external knowledge we have on the model parameters, and the information available in the data. The posterior probability ($P(\mathbf{x}|D)$) then describes the probability of a set of model parameters conditional on the data observed.

In a Bayesian analysis paradigm, therefore, a set of collected data is used to update a prior probability distribution for parameters of a model according to Bayes rule [80]:

$$P(\mathbf{x}|D) = \frac{P(D|\mathbf{x})P(\mathbf{x})}{P(D)} = \frac{P(D|\mathbf{x})P(\mathbf{x})}{\int P(D|\mathbf{x})P(\mathbf{x})d\mathbf{x}} \tag{4.1}$$

Here **x** are the parameters of the model being compared to the data, D.

The updated probability density $P(\mathbf{x}|D)$ (the posterior), therefore describes the probability density for the parameters **x** after including the observed data. The distribution of the posterior probability in the parameter space **x** is the only object needed for Bayesian inference. The posterior distribution remains a high-dimensional object however, having the same dimension as that of the model used $dim(\mathbf{x}) = dim(P(\mathbf{x}|D))$. Bayes rule therefore allows for the inclusion of prior information into the probability distribution, however evaluating this distribution and making use of such a high dimensional object poses its own challenges.

4.1.1 The Need for Markov Chains

In Bayesian inference it is often necessary to evaluate functions weighted by the posterior distribution of the form:

$$E\left[f(\mathbf{x})|D\right] = \frac{\int f(\mathbf{x})P(D|\mathbf{x})P(\mathbf{x})d\mathbf{x}}{\int P(D|\mathbf{x})P(\mathbf{x})d\mathbf{x}} \tag{4.2}$$

Here **x** are the parameters of the model being compared to the data, D. $f(\mathbf{x})$ is the function being evaluated over the posterior density e.g. the posterior expectation of a particular parameter $E[x_i]$ could be obtained by setting $f(\mathbf{x}) = x_i$.

Such integrals are in general not analytically solvable, hence numerical integration may be used. For high-dimensional parameter spaces, traditional integration schemes are inaccurate and inefficient, thus alternative methods such as Monte Carlo are used [82].

4.2 Markov Chain Monte Carlo

It is possible to perform an approximation to the integral in eqn 4.2 by evaluating the function at a series of points randomly drawn from the full posterior distribution:

$$E\left[f(\mathbf{x})|D\right] \approx \frac{1}{N}\sum_{i=1}^{N} f(\mathbf{X}_i) \tag{4.3}$$

where $\mathbf{X}_i$ is a randomly drawn sample from the posterior distribution eqn 4.1.

Conventional methods of drawing random samples from a complex posterior distribution are challenging and inefficient for high-dimensional parameter spaces [83].

Markov chains offer a method to efficiently make these samples. Such a Markov chain is a stochastic process consisting of an ordered series (chain) of points (steps) in a parameter space. The position of each step in the chain is dependent only on its immediately preceding step and the posterior probability evaluated at the current and previous position.

Markov chains therefore consist of a series of discrete jumps around the parameter space, this on its own is not necessarily of use. However, it is possible to define a set of rules for the chain that ensures that the density of steps in a particular region is proportional to the posterior being evaluated.

A chain with this property can easily be used to generate independent samples from the posterior. As the density of steps is proportional to the posterior, the position of any randomly chosen step from the chain will have the same distribution as a random sample from the posterior. In practice with finite chains, sufficiently separated steps in the chain may be used as a random sample.

The construction of such a Markov chain and the separation of steps required is discussed in §4.2.1 and §4.5 respectively.

These steps from the chain may then be used in eqn 4.3 to obtain expectation values for functions.

4.2.1 Metropolis Hastings

The Metropolis-Hastings algorithm [81][84] is a method to ensure that the equilibrium state (stationary distribution) of the Markov chain is proportional to the posterior density.

It consists of a random walk through the parameter space where the acceptance or rejection of a step is dependant on the relative posterior density at the proposed step position. This acceptance is biased towards accepting steps with a higher posterior probability, hence ensuring the chain has a higher density of steps in areas with high probability than in regions with low probability.

The procedure is as follows: for a Markov chain, after t steps at a point in parameter space $\mathbf{x}_t$, a step proposal function is used to generate a new position in the space $\mathbf{x}'$ according to:

$$\mathbf{x}' = \mathbf{x}_t + \mathrm{rand}(q(\mathbf{x}_t)) \tag{4.4}$$

Where q is some multivariate probability distribution which can in principle depend on the current position $\mathbf{x}_t$. This is equivalent to randomly sampling a simple proposal function through conventional means, and applying this as a small step relative to the current position in the chain.

This proposed step must then be either accepted or rejected. This is done randomly with probability of acceptance dependant on the relative posterior densities at the current and proposed points, this probability α is given by:

$$\alpha = \min\left[1, \frac{P(\mathbf{x}'|D)q(\mathbf{x}|\mathbf{x}')}{P(\mathbf{x}|D)q(\mathbf{x}'|\mathbf{x})}\right] \tag{4.5}$$

Where $q(\mathbf{x}'|\mathbf{x})$ is the probability density of the proposal function to propose a step to $\mathbf{x}'$ given the current position $\mathbf{x}$.

While a wide range of step proposal functions would yield a valid Markov chain, for efficient exploration and sampling of the posterior, the choice of proposal function is key. For the T2K MCMC analysis a hand-tuned multivariate Gaussian proposal is used.

In the case of a symmetric proposal such as this multivariate Gaussian, $q(\mathbf{x}'|\mathbf{x}) = q(\mathbf{x}|\mathbf{x}')$ the step acceptance equation may be simplified. Furthermore as the ratio of posterior probabilities is taken, the normalisation factor in eqn. 4.1 may be omitted giving:

$$\alpha = \min\left[1, \frac{P(D|\mathbf{x}')P(\mathbf{x}')}{P(D|\mathbf{x})P(\mathbf{x})}\right] \tag{4.6}$$

then making use of the definition of log-likelihood:

$$\ln \mathcal{L} = \ln\left(P(D|\mathbf{x})P(\mathbf{x})\right) \tag{4.7}$$

the acceptance probability can be written as:

$$\alpha = \min\left[1, \frac{\mathcal{L}(\mathbf{x}')}{\mathcal{L}(\mathbf{x})}\right] \tag{4.8}$$

A uniform random variable u is then generated in the range [0,1] which determines whether the step is accepted:

$$\mathbf{x}_{t+1} = \begin{cases} \mathbf{x}' & \text{for } u \leq \alpha \\ \mathbf{x}_t & \text{for } u > \alpha \end{cases} \tag{4.9}$$

If this step is accepted, a step at the position $\mathbf{x}'$ is appended to the chain, otherwise the current position $\mathbf{x}_t$ is appended. This process of step proposal, acceptance probability evaluation and acceptance or rejection is repeated at the new position.

This procedure will always accept steps proposed to a position with higher likelihood and will probabilistically accept steps to regions with lower likelihood with lower probability for regions with much lower likelihoods. It can be shown that following this prescription, the stationary distribution of steps in the chain is proportional to the posterior probability [80].

4.3 Burn In

As the posterior distribution is not a-priori known, the chain cannot be started in its stationary distribution. There are therefore a number of steps needed for the chain to converge to the region of high posterior density, this is the 'burn-in' period.

Identification of this burn-in period can be made through observation of the change in the likelihood as a function of step number. This likelihood will stabilise around a single value as seen in Fig 4.1(a). This alone is not however sufficient to indicate burn-in is completed, consideration of the parameters themselves must also be made to determine when equilibrium has been reached as in Fig 4.1(b) [85].

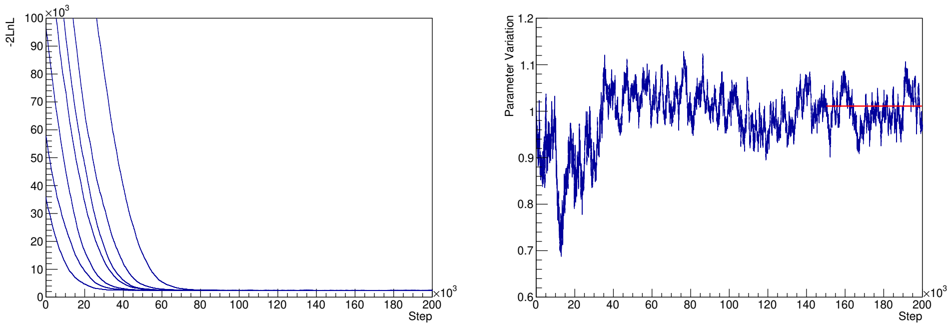

FIGURE 4.1: The convergence of the log-likelihood to the stationary distribution for seven chains running on T2K data (left) and the behaviour of a single parameter as the chain progresses (right) before reaching the equilibrium central value (red).

Once the likelihood and a random selection of the parameters are found to have stabilised, the chain is said to have passed burn-in, to avoid biasing the chain, all steps prior to this burn-in are discarded. The choice of stabilisation point is made conservatively, overestimation of burn-in does not bias the resulting chain, simply requiring a corresponding increase in the length of chains required.

4.4 Convergence

While infinitely long Markov chains are guaranteed to explore the full allowable range of all parameters, with a finite-length Markov chain, it is possible for the chain to converge to a local minimum. This chain can become trapped in this region and hence its step density would not be proportional to the posterior over the full space.

One method to identify this occurrence is to run multiple chains from differing start points, over-dispersed relative to the expected posterior distribution [85]. A sample of the obtained parameters may then be compared between chains for agreement.

4.5 Step Correlations

As the Markov chain method above makes proposals for steps centred around the current position of the chain eqn 4.4, successive steps in the parameter space are not independent. For the small step sizes needed to ensure a large proportion of steps are accepted, as required for efficient exploration, this step-to-step correlation is extremely high.

In order to make random samples of the posterior using a chain, one cannot simply select successive steps in the chain due to this large correlation between steps. Samples can however be taken using a sufficiently large gap between selected steps, so that the chain has sufficient opportunity to randomise between the sample points.

For each parameter in the fit, an autocorrelation measure can be used to assess the size of the gap needed for these samples to be independent. For a given gap (lag) between samples 'd', using a chain with length N, the autocorrelation is defined as:

$$R_{ii}(d) = \frac{\sum_{t=1}^{N-d}(x_i(t)-\bar{x}_i)(x_i(t+d)-\bar{x}_i)}{(N-d)\sigma_i^2} \tag{4.10}$$

Where $x_i(t)$ is the value of the i'th parameter in the model at step 't', $\bar{x}_i$ is the mean value of this parameter over the whole chain and σ_i is its standard deviation.

All parameters have high autocorrelation for low lag values, as the size of the steps taken are small compared to the parameter width σ_i. Hence successive steps are close together in the space. At higher lag, a greater number of random steps will have been accepted between the points being compared, hence the samples are less related and the autocorrelation will decrease.

This autocorrelation is also used to guide the choice of step proposal scale for each parameter. A 'long autocorrelation' on a parameter i.e. high autocorrelation out to large lag values, is indicative of the step proposal function being too narrow in that parameter and in need of broadening. This reduces the number of steps, and therefore likelihood evaluations needed to obtain independent samples of the posterior.

4.6 Parameter Evaluation

While the Markov chain itself contains all of the information needed for a reconstruction of the full posterior, there are a number of issues associated with simply providing the chain as a result. One major issue is the finite nature of the Markov chains produced. While a T2K result may include in excess of 150M steps, these are dispersed in a 772 dimensional space. As such, the step density in any region of space, even those at high posterior probability will be very low and subject to significant statistical fluctuation. Simply binning the chains in this space, even with extremely coarse binning would not result in a tractable number of bins or sufficient steps in each bin (two bins per parameter would require $\approx 10^{230}$ bins).

The dimensionality of the problem can be significantly reduced by considering only the parameters of interest from an oscillation perspective, the oscillation parameters: θ_{23}, θ_{13}, Δm^2_{32}, δ_{CP}. All other parameters in the fit are treated as 'nuisance' parameters, which may have an effect on the posterior distribution and therefore on the oscillation parameters, but are not themselves of interest from a long-baseline physics perspective. In Bayesian statistics, these nuisance parameters may be integrated over (marginalised):

$$P(\mathbf{x}_{\mathrm{Oscillation}}|D) = \int P(\mathbf{x}|D)d\mathbf{x}_{\mathrm{Nuisance}} \tag{4.11}$$

yielding a posterior density for just the oscillation parameters, in Markov chains, this integral simply corresponds to not binning the chain in the nuisance parameters. This results in a reduced dimension posterior in just the parameters of interest, but including the effect that the nuisance parameters can have on the oscillation parameters.

An example of marginalisation over nuisance parameters is shown in Fig 4.2. One implication of this integration over the space, is that the value of a parameter corresponding to the point with highest posterior density in the full space may not be the same as the point after marginalisation. This can occur if the posterior distribution is non-Gaussian.

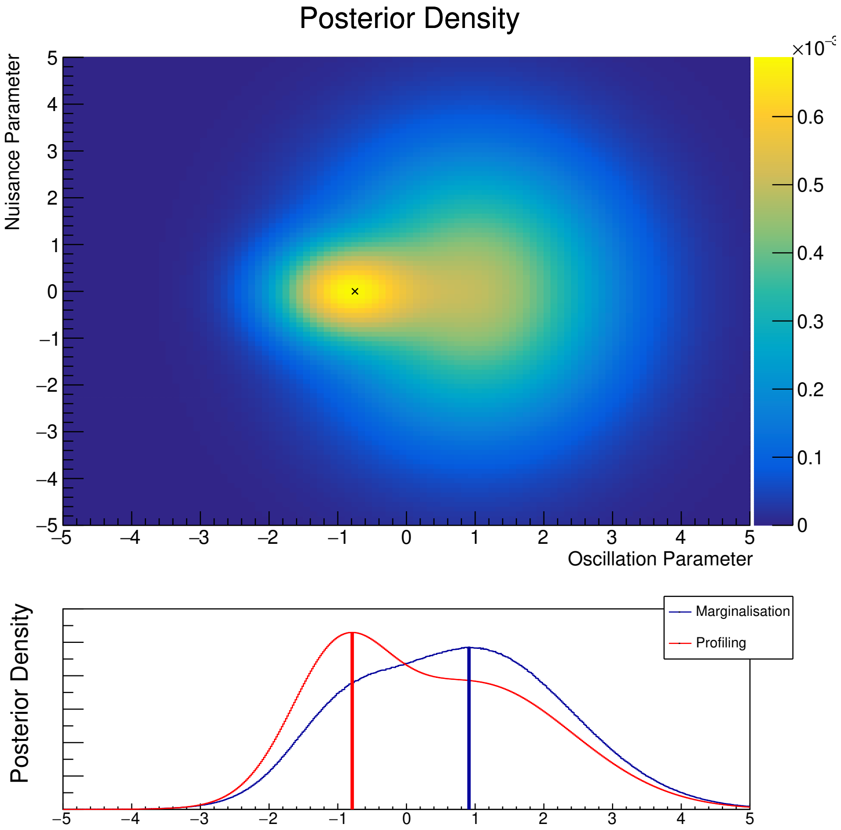

FIGURE 4.2: A two dimensional posterior distribution (top) with the highest likelihood marked. Bottom, the effect of marginalisation over the nuisance parameter compared to a profile method along the x axis, note the change in highest posterior density after marginalisation.

4.7 Credible Intervals

Having obtained a marginalised posterior density in a parameter of interest, it is desirable to assign an interval in which the true value has a given probability of lying. This can be done with a credible interval. This defines a section of the marginalised posterior for which a given proportion of the posterior lies within the identified region. For example, a 90% credible interval is any region which contains 90% of the integrated posterior probability and is defined as:

$$\int_I P(x_j|D)dx_j = 0.9 \tag{4.12}$$

Where $P(x_j|D)$ is the marginalised posterior density for parameter 'j' and I is the interval being integrated over.

In a Bayesian credible interval, given the data of the experiment, there is a 90% probability that the true parameter value lies within the interval. This is distinct from a Frequentist confidence interval, in which, were the experiment repeated a large number of times, the best-fit point would lie within the confidence interval 90% of the time.

The definition of a credible interval in eqn 4.12 does not however lead to a unique interval. A number of choices are available, this analysis uses the HDPI (highest posterior density interval). This selects intervals in which every point within the interval has higher marginalised posterior density than every point outside of the interval.

In practice, this is done by binning the marginalised posterior, then adding the bin with the largest number of MCMC steps to the interval, then the bin with the second most MCMC steps and so on. This is continued until the fraction of total steps within the interval exceeds the desired credible interval threshold. The region covered by the selected bins is then the quoted confidence interval. Using this definition, the point with highest marginalised posterior density is guaranteed to be included in the interval, however the interval may not be contiguous, consisting of a number of separate regions. This process can be easily generalised to multidimensional marginalised posteriors to create credible regions.

Chapter 5

MaCh3

MaCh3 (Markov Chain 3 flavour) is a Bayesian Markov chain based fitting framework used by T2K. This performs a simultaneous model-dependant fit to ND280 and SK data samples, this both constrains the desired oscillation parameters in addition to a parameterised model of the systematic uncertainties of the experiment such as neutrino flux and cross-section, so-called 'nuisance parameters'. This chapter will cover the overall goals of the MaCh3 analysis along with the data used and the details of the model being constrained.

5.1 Overview

While it is possible to extract oscillation parameters from T2K using only external knowledge of the neutrino beam and the samples at SK, such an analysis would be severely limited by large uncertainties on the neutrino interaction cross-section and flux [86]. To resolve this, ND280 was constructed in order to observe the beam and neutrino interactions before oscillation, therefore helping to decouple the effect of cross-section from oscillation.

ND280 is however a different detector technology to SK, with different energy thresholds, PID performances and target material, making direct comparison of event rates at the two detectors infeasible. MaCh3 has therefore adopted a model-dependant analysis approach. Here a model of neutrino interactions, flux etc. is simultaneously fit to both ND280 and SK data. The large samples at ND280 allow for a tight constraint on these model parameters, thus reducing the uncertainty on the predicted event distributions at SK, allowing for an increased sensitivity to oscillation effects.

5.2 Likelihood

As described in §4.1 the likelihood function must take account of both T2K data and prior information on the fit parameters.

In MaCh3 the data and MC are binned in reconstructed kinematics, and compared using a Poisson log-likelihood measure to evaluate the likelihood of the data given the MC prediction in that bin:

$$-\ln \mathcal{L}(D|\mathbf{x}) = \sum_{i}^{\text{Bins}} \left(n_{i,pred}(\mathbf{x},\boldsymbol{\theta}) - n_{i,obs} + n_{i,obs} \ln \left(\frac{n_{i,obs}}{n_{i,pred}(\mathbf{x},\boldsymbol{\theta})} \right) \right). \tag{5.1}$$

Where $n_{i,obs}$ is the number of data events seen in bin 'i' while $n_{i,pred}(\mathbf{x})$ is the MC predicted number of events in bin 'i' for the set of nuisance parameter values $\mathbf{x}$ and oscillation parameters $\boldsymbol{\theta}$. This is summed over all bins and samples in the fit, including ND280 and SK, to give the total sample contribution to the log-likelihood.

The prior constraint is included as a Gaussian covariance matrix $\mathbf{V}$ on the model parameters and contributes to the likelihood:

$$-\ln \mathcal{L}_{\text{prior}} = \frac{1}{2} \sum_{i,j}^{\text{Systematics}} \left((x_i - \mu_i)(\mathbf{V}^{-1})_{ij}(x_j - \mu_j) \right), \tag{5.2}$$

where μ_i is the prior mean for parameter i. The summation runs over parameters with explicit priors, some parameters are not constrained by external considerations and these are given equal prior probability across their whole range (a 'flat prior'), being constrained solely by T2K data. A similar prior constraint can be provided for the oscillation parameters, and added giving the total log-likelihood function used by MaCh3:

$$\begin{aligned} -\ln(P(D|\mathbf{x})P(\mathbf{x})) = -\ln \mathcal{L}_{Total} = &\sum_{i}^{\text{Bins}} \left(n_{i,pred}(\mathbf{x}) - n_{i,obs} + n_{i,obs} \ln \left(\frac{n_{i,obs}}{n_{i,pred}(\mathbf{x})} \right) \right) \\ &+ \frac{1}{2} \sum_{i,j}^{\text{Systematics}} \left((x_i - \mu_i)(\mathbf{V}^{-1})_{ij}(x_j - \mu_j) \right) \\ &+ \frac{1}{2} \sum_{i,j}^{\text{Osc Pars}} \left((\theta_i - \lambda_i)(\mathbf{U}^{-1})_{ij}(\theta_j - \lambda_j) \right) \end{aligned} \tag{5.3}$$

Where **U** is the prior uncertainty on the oscillation parameters.

This likelihood is equivalent to an unnormalised posterior probability, as such it can be used in the Metropolis-Hastings algorithm §4.2.1 to construct the desired Markov chain.

5.2.1 MCMC Details

As discussed in §4.5, in order to efficiently sample this likelihood, a good step proposal function is needed. For this MaCh3 uses a hand-tuned multivariate Gaussian proposal based on the prior constraint.

The tuning of this Gaussian is based on the autocorrelation observed for each parameter in a test fit. The principle adopted by T2K and used throughout the rest of this thesis is to take the point at which the autocorrelation first drops below 0.2 as the lag necessary to obtain independent samples of the posterior for the chosen parameter. The width of the Gaussian in each parameter is then tuned such that all parameters have approximately equal autocorrelation length. This autocorrelation length is then used when determining the number of steps required to have sufficient independent samples to create a given credible interval.

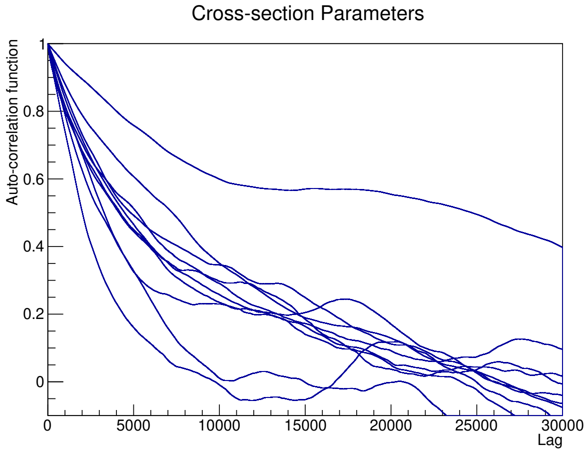

FIGURE 5.1: A set of autocorrelation functions as a function of lag for ten cross-section parameters in MaCh3. Some parameters have a more rapidly decreasing autocorrelation than others even within a single chain.

5.3 ND280 Samples

This analysis includes both neutrino and antineutrino samples at ND280 corresponding to T2K runs 2-9 for an exposure of 1.1531×10^{21} POT in FHC and 0.8336×10^{21} POT in RHC [87].

Due to the difference in construction of FGD1 and FGD2, notably FGD2 having water target layers, all ND280 samples are split by primary interaction vertex location into FGD1 and FGD2 samples.

All samples are required to have at least one forward going track in both an FGD and TPC along with a particle passing a right-sign muon PID cut (μ^- for FHC, μ^+ for RHC)[88]. Events passing these requirements are then categorised by number of observable right-sign pions in the TPCs (π^+ in FHC, π^- in RHC). In total there are three selections: CC0π, CC1π for zero and one pion respectively, and CC other for events with more than one pion or with photons or electrons.

The same set of cuts are used for RHC. As ND280 is magnetised and therefore has sign-selection capabilities, it is possible to construct samples of wrong-sign interactions ($\bar{\nu}_\mu$ events in FHC, ν_μ events in RHC). This is currently only performed in RHC due to the higher event rate of wrong-sign events in this mode. This primarily derives from the higher interaction cross-section for neutrinos compared to antineutrinos.

Six such RHC wrong-sign samples are included using the same cuts as above but with opposite lepton and pion charge. This is necessary in order to constrain the wrong-sign component of the flux at SK, where no sign-selection is possible.

A total of 18 samples are therefore included, six in FHC, three for each FGD all right-sign samples, along with 12 in RHC, six for each FGD, of which three are $\bar{\nu}_\mu$ and three ν_μ.

All of these samples are binned in reconstructed muon momentum and $\cos(\theta)$, the angle the outgoing muon makes with the incident beam direction.

5.4 Super-Kamiokande Samples

SK data includes both FHC and RHC samples corresponding to runs 1-10, with an exposure of 1.9664×10^{21} POT in FHC and 1.634556×10^{21} POT in RHC. The difference to the POT at ND280 is due to ND280 being inoperable for a large portion of some runs. Unlike ND280, SK is not magnetised and has no way of identifying the charge of an outgoing lepton, hence the samples are broken down only by magnetic horn current.

The current T2K analysis makes use of five data samples at SK. Three samples in FHC: one ring muon like (1Rμ), one ring electron like (1Re) and one ring electron one decay electron (1Re 1d.e.). In addition to two samples in RHC: one ring muon like (1Rμ) and one ring electron like (1Re).

The selection criteria for these samples are the same in FHC and RHC and use the reconstructed variables from fiTQun [64] see §2.4.3.

All events must be fully contained, i.e. no particles escape the inner-detector volume, as well as having their reconstructed vertex position within the fiducial volume.

For 1Rμ selections, events must consist of a single Cherenkov ring passing a muon PID cut with reconstructed neutrino energy (assuming CCQE) greater than 200MeV and at least one electron from the muon decay [89].

The 1Re and 1Re 1d.e. have very similar selection criteria; both must have a single Cherenkov ring which passes an electron PID cut, with visible energy above 100MeV and reconstructed neutrino energy below 1250MeV. Finally both must pass a π^0 rejection cut. The 1Re sample is associated with events that pass these criteria and do not have a decay electron, the 1Re 1d.e. sample has one decay electron. In the 1Re 1d.e. sample the primary interaction mode is CC1π^+ with the pion being produced below the Cherenkov threshold. Thus only the lepton ring is observed, this pion then decays via a muon into an above threshold electron a short period later.

No such 1Re 1d.e. sample is included for RHC due to the lower overall number of events in RHC, the lower cross-section for CC1π^- production relative to CC1π^+ and the higher capture cross-section for μ^- onto nuclei, preventing the observation of muon decay electrons.

The 1Rμ samples are binned in reconstructed neutrino energy, while the electron samples are binned in both reconstructed energy and the angle between the incident neutrino and the outgoing lepton.

5.5 Systematic Parameters

There are four major parameter classes in the MaCh3 analysis: flux, interaction cross-section, detector systematics and oscillation parameters. All but the final class are nuisance parameters and are in general marginalised over.

5.5.1 Flux

There are several causes of uncertainty on the flux of the T2K neutrino beam; hadron production uncertainties, number of protons in the proton beam and off-axis angle and alignment, as discussed in §2.2.3 all contribute. The uncertainty is evaluated using the beam simulation and hadron production data from NA61/SHINE [45] [44].

Using this it is found that there is a 5% uncertainty on the ν_μ flux at the flux peak of 600MeV in FHC, this uncertainty rises for the wrong-sign component, to 7% around the flux peak for $\bar{\nu}_\mu$ in FHC as can be seen in Fig 5.2.

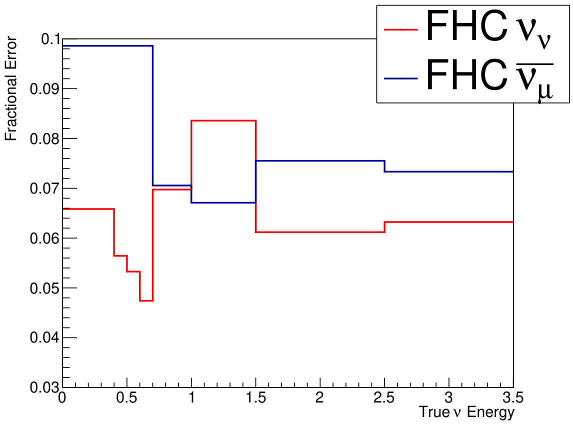

FIGURE 5.2: The prior fractional uncertainty on the neutrino flux parameters in their fit binning. ND280 FHC ν_μ and $\bar{\nu}_\mu$ fluxes shown.

The uncertainty is included in the fitter using 100 systematic parameters, each corresponding to a single neutrino flavour in a single beam mode and true energy range at one of the two detectors (ND280 and SK). The prior covariance matrix on these parameters can be seen in Fig 5.3.

In FHC, there are 11 ν_μ, 5 $\bar{\nu}_\mu$, 7 ν_e and 2 $\bar{\nu}_e$ parameters for each detector, the binning is such that there is finer granularity around the flux peak of 600MeV. Correspondingly in RHC, there are 11 $\bar{\nu}_\mu$, 5 ν_μ, 7 $\bar{\nu}_e$ and 2 ν_e bins for each detector with the same energy binning as in FHC. Each parameter acts as a normalisation factor for all events in the corresponding flavour, energy range and horn current.

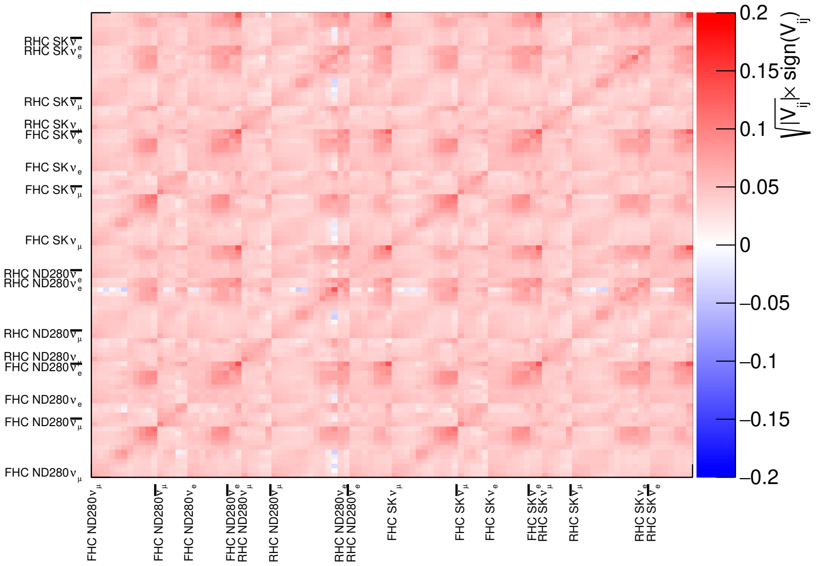

FIGURE 5.3: The prior fractional uncertainty on the neutrino flux parameters. The labels denote the first parameter in a group.

5.5.2 Cross-Section Model

Both ND280 and SK MC predictions make use of the generator NEUT [39]. This uses a Benhar spectral function for the nuclear model and the Rein-Sehgal model for resonant pion production [40][73]. These are tuned to MINERνA and bubble chamber data. The T2K cross-section model is composed of 'normalisation' and 'shape' parameters. Normalisation parameters simply apply a weight to a given type of event based on MC truth information. Shape parameters are more complex, these may apply different weights to different events depending not only on their interaction type but also on kinematics.

These are included in MaCh3 as a series of cubic polynomial splines, an example of this can be seen in Fig 5.4. For each shape parameter, the weight associated with a particular MC event is calculated at seven values around the point used during MC generation, a spline can then used to interpolate between these points.

At every step of the Markov chain, a value for each cross-section parameter is proposed. Each shape parameter evaluates its associated weight using this spline, with the product of all the normalisation and shape parameter weights being taken as the cross-section for that event.

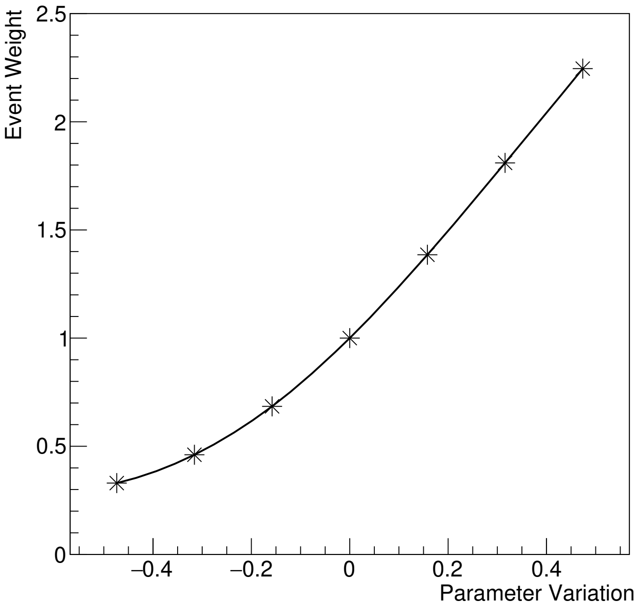

FIGURE 5.4: An example of a spline, used to calculate the non-linear impact of a parameter on a given MC event. Seven values are generated with interpolation used between these points.

In ND280 this cross-section weighting is done on an event-by-event basis, each event having its own associated set of splines. In SK however, prior to the fit, the events are binned in true and reconstructed energy. Event-by-event variations in the shape parameters are then made and the overall event rate response of each bin is stored. Splines corresponding to the response of each bin to parameter variations are then used in the fit to change the weight of all events associated with that bin.

This thesis is particularly interested by the parameters governing pion production, information on the other parameters of the model can be found in [73][90][91] and Appendix A.

For CC1π and NC1π interactions, the primary cross-section uncertainty comes from the form factors describing the struck nucleon. For this T2K uses Graczyk-Sobczyk form factors [92]. These form factors have both a vector and axial-vector component. While the vector component can be constrained by electron scattering experiments, there is an axial component that only affects neutrino interactions. It is this component that dominates the uncertainty in the cross-section.

This axial form factor is often parameterised by a dipole form factor:

$$G_A(W,Q^2) \propto C_5^A(Q^2) = \frac{C_5^A(0)}{\left(1 + \frac{Q^2}{{M_{\text{Res}}^A}^2}\right)^2} \tag{5.4}$$

This dipole factor has two free parameters: C_5^A and M_{Res}^A, which are included as the main free pion parameters in the T2K cross-section model.

In addition to the resonant pion production, there is a small contribution to CC1π and NC1π from the non-resonant isospin $I_{1/2}$ background. This is included as a Breit-Wigner amplitude that does not interfere with the resonant $I_{3/2}$ production.

These parameters have a prior derived from ANL, BNL, MINERνA and MiniBooNE datasets, however there is significant variation in the best-fit values between experiments as can be seen in Table 5.1. An anticorrelated uncertainty of 15.6% and 14% is therefore applied to C_5^A and M_{Res}^A respectively as can be seen in Fig 5.5. In addition a 42% uncertainty is applied to $I_{1/2}$.

Dataset	C_5^A	M_{Res}^A	$\text{I}_{1/2}$
ANL	1.14±0.05	0.85±0.04	1.71±0.14
BNL	0.90±0.03	1.15±0.05	0.92±0.08
MiniBooNE	0.94±0.005	1.17±0.03	1.60±0.13

TABLE 5.1: Existing fits to CC1π datasets showing significant variation in recovered pion cross-section parameters. Adapted from [90].

There is an additional $I_{1/2}$ non-resonant parameter for antineutrino interactions producing a negatively charged pion with momentum below 200MeV/c. This was added to provide antineutrino freedom relative to neutrino in pion production and is only applied to SK events. Due to the lack of available datasets covering this region, there is no motivated experimental prior uncertainty, instead a conservative 135% uncertainty is used to ensure stability in the fit [91].

Finally there are two normalisation parameters controlling coherent pion production, one for CC production and one for NC, both have a 30% uncorrelated uncertainty applied owing to the lack of significant experimental data for coherent pion production [90]. These are applied at both ND280 and SK.

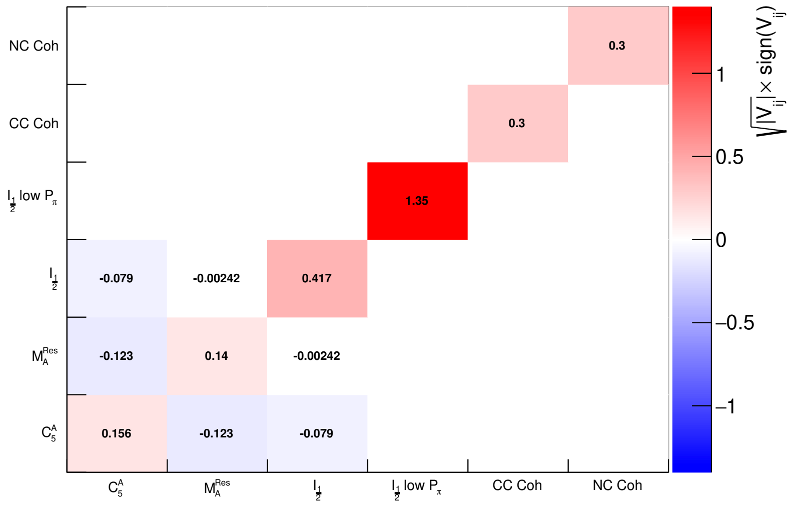

FIGURE 5.5: The prior uncertainty and correlation between the parameters of the T2K pion model. C_5^A, M_{Res}^A, $I_{1/2}$ and $I_{1/2}$low P_π are shape parameters controlled by splines while CC and NC Coherent are simple normalisations.

While the interactions are generated with untuned NEUT, the T2K NIWG (Neutrino Interaction Working Group) include a number of tunes to the MC to account for fits performed to external datasets.

These are included by providing a set of parameter values that are not necessarily the same as the values used by NEUT during generation (the ‘generated’ values). These events are weighted using the T2K cross-section model to this parameter set (the ‘prefit’ values). Thus the MC predicted event rates can be made to better match external datasets, the errors quoted above are therefore centred about the prefit value of these parameters.

5.5.3 Detector Systematics

The MaCh3 fit includes systematic uncertainties on both ND280 and SK, these uncertainties can come from a number of sources including uncertainty on detector mass, particle identification mismatch between data and MC and kinematic reconstruction.

ND280

The detector systematic uncertainties at ND280 are based on a comparison of the simulated detector performance compared to in-situ calibration techniques such as TPC laser calibration, or to control samples, such as cosmic ray muons [93]. Comparison between these well-understood control samples and the MC allows for estimation of the bias and uncertainty on the detector response.

The dominant systematic uncertainty in ND280 arises from uncertainty on secondary interactions (SI) of pions with nuclei in the detector medium. This uncertainty is constrained by external charged pion scattering experiments, however the uncertainty on these measurements must be included into the uncertainty of the detector response [94].

These systematic uncertainties are encoded in a set of parameters that affect the reconstructed properties of MC events. A random value of each systematic parameter is then chosen, based upon the expected uncertainty on each parameter, the impact of these parameter values on the reconstructed properties of MC events is then evaluated. These modified MC events are then used to create the event selections described in §5.3. This is repeated for 2000 random values of the underlying systematics, in order to build up a distribution of selected event rate in each bin of the ND280 samples.

Bins with sufficiently similar response are grouped together and a covariance matrix of the event rate uncertainty on these groups is generated from the throws [93]. The resulting grouped bins are then included in the MaCh3 fit as a series of 574 normalisation parameters, each effecting all events in a specific region of P—$\cos\theta$ space in each of the ND280 samples.

SK

The detector systematic uncertainties at SK are based on atmospheric neutrino and cosmic ray data collected at SK, in addition to expectations on detector performance from calibration measurements.

A total of 44 normalisation parameters are used for the five SK samples, broken down by true interaction category and reconstructed energy [95]. This binning is significantly coarser than the analysis binning, however this does not significantly affect the results obtained.

There are a total of 12 parameters for the FHC 1Re sample, with four categories based on MC truth information: oscillated $\nu_e + \bar{\nu}_e$ CC, $\nu_\mu + \bar{\nu}_\mu$ CC, intrinsic (beam) $\nu_e + \bar{\nu}_e$ and NC events, each associated with three parameters in increasing reconstructed energy. This is repeated for RHC 1Re.

For FHC 1Rμ there are a total of four categories: $\nu_\mu + \bar{\nu}_\mu$ CCQE + 2p2h (3 parameters), $\nu_\mu + \bar{\nu}_\mu$ CCnonQE (1 parameter), $\nu_e + \bar{\nu}_e$ CC (1 parameter) and NC (1 parameter). This is also repeated for RHC 1Rμ.

Finally for FHC 1Re 1d.e. selection, the same categories as the 1Re selection are used albeit with two bins in reconstructed energy for each category.

Included in this detector systematic matrix are uncertainties on pion secondary interactions in the water of the detector. Additionally, photonuclear effects (PN), describing the absorption of photons by nuclei without associated re-emission above the Cherenkov threshold are included.

Finally a single parameter controlling the SK energy scale is included with an uncertainty of 2.1%. The corresponding parameter is responsible for adding a fractional shift in reconstructed neutrino energy for all events.

The full SK detector matrix is shown in Fig 5.6. The generation of this prior constraint is described in more detail in §6.2.6.

5.5.4 Oscillation Parameters

MaCh3 uses an event-by-event oscillation weight calculator with a uniform density approximation for matter effects. All oscillation parameters are free in the fit, however, as T2K is not expected to be sensitive to $\sin^2\theta_{12}$ and Δm^2_{21} the PDG [15] uncertainty is used as a prior on these parameters. All other parameters are given a non-informative, flat prior. The parameter's prior best-fit point and uncertainty is show in Table 5.2.

Parameter	Best-Fit	1σ Prior Uncertainty
$\sin^2\theta_{12}$	0.307	0.013
$\sin^2\theta_{23}$	N/A	Flat
$\sin^2\theta_{13}$	N/A (0.0218 optionally)	Flat (0.0007 optionally)
Δm^2_{21}	7.53×10^{-5} eV^2	1.8×10^{-6} eV^2
Δm^2_{32}	N/A	Flat
δ_{CP}	N/A	Flat

TABLE 5.2: The prior central value and uncertainty used in MaCh3, no correlations between parameters are present in these priors.

The two mass orderings are represented by the sign of Δm^2_{32}. As it is known that the T2K dataset strongly rejects the region around Δm^2_{32}=0 i.e. no oscillation, a finite length Markov chain is unlikely to naturally transition between the two favourable regions of Δm^2_{32} for the normal and inverted ordering. This is resolved through the use of an explicit jump between orderings in the step proposal function. At every step there is a 50% chance that the proposed sign of Δm^2_{32} will be flipped, thus ensuring the chain is able to freely transition between the orderings.

No explicit prior on $\sin^2\theta_{13}$ is used during chain generation, however reactor experiments [96] have a stronger constraint than T2K on this parameter. Hence this prior is included as a weighting of the steps in the chain to obtain a 'with reactor constraint' result.

As the values of these physics parameters have a strong effect on the observed data distribution, for MC studies, some assumed value of the oscillation parameters are needed. For this, T2K uses values close to those seen in data as in Table 5.3 this is referred to as 'Asimov A' and is used throughout this work for MC studies.

Parameter	Asimov A
$\sin^2\theta_{12}$	0.307
$\sin^2\theta_{23}$	0.528
$\sin^2\theta_{13}$	0.0218
Δm^2_{21}	7.53×10^{-5} eV^2
Δm^2_{32}	2.509×10^{-3} eV^2
δ_{CP}	-1.601

TABLE 5.3: The values of the oscillation parameters used for sensitivity studies (Asimov A).

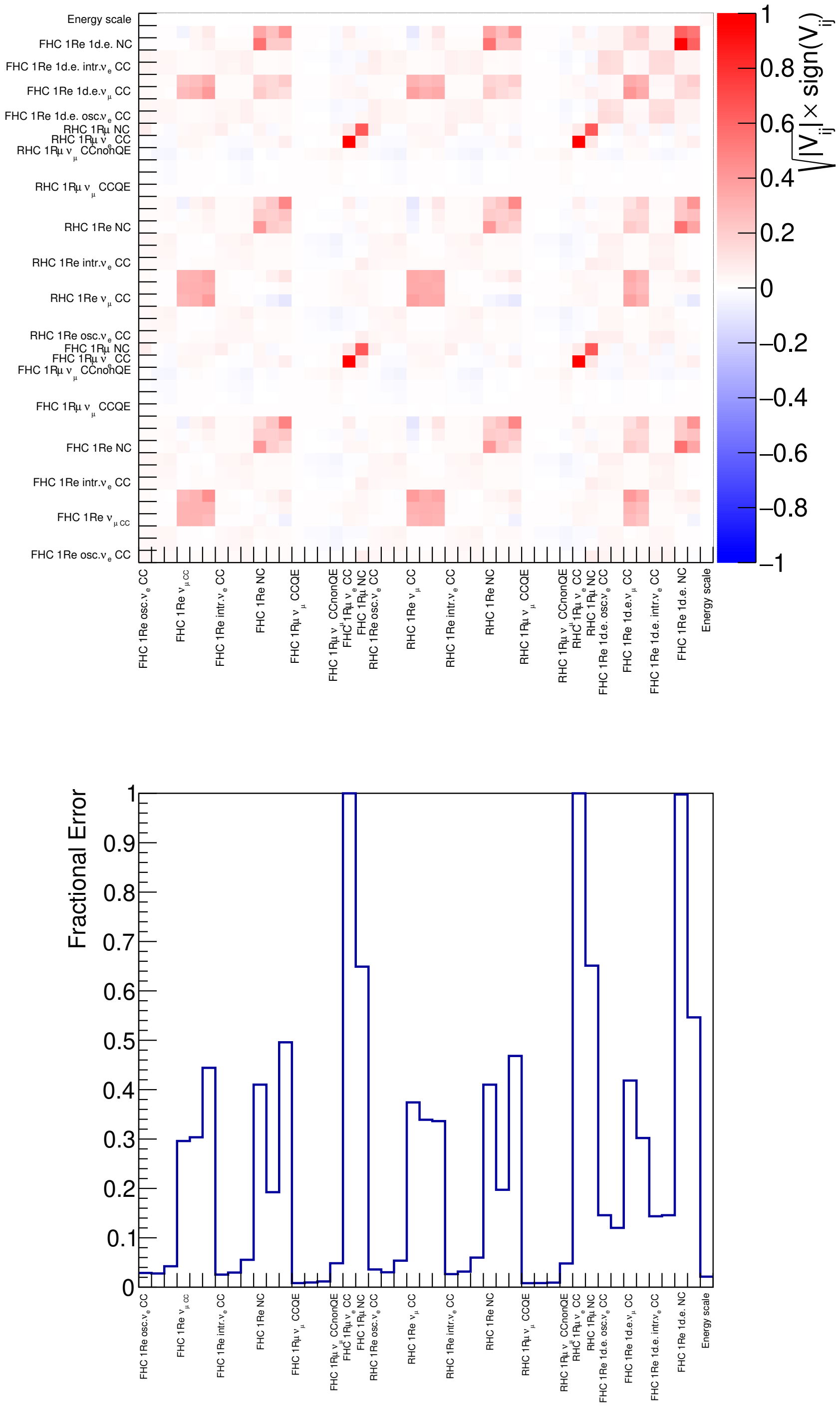

FIGURE 5.6: The prefit covariance matrix for the SK detector, SI, PN and energy scale uncertainties are included as a series of normalisation parameters applied to specific samples, interaction modes and reconstructed energies. The labels denote the start of a group of parameters in ascending energy.

Chapter 6

Neutral Current Pion Interactions in the T2K Oscillation Analysis

During the past decade of T2K analysis, continuous improvements have been made in the understanding of neutrino-nucleus interactions, both within T2K and in the wider community. These improvements have been incorporated in an increasingly expansive neutrino cross-section model used in the T2K oscillation analysis.

This model does not encompass all effects of relevance to oscillation measurement however. This chapter investigates the effect on the T2K fit from the treatment of, and, potential improvement to, one of the leading backgrounds in the oscillation sensitive SK samples, neutral-current pion interactions.

6.1 Motivation

As T2K continues to accumulate data, and reduces the statistical uncertainty in its samples, systematic uncertainties in the experiment will play an increasingly important role. If not properly constrained, these have the potential to limit the sensitivity of T2K to oscillation effects.

The current T2K analysis [97] includes 766 systematic parameters controlling neutrino flux, cross-section and detector uncertainties. This systematic model aims to encompass the inherent uncertainty in the experiment due to each of these effects.

Prior to the fit, flux and cross-section uncertainties are the leading systematic error source on the event rates in all SK samples, exceeding the statistical uncertainty in the 1Rμ and FHC 1Re samples [86]. The reduction in this uncertainty, provided by ND280 is therefore key to obtaining the most precise, unbiased, measurements of oscillation parameters.

The ND280 data provides a constraint on the predicted event rate for neutrino interaction modes that contribute to the signal CC0π events at SK, in addition to the expected rate of background events in those samples.

A breakdown of these samples by interaction and flavour can be seen in Table 6.1. In the one-ring samples without a decay electron (d.e.), CC0π interactions of the signal neutrinos are the largest contribution.

One large background in the one-ring samples without a decay electron is from CC1π signal events. While these may be considered backgrounds to the one-ring samples, they do include oscillation information and are of use to the analysis, provided their contribution can be precisely determined. For this, the CC1π samples at ND280 allow for a tight constraint on the CC1π cross-section, and therefore the contribution to the samples.

A major background, particularly in the RHC samples, is wrong-sign CC interactions of the correct flavour e.g. ν_μ CC events in the RHC 1Rμ sample. This wrong sign component is however constrained through a combination of the wrong-sign samples at ND280 in RHC and the flux and cross-section model.

	FHC			RHC	
Contribution	1Rμ	1Re	1Re 1d.e.	1Rμ	1Re
Right-Sign and flavour CC0π %	67.5	76.4	4.42	46.6	49.0
Right-Sign and flavour CC1π %	19.2	13.36	85.1	10.2	8.07
Right-Sign and flavour other CC %	3.00	0.54	4.20	1.38	0.90
CC Wrong-Flavour %	0.07	0.47	1.68	0.01	0.92
CC Wrong-Sign %	6.37	1.13	0.19	38.7	27.1
NC %	4.00	8.11	4.38	3.12	14.0

TABLE 6.1: The contributions to the total sample event rate in the five SK samples. Wrong-sign events are a major background in the RHC samples. Event rates taken for Asimov A oscillations and without near detector tuning.

The next leading background, particularly in the 1Re samples comes from neutral current interactions. Unlike ν_μ CC backgrounds, which have their event rate decreased due to the reduction in ν_μ flux at SK due to oscillation, NC interactions are possible from all neutrino flavours. These are therefore a constant background, independent of oscillation parameters. The contributions from different NC backgrounds are summarised in Table 6.2.

	FHC			RHC	
Background	1Rμ	1Re	1Re 1d.e.	1Rμ	1Re
NCπ^0 %	0.34	4.01	0.61	0.24	6.54
NC$\pi^\pm$ %	2.70	0.64	1.43	2.03	1.14
NC Coherent %	0.00	0.47	0.00	0.00	1.41
NC 1γ %	0.00	2.14	0.00	0.00	3.40
NC Other %	0.92	0.84	2.34	0.85	1.49
Total NC %	4.00	8.11	4.38	3.12	13.98

TABLE 6.2: The NC background contributions to the total sample event rate in the five SK samples. NC1π events are the most significant NC background, with NCπ^0 being dominant for 1Re and NC$\pi^\pm$ dominating for 1Rμ. Event rates taken for Asimov A oscillations and without near detector tuning.

At present T2K does not include any neutral current control samples, hence the uncertainty on these NC contributions derives mainly from external data or model predictions. While the uncertainty on some of these interaction modes is likely to be conservative, such as the 100% cross-section uncertainty on NC 1γ events, which have never been experimentally observed. Others, such as the NC1π interaction cross-section may be tighter than supported by external or T2K data.

In the current T2K analysis, these cross-sections are constrained via the pion cross-section model §5.5.2. The parameters of this model are fit using a prior constraint derived from separate fits to CC1π ANL and BNL bubble chamber data and fits to MINERνA and MiniBooNE for nuclear target data [90].

As was seen in Table 5.1, significant differences in best-fit value of C_5^A, M_{Res}^A and $I_{1/2}$ were found for these different datasets, hence a large prior uncertainty is used to cover the range of fitted values.

Due to this large prior uncertainty and the large CC1π dataset at ND280, the ND280 data provides a much stronger constraint on these pion cross-section parameters than the prior, as can be seen in Fig 6.1.

Both the prior and ND280 constraint on the pion cross-section model come from charged-current data samples. One concern is therefore the possibility that NC1π events are not well described by this CC1π constrained model. This can be a result

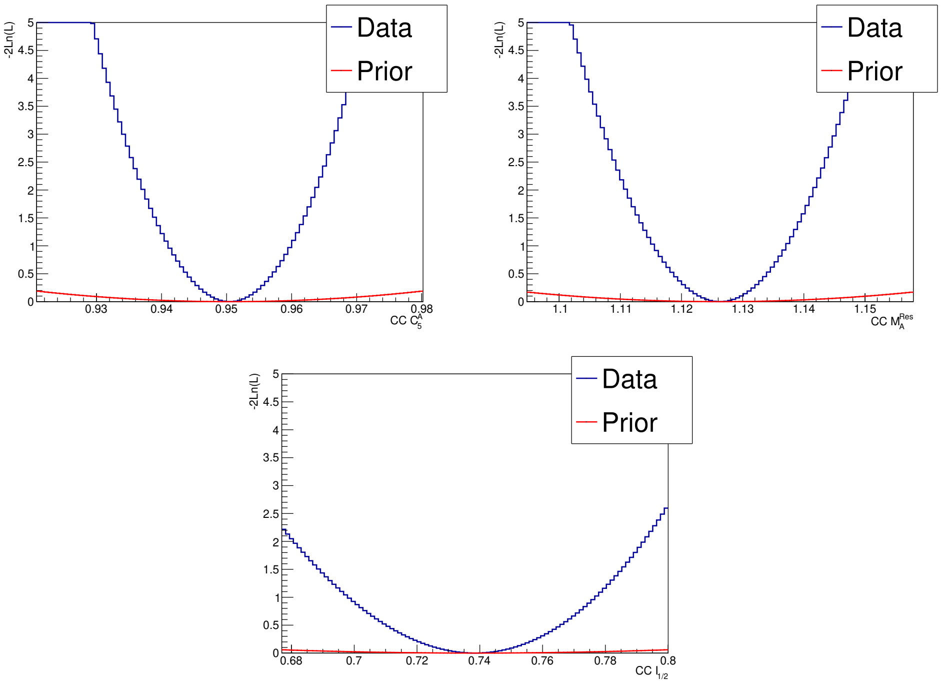

FIGURE 6.1: Log-likelihood scans of the pion cross-section parameters showing the 1D constraint from the prior uncertainty on the parameters and the constraint provided by ND280. The ND280 constraint is significantly tighter for all parameters than the prior constraint. Constraint is shown for the MC prediction about the prefit point. Note, correlations between parameters are not shown.

of a true physical phenomenon affecting NC events, or as a result of the different kinematic regions probed by the two interactions, such as the different contribution from the intermediate hadronic resonances.

This possibility has basis from theoretical considerations [98] and due to the extremely limited pre-existing experimental NC1π data, empirical evidence to counter this possibility is lacking.

MiniBooNE offers the most significant NC1π sample [99]. Comparison has been made between a pion cross-section model tuned to ANL and BNL CC1π data and this MiniBooNE NCπ^0 sample. This shows a significant difference in both shape and overall normalisation when extrapolating the CC measurements to MiniBooNE NCπ^0 events [100]. Even within MiniBooNE, differences between CC and NC pion data are seen when compared to generators, as can be seen in Fig 6.2 [101].

At present in the T2K cross-section model, the only freedom afforded to NC1π events relative to CC1π comes from the normalisation freedom on NC coherent events, the NC resonant and non-resonant component is entirely correlated with the corresponding CC components. As such, if the cross-section for NC1π is different

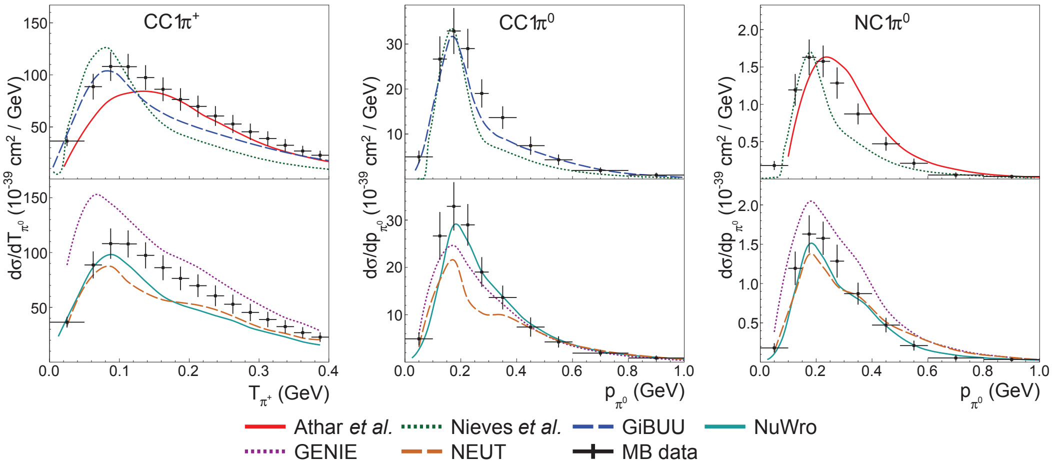

FIGURE 6.2: Comparison of theoretical predictions (top) and generator predictions (bottom) to MiniBooNE CC-1π^+, CCπ^0 and NCπ^0 data as a function of outgoing pion kinetic energy (left) and pion momentum (centre and right). The NEUT generator used at T2K underpredicts the MiniBooNE CC data, particularly in intermediate pion energy and momentum. The magnitude of this underprediction is smaller for the NC data. Reproduced from [101].

than that predicted from the CC1π data the model lacks the freedom to account for this difference in its current state.

6.1.1 Simulated Data Study

To investigate the potential impact of an incorrectly estimated NC1π cross-section, a simulated data study was performed with MaCh3. Here an 'Asimov' fit was performed in which the prefit MC prediction at ND280 and SK is used as the data sample. In this case however, the cross-section of all NC1π events were uniformly increased by 30% at both detectors. The choice of a 30% change is based upon existing NC1π rate measurements and is discussed in more detail in §6.2.4.

A portion of the simulated data is shown in Fig 6.3. For 1Rμ samples, NC1π events are predominantly reconstructed with low neutrino energy, below 0.5GeV. In 1Re these events reconstruct at low neutrino energy and with a broader angular distribution than the signal.

The effect of this simulated data on the ND280 samples is smaller, as can be seen in Fig 6.4. The changes occur primarily at low reconstructed muon momentum and in the forward direction.

A fit was then performed on this simulated data using the standard, unmodified current T2K analysis. The extracted posterior parameter distributions were then

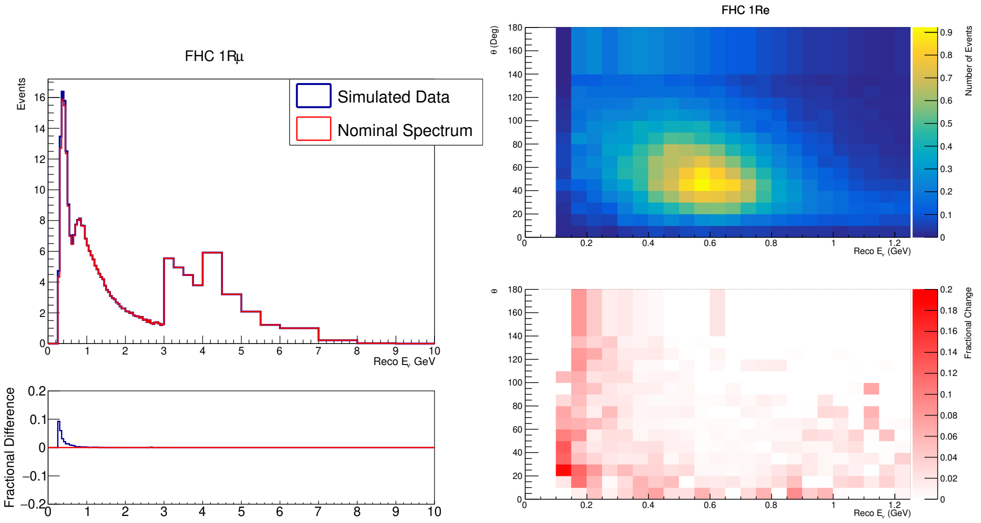

FIGURE 6.3: The effect of the 30% increase in NC1π cross-section on the FHC 1Rμ (left) and FHC 1Re (right) event distributions in the fit binning. For the full effect on the five SK samples see Appendix C.

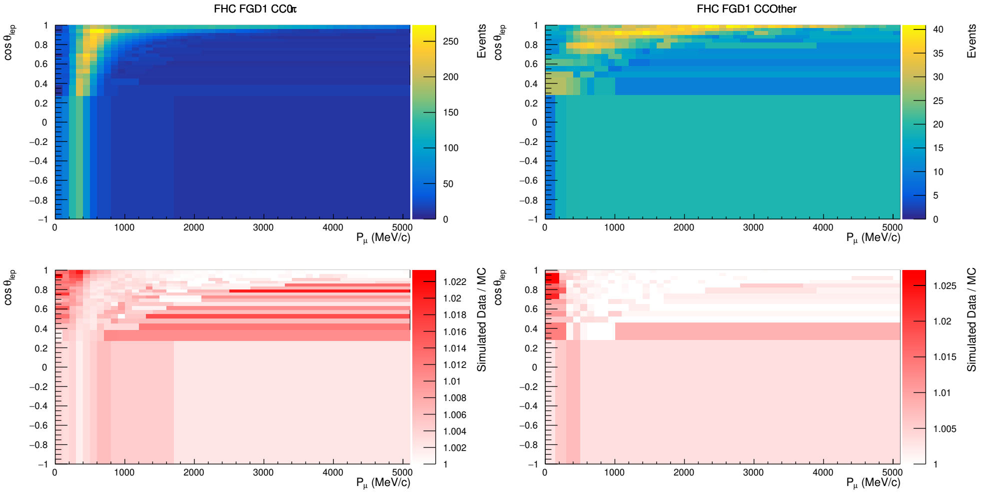

FIGURE 6.4: The effect of the 30% increase in NC1π cross-section on the FHC ND280 samples, CC0π (left) and CC Other (right) in the fit binning. For the full effect on the ND280 samples see Appendix C.

compared to the results from an Asimov fit without the 30% increase in NC1π event rate.

For each parameter in the analysis, a Gaussian fit was performed to the posterior distribution, marginalised over all other parameters in the fit. The mean and standard deviation of this Gaussian fit was taken as the central value and 1σ width of the corresponding parameter. The impact of the simulated data on a section of the extracted neutrino flux can be seen in Fig 6.5.

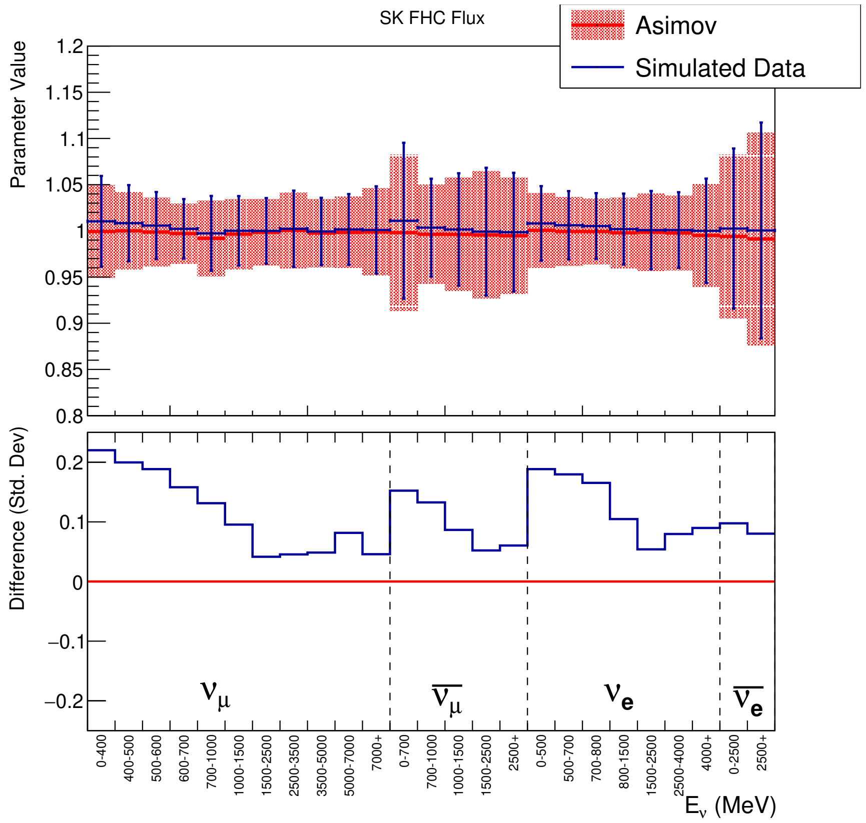

FIGURE 6.5: The post-fit parameter central value and posterior width for the FHC SK flux systematic parameters. The simulated data fit shows an overall increase in neutrino flux for all flavours. The difference in each parameter is given as a ratio to the postfit 1σ standard deviation. There is a strong dependence on neutrino energy, with the low energy flux being biased more significantly than the higher energies.

This shows an overall increase in the extracted flux normalisation, with the most significant impact occurring at low neutrino energy, with these parameters biased by 20% of their postfit uncertainty, corresponding to a 1.5% increase in flux normalisation in this region. As NC1π event kinematics favour reconstruction with low incident neutrino energy, this indicates that the fit is using the freedom in the flux model to recreate the observed increase in event rate at low reconstructed energy.

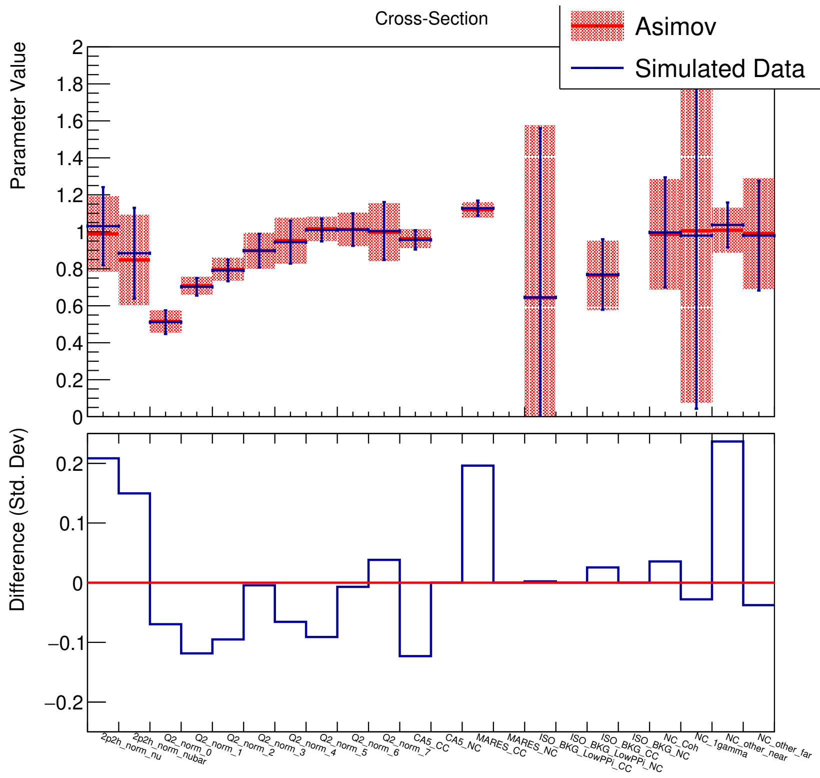

FIGURE 6.6: The post-fit parameter central value and width for a selection of cross-section parameters. The simulated data fit shows a bias in the recovered central values which bias the predicted event spectra at SK. For the full effect on the cross-section parameters see Appendix C.

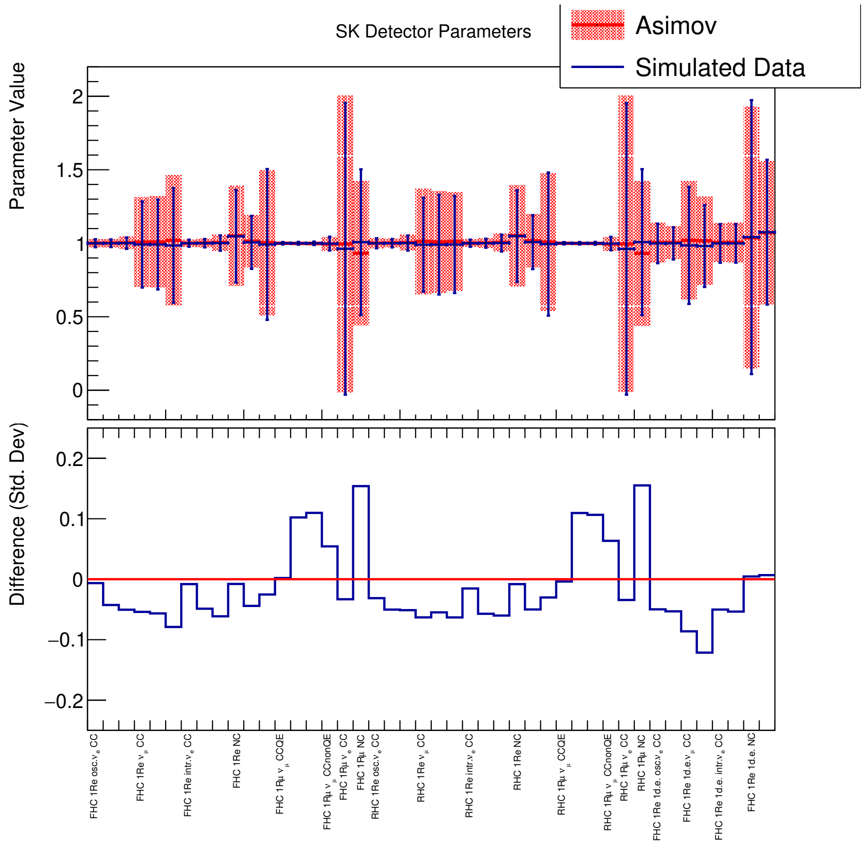

FIGURE 6.7: The post-fit parameter central value and posterior width for the SK detector systematic parameters. The simulated data fit shows a bias towards lower ν_μ CC background contribution in the 1Re samples and higher NC contribution in the 1Rμ samples.

As the flux affects both NC and CC events however, this has the side-effect of increasing the predicted CC event rate at SK. As these are the events containing oscillation information, this has the potential to bias oscillation results.

There are also changes in the cross-section parameters Fig 6.6, notably, there is a 4.2% and 3.6% increase in 2p-2h normalisation for neutrino and antineutrino respectively, representing a bias of approximately 20% of the postfit error. This is significant as the SK energy reconstruction for 2p-2h events is biased towards lower energies compared to CCQE, hence this may bias the expected position of an oscillation dip in the 1Rμ samples. This level of bias is of interest to future experiments, the 2p-2h error budget for HK for example is 5% [102]. The bias introduced by an NC1π cross-section mismodelling has the potential to use almost the entirety of this budget in the current fit.

The Q^2 parameters controlling the CCQE cross-section show a small overall decrease, this acts to counteract the increase in the overall neutrino flux to keep the total sample event rate close to the simulated data.

The pion cross-section parameters are pulled, with a decrease in C_5^A and an increase in M_{Res}^A corresponding to a bias towards increased cross-section at higher Q^2. However, the impact on the total predicted event rate at SK is small.

Other NC parameters are also pulled. NC other near, which acts as a normalisation parameter on NC other events at ND280, is increased by 2.9% while the corresponding SK parameter is decreased. In addition the NC 1γ normalisation parameter is decreased by 2.6%.

These changes are driven by the need to reproduce the event samples seen at ND280, however, as the proportion of NC1π events in the samples at SK and ND280 are different, the model parameter values that are able to fit ND280 simulated data do not yield the simulated data event distribution in the SK samples.

This can be understood by comparing the fractional changes in the event rate of the ND samples Fig 6.4 to those seen in the SK samples Fig 6.3. The ND280 samples show increases of up to 5.0% while the SK samples have a significantly greater NC1π component, with increases in some fit bins of up to 10%. These ND280 driven changes to the flux and cross-section parameters would be expected to contribute up to approximately a 5% change in predicted SK event rates. The remaining difference must therefore be contained in parameters impacting the SK samples only. There are two such parameter sets; the SK detector systematics and the oscillation parameters.

The impact of the simulated data on the recovered SK detector systematic parameters can be seen in Fig 6.7. The SK detector systematics are separated into interaction types as discussed in §5.5.3, hence there is freedom in the fit to independently change the contribution of different event types to the SK samples. The 1Re samples show a bias towards a reduced ν_μ CC contribution and a small reduction in the NC contribution. The 1Rμ samples show a strong bias towards increased NC, increasing the contribution of NC events in these samples by 8%.

While these shifts are all smaller than the pre- and post-fit uncertainty on the corresponding parameters, the effect on the predicted spectra at SK are significant, and are capable of recreating much of the increase seen in the simulated data samples at SK.

In order to investigate the impact of these cross-section and detector systematics on the predicted event distribution, steps were taken from the simulated data chain. The SK samples were then weighted according to a subset of these parameters at each step, with all other parameters being held at their pre-fit values. A distribution of the predicted event rate in each fit bin was built up, and the mean of this distribution is plotted in Fig 6.8.

As the flux and cross-section parameters are tightly linked, their contribution is considered together. Cross-section and flux have only a small impact on the 1Rμ samples, however they have a significant impact on the 1Re samples at reconstructed energies around 300MeV. In total, the cross-section and flux causes a 1.1% (1.7%) increase in the predicted event rate in the FHC (RHC) 1Re samples.

The SK detector parameters have a more significant impact at the lowest reconstructed neutrino energies, reproducing much of the simulated data event rate increase in this region for both 1Re and 1Rμ. The effect on the total event rate is however much less significant, owing to the limited impact of these parameters at higher energies with higher event rates. The total increase in event rate is 0.44% for FHC 1Re and 0.06% for FHC 1Rμ.

While much of the change in the samples is absorbed by these cross-section and

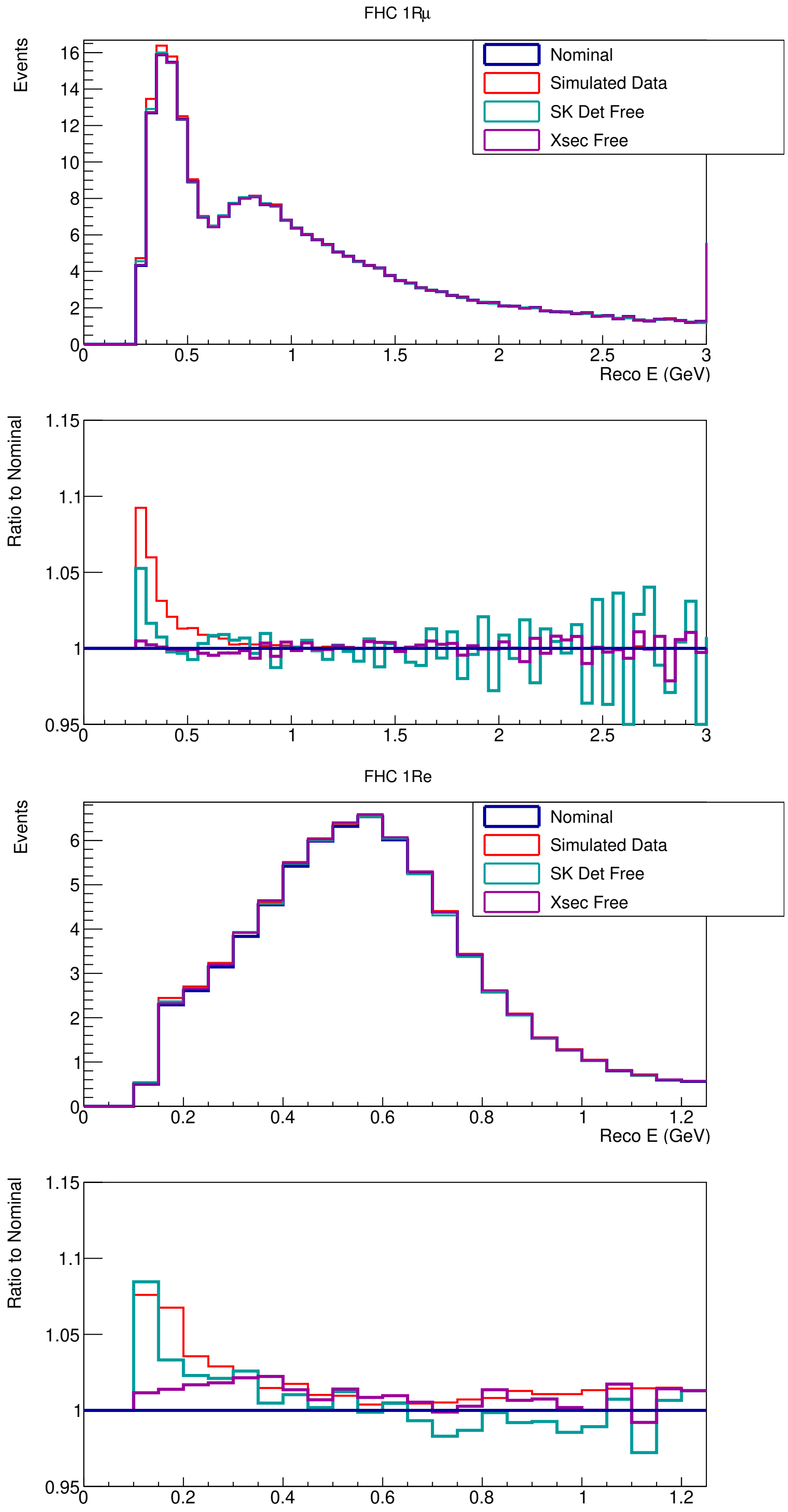

FIGURE 6.8: The impact of the fitted SK detector and flux and cross-section parameters on the predicted SK event spectra for the FHC 1Rμ sample (top) and the FHC 1Re sample (bottom). At low energies the effect of the bias in the SK detector systematics is to recreate much of the excess seen in the simulated data.

SK detector uncertainty, the remaining difference between the predicted and observed event distributions may cause a bias in the extracted oscillation contours. The impact of the simulated data on the oscillation contours can be seen in Figs 6.9 and 6.10. Note the slight variation in the contours seen around $\delta_{\mathrm{CP}} = 2$ is a result of MCMC statistics and does not correspond to a significant difference.

There is a small bias introduced into $\sin^2\theta_{13}$ before the application of the stronger reactor $\sin^2\theta_{13}$ constraint. The fit lacks the freedom necessary to fully recreate the increase in the 1Re sample event rate with the nuisance parameters alone.

As the fitter lacks the necessary freedom to correctly predict the type and distribution of events in the 1Re samples, the overall increase in event rates in the e-like samples are being interpreted as an increase in the probability of ν_μ to ν_e oscillation eqn 1.18. This event rate increase is present in both FHC and RHC, hence can be explained through an increase in the loosely constrained $\sin^2\theta_{13}$.

In the disappearance parameters, the $\sin^2\theta_{23}$ credible interval shows a broadening. As the probability of ν_μ to ν_μ oscillation depends upon $\sin^2 2\theta_{23}$ as in eqn 1.17, the oscillation probability is approximately symmetric about $\sin^2\theta_{23} = 0.51$ (the slight difference from 0.5 being due to higher order terms).

An increased background around the oscillation maximum in the 1Rμ samples will be interpreted as a reduction in the magnitude of the oscillation effect, and therefore of $\sin^2 2\theta_{23}$. This has the effect of biasing the credible interval away from the maximum disappearance probability of $\sin^2\theta_{23}= 0.51$. Due to the symmetry around this point the contour is widened.

The mass squared splitting also shows a slight broadening and bias towards higher values of $|\Delta m^2_{32}|$, this is caused by the increase in event rate seen at low reconstructed neutrino energy, slightly shifting the position of the oscillation dip in the 1Rμ samples towards higher reconstructed energy.

The addition of reactor constraints causes a slight shift towards the upper octant i.e. $\sin^2\theta_{23}> 0.5$. With the tight reactor constraint on $\sin^2\theta_{13}$, an increase in FHC and RHC 1Re sample event rate can be explained by a higher value of $\sin^2\theta_{23}$, as in eqn. 1.18.

From this it can be seen that the current T2K cross-section model is unable to

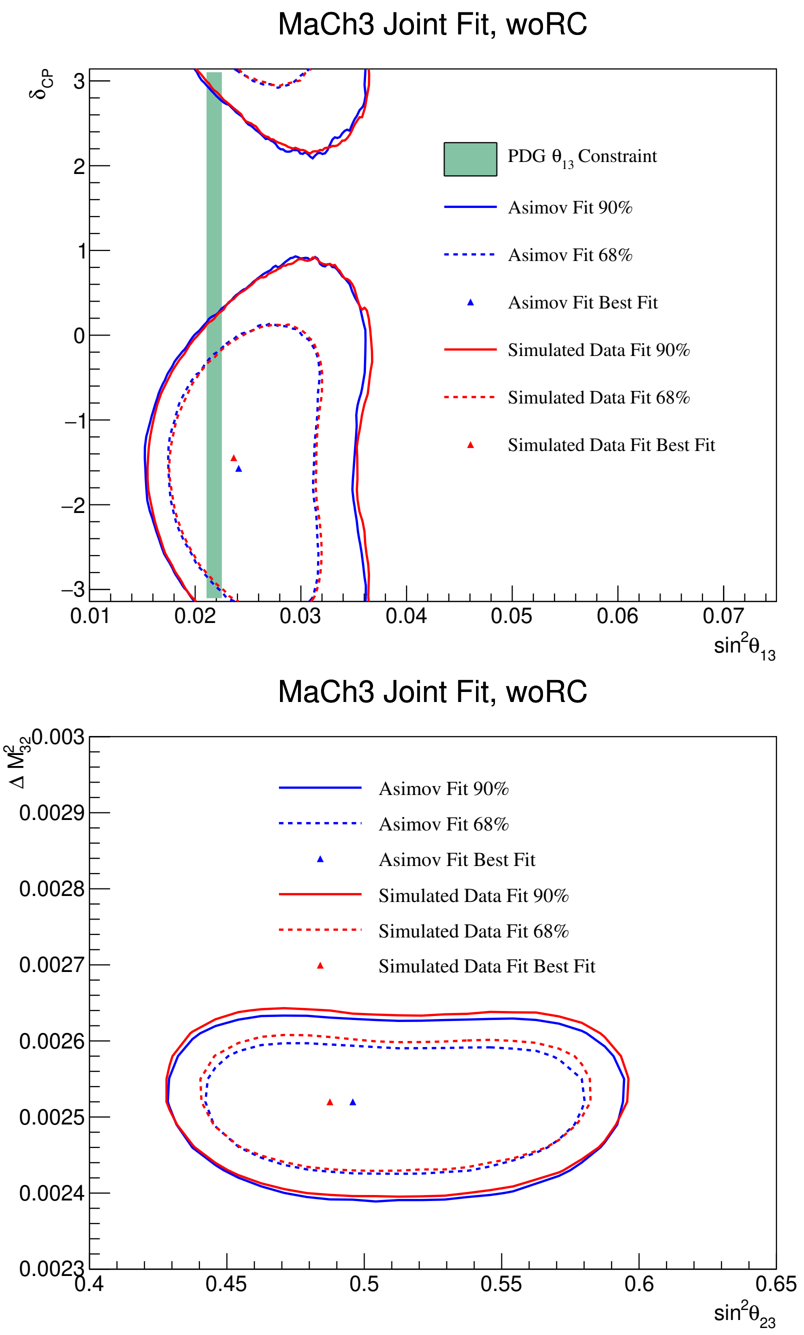

FIGURE 6.9: Two dimensional posterior credible regions, marginalised over all other parameters for the four oscillation parameters T2K has sensitivity to. Here shown for two joint ND280 and SK fits, one an Asimov fit to the prefit MC in blue, and an identical fit but with NC1π cross-section uniformly increased by 30%. Top for $\sin^2\theta_{13}$ against δ_{CP} marginalised over both mass orderings, with the constraint from reactor experiments on $\sin^2\theta_{13}$ shown but not applied. Bottom for $\sin^2\theta_{23}$ against Δm^2_{32} for normal ordering without reactor constraint. Both show a slight bias in the recovered credible regions.

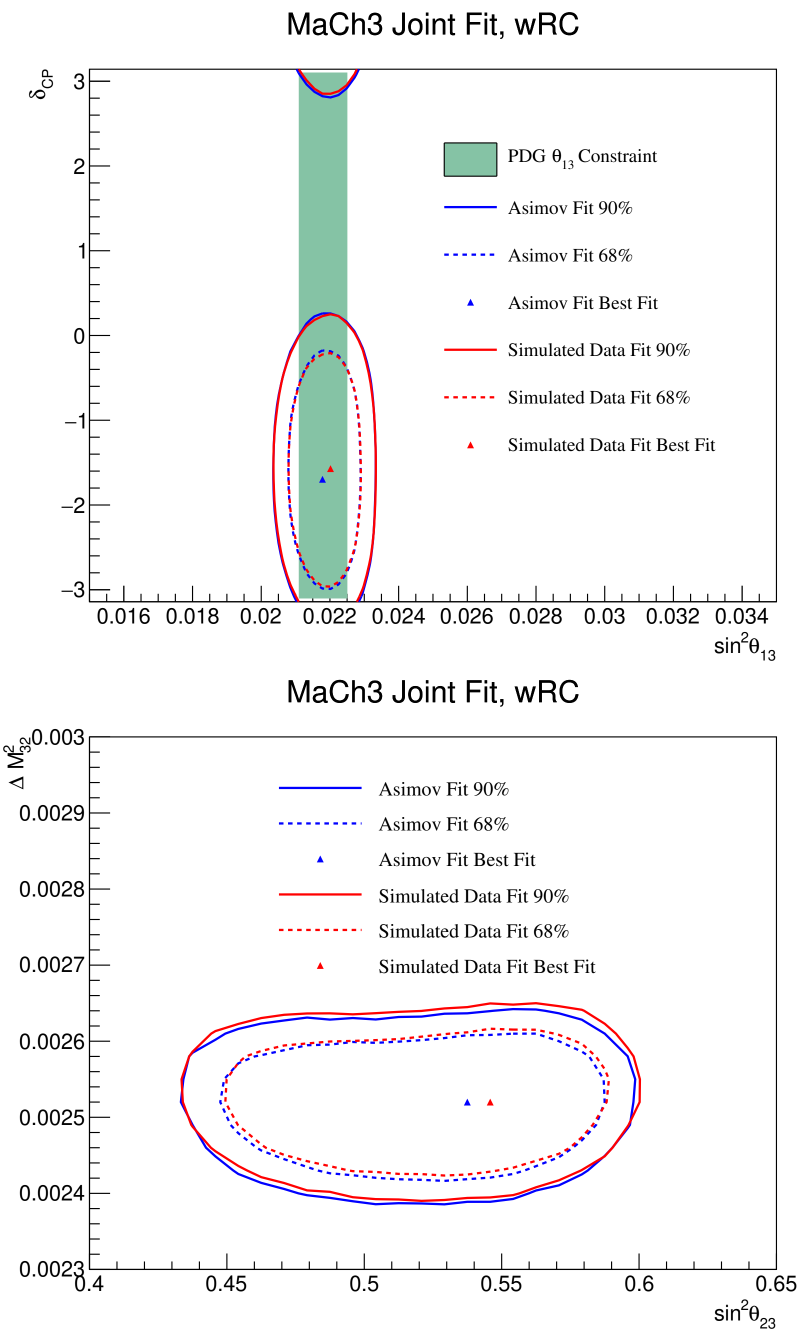

FIGURE 6.10: The two dimensional posterior credible regions, marginalised over all other parameters of Fig 6.9 after applying the reactor experiment constraint on $\sin^2\theta_{13}$. Upper, marginalised over both mass orderings, lower showing only the normal ordering.

correctly identify and correct for an increase in NC1π event rate relative to that predicted by the CC dominated ND280 samples. These differences, if present have the potential to bias both the nuisance parameters in the fit in addition to the oscillation parameters.

Sources of such biases in the T2K fit must be identified and corrected where possible, both to improve the reliability of the fit and reduce dependence on model assumptions.

6.2 NC π^0 Sample

In order to resolve the potential bias from NC1π events, the fitter needs to be able to accurately predict the NC1π event rate. In the case of different NC and CC cross-sections as above, this requires additional freedom to vary the NC1π cross-section separately to CC1π. This must be coupled with a constraint on such parameters, either from external data or from samples in the analysis.

6.2.1 Motivation

As discussed in §6.2.4 there is very limited external NC1π data to constrain the NC to CC pion cross-section, and, as with the CC1π measurements [90], agreement between experiments is often not present.

It is therefore necessary to add a sample or samples into the analysis to provide this NC constraint. In principle, a near detector could be used to directly measure these interactions. ND280 at present has no NC1π samples and the small backgrounds present in the CC samples are not sufficient to provide a significant constraint as can be seen in Fig 6.11.

These backgrounds to the ND280 samples therefore lack the power to constrain the NC1π cross-section on their own. There is also the potential for over fitting to statistical fluctuations if these backgrounds are given significant cross-section freedom relative to the CC signal.

Construction of an NCπ^+ sample at ND280 is limited by the significant background from wrong sign CC interactions. These produce a muon of like charge to the π^+ and are challenging to separate from the signal. A previous study has achieved

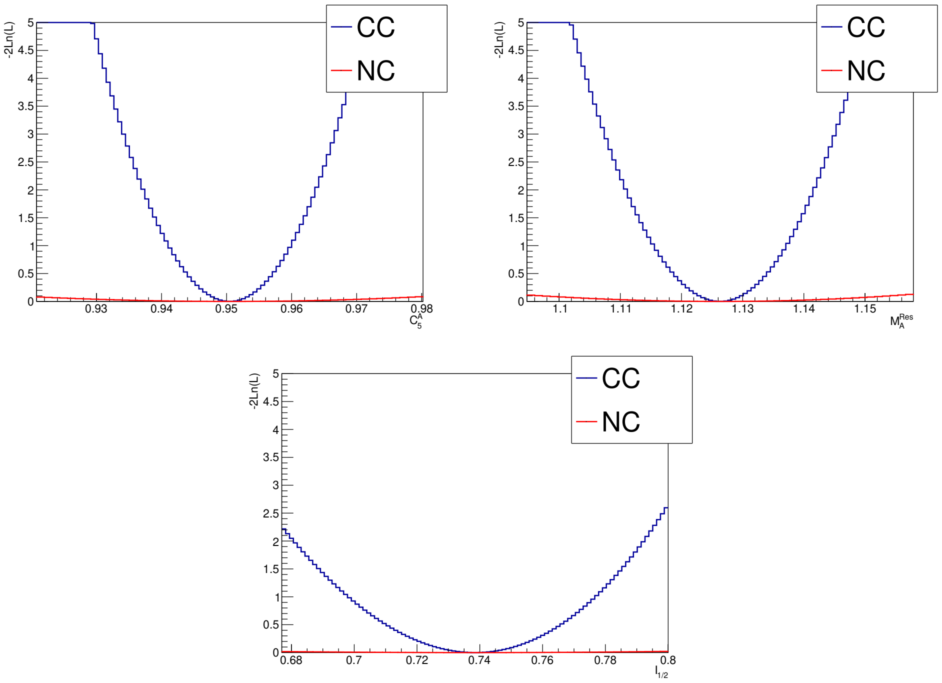

FIGURE 6.11: Log-likelihood scans of the pion cross-section parameters showing the 1D constraint on the pion parameters provided by CC and NC interactions separately in ND280. Constraint is shown for the MC prediction about the prefit point. Note, correlations between parameters are not shown.

NCπ^+ sample purities of 21% in ND280. Due to the significant background, systematic uncertainties dominate this sample, resulting in a limited extracted constraint on NC1π cross-section of $\sigma_{Data}/\sigma_{MC} < 1.43(68\% C.L.)$ [103].

NCπ^0 samples can be produced in the PØD. Previous studies in this have obtained ratios of observed to expected event rates of 0.85 ± 0.09(Stat)± 0.21(Syst) ± 0.12 (flux) and (0.79 ± 0.08(Stat)± 0.20(Syst) ± 0.12 (Flux)) [104] for measurements with (without) water in the PØD.

These measurements are therefore in agreement with the MC prediction. The uncertainty is however limited by the systematic uncertainties, partially owing to the 49% (46%) NCπ^0 purity available in the PØD samples. In addition, due to the construction of the PØD these samples include a <60° angle cut on the π^0, limiting the applicability to the high angle region which causes significant background in the 1Re SK samples.

There is one additional sample of NC events available at T2K, an SK NCπ^0 sample. This has a number of advantages: the threshold for π^0 detection in SK is extremely low, the same 4π acceptance detector can be used as for the oscillation samples, a high sample purity is possible, partly due to the reduced ν_μ CC contribution as a result of ν_μ to ν_τ oscillation.

6.2.2 SK NCπ^0 Selection

An NCπ^0 event in SK results in a single π^0 and possibly a proton or neutron escaping the nucleus. Due to the limited available energy in the T2K beam, only a small fraction of these protons will be above Cherenkov threshold and in principle detectable at SK. The neutrons produced are likewise unobservable in SK as these do not produce Cherenkov light. While the addition of gadolinium into SK will allow for neutron tagging, the data from T2K runs 1-10 were collected prior to this addition.

In practice therefore, only the π^0 can be detected at SK. The dominant decay mode for this π^0 is via two photons. Each photon then pair produces an electron and positron, resulting in a shower of electrons in the detector.

If the two showers are sufficiently angularly separated and energetic, two distinct, 'fuzzy', electron-like rings will be seen in the detector. As no charged pions or muons are present in this process, there are no associated Michel electrons from muon decay.

The experimental signature of an NCπ^0 event in SK is therefore two electron-like rings with no associated decay electrons or any additional particles.

In order to make a selection of these events a figure-of-merit must be adopted, due to the limited event rate at SK a statistical power motivated FOM was used:

$$\text{FOM} = \frac{S}{\sqrt{S+B}} \tag{6.1}$$

Where S is the total number of signal NCπ^0 events and B is the number of background events in the sample.

The sample selection described here is based upon the work selecting NCπ^0 and 1Re events in SK [89][105] using fiTQun reconstruction [64].

The cuts are composed of the standard T2K data quality requirement on the beam and SK in addition to the requirement that the SK event time be coincident with a 12μs window around the expected arrival time of the beam [106]. These cuts are applied to all T2K analyses and are not altered here. Subsequent cuts are applied sequentially as follows:

1. The event is fully contained within the ID volume
2. The reconstructed event vertex is within the fiducial volume
3. A visible energy in the ID of greater than 100MeV
4. No decay electrons are observed
5. A two ring hypothesis is preferred by fiTQun
6. A π^0 fit hypothesis is preferred over a single electron

Cut Application

Each of these cuts is intended to remove a background to the NCπ^0 signal or events which are unlikely to be correctly reconstructed by fiTQun. The target of each cut and the distribution of MC events around each cut point are described below.

For the MC prediction, the MC is weighted according to the Asimov A oscillation probability, using the parameters described in Table 5.3. The ND280 flux and cross-section tune has not been applied, as such there is approximately a 20% systematic uncertainty on the MC prediction.

The data is shown overlaid on the MC prediction for each cut. This is to validate that the MC and data agree within systematic and statistical variation around the cut point, however this data was not used during the cut tuning process.

1. Fully Contained

To reduce the probability that the event occurred outside of the ID volume or that some energy in the event was carried outside of the ID by a penetrating particle, the event is required to be fully contained within the ID volume. This is done using a cut on the observed outer detector PMT response. As with other T2K SK samples, the same cut on the number of hit PMTs in the highest OD charge cluster is used as this determining factor.

In addition, a cut of 30MeV is used on the reconstructed 1Re momentum to remove non-beam related backgrounds.

2. Fiducial Volume

The Cherenkov light from particles produced close to the detector wall is likely to hit only a small number of PMTs, making accurate reconstruction challenging. A cut on reconstructed vertex position is included in order to eliminate these. The distance of the reconstructed event vertex (assuming the 1Re hypothesis) from any ID wall must be greater than 80cm.

In addition, there is a cut on the vertex position from the wall, along the outgoing lepton direction. In this sample the 1Re hypothesis is used, and the reconstructed vertex position must be greater than 170cm from the detector wall along this direction.

The effect of this cut on the MC can be seen in Fig 6.12, after the application of the fully contained requirement.

3. Visible Energy

π^0 decay photons are expected to have a minimum combined energy of 135MeV from the π^0 rest mass. The inclusion of a cut on the visible energy allows for the removal of difficult to reconstruct low energy events such as $\pi^\pm$ just above Cherenkov threshold. This is implemented as a requirement on the reconstructed 1Re momentum being greater than 100MeV as can be seen in Fig 6.13.

4. Decay Electron Tag

As no charged pions or muons are present in an NCπ^0 interaction, no decay electrons should be present. A cut is therefore placed requiring there be no associated decay electrons based on the fiTQun decay electron tag. This can be seen in Fig 6.14.

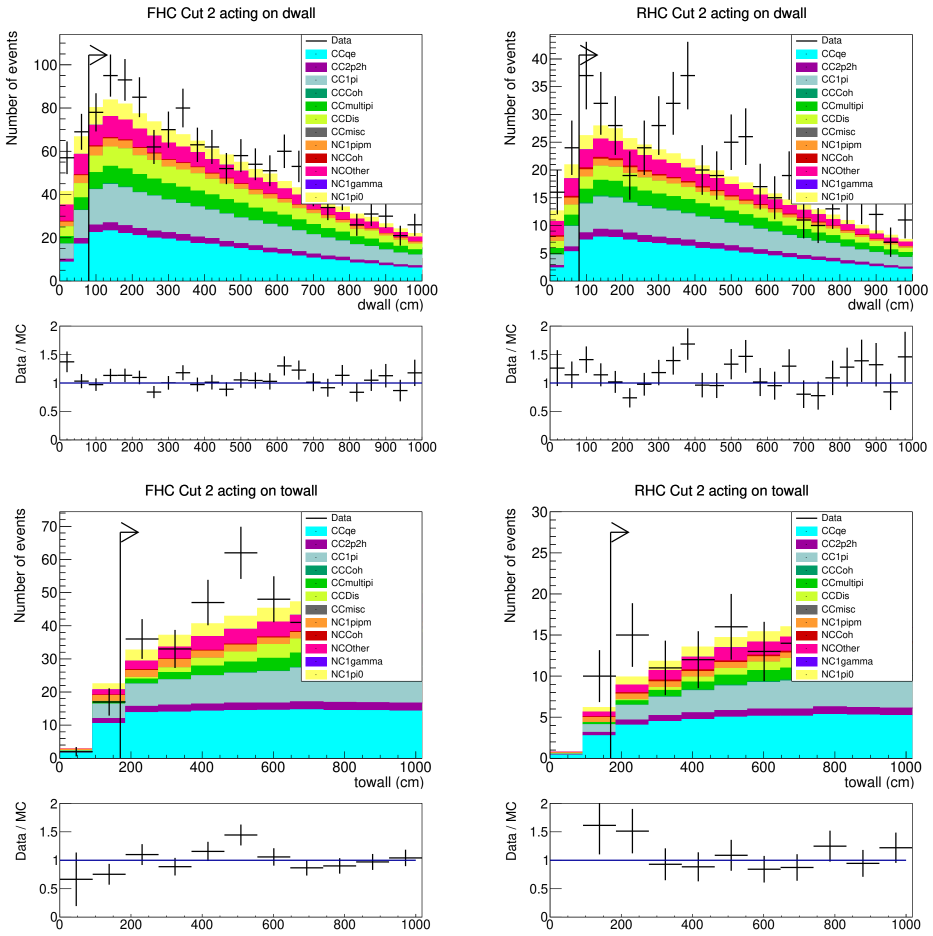

FIGURE 6.12: The fiducial volume cuts used in the NCπ^0 selection, top: a cut acting on the reconstructed vertex distance from the detector wall, bottom: a cut on the reconstructed vertex distance from the wall along the direction of the reconstructed lepton from a 1Re fit. The selection is shown by the black arrow. The RHC towall cut shows a fluctuation in the data relative to the MC about the cut point however, this is within expected statistical variation.

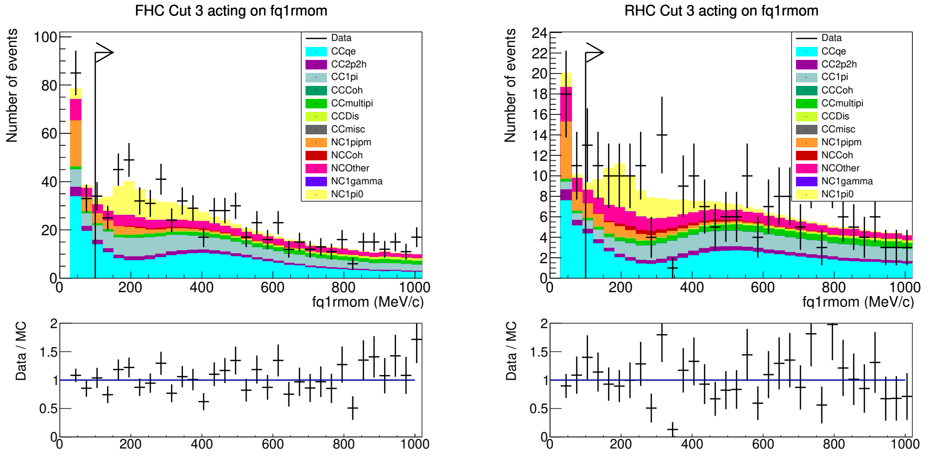

FIGURE 6.13: The visible energy cut used to eliminate CC and NC$\pi^{\pm}$ backgrounds, this is applied as a function of reconstructed 1Re momentum.

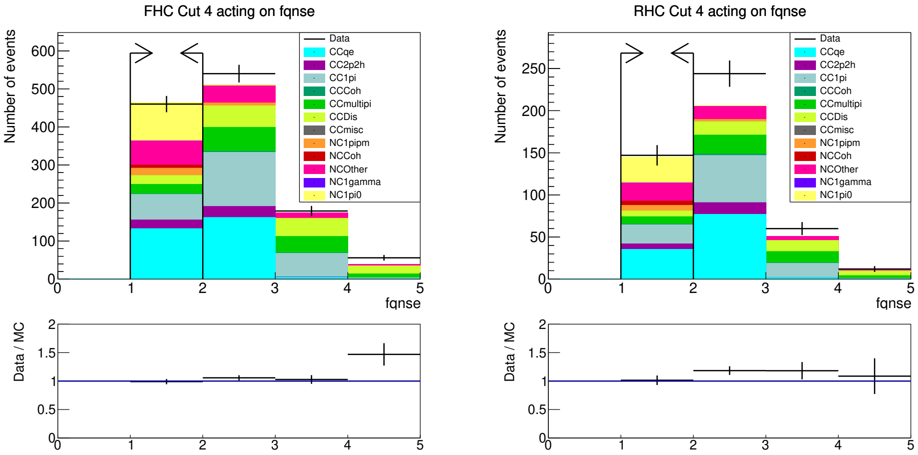

FIGURE 6.14: The decay electron tag cut is applied to the number of fiTQun sub-events. Events without a decay electron tag have a single such sub-event, this is effective in removing ν_μ CC events as well as events with charged pions in the final state. Excellent agreement between the MC and data is seen in the cut region.

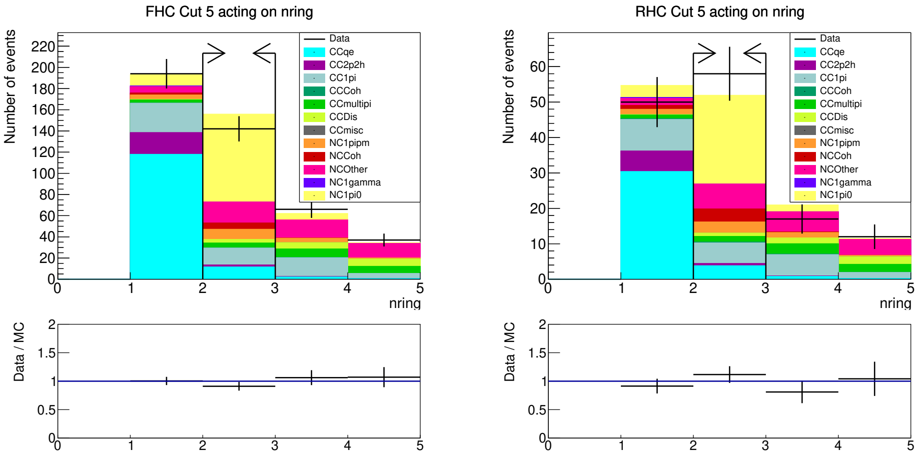

FIGURE 6.15: The number of rings cut is used to reduce the CCQE background in addition to events with multiple pions in the final-state. Agreement within expected bounds is seen.

5. Number of Rings

This analysis makes use of a two-ring π^0 sample. While one-ring samples can be constructed, the available number of events is limited, reducing the ability to constrain the cross-section. The number of rings, as defined by the fiTQun multi-ring fitter for the best-fit hypothesis must be equal to two as can be seen in Fig 6.15.

6. Electron Exclusion

The T2K 1R*e* samples include a cut to exclude π^0 events, this is based on the relative likelihood of the one ring electron hypothesis to the likelihood of a dedicated fiTQun

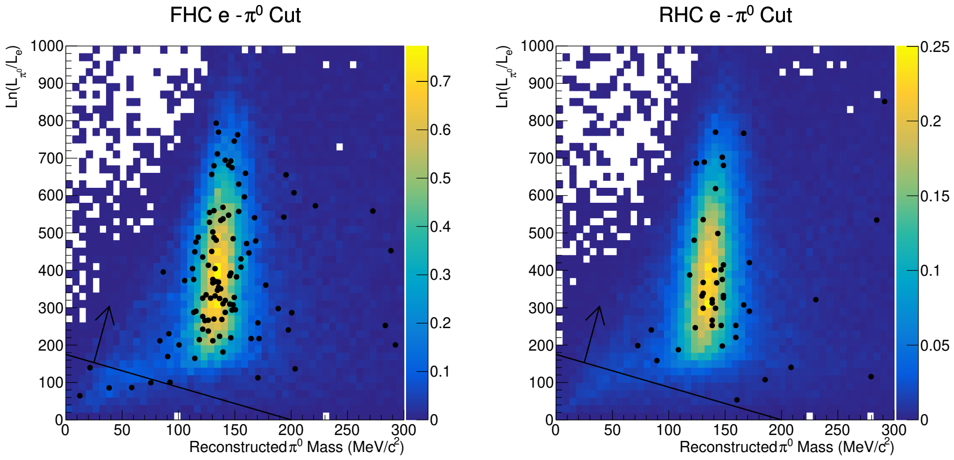

FIGURE 6.16: The cut used to separate CC ν_e interactions from NC1π. This is applied as a function of reconstructed π^0 mass. CC ν_e events which predominantly lie close to the origin at lower likelihood ratio are excluded. The observed data after all previous cuts is shown by the points while the histogram shows the expected distribution of all events.

π^0 fit.

This cut is applied as a function of reconstructed π^0 mass. In order to ensure the NCπ^0 sample does not have any overlap with the 1Re selections and to exclude true ν_e CC events, the inverse cut is applied. This can be seen in Fig 6.16.

An additional constraint may be added on the particle identification for the two rings, requiring both be electron-like. However owing to the difficulty of the inclusion of these variables into the detector systematic evaluation, this cut has been omitted. Future analyses would however benefit from the inclusion of a similar PID cut.

Data Validation

For each of the cuts described in §6.2.2 it is necessary to validate that the data agrees with the MC in the region about the cut point, within the expected bounds of statistical deviation. A discrepancy may indicate that the MC generation process does not accurately reflect either the underlying events or the reconstruction properties of the detector. Such a case may require a more detailed investigation of the simulation before proceeding.

A set of criteria were therefore used to determine if the data and MC were discrepant and required further investigation. For the non-categorical variables, the two bins closest to the cut point must both have their data points more than 1 standard deviation from the MC prediction in either direction.

As there are six non-categorical cuts, there is a 36% probability that one contains such a fluctuation from chance alone. Hence a single deviation amongst all cuts is not considered evidence that the data and MC are discrepant overall. Two or more deviations would therefore be considered a discrepancy, requiring further investigation.

Only a single greater than one sigma fluctuation in both bins was observed, occurring in the RHC towall cut Fig 6.12, as this cut is extremely early in the analysis chain and the fluctuation is not seen in the corresponding FHC cut, the data is considered to be in agreement with the MC about the cut points.

For the categorical variables, the selected category must not exceed two standard deviations from the MC prediction in any of the four cuts. This does not occur in the data.

In the final cut Fig 6.16 the number of excluded events in FHC is 5 on an expected number of 3.89 while no events are cut in RHC on an expectation of 1.05, both within expected statistical fluctuation.

Sample Event Rates

The resulting sample is enriched in NCπ^0 events, with the major backgrounds arising from ν_μ NC Other, ν_μ CC1π and NC$\pi^\pm$ interactions. The total NCπ^0 purity is 56.0% (50.7%) in FHC (RHC). Including NC coherent events which have the same experimental signature, yields a sample purity of 59.9% (57.9%). The purity here is lower than seen with previous SK NCπ^0 samples [105], this is primarily a result of the lack of an electron-like requirement on the two Cherenkov rings.

In total the FHC (RHC) sample is expected to contain 150.8 (60.8) events, with 84.5 (30.8) signal NCπ^0 events, combined, these have the statistical power to constrain the total NCπ^0 event rate to within 12.6%. This is a significant improvement over the 30% uncertainty on the rate obtained at the PØD [104].

The breakdown of the two samples by true neutrino and interaction is shown in Tables 6.3, 6.4. The larger ν_μ CC contribution relative to $\bar{\nu}_\mu$ CC in the RHC sample, is due to the higher cross-section for neutrino interaction relative to antineutrino, in addition to the high energy tail of the ν_μ flux as seen in Fig 2.9. In total, 74.7% (73.7%) of all true NCπ^0 events passing the fully-contained and fiducial volume cuts make it into the final FHC (RHC) sample.

	ν_μ	ν_e	$\bar{\nu}_\mu$	$\bar{\nu}_e$	$\nu_\mu \to \nu_e$	$\bar{\nu}_\mu \to \bar{\nu}_e$	Total
CCQE	4.59	0.92	0.29	0.13	1.62	0.02	7.57
CC1π	9.20	2.37	0.61	0.34	2.39	0.05	14.96
CC coherent	0.17	0.04	0.03	0.02	0.04	0.00	0.30
CCnπ	3.29	0.71	0.14	0.09	0.12	0.01	4.36
CC DIS	2.77	0.33	0.04	0.02	0.02	0.00	3.17
NCπ^0	79.64	1.66	2.99	0.17	0.00	0.00	84.47
NC$\pi^{+/-}$	8.06	0.23	0.36	0.02	0.00	0.00	8.67
NC coherent	5.23	0.11	0.45	0.02	0.00	0.00	5.82
NC other	17.74	0.65	0.79	0.06	0.00	0.00	19.25
2p-2h	1.04	0.22	0.07	0.03	0.26	0.00	1.63
NC 1γ	0.09	0.00	0.00	0.00	0.00	0.00	0.10
CC Other	0.40	0.08	0.02	0.01	0.03	0.00	0.53
Sample totals	132.22	7.32	5.78	0.92	4.49	0.09	
Total	150.82						

TABLE 6.3: The pre-ND280 tune oscillated event rates for the FHC NCπ^0 sample broken down by interaction mode and neutrino type. All NC events are counted with their unoscillated flavour. AsimovA oscillation parameters applied.

Sample Kinematics

There are a number of kinematics of interest in this sample, both to understand the underlying physics of the events and the reconstruction in the detector. One indicator of this detector accuracy is reconstructed π^0 mass. As the true π^0 mass width is only 7.8eV [15] all NCπ^0 interactions produce pions with invariant mass very close to the on-shell π^0 mass of 135MeV/c^2. Any spread in reconstructed π^0 mass above this gives an understanding of the detector reconstruction accuracy of NCπ^0 events.

The π^0 reconstructed mass is based upon the reconstructed energies of the two decay photons E_{γ_1} and E_{γ_2} and the opening angle θ between these:

$$M^2_{\pi^0} = 2E_{\gamma_1}E_{\gamma_2}(1-\cos\theta) \tag{6.2}$$

	ν_μ	ν_e	$\bar{\nu}_\mu$	$\bar{\nu}_e$	$\nu_\mu \to \nu_e$	$\bar{\nu}_\mu \to \bar{\nu}_e$	Total
CCQE	1.14	0.25	0.74	0.22	0.11	0.20	2.67
CC1π	2.29	0.63	1.51	0.56	0.22	0.29	5.50
CC coherent	0.04	0.01	0.07	0.04	0.00	0.05	0.21
CCnπ	0.79	0.21	0.38	0.13	0.03	0.02	1.56
CC DIS	0.61	0.12	0.09	0.03	0.01	0.00	0.85
NCπ^0	10.05	0.41	14.85	0.32	0.00	0.00	25.63
NC$\pi^{+/-}$	1.38	0.07	1.39	0.04	0.00	0.00	2.87
NC coherent	0.63	0.03	2.93	0.05	0.00	0.00	3.64
NC other	4.43	0.21	2.10	0.08	0.00	0.00	6.82
2p-2h	0.24	0.06	0.16	0.05	0.02	0.04	0.56
NC 1γ	0.01	0.00	0.01	0.00	0.00	0.00	0.03
CC Other	0.10	0.02	0.05	0.01	0.00	0.00	0.19
Sample totals	21.73	2.02	24.28	1.52	0.39	0.60	
Total	50.54						

TABLE 6.4: The pre-ND280 tune oscillated event rates for the RHC NCπ^0 sample broken down by interaction mode and neutrino type. All NC events are counted with their unoscillated flavour. AsimovA oscillation parameters applied.

The energies of the two photon rings are based on the dedicated π^0 fiTQun reconstruction. A peak around the π^0 mass can be seen in the reconstructed π^0 mass distributions in Fig 6.17 resulting from true NCπ^0 events.

A Gaussian fit to all MC events in the 110—160MeV/c^2 range about the π^0 mass peak yields a standard deviation of 15.63 ± 0.16 MeV/c^2 (15.85 ± 0.12 MeV/c^2) for FHC (RHC). This compares favourably to the approximately 17.5MeV/c^2 standard deviation of MiniBooNE [107] using similar detector technology, and the 38MeV/c^2 width of the PØD NCπ^0 sample [104]. This indicates excellent reconstruction of both the energy and angle of the decay photons.

Of particular importance to the Rein-Sehgal model that underpins the T2K pion cross-section treatment, is the invariant mass of the intermediate state, Fig 1.12. Due to the lack of sensitivity to outgoing hadrons at SK this mass cannot be accurately reconstructed, however the MC truth distribution Fig 6.18 shows peaks at the expected position from the Rein-Sehgal model. The dominant contribution arises from the $\Delta(1232)$ resonance, showing a peak around an invariant mass of 1232MeV/c^2. The distribution away from this peak arises from other resonances in the Rein-Sehgal

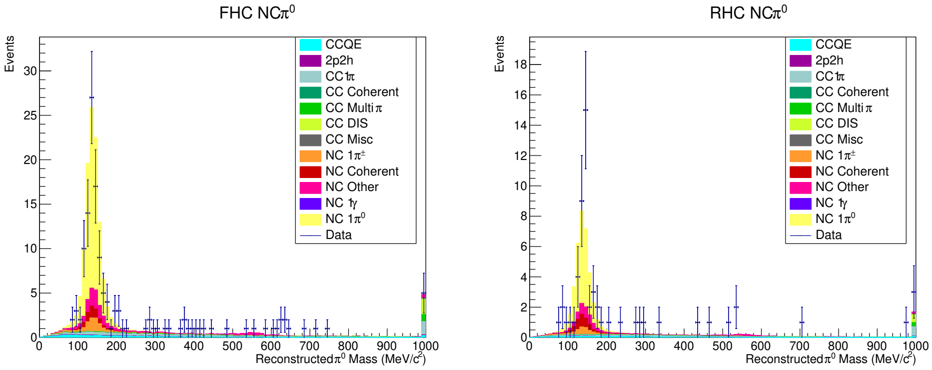

FIGURE 6.17: The distribution of reconstructed π^0 mass for the NCπ^0 sample, a large peak is seen around the π^0 mass of 135MeV/c^2 for both true NCπ^0 events and other NC interactions. The data distribution is shown overlaid.

model as well as the $I_{1/2}$ background.

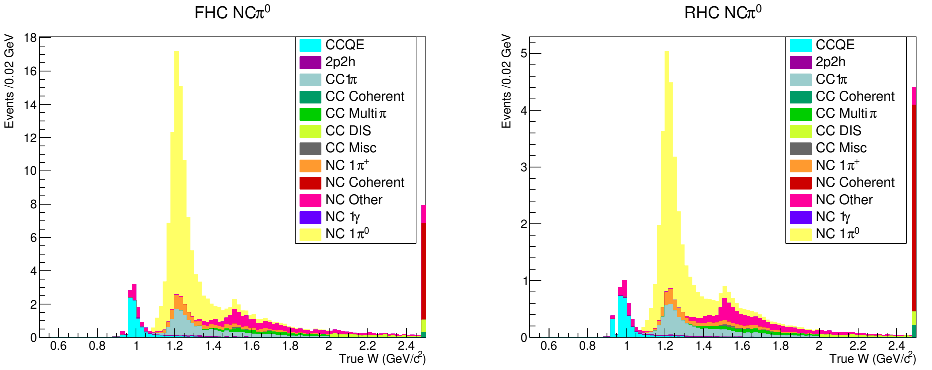

FIGURE 6.18: The MC truth invariant mass of the intermediate resonant nuclear state, a large peak about the Δ^0 and Δ^+ mass of 1232MeV/c^2 can be seen in the NCπ^0 interaction mode.

The T2K pion cross-section model provides both normalisation freedom and freedom as a function of the squared momentum transfer to the nucleus, Q^2, defined as:

$$Q^2 = -\mathbf{q}^2 \tag{6.3}$$

Where $\mathbf{q}$ is the four momentum of the weak boson as in Fig 1.12. The distribution in true Q^2 is shown in Fig 6.19.

NCπ^0 events are more prevalent at low Q^2 with CC backgrounds having a more broad distribution in Q^2. NC coherent interactions are only possible at low Q^2 where coherent scattering of the weak boson across the whole nucleus is possible. Due to the lack of an outgoing charged lepton in NC1π events, accurate reconstruction of Q^2 is not possible in SK. Lower Q^2 interactions do however produce lower momenta outgoing pions.

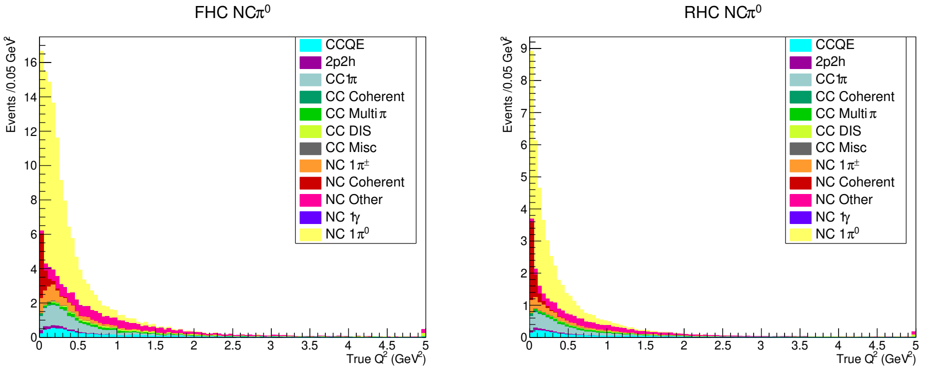

FIGURE 6.19: The true Q^2 distribution of events in the NCπ^0 sample. Interaction cross-section decreases as Q^2 increases for all interactions.

The momentum of the outgoing π^0 controls the total energy visible in the detector. The distribution of true π^0 final-state momenta for events with a true π^0 in the NCπ^0 sample can be seen in Fig 6.20. NCπ^0 events have a broad range of π^0 momenta with a peak at 170MeV.

The low energy threshold for π^0 selection allows for low momenta π^0 events to be included. This low momentum region is of particular interest as a potential cross-check on the extrapolation from the higher momentum kinematic region detectable at ND280 [108] to low momentum sub-Cherenkov pions of relevance to the SK 1Re 1d.e. sample.

π^0 momentum can be reconstructed as the vector sum of the momenta of the two Cherenkov rings in the π^0 fit hypothesis.

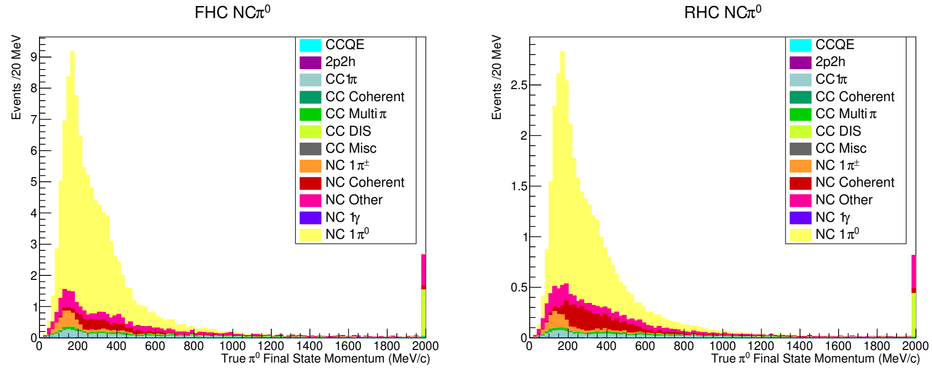

FIGURE 6.20: The MC truth distribution of the highest momentum π^0 in the final state. Note, events without π^0's are not included.

6.2.3 Parameterisation

In the current T2K cross-section model, the addition of this NCπ^0 sample would have little impact on the pion cross-section parameters. The large CC1π sample at ND280 would dominate over the small NCπ^0 sample. In addition, the current model lacks the freedom to independently alter the NC1π and CC1π cross-sections. Some freedom must therefore be added to the model.

A simple normalisation parameter on NC1π cross-section would allow for the NCπ^0 sample to provide a constraint on the total NC1π cross-section. However, the kinematic regions covered by the NCπ^0 sample and the background to the 1Rμ and 1Re samples are not the same. This can be seen in Fig 6.21 which shows a comparison between the Q^2 distribution for true NCπ^0 events in the FHC NCπ^0 sample and in the FHC 1Re sample. There is a significant difference in the shape of this distribution due to the different selection criteria for the samples.

If the Q^2 dependence of the cross-section for CC1π and NC1π events are different, then an NC1π cross-section constrained by the NCπ^0 samples for total rate and by CC1π samples for the Q^2 shape, may incorrectly predict the NC1π background to the one-ring samples. Some Q^2 freedom in the NC1π cross-section model would therefore be advantageous over a simple normalisation parameter alone.

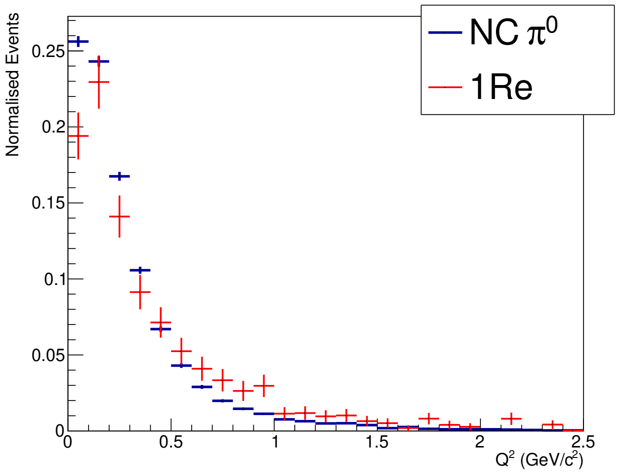

FIGURE 6.21: The MC distribution of Q^2 for true NCπ^0 events in the NCπ^0 and 1Re samples, with NCπ^0 event rate normalised. There is a significant difference in the Q^2 shape. The NCπ^0 sample shows a more rapid drop-off with Q^2 than the NCπ^0 background in the 1Re sample. Error bars show the MC statistical uncertainty.

The current T2K pion cross-section model, based on the Rein-Sehgal model includes this Q^2 shape freedom through a resonant axial mass parameter $\mathrm{M}^{A}_{\mathrm{Res}}$ as in eqn 5.4. One option is therefore to separate the T2K pion cross-section model into a CC and NC component, applying separately to CC1π and NC1π events exclusively.

This gives complete independence of NC and CC cross-section ensuring the NC1π background to the SK one-ring samples are constrained exclusively by NCπ^0 events.

This naturally includes the shape freedom desired, in the context of the Rein-Sehgal motivated cross-section model, as well as allowing for a direct comparison between the resulting NC and CC pion cross-section parameters.

The inclusion of such an NC pion cross-section model does introduce a significant amount of freedom to an important background of the oscillation samples. This has the potential to reduce the oscillation sensitivity of the experiment if not constrained. As will be seen in §6.3.1 any such effect is small compared to the limited statistics available at T2K and does not significantly bias the oscillation contours even without the constraint from the NCπ^0 samples.

In addition to these two resonant parameters, the pion model includes contribution from the non-resonant $\mathrm{I}_{1/2}$ background. It has been found that many events with low momentum charged pions can be selected in the 1Rμ SK samples, hence to provide additional freedom in this region, the $\mathrm{I}_{1/2}$ background parameter is split into two. One for non-resonant antineutrino events with outgoing negatively charged pions of momentum below 200MeV/c and one for all other non-resonant events.

To prevent incidental correlations between the CC pion samples and the NC samples from these parameters, these are also separated into CC and NC components. It is not expected however that the SK NCπ^0 sample will provide any significant constraint to these non-resonant parameters.

The parameterisation used for this study expands upon the pion parameters of the T2K model and consists of 10 cross-section parameters:

1. CC C^{A}_{5} — The normalisation to the CC axial form-factor, applies to CC1π events.

2. NC C_5^A — The normalisation to the NC axial form-factor, applies to NC1π events.
3. CC M_{Res}^A — A shape parameter affecting the Q^2 dependence of the CC axial form-factor, applies to CC1π events.
4. NC M_{Res}^A — A shape parameter affecting the Q^2 dependence of the NC axial form-factor, applies to NC1π events.
5. CC $I_{1/2}$— A normalisation parameter affecting the non-resonant CC production cross-section, applies to CC1π events.
6. NC $I_{1/2}$— A normalisation parameter affecting the non-resonant NC production cross-section, applies to NC1π events.
7. CC $I_{1/2}$ low P_π— A normalisation parameter affecting the non-resonant antineutrino CC production cross-section with a negatively charged pion of momentum < 200MeV/c, applies to CC1π events.
8. NC $I_{1/2}$ low P_π— A normalisation parameter affecting the non-resonant antineutrino NC production cross-section with a negatively charged pion of momentum < 200MeV/c, applies to NC1π events.
9. CC coherent— A normalisation parameter controlling the CC coherent pion production cross-section, applies to CC coherent events.
10. NC coherent— A normalisation parameter controlling the NC coherent pion production cross-section, applies to NC coherent events.

Parameters 1—8 are included as spline parameters, having a non-linear effect on the cross-section of a given event with parameter variation. While parameters 9 & 10 are included as a simple normalisation on the corresponding event type.

As the parameters in this expanded model directly derive from the current T2K cross-section model, the same response calculations can be used to evaluate the impact of these parameters on a given event. As with other spline parameters, the weight for each event is calculated over a range of values of each parameter and a cubic polynomial spline is used to interpolate between these discrete points.

As the response function for pion production works for both CC and NC events, these weights may be generated in the standard T2K analysis flow and then separated into charged and neutral-current events with corresponding CC or NC parameter.

6.2.4 Cross-Section Prior

For any Bayesian analysis, it is necessary to ascribe a prior constraint on the parameters of the model. As the prior constraint on pion production at T2K is derived entirely from CC data [90], this prior can be re-used for the CC parameters above.

For NC1π however a new prior constraint from available NC1π data must be made, this is challenging due to the limited available NC1π data.

A selection of NC1π cross-section measurements can be seen in Table 6.5. All ratio measurements show significant uncertainty on top of the uncertainty on the underlying CC cross-sections being compared to.

Source	Target	NC/CC Ratio	Value
ANL [109]	H_2	$\sigma(\nu_\mu p \rightarrow \nu_\mu p \pi^0)/\sigma(\nu_\mu p \rightarrow \mu^- p \pi^+)$	0.09 ± 0.05
ANL [109]	H_2	$\sigma(\nu_\mu p \rightarrow \nu_\mu n \pi^+)/\sigma(\nu_\mu p \rightarrow \mu^- p \pi^+)$	0.12 ± 0.04
ANL [110]	D_2	$\sigma(\nu_\mu n \rightarrow \nu_\mu p \pi^-)/\sigma(\nu_\mu n \rightarrow \mu^- n \pi^+)$	0.38 ± 0.11
Gargamelle [111]	$C_3H_8CF_3Br$	$\sigma(\nu_\mu p/n \rightarrow \nu_\mu p/n \pi^0)/2\sigma(\nu_\mu n \rightarrow \mu^- p \pi^0)$	0.45 ± 0.08
CERN PS AP [110]	Al	$\sigma(\nu_\mu p/n \rightarrow \nu_\mu p/n \pi^0)/2\sigma(\nu_\mu n \rightarrow \mu^- p \pi^0)$	0.40 ± 0.06
BNL [112]	Al	$\sigma(\nu_\mu p/n \rightarrow \nu_\mu p/n \pi^0)/2\sigma(\nu_\mu n \rightarrow \mu^- p \pi^0)$	0.248 ± 0.085
NEUT (untuned)	CH_2	$\sigma(\nu_\mu p/n \rightarrow \nu_\mu p/n \pi^0)/2\sigma(\nu_\mu n \rightarrow \mu^- p \pi^0)$	0.44 at 2GeV
ANL [109]	D_2	$\sigma(\nu_\mu n \rightarrow \nu_\mu p \pi^-)/\sigma(\nu_\mu p \rightarrow \mu^- p \pi^+)$	0.11 ± 0.022

TABLE 6.5: Measurements of NC to CC pion production cross-section for a range of interaction modes. Most show significant fractional error on their measurements and in the case of NCπ^0 / CCπ^0 disagreement between experiments. Adapted from [113].

Additional data is available from MiniBooNE for NCπ^0 production on a nuclear target [99]. This yields a ν_μ NC1π cross-section on CH_2 of $4.76 \pm 0.05_{stat} \pm 0.76_{syst} \times 10^{-40}\text{cm}^2/\text{nucleon}$ at a mean energy of 808MeV, this compares to 6.15×10^{-40} for NEUT at this energy, a 22% difference.

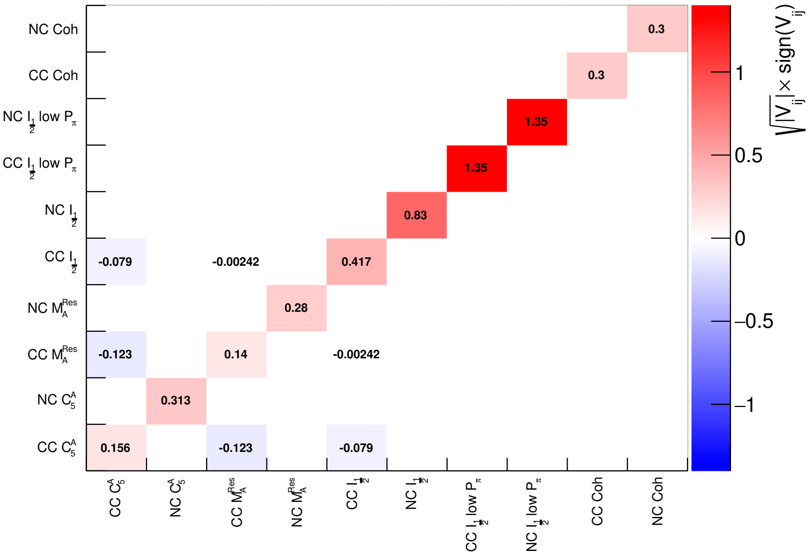

FIGURE 6.22: The prior uncertainty on the expanded pion treatment. The CC parameters inherit from the combined CC and NC parameters of Fig 5.5. The NC parameters are conservatively chosen to cover the range of values seen in external NC datasets.

Considering these measurements and the lack of direct fits to C_5^A and M_{Res}^A, an uncorrelated uncertainty of 30% was chosen for both NC C_5^A and NC M_{Res}^A in order to ensure sufficient Q^2 shape freedom. For NC $I_{1/2}$ a prior uncertainty of 80% was selected as a conservative estimate, it is not expected that the SK NCπ^0 sample will provide significant constraint due to the dominance of the $\Delta(1232)$ resonance over the $I_{1/2}$ background. For $I_{1/2}$ low P_π the T2K model currently includes a 135% uncertainty, motivated by the need to ensure stability of the fit, which was not expected to have any significant data constraint [91]. The same uncertainty therefore was chosen for NC $I_{1/2}$ low P_π, motivated by the same stability argument. These uncertainties and correlations for the pion model are shown in Fig 6.22.

Overall, these prior uncertainties correspond to an uncertainty on the NCπ^0 event rate in the NCπ^0 sample of approximately 60%. This is sufficient to conservatively cover the disparity between the NEUT generated cross-section and Gargamelle, CERN PS AP, and BNL results in addition to providing a significant amount of Q^2 shape freedom. The central values of the priors are the same as for the CC parameters.

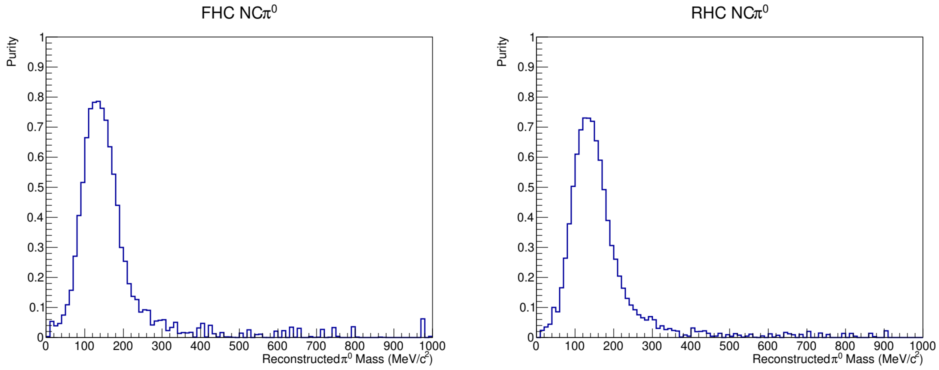

FIGURE 6.23: The true NCπ^0 purity as a function of reconstructed π^0 mass for the FHC and RHC samples. Both show a high purity around the π^0 mass peak of 135MeV, with backgrounds dominating outside of this region.

6.2.5 Binning selection

To make maximum use of the new NCπ^0 samples, it is necessary to choose a variable or set of variables to perform the fit in. For this there are a number of potential options:

The same $E_{rec}\cos\theta$ binning as the 1Re sample would allow for a direct estimation of the background to the 1Re samples. This however relies on binning a selected two-ring event in variables derived from a single-ring fit. The fiTQun fit to the event may be prone to instability fitting one-ring kinematics to such events, in addition to the challenging interpretation of such a reconstruction.

In order to simplify the analysis, it was decided to perform the fit in a single variable. Due to the omission of the PID cut and the associated reduction in total sample purity, reconstructed π^0 mass was used, this provides additional separation between signal and background. Note that with a greater sample purity, a two-dimensional fit to pion momentum and angle should be investigated as a potential improvement.

The purity of true NCπ^0 events as a function of reconstructed π^0 momentum can be seen in Fig 6.23. At the signal peak, seen around the π^0 mass of 135MeV/c^2, the purity of the FHC (RHC) sample reaches 79% (73%), significantly higher than the average sample purity of 56.0% (50.7%).

As such, performing a fit with bins in reconstructed π^0 mass has the potential to improve the statistical sensitivity of the sample to the NCπ^0 signal.

The π^0 mass binning was selected by requiring a minimum of one nominal

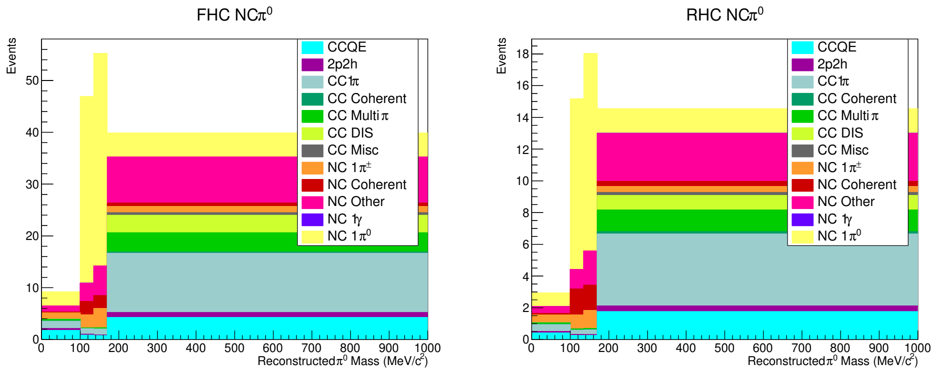

FIGURE 6.24: The distribution of events by true interaction mode in the binning used in the fit. A large fraction of all backgrounds reconstruct with high π^0 mass.

MC predicted event per fit-bin and requiring that the width of the bins be larger than the reconstruction resolution, which here is the full width of the distribution ~31.3MeV/c^2.

It was decided to separate the π^0 mass peak into two bins about the true π^0 mass. The width of each bin being 35MeV/c^2, slightly larger than the distribution width. As the remaining regions contain very little signal, each was given a single bin. Due to the similarity in the distributions, both the FHC and RHC samples were given the same binning. In total, each sample used four bins with reconstructed π^0 mass ranges of: 0-100, 100-135, 135-170 and 170+. The breakdown of events by interaction mode in this binning can be seen in Fig 6.24.

The minimum bin width is therefore 35MeV/c^2, larger than the 31.3MeV/c^2 reconstruction precision and the minimum number of predicted events in any bin is 3.0. The majority of backgrounds lie in the highest reconstructed mass bin while the signal NCπ^0 lies in the central 100-170MeV/c^2 bins.

6.2.6 Super-K Detector Systematics

In order to properly account for the uncertainty in this NCπ^0 sample, it is necessary to consider the impact of the detector and the event reconstruction on the SK samples.

Systematic effects, such as the uncertainty on detector fiducial volume have the potential to impact the purity, efficiency and distribution of events in each T2K SK sample. Each cut used in the SK event selection is susceptible to variation in the underlying variable being cut upon. Such variations will depend on the topology of the events, in addition to their kinematics. The freedom provided by these systematic effects must be included in the fit along with a prior uncertainty deriving from data or estimates of their uncertainty.

One-ring systematics

For the one-ring SK samples, the selections depend upon a fiducial volume requirement, the number of reconstructed rings, particle ID of the ring, a decay electron tag, and, in the case of the 1Re samples, an e-π^0 likelihood cut. The difference between the MC prediction for these variables and the real detector response must therefore be evaluated.

For the fiducial volume uncertainty, data—MC comparisons of the reconstructed vertex position for stopping cosmic ray muons are used. These muons pass into the ID region above Cherenkov threshold, drop in energy and stop. As these are known to be entering the ID at zero wall distance, the difference between the MC and data reconstructed position of these types of event can be used to estimate the systematic uncertainty on vertex reconstruction.

A difference of 2.5cm is seen between the MC and data distribution. In the worst case, in which all events shift towards the detector wall, this corresponds to a 0.43% change in event rate in each sample [95].

For the decay electron tag, the stopping cosmic ray sample is again used. A stopped muon should produce a single decay electron. The difference in number of tagged electrons in a tuned stopping cosmic muon sample, compared to the data, can be used as an estimate of the detector induced uncertainty on false positive and false negative tagging efficiency. This is summarised in Table 6.6.

	Data	Tuned MC	Detector Uncertainty
Tagging Efficiency	84.7±0.2%	86.0±0.2%	1%
False Positive Tagging Rate	0.21±0.02%	$(9.5\pm0.6)\times10^{-3}$%	0.2%

TABLE 6.6: The stopping cosmic ray muon decay electron tag efficiency for data and tuned MC. The data MC difference is used as the detector uncertainty on tagging efficiency. Reproduced from [95]

The uncertainty of cuts on number of reconstructed rings, particle ID and π^0 likelihood are considered separately for each event topology.

Different methods are used to estimate the uncertainty on each topology. The 1Rμ samples primarily use an atmospheric neutrino fit as can be seen in Table 6.7.

Event Type	Ring counting	Particle ID
ν_μ CC1μ	Atmospheric ν fit	
ν_μ CC other	Atmospheric ν fit	
ν_e CC	100%	
NC	Atmospheric ν fit = 64.5%	

TABLE 6.7: The systematic uncertainty constraint on the topologies contributing to the SK 1Rμ selections. Note that topologies with a single source quoted have uncertainty on all three of these cuts included into a single error. Reproduced from [95].

This atmospheric fit makes use of atmospheric neutrino interactions from five years of SK data collection, allowing for a significantly higher number of interaction events than in the T2K dataset. The atmospheric data is separated into three selections based purely on the number of observed decay electrons, 0, 1, and 2+. Each sample is split into different regions of the detector, based on reconstructed distance from the nearest detector wall and distance to the wall along the reconstructed outgoing lepton direction.

Each sample in each detector region is then binned in the fiTQun likelihood ratios used by the T2K sample cuts. The atmospheric MC is similarly selected and binned, then fit to these data samples in each sample, detector region and fiTQun variable simultaneously. This fit is performed with a model-dependant MCMC approach, a model of flux, cross-section and oscillation is included, in addition to detector uncertainties.

These detector uncertainty parameters directly alter the fiTQun likelihoods for each true topology in each detector region separately. A shape-only log-likelihood measure is then used to compare this altered MC to the atmospheric data in each of the reconstructed fiTQun likelihoods, thus obtaining the best reproduction of the observed likelihood distributions.

The end result of this is a Markov chain containing information about the preferred distribution of the reconstructed fiTQun likelihoods for each final state topology, in each region of the detector.

By sampling steps from this chain, a distribution of the predicted number of selected events in the T2K samples by final state topology may be constructed. The mean and variance of this distribution relative to the number selected in the T2K MC gives an estimate of the uncertainty on the selection efficiency for that topology [114].

Comparing the predicted event rate for NC$\pi^{\pm}$ with these fiTQun shifts, applied to the T2K MC, a large overall reduction is seen compared to the unshifted MC. Yielding a 52% uncertainty on NC$\pi^{\pm}$ selection efficiency, this is the primary driver of the 64.5% uncertainty on all NC events in the 1Rμ samples [95].

Event Type	Ring counting	Particle ID	π^0 rejection
ν_e CC1e	Atmospheric ν fit		
ν_e CC other	Atmospheric ν fit		
ν_μ CC DIF	16%		
ν_μ CC non-DIF	36.1%		
ν_μ CC other	100%	50%	100%
ν_μ CC π^0 other	Hybrid π^0		
NCπ^0	Hybrid π^0		
NC π^0 other	Hybrid π^0		
NC 1γ	ν_e CC1e + 1%		
NC$\pi^{\pm}$	100%	100%	100%
NC other	100%	100%	100%

TABLE 6.8: The systematic uncertainty constraint on the topologies contributing to the SK 1Re selections. Note that topologies with a single source quoted have uncertainty on all three of these cuts included into a single error. Reproduced from [95].

In the 1Re samples, the same uncertainty on fiducial volume and decay electron tagging is used, however additional uncertainties must be considered due to the significant π^0 background in the 1Re sample as can be seen in Table 6.8.

The same atmospheric neutrino fit is used for ν_e CC events, however for events with a π^0 a 'hybrid π^0' sample is used. This takes a true π^0 MC event and substitutes one of the two photon decay rings for an atmospheric 1Re or decay electron event with equal reconstructed energy. The detector response from the remaining MC photon is then overlaid on the atmospheric event and the full event is reconstructed with fiTQun.

The fiTQun reconstructed likelihoods of these hybrid events can then be compared to the pure MC event it is derived from to determine the uncertainty on selecting a true NCπ^0 event as 1Re [95]. For the NCπ^0 + other and CCπ^0 topologies a similar approach is used but with an additional MC particle corresponding to the non-π^0 component [115].

Muon decay-in-flight events can be misreconstructed as 1Re events, here an above-Cherenkov muon decays, producing an electron, if this electron is aligned with the muon direction, an overlapping muon and electron ring will be observed. Uncertainty on the selection of these events is based on a comparison of the selection efficiency for true DIF MC events selected by the 1Re selection and a truth-level selection. This is added in quadrature with the uncertainty due to the muon polarisation to obtain a 16% uncertainty [116].

The uncertainty on ν_μ CC events is derived from comparing the 1Re selection efficiency for stopping cosmic ray muons in data to tuned MC [95].

The remaining event topologies; ν_μ CC other, NC$\pi^\pm$, and NC other are each given uncorrelated conservative uncertainties on ring counting, PID and π^0 rejection efficiency.

NCπ^0 Systematics

For the NCπ^0 sample, some of these systematic uncertainties are not applicable owing to the different cuts used in the selection, hence in total, four systematics are used [117]:

1. Fiducial Volume: A fully correlated uniform 0.5% uncertainty on the event rate in all samples.
2. Decay electron tag: Correlated uncertainty on the efficiency of tagging true decay electrons and mis-tagging events without such decay electrons.
3. Muon decay-in-flight (DIF): A 16% uncertainty on the rate of events with a muon that decays while above Cherenkov threshold.
4. Multi-ring atmospheric constraint: Uncertainty on the number of reconstructed rings and fiTQun e/π^0 likelihood ratio.

Of these, the most significant for the NCπ^0 sample is the multi-ring atmospheric constraint, derived from a fit of SK atmospheric data.

This procedure is similar to the single-ring atmospheric constraint. The SK atmospheric MC and data are separated into five single-ring and three multi-ring samples. This is selected by the fiTQun reconstructed number of rings, decay electrons and, in the one-ring samples, by either an e-like or μ-like ring. These samples are then binned in a series of chosen fiTQun reconstructed likelihood ratios e.g. the e/π^0 PID ratio. For each of these ratios a set of 'shift and smear' parameters are used for each final state topology and visible energy range. These allow for independent variation of the reconstructed likelihoods of an event according to its topology and visible energy.

A shape-only fit is then performed between the MC and data in all of the chosen reconstructed likelihoods and visible energy ranges with the shift and smear parameters free. This fit includes atmospheric flux, cross-section and oscillation nuisance parameters. A modified version of MaCh3 is used to perform this MCMC fit. For more information see Appendix B. The result of this fit is a Markov chain, encoding the biases and uncertainties on the PID distributions of different event topologies in different visible energy ranges, as constrained by atmospheric data.

Inclusion into MaCh3

At present, the parameters of these systematic uncertainties are not directly included in the fit, instead, their impact on the samples is evaluated prior to the fit and included as a binned normalisation response. A series of uncorrelated throws of these systematics is made with their expected uncertainties above. For the multi-ring atmospheric constraint, steps from the chain are used, the values of the shift and smear parameters at a given step being used rather than a throw.

For each evaluation, the full SK 19b MC is weighted and its reconstruction likelihoods adjusted, according to the systematics being applied. The SK event selections are then applied to this shifted and weighted MC to construct the T2K samples. This is then coarsely binned in the reconstructed variable used by the sample in the T2K fit; neutrino energy for the one-ring samples and π^0 mass for the NCπ^0 sample. The event rate of different interaction modes and neutrino flavours in each sample bin is stored for that evaluation and this process is repeated a total of 1000 times.

Each sample groups different neutrino flavours and interaction modes depending upon the significance of the contribution to the sample. The event rates from the throws are grouped into these categories for each sample, e.g. for the 1Rμ samples, ν_μ CCQE-like events dominate, with ν_μ non-CCQE being a major background, these are therefore grouped separately.

A covariance matrix is then generated in this binning for the throws compared to the nominal (post-ND280 tune) prediction:

$$Cov_{ij} = \frac{1}{Throws - 1} \sum_{Throws} \left(\frac{N_i^{Throw}}{N_i^{Nominal}} - 1 \right) \left(\frac{N_j^{Throw}}{N_j^{Nominal}} - 1 \right) \tag{6.4}$$

Where N_i^{throw} is the number of predicted events in a given interaction mode group and kinematic bin 'i' for a specific throw.

By taking the ratio relative to the nominal event rate in the bin, systematics that cause an overall bias in the event rate have their biases and spread combined in quadrature. This ensures coverage of the systematics over the range likely to be seen in the data. Each of these bins of given interaction modes and neutrino flavours is given a parameter in the fit which acts as a normalisation parameter for the corresponding events. The above covariance matrix acts as its prior uncertainty.

Parameterisation

As with the other one-ring systematics, the NCπ^0 systematics are included as a series of normalisation parameters impacting particular interaction modes in specific kinematic regions of the sample. The choice of this parameterisation makes use of the predicted event types in the sample, grouping events by signal and the dominant backgrounds.

For the NCπ^0 sample therefore, true NCπ^0 and NC coherent interactions, both dominated by a final state consisting of a single π^0 were grouped together. The most significant background originates from CC interactions. These are dominated (70%) by ν_μ or $\bar{\nu}_\mu$ events. The remaining most significant contributions arise from NC$\pi^\pm$

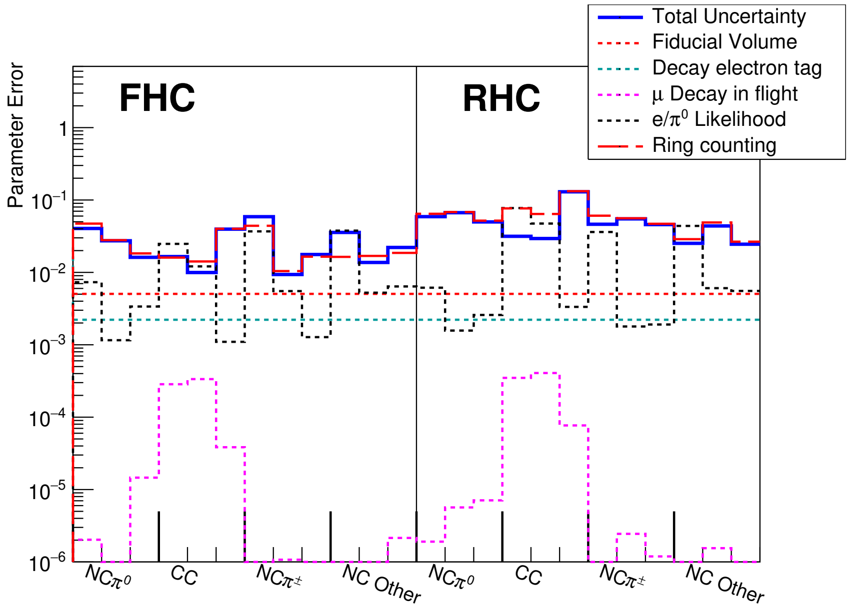

FIGURE 6.25: The contributions from different detector systematic uncertainties to the overall FHC and RHC NCπ^0 samples. The total uncertainty is dominated by the uncertainty on Cherenkov ring counting and the e/π^0 likelihood ratio. The labels show the first parameter in a set, binned in reconstructed π^0 mass.

and NC other events, each of which are given their own parameters, with the small NC 1γ background grouped into NC other.

For the kinematic binning, a similar approach to that currently employed for the 1R*e* samples was used. The signal was split into three regions, a central region containing 70% of all signal events and two side regions each containing approximately 15% of all signal events. This was achieved with binning of 0—120, 120—150, 150+ MeV/c^2 in reconstructed π^0 mass. Having 16%, 62% and 22% of all signal events in each bin respectively, while being symmetric about the true π^0 mass of 135MeV/c^2.

The final parameter uncertainty in this binning is shown in Fig 6.25, broken down by systematic contribution, with the atmospheric constraint split into its two components; the uncertainty on ring counting and on the e/π^0 PID. The contributions add in quadrature, with the exception of ring counting and e/π^0 PID, which are correlated.

The dominant contribution to the total uncertainty on the signal NCπ^0 arises from ring counting. While e/π^0 PID has a significant impact on the low reconstructed π^0 mass background parameters. This low π^0 mass region has a high concentration of the CC background removed by the e/π^0 cut of Fig 6.16, hence this systematic has a more significant effect on the low mass bins.

The next leading uncertainty after the multi-ring atmospheric fit is the uniform 0.5% fiducial volume uncertainty. Decay electron tagging uncertainty contributes a uniform 0.22% to all bins.

The correlation between these parameters can be seen in Fig 6.26. Due to the small number of systematics shared between the NCπ^0 samples and the one-ring samples there is very little correlation between these two sets of parameters. Strong positive correlation is however seen between the signal NCπ^0 parameters, indicating that the dominant number of rings systematic is independent of reconstructed π^0 mass for NCπ^0 and NC coherent events.

6.3 Sensitivity Studies

6.3.1 Impact of expanded cross-section parameterisation

The addition of NC1π specific cross-section parameters will provide the fit with additional freedom, it is therefore necessary to ensure that this freedom does not itself introduce a bias or undesirable behaviour.

An Asimov fit was therefore run, including these parameters and the NCπ^0 samples and compared to a standard Asimov fit result. There is a small bias introduced into the flux, Fig 6.27 shows an overall increase in flux with very little energy dependence. The magnitude of this bias (0.2%) is however considerably smaller than both the post-fit parameter error and the simulated data impact of Fig 6.5.

The cross-section parameters show a more significant change. Fig 6.28 shows a 2% increase in NC coherent cross-section and a 3% increase for NC other at SK. Other parameters however show much smaller effects, and are smaller than the NC1π simulated data. As the CC $I_{1/2}$ low P_π parameter applies only to antineutrino events with a sub 200MeV negatively charged pion at SK, the impact of the shift seen here on the SK samples is extremely small.

In the SK detector systematics shown in Fig 6.29, a 6% shift is seen in the poorly constrained ν_e CC background to the 1Rμ samples. The only other significant impact is a reduction in the 1Re NC parameters of up to 2.5%.

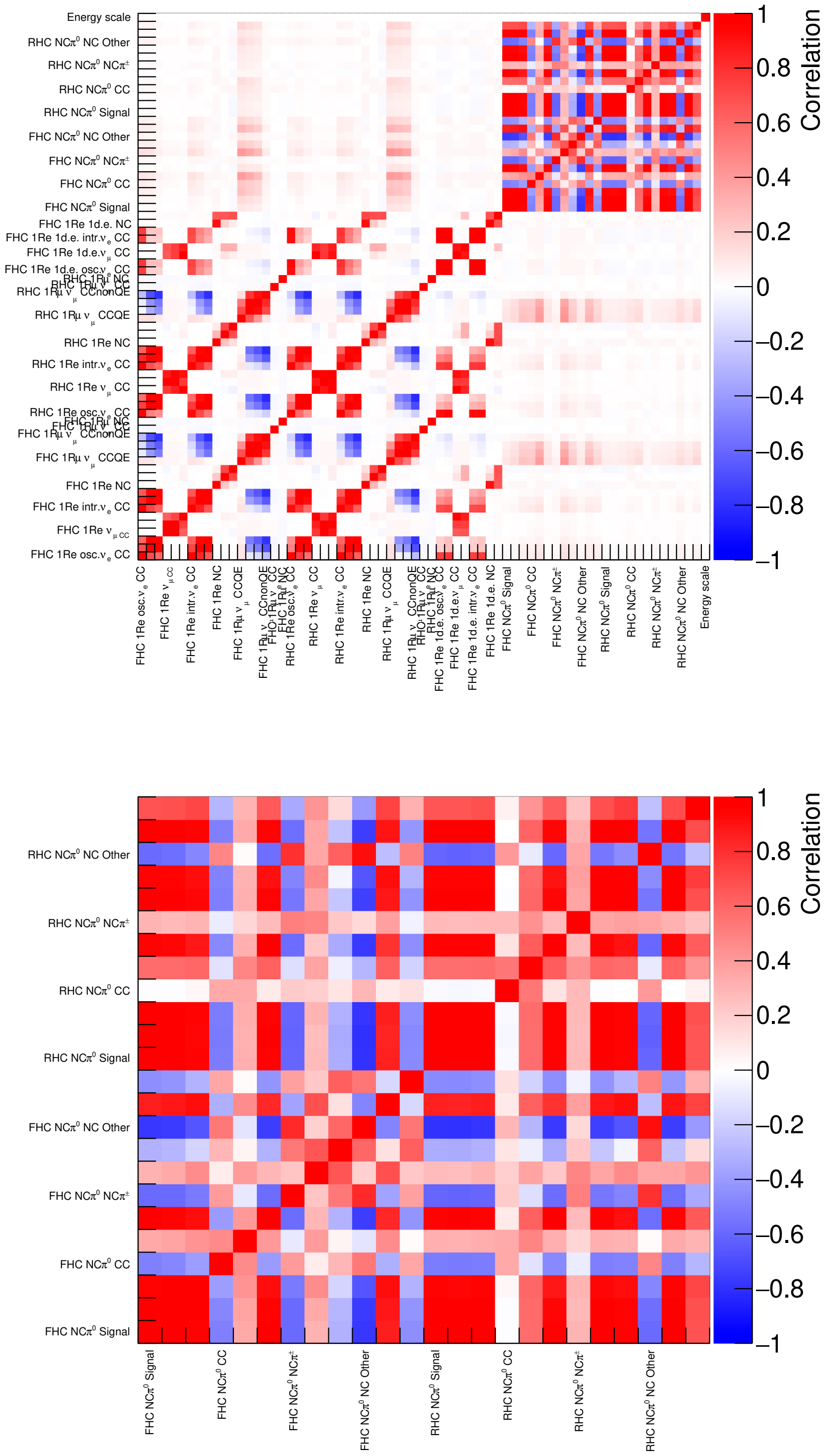

FIGURE 6.26: The correlation between SK detector systematic parameters, top for all parameters, bottom for the NCπ^0 samples only. Very little correlation is seen between the NCπ^0 samples and the one-ring samples owing to the limited overlap in the systematic uncertainties that apply to both.

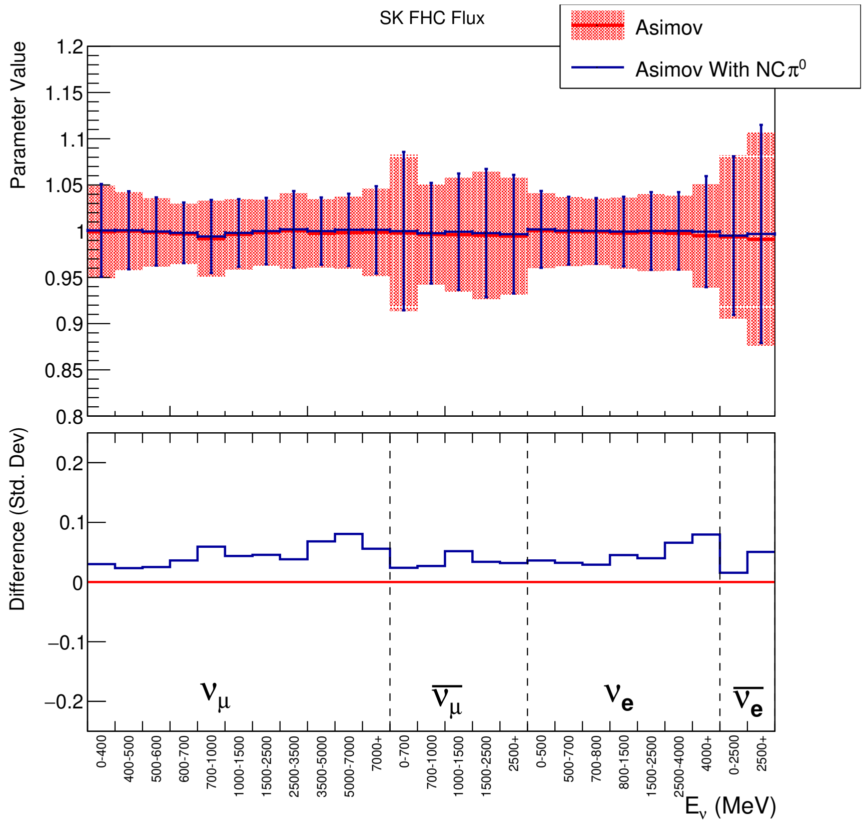

FIGURE 6.27: The impact of the addition of the NCπ^0 sample, in conjunction with the new NC1π parameters on a selection of flux parameters. There is a bias, however of significantly reduced magnitude than the simulated data of Fig 6.5

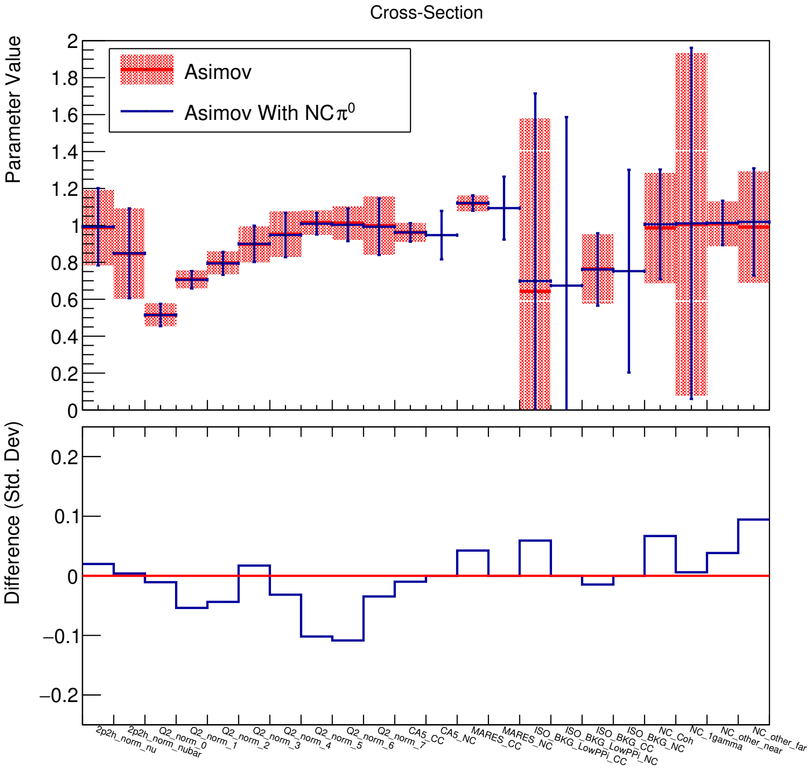

FIGURE 6.28: The constraint on the cross-section parameters with the NCπ^0 sample. The NC coherent and NC other far parameters are pulled higher, with a similar magnitude of change as that seen in the simulated data.

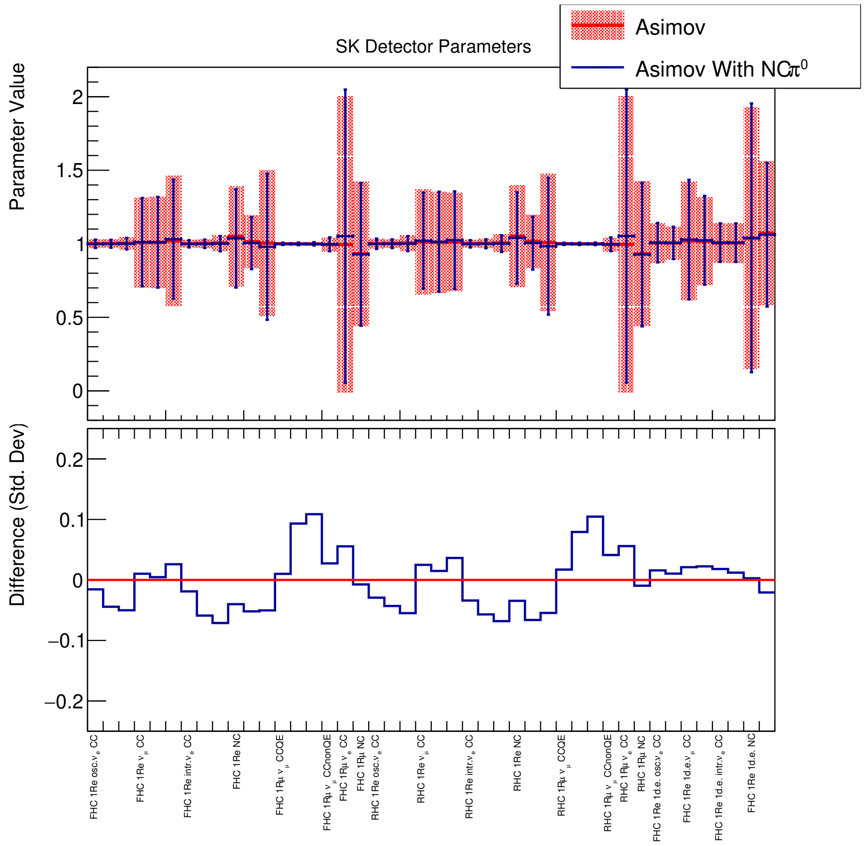

FIGURE 6.29: The constraint on the SK detector parameters. The addition of NCπ^0 causes a slight decrease on the 1Re NC parameters and a significant increase in the 1Rμ ν_e CC parameters.

Finally, the addition of the sample does not cause any change in the recovered oscillation contours, as can be seen in Fig 6.30. The NCπ^0 samples are not expected to provide any additional oscillation sensitivity, hence the contours do not become more tightly constrained. In principle, the additional cross-section uncertainty on NC1π events could cause a reduction in sensitivity however any such effect cannot be readily seen.

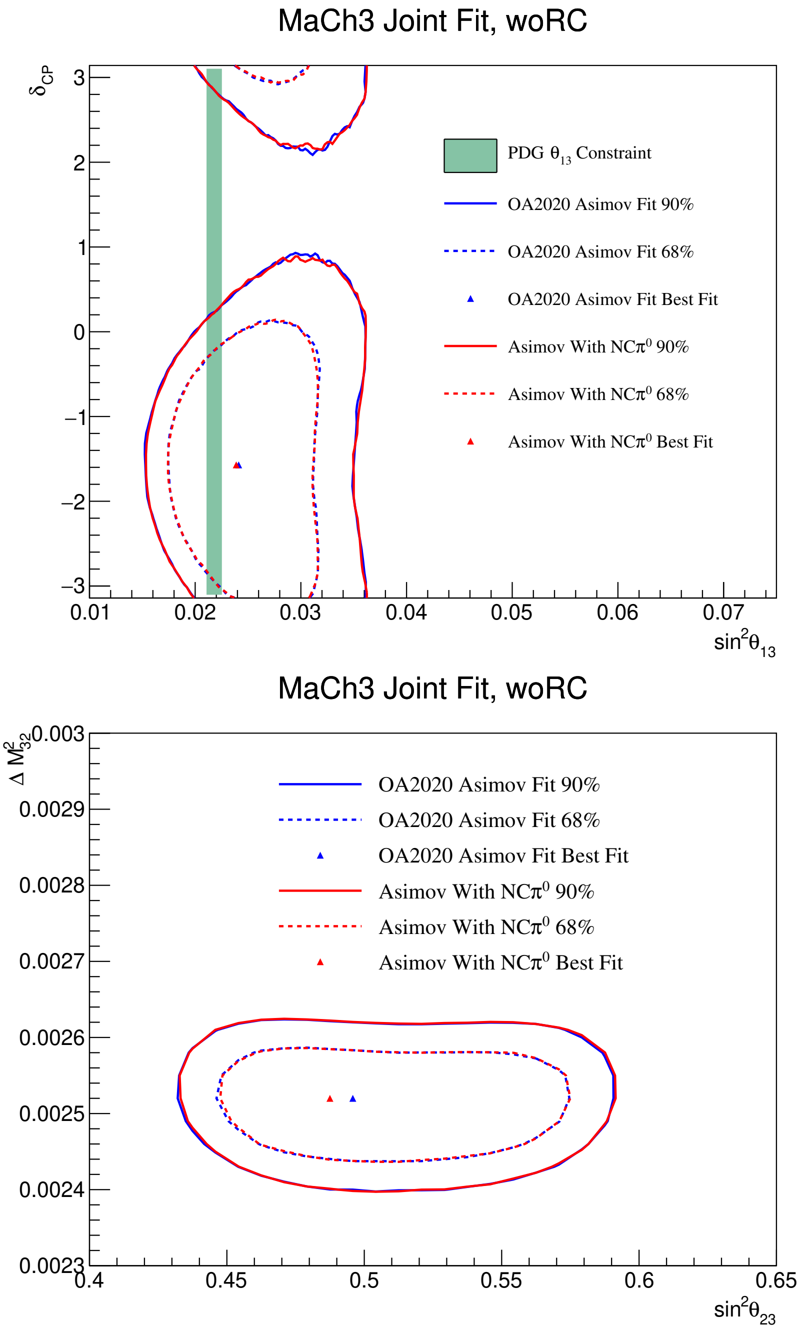

FIGURE 6.30: The impact of the addition of the NCπ^0 samples and new NC1π cross-section parameters on the recovered oscillation contours.

The impact of the additional parameters and samples is therefore most significant in NC coherent, and NC other cross-section, in addition to the ν_e contribution to the 1Rμ samples. These effects are however significantly smaller than the post-fit uncertainty on the parameters, and have a smaller impact on the samples than the magnitude of the simulated data study in §6.1.1.

6.3.2 Simulated Data Studies with NCπ^0

In order to assess the ability of the NCπ^0 to reduce or eliminate the bias seen in the simulated data study §6.1.1 a similar simulated data study was performed with the addition of the NCπ^0 sample and the NC parameters.

The NC1π event rate in all samples was uniformly increased by 30% at both ND280 and SK and a fit performed.

The impact on the central values and credible intervals of the parameters in the fit can be seen in Figs 6.31 — 6.34.

The flux parameters show a significant reduction in the bias seen compared to the simulated data fit of §6.1.1. The maximum bias is reduced from 23% of the post-fit uncertainty to 6% and the observed dependence on neutrino energy is eliminated, this indicates that the fit is no longer using the freedom in the neutrino flux to emulate the excess seen at low reconstructed energy in the T2K samples.

The cross-section parameters Fig 6.32 show a reduction in the bias seen in the 2p-2h parameters, the ν 2p-2h normalisation parameter bias decreases from 21% of postfit uncertainty to 8%. The CCQE Q^2 normalisation parameters show little overall change.

There is a reduced shift in the dominant C_5^A and $\mathrm{M}_{\mathrm{Res}}^A$ pion parameters, however the $\mathrm{I}_{1/2}$ and $\mathrm{I}_{1/2}$ low P_π parameters are shifted more. Of the new NC pion parameters, the most significant impact can be seen in NC C_5^A which is increased from its pre-fit value of 0.95 to 1.10.

The effect of this simulated data on the post-fit pion parameters in the C_5^A $\mathrm{M}_{\mathrm{Res}}^A$ space can be seen in Fig 6.33. The CC parameters correctly cover the pre-fit point to 1σ while the NC parameters show a clear shift to higher C_5^A and overall higher NC1π event rate. Due to the large CC1π sample at ND280, the constraint on the CC parameters is stronger than on the NC parameters. The limitations in Q^2 shape

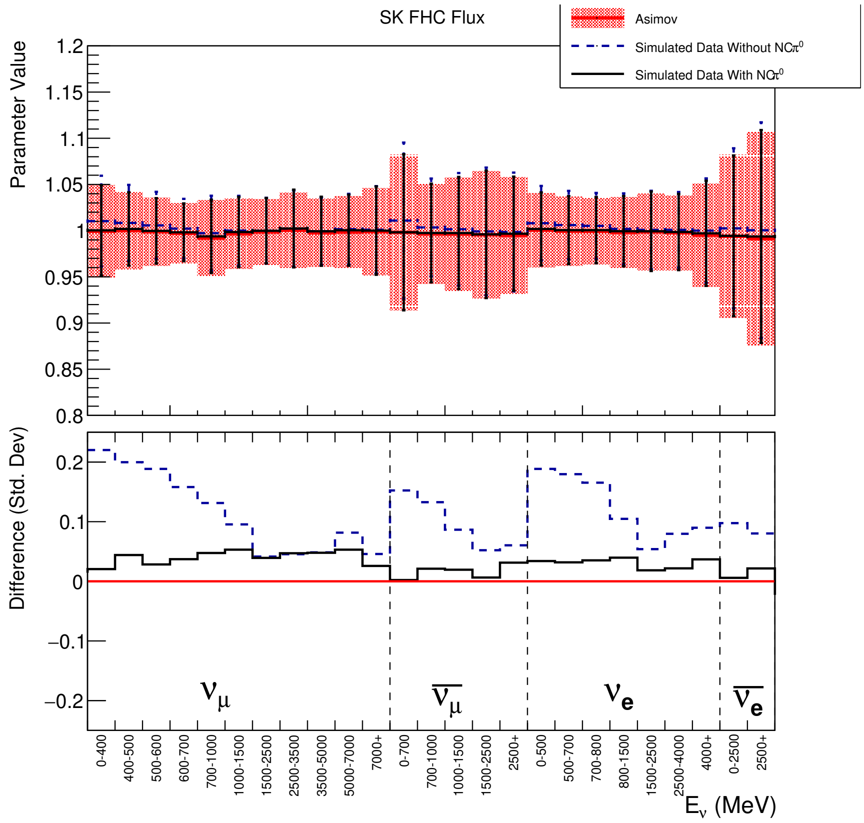

FIGURE 6.31: The post-fit parameter central value and posterior width for the FHC SK flux systematic parameters. The dashed line shows the parameters from the fit without the NCπ^0 sample of §6.1.1 while the solid line shows the fit with the NCπ^0 sample. There is a significant reduction in the bias seen, particularly at low energy.

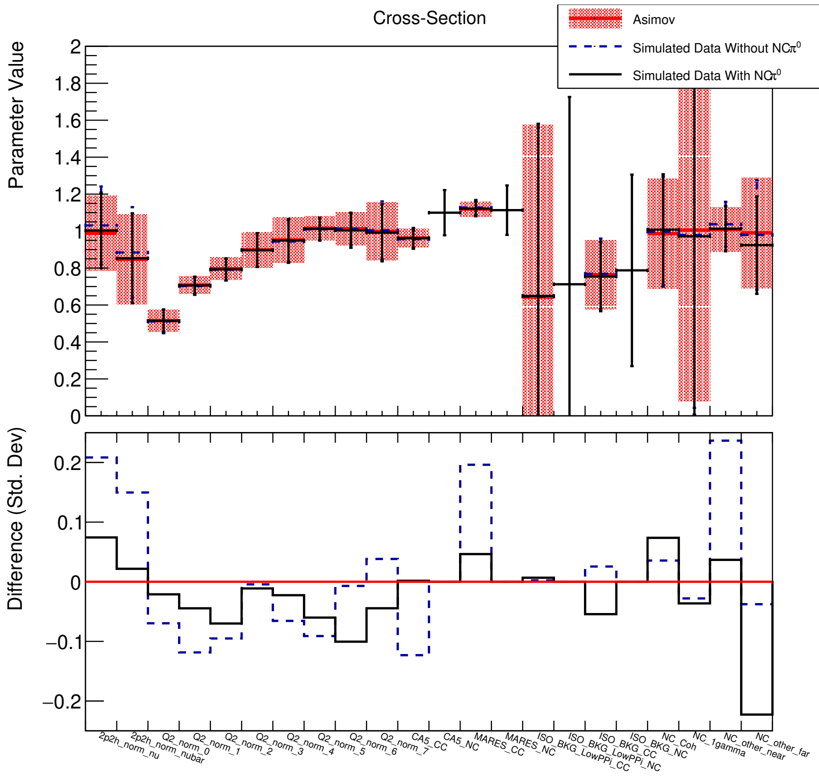

FIGURE 6.32: The post-fit parameter central values and width for a selection of cross-section parameters. The parameters in the fit with NCπ^0 show a reduction in bias in a number of parameters, particularly the 2p-2h normalisation parameters.

determination of the NCπ^0 sample can be seen by the limited constraint provided along contours of constant event rate.

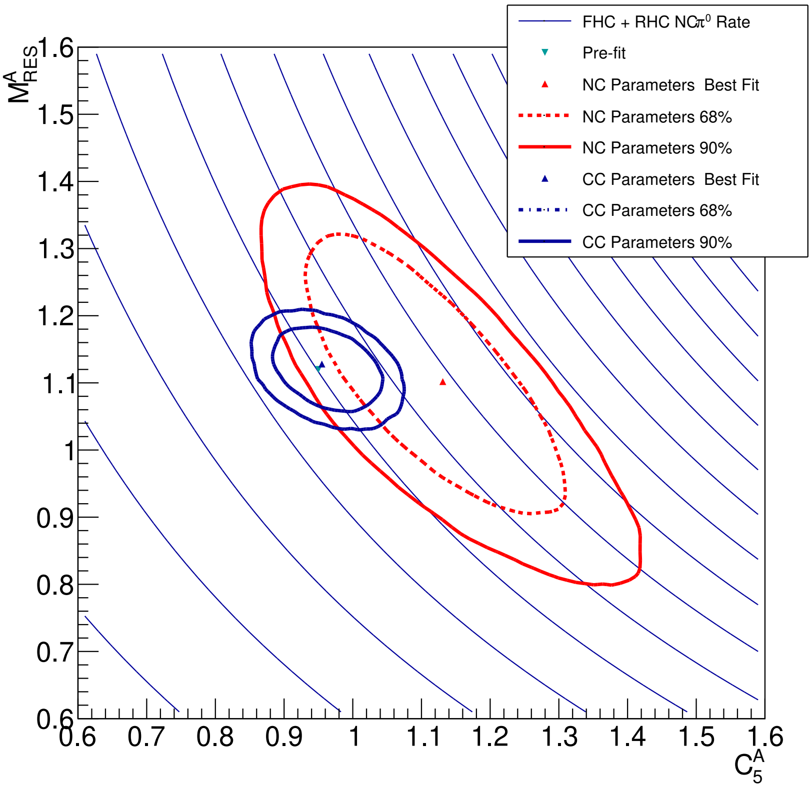

FIGURE 6.33: The C^A_5 and M^A_{Res} credible regions for CC and NC modes, overlaid on contours of constant event rate in the FHC and RHC NCπ^0 samples. The NC parameters show a shift towards higher C^A_5 and slightly lower M^A_{Res}. Event rate lines show a change of 20 events in the combined FHC + RHC sample, increasing with C^A_5 and M^A_{Res}.

The bias on NC other near is significantly reduced from 24% of the postfit uncertainty to 4%. The most significant non-NC1π related change with the addition of the NCπ^0 sample is the reduction in the post-fit central value of NC other far which is pulled by 22% of its postfit uncertainty. NC other events do however constitute a smaller fraction of events in the SK samples than NC1π events, hence the impact of this bias is significantly less prominent than the change in the simulated data.

The recovered SK detector systematic parameters show a reduced bias in the background components of most samples, see Fig 6.34. In the 1Re samples, the ν_μ CC parameter bias is almost eliminated at low reconstructed energy. The most significant reduction in bias can be seen in the 1Rμ NC parameters, decreasing from 15% to 6% of its postfit uncertainty.

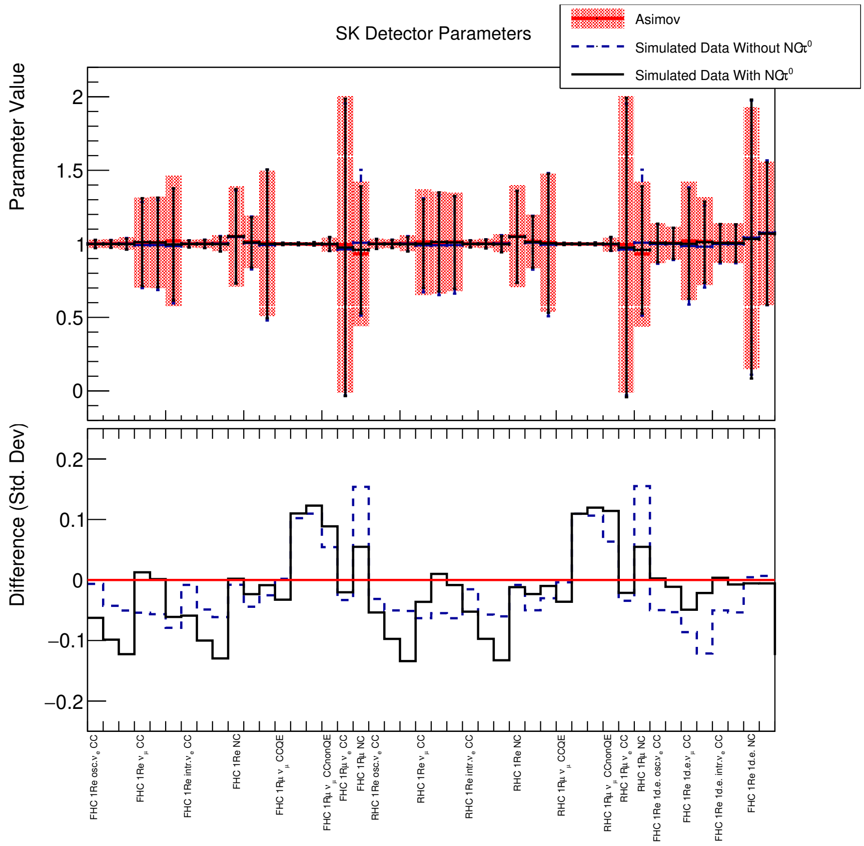

FIGURE 6.34: The post-fit parameter central value and width for the SK detector systematic parameters. There is a reduction in the bias seen in these parameters for many of the background parameters upon the addition of the new sample.

Overall the impact of this fit on the predicted event distributions at SK can be seen in Fig 6.35. Here the same increase in event rate at low reconstructed neutrino energy as in §6.1.1 is provided by the new NC1π cross-section parameters. This therefore reduces the need for the SK detector systematics, flux and other cross-section parameters to shift their values in order to recreate the observed spectrum.

The impact on the recovered oscillation parameters can be seen in Fig 6.36, these credible regions match the Asimov constraint very closely and show a reduced bias compared to the simulated data fit performed without the NCπ^0 sample in Fig 6.9.

Overall, from the simulated data study in §6.1.1, it can be seen that differences in NC1π cross-section relative to CC1π cross-section have the potential to bias both the T2K nuisance parameters in addition to the oscillation parameters. In addition, these biases apply to parameters not intended to absorb such changes, limiting the sensitivity to the underlying effect a given systematic was designed for.

The addition of SK NCπ^0 samples, in conjunction with an expanded NC1π cross-section parameterisation does not in and of itself introduce any significant bias or reduce the sensitivity of T2K to oscillation effects, as described in §6.3.1.

As seen in §6.3.2, the NCπ^0 samples do however provide the NC1π specific sensitivity required to identify a change in NC1π event rate independently of the CC1π rate and constrain the relevant cross-section parameters. This then reduces or eliminates the biases seen in both the nuisance and oscillation parameters from the simulated data studies performed without these additions of §6.3.1.

6.4 Data Fits

In order to investigate the impact of this improved treatment on the T2K data fit results, a full fit to T2K run 1-10 data was performed. The results with the inclusion of the NCπ^0 samples and NC1π cross-section parameters can then be compared to the results from the current T2K result before these additions [97].

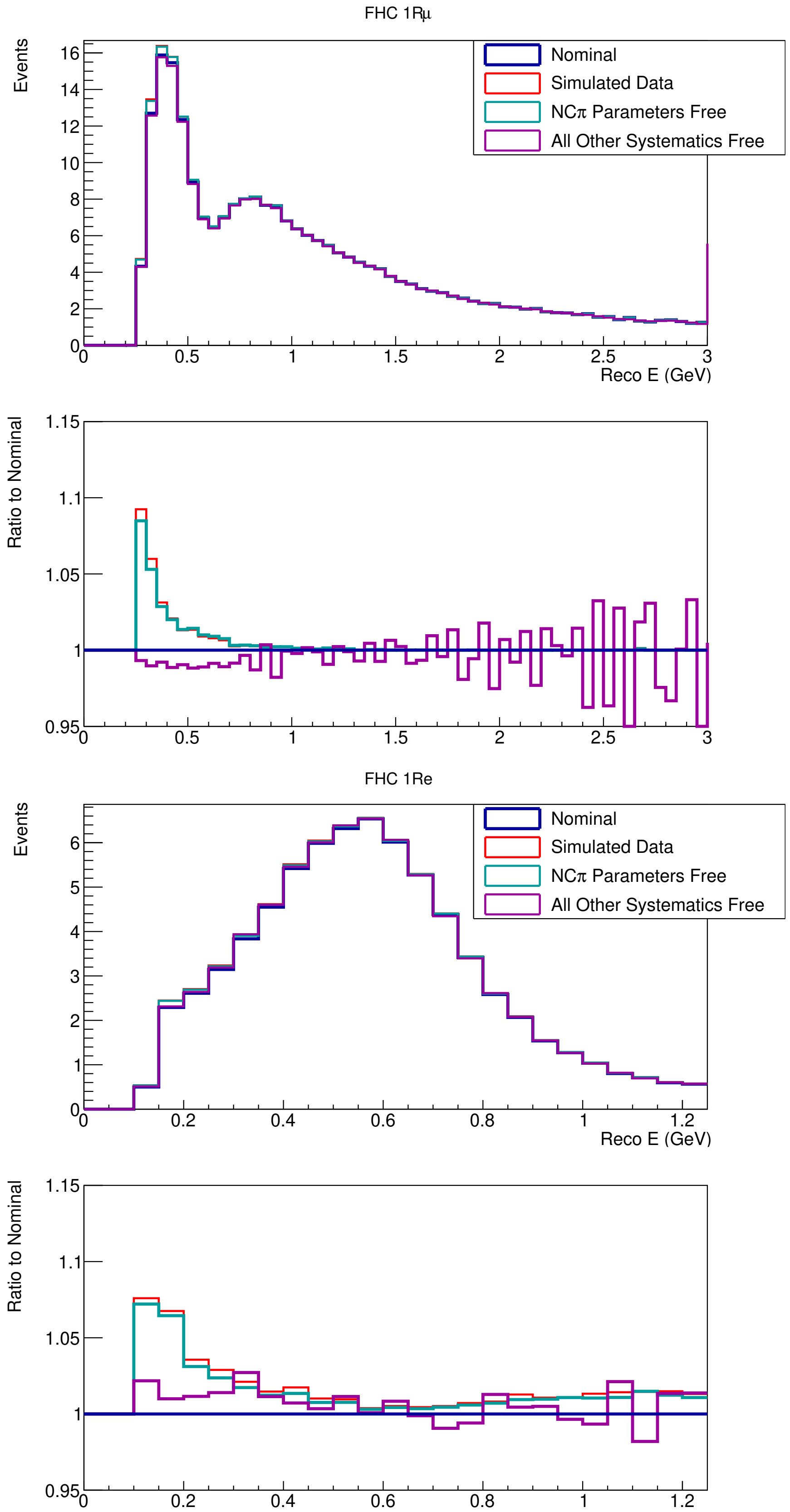

FIGURE 6.35: The impact of the fitted SK detector and flux and cross-section parameters on the predicted SK event spectra for the FHC 1Rμ sample (top) and the FHC 1Re sample (bottom). The prediction is split into the impact of the NC1π cross-section parameters alone (cyan) and all other flux, cross-section and SK detector parameters combined (purple). The NC1π parameters are able to correctly absorb a large majority of the observed simulated data increase, with the remaining cross-section and SK detector parameters contributing significantly less than seen in Fig 6.8.

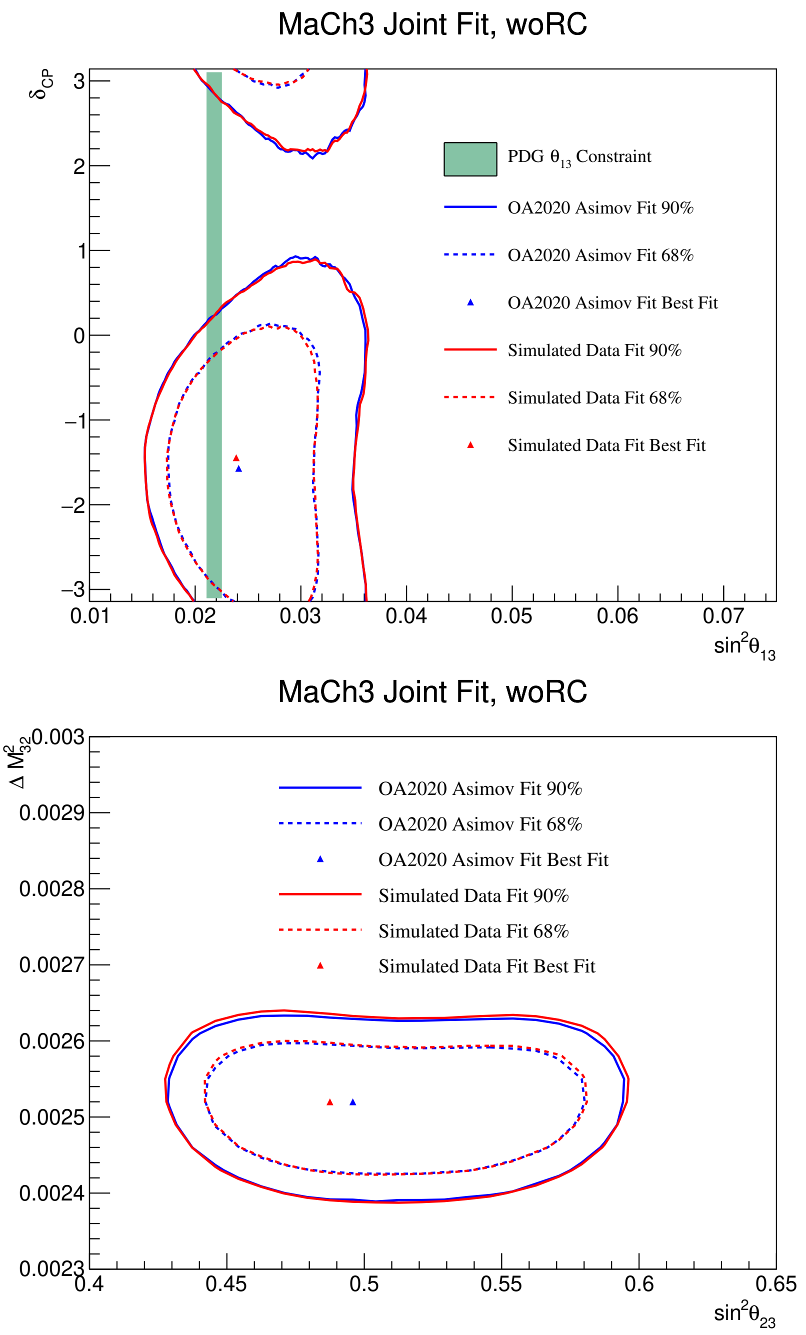

FIGURE 6.36: Two dimensional posterior credible regions, marginalised over all other parameters for the four oscillation parameters T2K has sensitivity to. Here shown for two joint ND280 and SK fits, one an Asimov fit to the pre-fit MC in blue, and a fit with NC1π cross-section uniformly increased by 30% including the new NC pion cross-section parameters and the NCπ^0 samples. Top marginalised over both mass orderings, bottom for normal ordering, without reactor constraint. The bias in the contours seen in Fig 6.9 is almost eliminated with the addition of the new parameters and the NCπ^0 samples.

6.4.1 Data Validation

While the standard T2K samples have been validated for the recent analysis, the NCπ^0 samples must also be verified. The impact of the imposed cuts were validated in the manner described in §6.2.2, this confirmed that the cuts were not being imposed in a region with significant data-MC discrepancies.

The accumulation of events in the samples as a function of POT exposure can be seen in Fig 6.37. Neither sample shows regions with an excessively high or low selection rate nor, any simultaneous events.

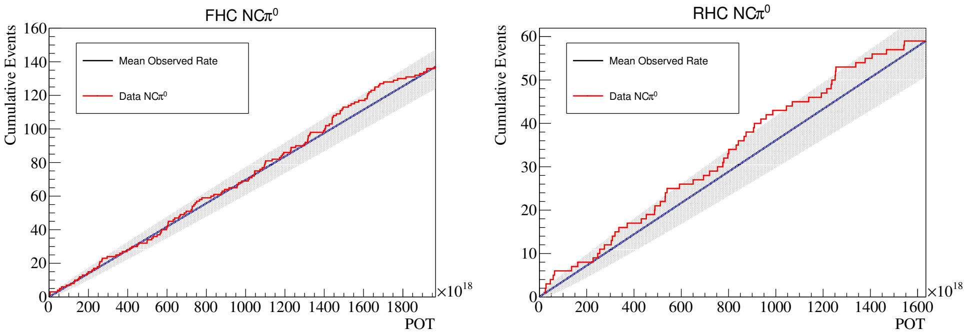

FIGURE 6.37: The accumulation of selected events in the NCπ^0 samples with POT. The grey band shows the 1σ statistical uncertainty on the mean event rate. There are no major discrepancies between the observed data and the mean accumulation rate.

The distribution of the data in the sample binning can be seen in Fig 6.38. The data shows a reduction in rate relative to the MC for the region with high NCπ^0 purity, while the background dominated high reconstructed mass region shows an excess in both the FHC and RHC samples.

It is therefore to be expected that the fit will decrease the NCπ^0 cross-section relative to the pre-fit prediction. This is the same behaviour as observed in the CC1π model, where there is an approximate 20% reduction in CC1π event rate upon fitting to data.

As the CC cross-section is well constrained by ND280, the excess at high π^0 mass is likely to be absorbed by the detector systematic uncertainties in this region.

6.4.2 Data Fits

These NCπ^0 data distributions were included in a fit to T2K run 1-10 data with the expanded NC1π cross-section described above. The impact of this on the recovered

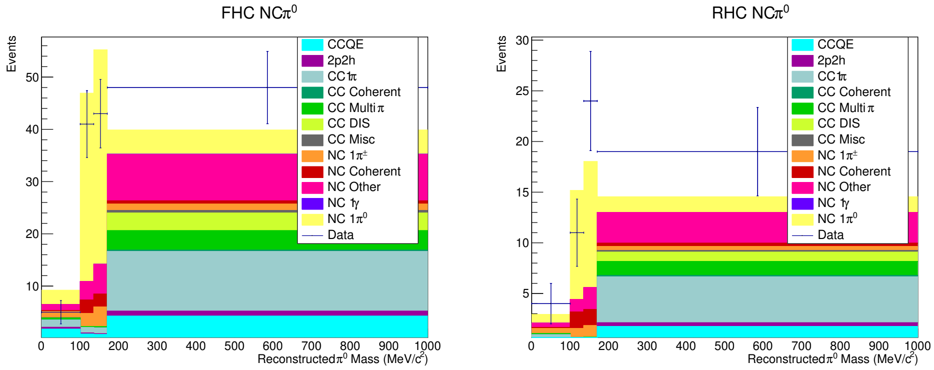

FIGURE 6.38: The observed NCπ^0 data distribution in the fit binning compared to the pre-fit prediction.

flux parameters can be seen in Fig 6.39. As was seen in the simulated data study §6.3.2 the impact is most pronounced at low neutrino energy, with up to a 1.9% reduction in FHC neutrino flux in this region. This is very compatible with the up to 1.5% change observed in this simulated data study.

There is however a difference in behaviour for RHC, showing a decrease in flux for $\bar{\nu}_\mu$ across the whole energy range. As the NC1π cross-section model has no explicit neutrino-antineutrino freedom, any observed FHC/RHC discrepancies in the NCπ^0 sample event rates must be accounted for in the flux parameters. The NCπ^0 samples therefore have some ability to constrain the ratio of FHC to RHC flux.

As was seen in the simulated data study of Fig 6.6, the 2p-2h normalisation parameters are some of the most impacted by the NC1π changes. This is repeated with the data fit results of Fig 6.40. Here the 2p-2h neutrino normalisation is decreased while antineutrino is increased.

In the current T2K CC cross-section model, there is very limited neutrino-antineutrino freedom. The 2p-2h parameters represent the most significant such freedom, having different, uncorrelated normalisation and shape freedom for neutrino and antineutrino interaction. A change in the ratio of FHC to RHC flux may therefore be absorbed into this neutrino antineutrino freedom. As 2p-2h events in T2K primarily come from higher energy neutrinos, above 0.5GeV, this different behaviour acts to cancel out much of the difference seen in the RHC $\bar{\nu}_\mu$ flux decrease at high energy.

The largest changes in the cross-section parameters however occur in NC parameters. Notably NC C_5^A and NC M_{Res}^A show distinctly different behaviour to their CC counterparts. NC C_5^A is decreased while NC M_{Res}^A increases, both by more than

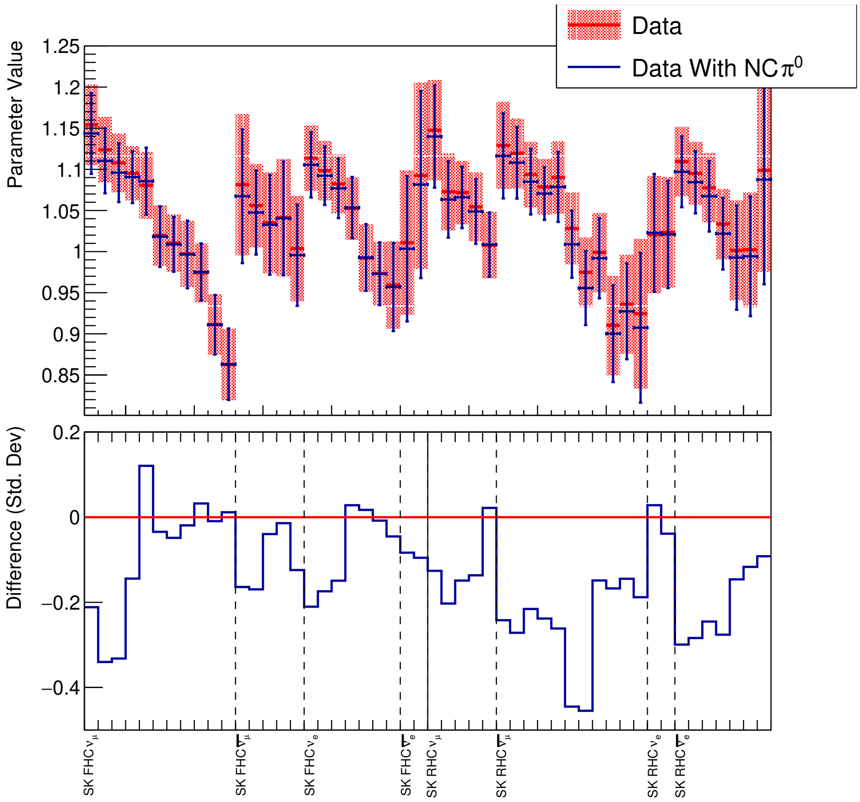

FIGURE 6.39: The recovered values for the SK flux parameters of a fit to T2K data including the NCπ^0 sample and the NC1π cross-section parameters, compared with a standard T2K fit. The parameters are grouped by horn current and true neutrino flavour, in ascending energy. Both fits show a preference for higher flux at low energies, however the fit with NCπ^0 has a 1% reduction in flux at low energy across all neutrino flavours.

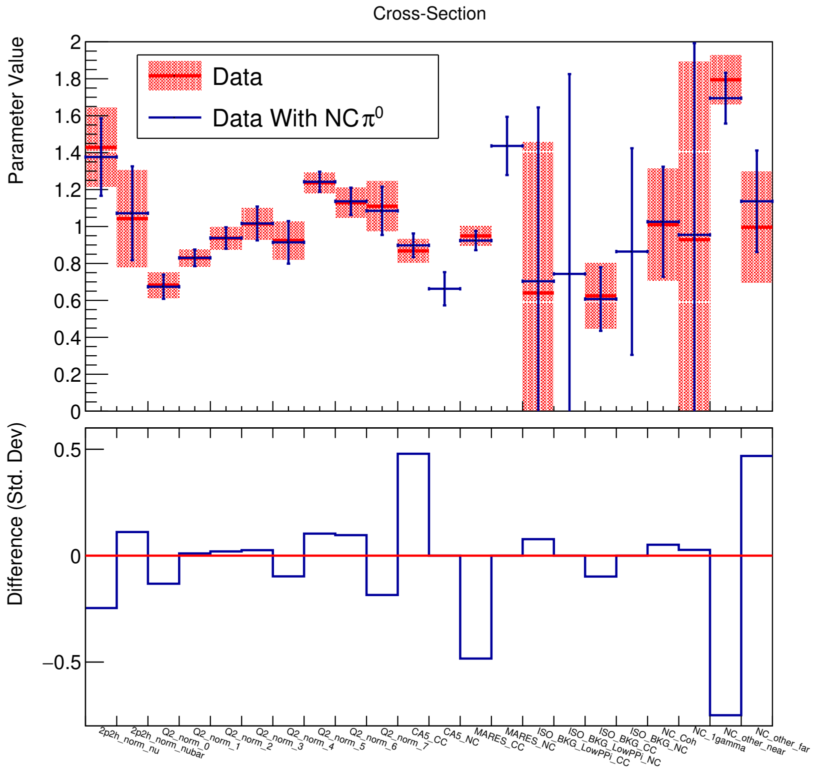

FIGURE 6.40: The recovered values for a selection of cross-section parameters for a fit to T2K data including the NCπ^0 samples and NC1π cross-section parameters. The most notable changes relative to the standard T2K fit are seen in the NC other at ND280 and the neutrino 2p-2h parameters.

their post-fit uncertainty. The corresponding CC parameters are pulled by 50% of their postfit uncertainty in the opposite directions. This results in a change in the Q^2 shape but little change in overall CC1π event rate.

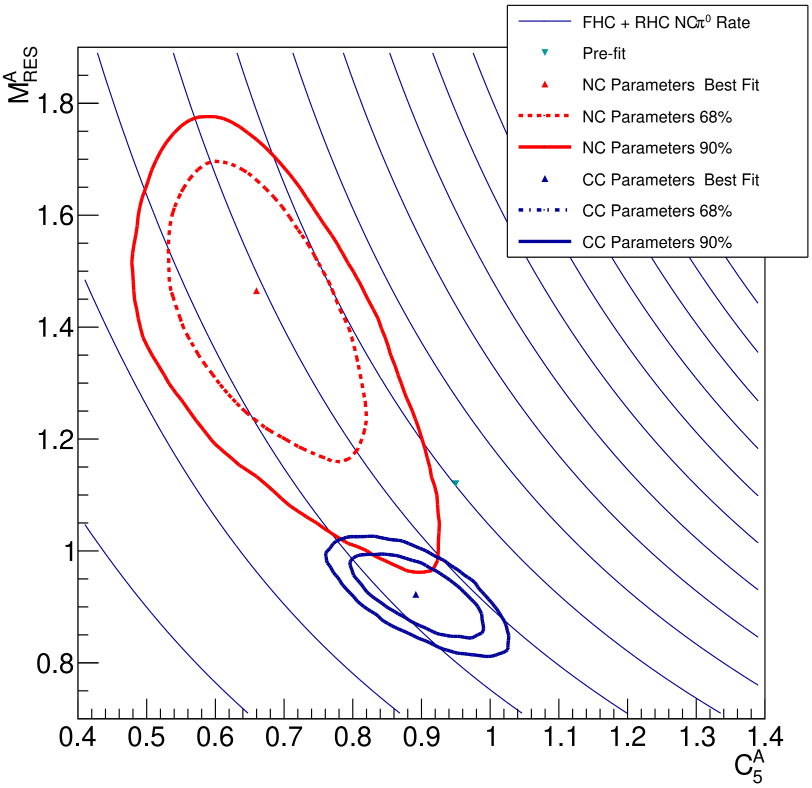

FIGURE 6.41: The recovered credible regions for the C^A_5 and M^A_{Res} parameters, marginalised over all other parameters in the fit. Both sets of parameters recover a similar total NCπ^0 sample event rate, and lower than the pre-fit prediction. The NC parameters however prefer higher values of M^A_{Res} and lower C^A_5. Rate contours correspond to a change of 20 NC1π events in the summed FHC + RHC sample.

A comparison between the credible regions for the NC and CC pion parameters in the C^A_5— M^A_{Res} space can be seen in Fig 6.41. Both NC and CC parameters correspond to a reduction in pion event rate relative to their pre-fit parameter values. The NC parameters prefer significantly higher values of M^A_{Res} than the CC parameters, with overlap at the 90% level but not at 68%.

The effect on the NC1π event rate in the NCπ^0 samples from these parameters can be seen in Table 6.9. Here the event rate of NC1π events in the NCπ^0 sample, as predicted by the posterior distribution of the pion parameters, is shown relative to the pre-fit prediction.

	FHC NCπ^0		RHC NCπ^0	
	Mean	Std Dev	Mean	Std Dev
NC (posterior/prior)	0.844	0.098	0.812	0.116
CC (posterior/prior)	0.722	0.044	0.687	0.0591
NC/CC ratio	1.17 ± 0.15		1.18 ± 0.20	

TABLE 6.9: The posterior predicted NC1π event rate in the NCπ^0 samples, relative to the rate predicted by the pre-fit pion parameter values. The NC and CC refer to using the recovered NC1π or CC1π cross-section parameters to predict this event rate. Both show a decrease in predicted event rate, with the constraint provided by the NC parameters being half as strong as that of the CC parameters.

The NC parameters predict a mean event rate 17% higher than the value predicted by the CC parameters, this change is of similar magnitude to the error on this measurement however.

The major impact of the separation into NC and CC parameter is therefore a change in the cross-section as a function of Q^2, with cross-section for high Q^2 NC1π events increased relative to the current T2K result and low Q^2 events reduced. As higher Q^2 events tend to be reconstructed with higher neutrino energy, this has the effect of increasing the expected background in the region around the flux peak, and decreasing the backgrounds expected at low reconstructed energy. However the impact of this will be smaller than a change that directly affects the total NC1π cross-section.

In order to investigate the contributions of ND280 and SK data to this NC1π cross-section constraint, two additional fits were run. Firstly, an ND280 only fit with the new NC1π cross-section parameters, then a joint ND280 and SK fit, in which the ND280 NC1π cross-section was linked to the CC1π cross-section. The constraint provided on NC C_5^A and NC M_{Res}^A for these can be seen in Fig 6.42.

Both the ND280 and SK only constraints have overlap in the 68% contour, showing compatibility in extracted cross-section from the different datasets. The SK contour shows a stronger constraint on total NC1π cross-section than the ND280 constraint. The ND280 result however has a stronger constraint on Q^2 shape than SK. The observed preference for higher NC M_{Res}^A in the combined fit therefore derives primarily from the ND280 data.

While the recovered NC M_{Res}^A value (1.36±0.15) GeV is significantly higher than the (0.88±0.05) GeV value for CC M^{A}_{Res} , as was seen in Fig 6.42, care must be taken in interpretation of this difference. The ND280 constraint on Q^2 shape is reliant on the use of background NC1π data from ND280 CC samples. This has the potential to be subject to over-fitting, the significant cross-section freedom given to NC1π events may allow these to be used to recreate behaviour seen in ND280 data that the standard T2K model lacks the freedom to fully reproduce.

The slight preference for an increase in NC1π event rate, relative to that predicted by the CC parameters, as in Table 6.9 is a real effect and supported by the NCπ^0 sample data. The preference for higher M^{A}_{Res} values may however be an artefact of the fit and should be corroborated by an NCπ^0 binning with more Q^2 sensitivity, before concluding that such an effect is a true property of NC1π interactions.

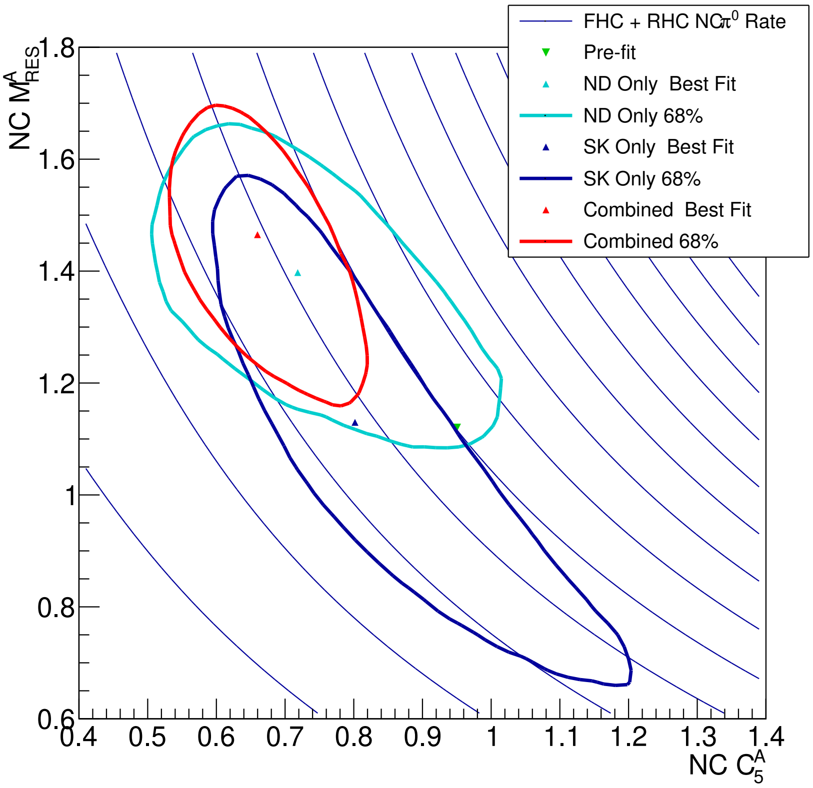

FIGURE 6.42: The recovered credible regions for the NC C^{A}_{5} and NC M^{A}_{Res} parameters for: a fit to ND280 data only, a fit with only SK constraining NC1π cross-section, and a combined fit with constraint from both detectors. The SK fit gives a tight constraint on total event rate, but with a weak Q^2 sensitivity, while the ND280 fit provides some Q^2 constraint but little for the total event rate. The combined fit inherits the desirable characteristics of both.

The addition of the NCπ^0 sample has an additional impact on the NC other parameters, as seen in Fig 6.40, the cross-section for NC other events at ND280 is reduced from 1.79 times the pre-fit value to 1.69. This indicates that some of the high extracted cross-section for NC other events at ND280 is a result of imitating the high Q^2 impact of NC1π events. NC other far is increased to 1.15 times its pre-fit value, bringing this closer to the ND280 rate, though still not in agreement.

The SK detector systematics largest change is in NC parameters. As can be seen in Fig 6.43, relative to the current T2K result, there is a 10% reduction in NC contribution in the 1Rμ samples. The NC parameters in the 1Re samples show a similar change but with an energy dependence in their behaviour, with higher reconstructed energy events being more significantly impacted.

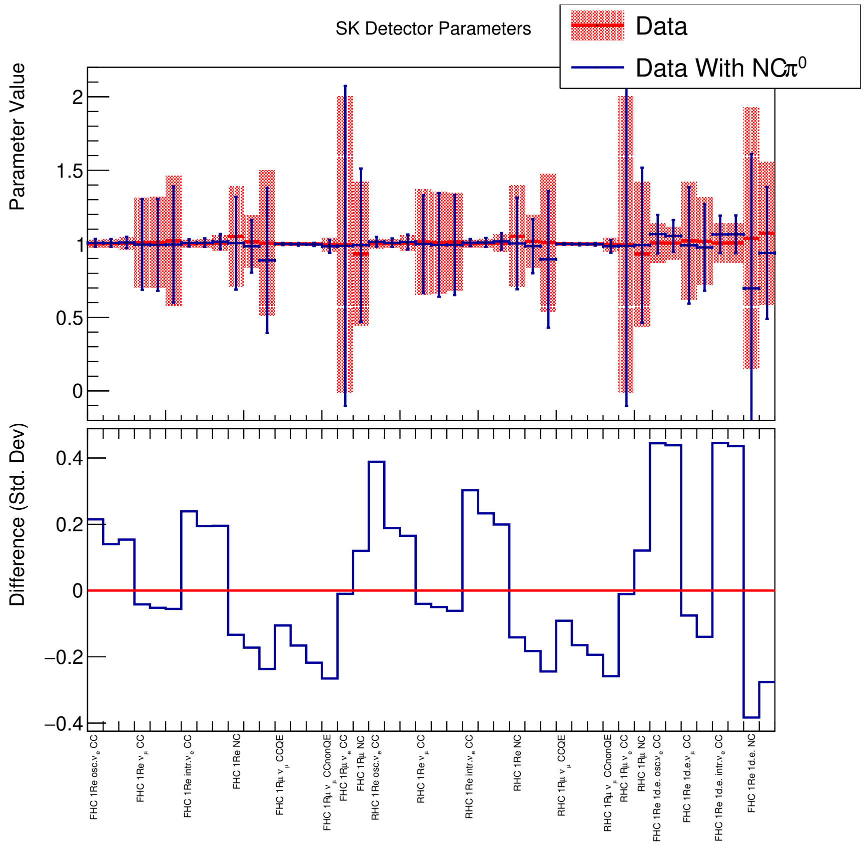

FIGURE 6.43: The recovered credible intervals for the SK detector systematic parameters. Comparing a fit to T2K data with and without the inclusion of NCπ^0 samples and NC1π cross-section parameters. Most parameters are unchanged however the NC parameters are decreased, with the 1Rμ NC parameters decreased by 10%.

The effect on the recovered oscillation parameters is small, as can be seen in Fig 6.44. There is a small broadening in Δm^2_{32}, similar in magnitude to the effect

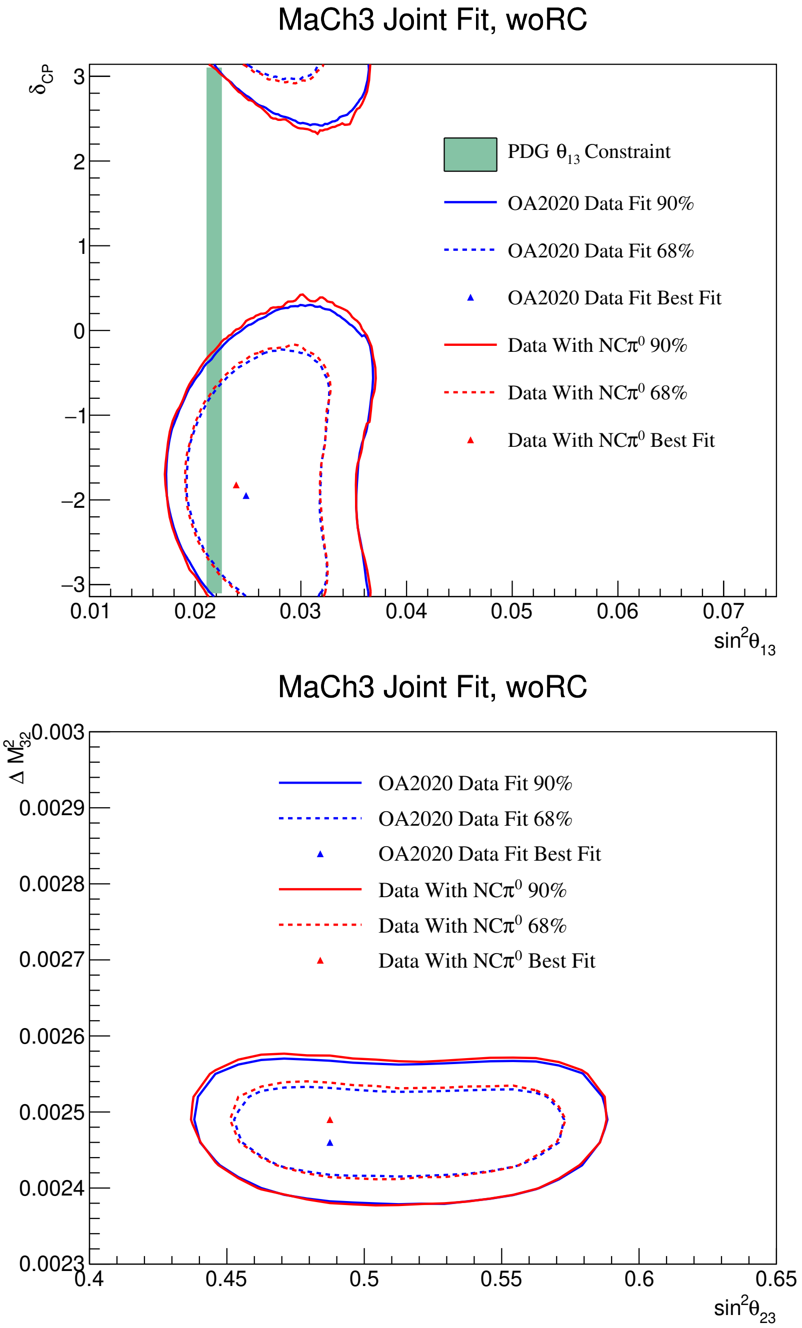

FIGURE 6.44: The recovered two dimensional posterior credible intervals for the four oscillation parameters with which T2K has sensitivity. Shown for two fits, the current T2K result (blue) and the result with the addition of the NCπ^0 samples and the new NC1π cross-section parameters, both before the imposition of the reactor $\sin^2\theta_{13}$ constraint.There is a slight broadening in $\sin^2\theta_{13}$ and Δm^2_{32} as was seen in the simulated data study, however this effect is small.

observed in the fake-data study of Fig 6.36 however the change in other parameters is minimal.

6.4.3 Data Fit Conclusion

The addition of an SK NCπ^0 sample into the T2K oscillation analysis can provide a direct constraint on NC1π cross-section, one of the most significant backgrounds in the SK physics sensitive samples. One potential method of including this sample and an associated NC1π cross-section parameterisation has been shown. Such an addition results in a number of fit parameters shifting compared to the current T2K analysis. Such shifts are contained within the 1σ postfit uncertainty, however the effect of such shifts on the predicted event spectra can still be significant at low reconstructed energy. For some parameters, such as NC other and 2p-2h the shifts are comparable to the error budget for these processes allowable in HK [102].

6.5 Outlook

A data-driven measurement of the NC1π background using the same detector as the physics sensitive samples offers the potential for a reduction in bias for several parameters in the fit, notably flux, 2p-2h and SK detector systematics. While the direct effect on oscillation sensitivity from this sample is minimal, it does offer the potential to alter other aspects of the analysis and increase oscillation sensitivity.

One such area is the $e - \pi^0$ cut applied in the selection of SK 1Re samples. This cut primarily removes NCπ^0 events, however approximately 6% of the signal CC ν_e events are also removed by this cut [89]. It would therefore be possible to increase the number of selected signal CC ν_e events by up to 6% by including data outside of this $e - \pi^0$ cut.

Such a sideband sample would have an increased NCπ^0 background relative to the main 1Re samples. The increased confidence in the estimation of the NCπ^0 background contribution in these sidebands could allow these previously unused events to contribute to the sensitivity of the statistics limited $\nu_e / \bar{\nu}_e$ appearance, this channel having the greatest sensitivity to CP violation in T2K.

At present, much of the impact of the simulated data studies is absorbed by the large SK detector systematic uncertainties on NC1π contributions to the one-ring samples, muting the impact on oscillation parameters. As SK continues to collect data, improvement to detector systematic evaluation will reduce this prefit error, the fit will therefore face a higher likelihood penalty for the detector systematic shifts required to recreate the observed spectra at SK.

A number of improvements to the NC1π treatment described here are possible. A more theoretically motivated model of the difference between CC and NC pion interactions is desirable. Rather than making use of the weak form factor to provide normalisation and Q^2 freedom, other differences in the properties of NC1π and CC1π interactions may be of interest, such as the distribution of the invariant hadronic mass W.

An improved sample, based on the multi-ring fiTQun reconstruction with PID cuts, and a new binning in more kinematically sensitive variables would be of benefit. One such choice of variables would be reconstructed π^0 momentum and angle relative to the incident neutrino beam. Due to the lack of other observable outgoing particles from NCπ^0 events, these two variables provide the full kinematic information that can be reconstructed in SK. Such a sample may be useful in cross-checking the predictions of the pion production model, which has been extensively used with samples binned in reconstructed lepton kinematics at T2K but less frequently in binnings sensitive to pion kinematics.

In the future this sample may prove useful at HK, unlike T2K's statistics limited sensitivity to CP violation, HK will be limited by its systematic uncertainties. The impact of uncertainty on the NC1π background to this measurement will therefore be greater than that seen for the studies with T2K data.

Further in the future, with either an expanded near-detector suite, or with external constraint on NCπ^0 cross-section, the NCπ^0 sample has sensitivity to sterile neutrino oscillation. As all non-sterile neutrino flavours contribute to NC1π event rate, any reduction in SK NCπ^0 sample event rate beyond that predicted by the flux and cross-section model is indicative of oscillation of ν_μ to sterile. Due to the energy and baseline of T2K, such a measurement would be most sensitive to low square mass difference sterile neutrinos ($\Delta m^2_{41} \approx 5\times10^{-3}$ eV^2), this area is not currently well covered by other experiments [118].

One additional use may be for detector cross-calibration. With an additional water cherenkov detector in the near-detector suite, as proposed by HK, a sample of NCπ^0 events may be constructed at this detector. Such a sample would derive from the same flux as seen in the far detector, with similar reconstruction and detector thresholds. The properties of these events such as reconstructed π^0 mass may then allow for direct comparison of the reconstruction performance of the two detectors.

Chapter 7

Charged-current ν_e and $\bar{\nu}_e$ cross-section measurement at the IWCD

The IWCD fit is a semi-frequentist, binned near-detector fit, used to investigate the potential physics sensitivity of the IWCD. This fit yields constraints on incident neutrino flux and parameters of a neutrino cross-section model that can then be used as an input for the far-detector. The results from this are used to refine the analysis technique and identify the impact of different systematic uncertainties on the available physics constraints. In addition, these results can be used to investigate the effect of modifications to the IWCD detector design and configuration on the physics sensitivity.

7.1 Motivation

One of the major physics goals of Hyper-Kamiokande is the detection, and subsequent precision measurement of neutrino CP violation [66]. Results from T2K [97] already show a 2σ tension with the no CP violation hypothesis. However obtaining the necessary statistics for a 5σ discovery is infeasible at T2K given the small size of SK, it is therefore necessary to construct a new detector, HK.

In addition to the increase of statistics required for a 5σ discovery, systematic uncertainties will play an important role in HK's sensitivity to this effect. The ability for HK to exclude CP conservation as a function of the true value of δ_{CP} is shown in Fig 7.1.

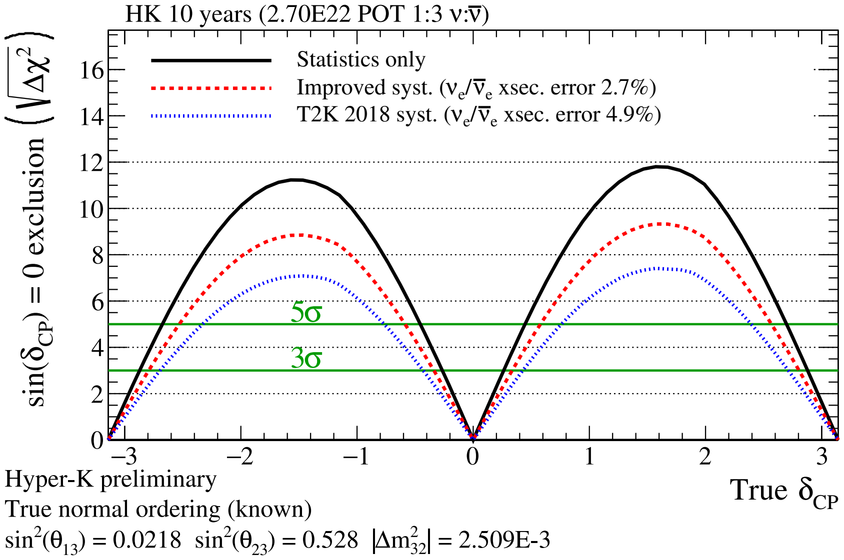

FIGURE 7.1: The ability of HK to exclude CP conservation as a function of the true value of δ_{CP}. There is a significant dependence on the assumed electron neutrino to antineutrino cross-section uncertainty.

In studies of HK sensitivity it has been found that the uncertainty on the ν_e and $\bar{\nu}_e$ interaction cross-section is the leading source of systematic uncertainty limiting the CP violation sensitivity [66]. The current uncertainty is theoretically motivated and driven by the differences in contribution from radiative corrections to the outgoing charged lepton for muons and electrons [119]. If the IWCD is able to reduce this uncertainty, a corresponding improvement in CP sensitivity of HK is possible.

7.2 Detector Properties

The current IWCD design, ‘the 750m design’ features an 8m diameter, 6m tall inner detector placed 750m downstream of the target and instrumented with mPMTs, as described in §3.4. This is an evolution of a previous design ‘the 990m design’ that made use of a 7.4m diameter, 10.4m tall ID, similarly instrumented with mPMTs and located 990m from the target. An existing MC production for this latter design exists, and due to the time required to regenerate this for the 750m design, it was decided to make use of this existing MC with some modifications to account for the expected differences.

7.2.1 MC Properties

The MC used was generated for a detector situated within a 52.5m deep shaft and covering off-axis angles ranging from 1 to 4°. The ID volume is 10.4m tall with a diameter of 7.4m, enclosing 450m^3 of water. To reduce the time taken to generate the MC, no events are generated for the OD volume. It is assumed that these events would be efficiently removed either by the OD veto or by fiducial volume cuts in the ID.

The MC uses the T2K 2016 flux model with a 320kA magnetic focusing horn current. A total exposure corresponding to 3.24×10^{21} (4.165×10^{21}) protons on target in FHC (RHC) mode has been generated. This exposure is evenly split between seven off-axis detector positions, resulting in approximately 0.462×10^{21} (0.595×10^{21}) POT of data for each position in FHC (RHC) mode. HK will collect approximately three times the POT exposure in RHC as in FHC, this is to allow for approximately equal number of ν_e and $\bar{\nu}_e$ events to be observed in the far detector.

NEUT 5.3.6 [39] is used for event generation, including 2p-2h events and the Berger-Sehgal charged-current coherent pion production model. The GEANT4 [120] based application WCSim [121] is used for propagation of the resulting interaction products within the detector volume, and for PMT response to the cherenkov light produced. For reconstruction of events, fiTQun [64] is employed, as currently in use at SK.

7.2.2 750m Design

In order to apply the MC generated for the 990m detector design described above to the new 750m design there are two major adjustments required; a correction for the incident flux and secondly for the different fiducial volumes. The flux is increased at all positions by the inverse square relationship:

$$\text{Flux(750m)} = \left(\frac{990}{750}\right)^2 \times \text{Flux(990m)}. \tag{7.1}$$

Due to the line source nature of the pion and kaon decay pipe, the energy dependence of the flux at 750m will be slightly different to that at 990m. The binned fit approach adopted here has quite coarse bins in off-axis angle, no smaller than

0.5°, hence it is not expected that this difference will have a large impact on the sensitivities discussed here. Therefore it is sufficient to use this MC with a prior flux constraint, and the associated correlations from the 750m position.

The detector volume in this design is lower than in the MC being used, this results in a reduction in selected event rate. To account for this, events can be reweighted by the ratio of fiducial volumes in the two designs. Each sample used in the fit has different fiducial volume cuts, thus each selection must be weighted separately.

7.3 1R*e* Cut Selection

As the electron neutrino flux is a small component of the total neutrino flux, Fig 2.8, electron neutrino interaction events make up only 1.5% of all interaction events in the detector. In order to make precise measurements of the electron neutrino interaction cross-section it is necessary to select a sample of events enriched in electron neutrino interactions.

The fiTQun reconstruction of events considers many interaction hypotheses and evaluates the best-fit likelihood of each hypothesis matching the observed detector response. These hypotheses include electron, muon and π^0 interaction events. The relative likelihoods of these hypotheses can be used to identify the desired events. Kinematic variables can also be used to separate signal events from backgrounds. These include reconstructed lepton momentum as well as π^0 mass. As discussed in Chapter 6, NCπ^0 events are a significant background for 1R*e* selections due to the potential for the π^0 decay photons to overlap or have a ring missed in the reconstruction.

A further significant background for electron neutrino cross-section measurements is the effect of entering gamma events. These are produced by neutrino interactions upstream of the ID volume such as NCπ^0 events, these yield high-energy photons. Such photons may penetrate into the ID region and then pair produce, resulting in an electron like response in the detector with no OD light. These events have the potential to be a major source of systematic uncertainty for the ν_e cross-section measurement at low energy.

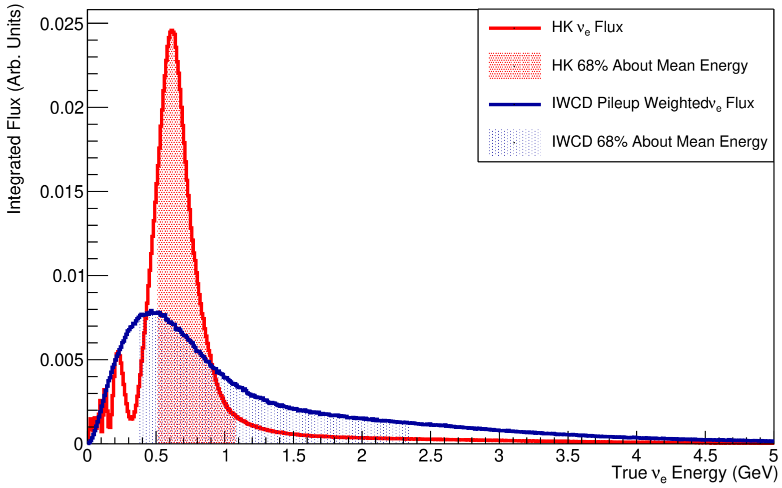

FIGURE 7.2: The total ν_e flux measured by IWCD over the full 1-4° off-axis range and that present at HK. The highlighted regions show 68% of the incident flux symmetrically about the mean. The IWCD Flux has a significantly broader distribution than the oscillated HK spectrum. Both fluxes are normalised to a total integral of one with oscillation parameters $\sin^2\theta_{23} = 0.51$, $\Delta m^2_{23} = 2.51 \times 10^{-3}$ eV^2 and $\delta_{CP} = 0$.

In order to include the effect of these events, a separate MC production for interaction events in the OD and surrounding soil is made. Events with particles depositing more than 50MeV of energy in the OD region are excluded, it being assumed to have been removed by an OD activity cut, the resulting entering photons are included in the analysis selections. These photons are well attenuated by the water in the ID, hence, with an appropriate fiducial volume cut, these can be efficiently removed from the 1Re selections.

Consideration must also be given to the goal of the IWCD measurement when making such a 1Re selection. The oscillated ν_e appearance flux at HK has a quite different energy distribution to the intrinsic ν_e flux present at the IWCD, as can be seen in Fig 7.2. The goal of the IWCD ν_e cross-section measurement is to constrain the event rate in the HK 1Re sample. Due to the energy range of the oscillated HK ν_e flux and the one-ring requirement, this sample is dominated by ν_e CC0π events.

The goal of the IWCD measurement should therefore be focused at ν_e CC0π events in the energy range of interest to HK. The choice of signal definition is therefore a ν_e charged current event with no final state pions above the detection threshold (CC0π) and with a true vertex position greater than 75cm from the nearest wall, motivated by the known range of entering γs.

Using this signal definition alone for cut tuning purposes risks optimising towards a selection with high efficiency in the high energy tail of the IWCD ν_e flux of Fig 7.2. This would therefore constrain the ν_e interaction cross-section in a kinematic regime unrepresentative of the HK sample. The figure of-merit adopted therefore is:

$$\mathrm{FOM} = \frac{S(E_\nu < 1\mathrm{GeV})}{\sqrt{S+B}} \tag{7.2}$$

Where $S(E_\nu < 1\mathrm{GeV})$ is the number of selected signal (CC0π ν_e) events with true neutrino energy below 1GeV and B is the total number of backgrounds in the sample of any energy. This ensures the selection optimises the statistical power of the sample in the sub-GeV region of relevance for HK.

As discussed in §3.4, at larger off-axis angles, the neutrino beam has a greater fraction of electron flavour. This region therefore has an increased signal to background ratio and a corresponding increase in sensitivity to changes in cross-section. The region from 2.7-4.0° alone was therefore used for cut tuning.

The following cuts on reconstructed fiTQun properties are applied sequentially:

1. The event is fully contained within the ID volume
2. The event has visible energy greater than 100MeV
3. The event has no reconstructed decay electrons
4. A 1Re fit hypothesis is preferred over a 1Rμ hypothesis
5. A 1Re fit hypothesis is preferred over a π^0 hypothesis as a function of reconstructed π^0 mass
6. The event is reconstructed within the fiducial volume
7. A one-ring hypothesis is preferred over a two-ring hypothesis
8. A 1Re fit hypothesis is preferred over a π^0 hypothesis as a function of reconstructed electron momentum

Cuts 4—8 have their cut points chosen in an iterative process in order to maximise the final sample figure-of-merit eqn 7.2.

1. Fully Contained

Due to the small size of the IWCD, a large fraction of events with muons are likely to escape the ID volume. The IWCD simulation does not include an OD region nor an OD veto. Therefore a cut is placed on muons with sufficient true energy to escape the ID volume, along their outgoing direction from the interaction point. This is in place of an effective simulation of the OD response to such muons. No such requirement is placed on any other particles.

2. Visible Energy

Due to the low flux and neutrino interaction cross-section at energies below 100MeV it is not expected that there will be a significant number of ν_e CC0π events with visible energy below 100MeV. Such events are likely to be a result of non-beam backgrounds. Additionally, this is not a region of interest for the HK ν_e appearance measurement. In practice this visible energy cut is applied to the reconstructed momentum of the 1Re hypothesis.

3. Decay Electron Tag

Signal ν_e CC0π events have no final state muons nor pions and hence should not have any associated decay electrons. A cut is therefore placed on the fiTQun decay electron tag.

4. Electron-Muon Likelihood

Due to the dominance of ν_μ flux in the HK beam, the large contribution of ν_μ CC events must be removed. This is performed making use of the fiTQun 1Rμ and 1Re fit hypotheses.

The $e - \mu$ cut acts on the log of the ratio of the electron hypothesis likelihood to the likelihood of the muon hypothesis. In order to improve the cut selection, the placement of this cut is dependant on the reconstructed lepton momentum, assuming an electron hypothesis. Fig 7.3 (top) shows the distribution of signal ν_e CC0π present in the sample in this $e - \mu$ likelihood — reconstructed lepton momentum space. Fig 7.3 (bottom) shows the distribution of background ν_μ CC events that this cut is designed to remove. The line indicates the boundary of the region removed by this cut.

At high momentum there is clear separation between signal and background events, however at low momentum the separation becomes less clear. Due to the large difference in rate of ν_μ CC events to ν_e CC0π events the cut used must be placed in quite an electron-like region at low energy.

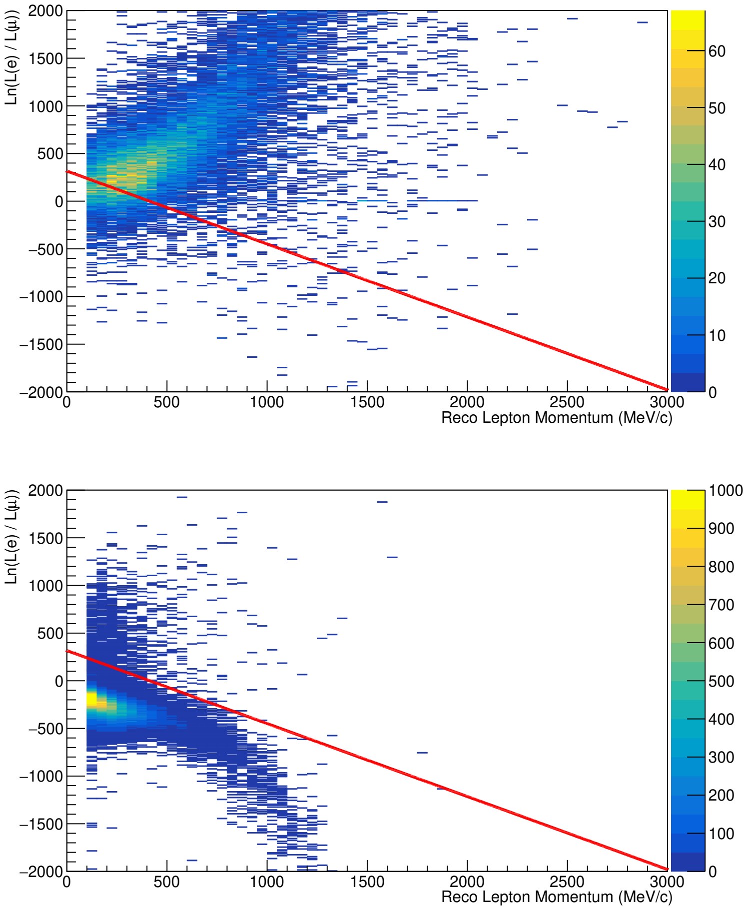

FIGURE 7.3: The distribution of events in reconstructed electron-muon likelihood ratio vs reconstructed lepton momentum. CC0π ν_e signal events (top) are broadly distributed with increasing electron-like reconstruction accuracy at high reconstructed lepton momentum. Background events (bottom) have significant overlap with signal events at low reconstructed lepton momentum. The red line denotes the boundary of the cut used, events below this line are removed.

5. Electron-π^0 Likelihood

Neutral current π^0 events are a major source of background in the electron-like sample. Many of these can be removed through the use of the π^0 reconstruction provided by fiTQun. The likelihood ratio of the π^0 hypothesis to the electron hypothesis can be used in conjunction with the reconstructed kinematics of the event.

Fig 7.4 (top) shows the distribution of true ν_e CC0π events in π^0 — electron likelihood ratio vs reconstructed π^0 mass space. The signal population is well concentrated around low reconstructed π^0 mass and low π^0 — electron likelihood ratio. True NCπ^0 backgrounds are shown in the same space in Fig 7.4 (bottom), a large number of events are concentrated around the π^0 mass of 135MeV as a result of on-shell NCπ^0 production. There is a significant population of background events at low reconstructed π^0 mass overlapping with the signal population. These are events with co-linear π^0 decay photons, or events in which one of the photon rings is not detected.

A cut on π^0 mass and π^0 — electron likelihood can be used to significantly reduce the NCπ^0 background contribution to the sample.

6. Fiducial Volume

Due to the granular nature of the photosensors, events occurring close to the detector wall with outgoing charged particles above Cherenkov threshold, directed towards the ID wall, will only be detected in a small number of PMTs. The reconstruction accuracy of these events will therefore be adversely affected. Further, entering gamma backgrounds produce a similar detector response to electron neutrino interactions, these can only be effectively eliminated through the use of a fiducial volume cut. The distribution of reconstructed vertex position in the ID relative to the detector wall for these entering gamma events can be seen in Fig 7.5. This shows an exponential behaviour with distance from the ID wall, hence the fiducial volume is limited by the acceptable number of entering gamma events in the 1Re samples.

To reduce the effect of these factors on the resulting sample, a cut on reconstructed vertex distance from the wall of 100cm is used, as seen in Fig 7.6. This ensures that the entering gammas are attenuated to a low enough level to not severely

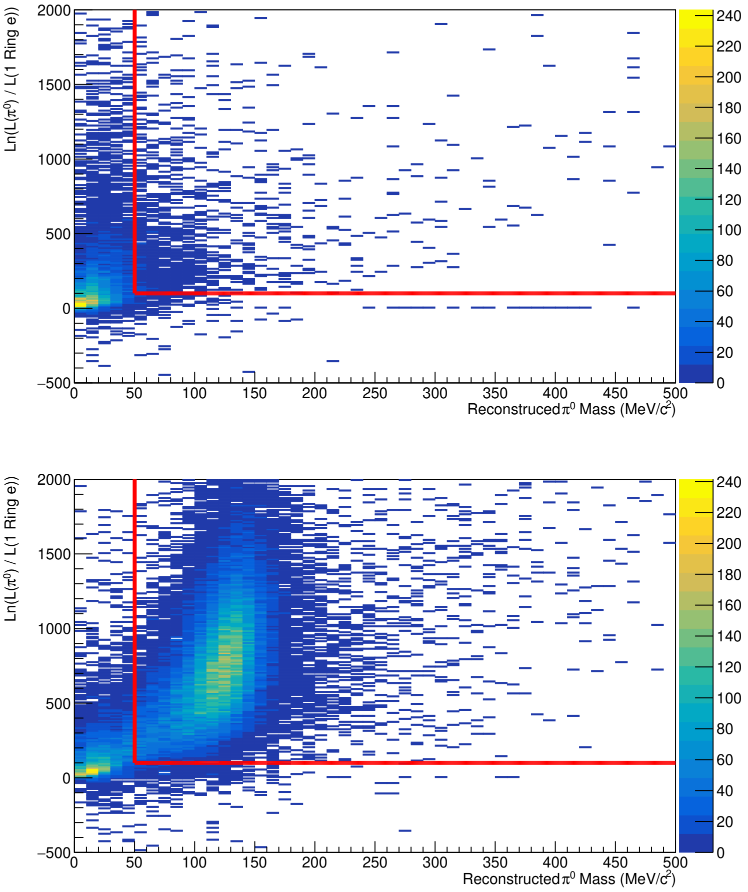

FIGURE 7.4: The distribution of signal (top) and background NCπ^0 events (bottom) in reconstructed π^0 — 1 ring electron likelihood ratio plotted against reconstructed π^0 mass, assuming the π^0 hypothesis. There is a large, broad resonance in the background sample at reconstructed masses around the π^0 mass, this can be removed effectively with a simple cut.

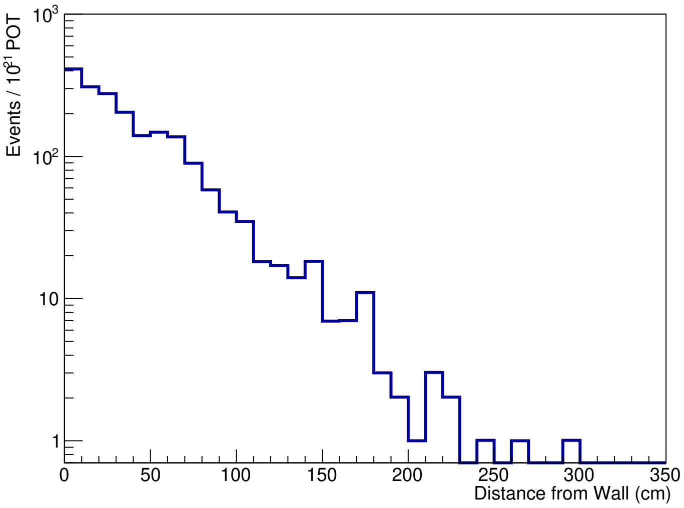

FIGURE 7.5: Entering γ events as a function of reconstructed distance to the ID wall.

affect the resulting fit and also ensures that selected events occur far enough away from the wall to be reconstructed well. With this fiducial volume cut the total active volume of the inner detector is 113m^3 corresponding to 38% of the total inner detector volume of the 750m design.

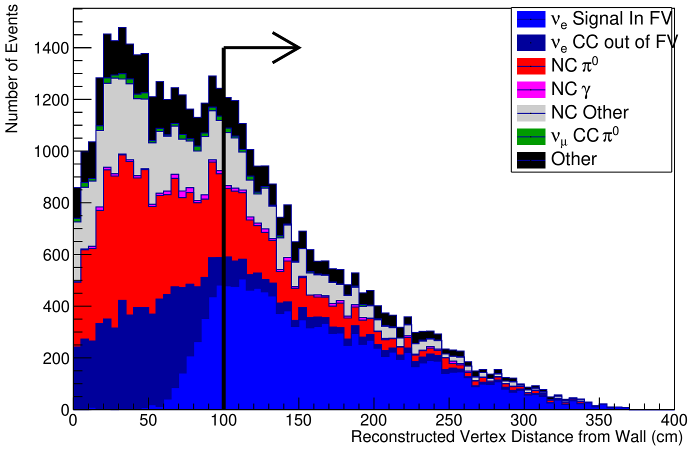

FIGURE 7.6: The breakdown of events with reconstructed distance to the ID wall. The in FV is defined as a true vertex greater than 75cm from the ID wall. Entering γ events are not shown.

7. Number of Rings

As the desired CC0π signal has only a single outgoing above Cherenkov threshold charged particle, the resulting event should be reconstructed as a single ring event. Background pion production events are likely to produce two or more non-overlapping Cherenkov rings.

In order to separate these events, the fiTQun multi-ring fits can be used. Taking the likelihood ratio of the most likely two-ring fit to the 1R*e* fit gives a measure of the preference for multiple rings in the reconstruction. As the likelihood of multiple rings being fit is expected to increase with visible energy in the detector, this cut is performed as a function of 1R*e* reconstructed electron momentum.

The distribution of signal and background events in this likelihood ratio space can be seen in Fig 7.7. The signal CC0π events (top) are distributed over a wide range of reconstructed electron momenta but at low likelihood ratio. This is in contrast to the background events (bottom) which are prominent at low reconstructed lepton momentum and distributed broadly in the likelihood ratio.

Fig 7.7 (top) shows the distribution of signal events in the rings likelihood — 1 ring electron hypothesis reconstructed momentum space.

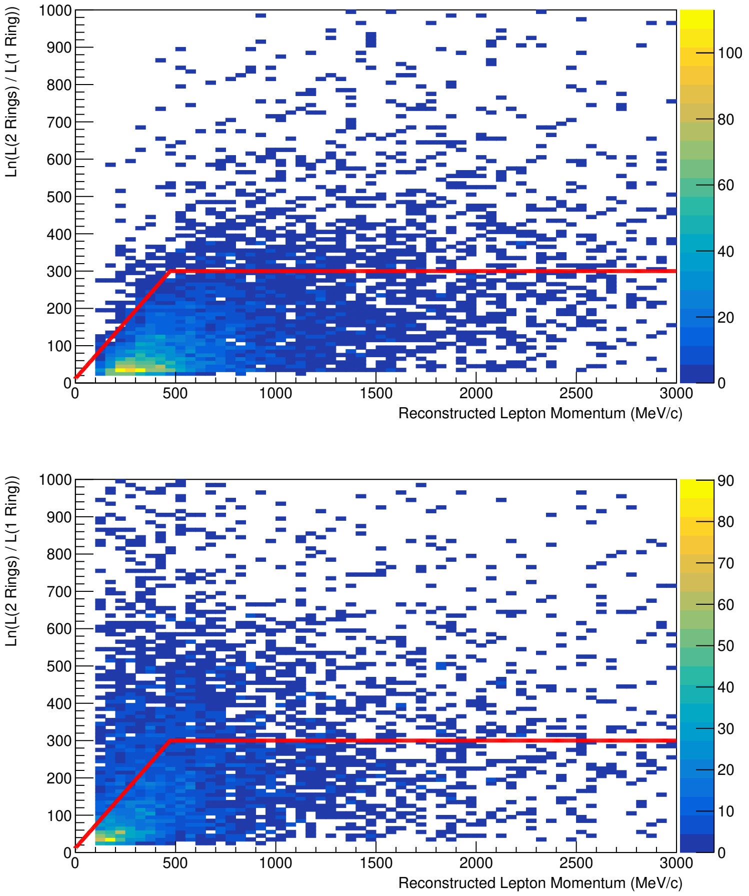

FIGURE 7.7: The distribution of events using the likelihood ratio of the most likely two ring fit to a one ring electron fit. These are plotted against the reconstructed electron momentum in the one ring fit. Signal events (top) are distributed over a wide range of reconstructed momenta and at low likelihood ratio. Background events (bottom) are composed primarily of NC events. The cut used is shown by the red line, events above this line are discarded.

8. Electron-π^0 Likelihood with Momentum

A significant NCπ^0 background is present at low reconstructed lepton momentum. Many of these backgrounds can be removed through the use of a cut acting on π^0 — electron likelihood ratio and reconstructed electron momentum.

Fig 7.8 shows the signal (top) and background (bottom) distribution of MC events in this space. Separation between signal and background is strongest at low momentum, here it is more likely that the interaction π^0 has very low momentum, hence its two decay photons will have larger angular separation and thus two non-overlapping rings will be seen in the detector.

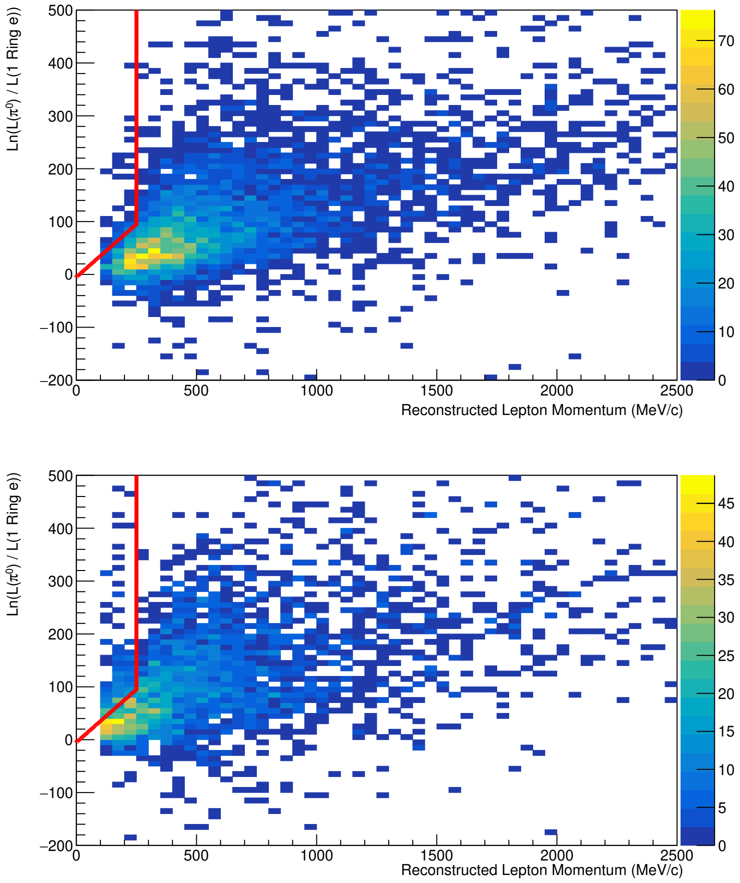

FIGURE 7.8: There is a small separation between signal events (top) and all background events (bottom) at low reconstructed electron momentum, the background distribution stretches to regions with higher reconstructed π^0 — 1 ring electron likelihood ratio, hence a cut can be applied here, reducing NCπ^0 contribution to the sample at low reconstructed energies.

7.4 Analysis Samples

7.4.1 ν_e CC0π Sample

The application of these cuts greatly reduces the background contamination of the sample. The predicted number of events broken down by interaction mode and off-axis angle is summarised in Table 7.1.

The breakdown of the sample by interaction type and neutrino flavour as a function of reconstructed neutrino energy for the 2.7-4.0° positions is shown in Fig 7.9.

	FHC		RHC	
Off-Axis Angle	1-2.7°	2.7-4°	1-2.7°	2.7-4°
$\nu_e(\bar{\nu}_e)$ CCQE	6 108	6 364	(10 890)	(6 374)
$\nu_e(\bar{\nu}_e)$ 2p2h	1 268	1 065	(2 009)	(1 072)
$\nu_e(\bar{\nu}_e)$ CC1π	1 573	1 410	(2 807)	(1 413)
$\nu_e(\bar{\nu}_e)$ CC Multi π	137	129	(213)	(35)
$\nu_e(\bar{\nu}_e)$ CC Other	28	33	(35)	(19)
$\nu_\mu(\bar{\nu}_\mu)$ CC	435	144	(152)	(72)
$\bar{\nu}_\mu(\nu_\mu)$ CC	2	4	(434)	(104)
$\bar{\nu}_e(\nu_e)$	635	816	(7 298)	(6 372)
NC 1 γ	590	209	1 387	344
NC 1 π^0	5 035	1 790	12 456	3 327
NC Other	2 661	1 159	5 437	1 824
Total $\nu_e(\bar{\nu}_e)$ CC	9 114	9 001	(15 954)	(8 913)
Total Backgrounds	9 358	4 122	27 164	11 932
Total	18 472	13 123	43 118	20 845
$\nu_e(\bar{\nu}_e)$ CC Purity	49.3%	68.6%	(37.0%)	(42.8%)
$\nu_e + \bar{\nu}_e$ CC Purity	52.8%	74.8%	53.9%	73.3%

TABLE 7.1: The number of events in the electron-like selection broken down by incident neutrino and interaction mode after applying weighting to the new detector design and an off-axis angle dependant pileup induced efficiency Fig 7.14. The exposure in FHC is 7×10^{21} POT and 20×10^{21} POT in RHC. The more on-axis positions have significantly increased neutral current background than the off-axis regions as a result of the decreased ν_e/ν_μ ($\bar{\nu}_e/\bar{\nu}_\mu$) ratio in the incident flux at the on-axis positions.

The selection is dominated by CC0π ν_e events, at low reconstructed energies the backgrounds are dominated by neutral current interactions, primarily NCπ^0 events.

NC 1γ events reconstruct with energies between 200 and 500MeV. In the fit, these events have a 100% prior uncertainty on their cross-section and are thus a major source of electron neutrino event rate uncertainty in this energy region.

Applying these same electron-like cuts to RHC MC yields the event selections shown in Fig 7.10 (right). Here the breakdown is shown integrated over all off-axis angles and includes the reduction in efficiency associated with pileup as described in §7.5.2. The more on-axis regions have higher event rates due to the greater neutrino flux, additionally these regions also have higher NC background event rate due to the greater ν_μ flux at high energy closer to the beam axis.

As a result of the reduced interaction cross-section for antineutrinos compared to neutrinos, the contribution of ν_e in the RHC 1Re sample (wrong-sign component) is considerably larger than the corresponding $\bar{\nu}_e$ contribution in the FHC 1Re sample.

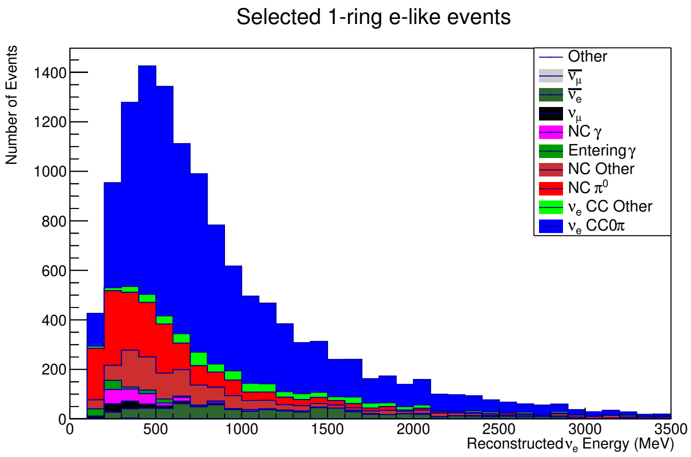

FIGURE 7.9: The breakdown of selected events as a function of reconstructed neutrino energy (assuming a CCQE interaction) for the most off-axis detector positions 2.7-4.0° with an exposure of 3×10^{21} POT. There is a significant population of NC events at low reconstructed neutrino energy, with NC γ events in particular clustered at energies around 300MeV.

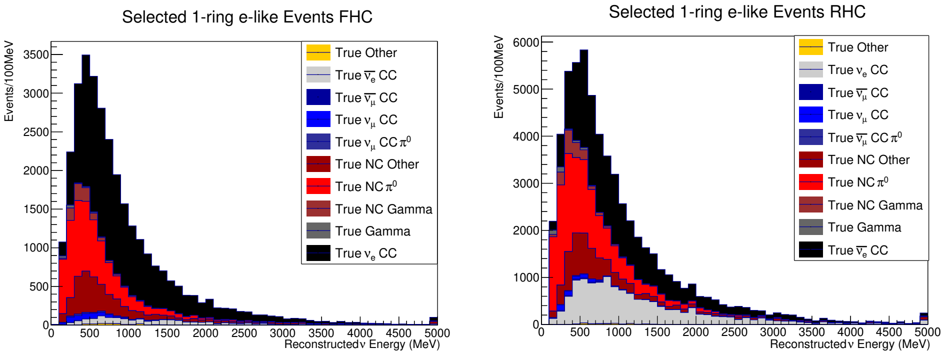

FIGURE 7.10: The breakdown of selected electron-like events by true neutrino and interaction mode. The FHC sample (left) has an exposure of 7×10^{21} POT and the RHC sample (right) has 20×10^{21} POT. There is significant wrong-sign ν_e contamination in the RHC sample not seen in the FHC sample.

7.4.2 NC Control Sample

In order to constrain the considerable NC background in the selected ν_e sample, a separate measurement of this NC contribution is desirable. IWCD makes use of a neutral current control sample in order to constrain both the incident flux as well as the cross-section parameters for NC interactions.

The selection of these events is simpler than the 1R*e* selection, due to the larger contribution of NC interactions to the total event rate. The following cuts are used:

1. The event is fully contained within the ID volume

2. The event has no reconstructed decay electrons

	FHC			RHC		
Off-Axis Angle	1-2°	2-3°	3-4°	1-2°	2-3°	3-4°
NC 1 γ	23	23	16	71	34	16
NC 1 π^0	30 452	28 063	14 085	79 624	47 207	23 449
NC Other	19 267	15 579	9 136	42 755	23 757	13 130
$\nu_\mu(\bar{\nu}_\mu)$ CC	5 104	3 803	1 699	(2 039)	(862)	(313)
$\bar{\nu}_\mu(\nu_\mu)$ CC	19	31	14	(2 669)	(2 171)	(1 307)
$\nu_e(\bar{\nu}_e)$ CC	2 401	3 388	2 681	(5 102)	(4 288)	(2 843)
$\bar{\nu}_e(\nu_e)$ CC	293	508	489	(3 929)	(4 204)	(3 173)
Total NC	49 742	43 665	23 237	122 450	70 998	36 595
Total Backgrounds	7 817	7 730	4 883	13 739	11 525	7 600
Total	57 560	51 395	28 120	136 189	82 523	44 195
NC Purity	86.4%	85.0%	82.6%	90.0%	86.0%	82.8%

TABLE 7.2: The number of events in the NC selection broken down by incident neutrino and interaction mode after applying an off-axis dependant pileup induced efficiency. The exposure in FHC is 7×10^{21} POT and 20×10^{21} POT in RHC. Due to the reduced pileup in RHC Fig 7.14. there are significantly more selected events in RHC operation at low off-axis angles compared to the FHC event rates.

3. The event is reconstructed in the fiducial volume
4. The 1Re hypothesis is preferred over a 1Rμ hypothesis
5. A two-ring hypothesis is preferred over a one-ring hypothesis
6. A π^0 fit hypothesis is preferred over a 1Re hypothesis as a function of reconstructed π^0 mass

The breakdown of the resulting selection by interaction mode is shown in Table 7.2 and Fig 7.11 (top). For comparison, the distribution of background events in the ν_e CC sample can be seen in Fig 7.11 (bottom). The NC sample shows a prominent peak in NCπ^0 events at incident neutrino energies of around 700MeV, this peak is shifted to slightly higher values for the background contribution to the ν_e sample and has relatively a longer high energy tail.

The NC sample lacks the significant NC γ contribution seen in the backgrounds of the ν_e CC sample, hence, this background does not get significantly constrained by the NC control sample.

7.4.3 ν_μ CC Control Sample

To constrain the incident flux and to get a precise measurement of both ν_μ and $\bar{\nu}_\mu$ cross-sections necessary for a precise $\sigma(\nu_e)/\sigma(\nu_\mu)$ cross-section ratio measurement,

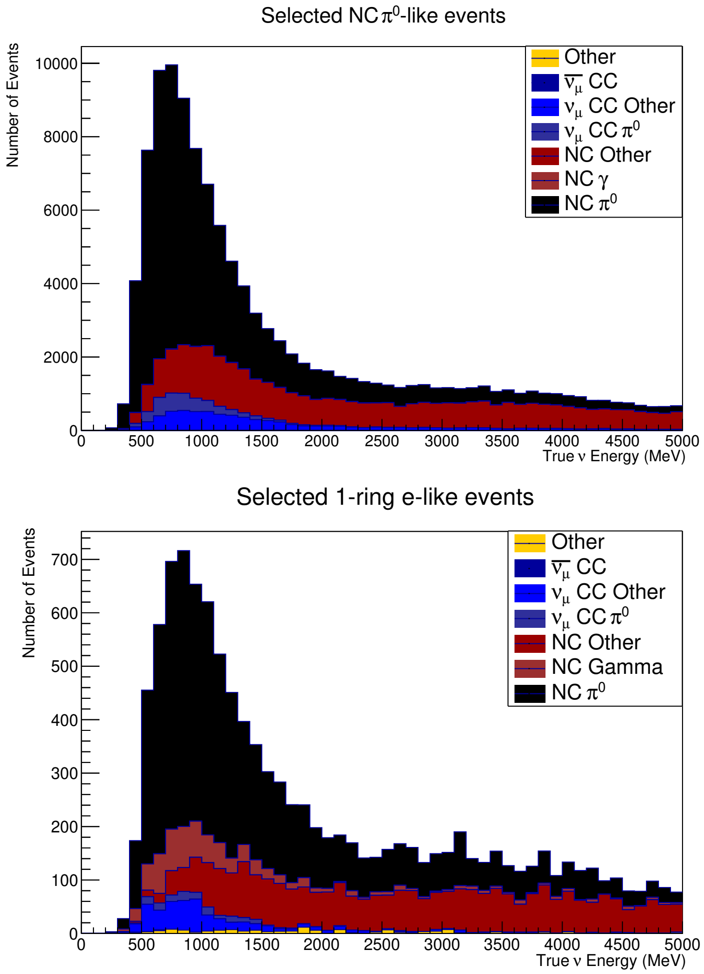

FIGURE 7.11: The NC control sample used in the fitter to constrain cross-section parameters (top). The background contribution to the ν_e CC sample (bottom) shows the energy distribution and interaction mode of all non-ν_e or $\bar{\nu}_e$ CC events that passed the electron-like selection criteria. The shape of the two distributions match closely. NC γ does not contribute significantly to the NC control sample but is a significant background to the electron-like sample.

	FHC			RHC		
Off-Axis Angle	1-2°	2-3°	3-4°	1-2°	2-3°	3-4°
$\nu_\mu(\bar{\nu}_\mu)$ CCQE	216 679	381 472	274 443	(351 168)	(384 253)	(254 718)
$\nu_\mu(\bar{\nu}_\mu)$ 2p2h	42 993	51 712	26 867	(76 511)	(58 123)	(27 156)
$\nu_\mu(\bar{\nu}_\mu)$ CC1π	55 813	49 265	15 786	(80 033)	(46 934)	(15 049)
$\nu_\mu(\bar{\nu}_\mu)$ CC Multi π	2 555	915	446	(3 432)	(752)	(197)
$\nu_\mu(\bar{\nu}_\mu)$ CC Other	597	472	285	(410)	(126)	(57)
$\bar{\nu}_\mu(\nu_\mu)$ CC	2 794	5 120	5 110	(73 449)	(77 984)	(62 570)
$\nu_e(\bar{\nu}_e)$ CC	281	439	416	(350)	(336)	(249)
$\bar{\nu}_e(\nu_e)$ CC	10	19	14	(232)	(206)	(214)
NC 1 γ	27	30	9	70	26	5
NC 1 π^0	2 697	2 112	1 046	6 387	3 295	1 701
NC Other	15 828	11 246	6042	35 656	17 022	8 876
Total $\nu_\mu(\bar{\nu}_\mu)$ CC	318 637	483 836	317 827	(511 554)	(442 376)	(297 177)
Total Backgrounds	21 637	18 966	12 637	116 144	98 869	73 615
Total	340 274	502 802	330 464	627 688	541 245	370 792
$\nu_\mu(\bar{\nu}_\mu)$ CC Purity	93.6%	96.2%	96.2%	(81.5%)	(81.8%)	(80.1%)
$\nu_\mu + \bar{\nu}_\mu$ CC Purity	94.5%	97.2%	97.7%	93.2%	96.1%	97.0%

TABLE 7.3: The number of events in the muon selection broken down by incident neutrino and interaction mode after applying an off-axis dependant pileup induced efficiency. The exposure in FHC is 7×10^{21} POT and 20×10^{21} POT in RHC. Due to the reduced pileup in RHC Fig 7.14 there are significantly more selected events in RHC operation at low off-axis angles compared to the FHC event rates. Due to the increased CC cross-section of neutrinos on nuclei over antineutrinos there is significant wrong sign ν_μ contamination in the RHC sample.

two muon-like control samples are used. These events are selected using a simple series of cuts:

1. The event is fully contained within the ID volume
2. The event has fewer than two decay electrons
3. The event is reconstructed in the fiducial volume
4. The event has reconstructed muon momentum of greater than 200MeV/c
5. The 1Rμ hypothesis is preferred over a 1Re hypothesis
6. A one-ring hypothesis is preferred over a two-ring hypothesis

Due to the high muon flavour purity of the beam at the near detector site, a high purity of muon-like events is achievable, Table 7.3 shows the breakdown of these selected events with off-axis angle. The RHC sample has a significant wrong-sign muon background caused by the high $\nu/\bar{\nu}$ cross-section ratio.

The breakdown as a function of reconstructed neutrino energy is shown in Fig 7.12. The purity of selected events is decreased at low reconstructed neutrino energy due to the significant NC event population in this region caused by low momentum-transfer events.

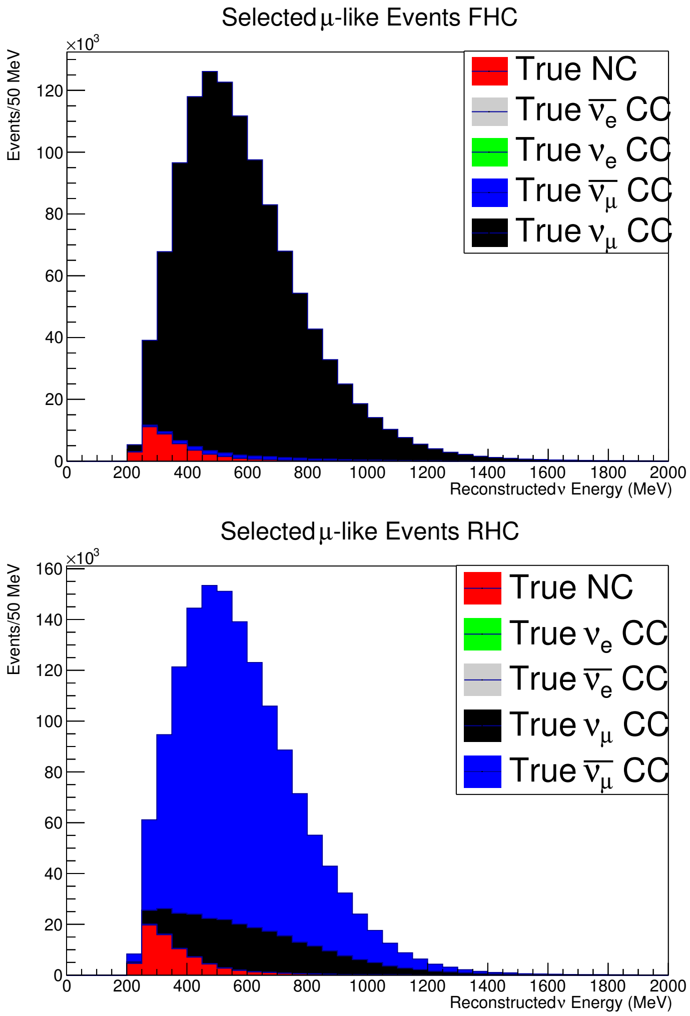

FIGURE 7.12: The one ring muon-like control samples in FHC (top) and RHC (bottom) as a function of reconstructed neutrino energy. The exposure is 7×10^{21} POT in FHC and 20×10^{21} POT in RHC.

7.5 Cross-Section Fitting

In order to extract the sensitivity of the IWCD to ν_e and $\bar{\nu}_e$ cross-section, a fit to these 1Re samples must be made. Such a fit must however consider nuisance parameters that can affect these samples and are not known precisely before the fit. The IWCD fit therefore makes use of an approach similar to that described in Chapter 6.

Each of these six samples are binned in reconstructed variables, a parameterised model of the systematic uncertainties in the experiment is then used to weight MC, this is then binned and compared to the original samples with a bin-by-bin negative log-likelihood measure. This is then augmented with a prior constraint on the parameters of this model. Unlike the MCMC approach used in MaCh3 however this likelihood is then minimised and a covariance matrix constructed about this minimum.

The ν_e and $\bar{\nu}_e$ cross-section component of the resulting covariance matrix may then be used as an estimate of the sensitivity of the IWCD to these effects.

7.5.1 Binning

The 1Rμ samples are binned in reconstructed lepton momentum, reconstructed lepton angle to the incident beam and reconstructed off-axis angle. The NCπ^0 samples are binned in reconstructed pion momentum, reconstructed π^0 invariant mass and reconstructed off-axis angle.

Due to the low event rate, the electron samples are binned in reconstructed neutrino energy and reconstructed off-axis angle only. The distribution of events in the 1Re samples in the binning used in the fit can be seen in Fig 7.13. Six off-axis bins are used for both the 1Rμ and NCπ^0 samples while the 1Re sample uses two.

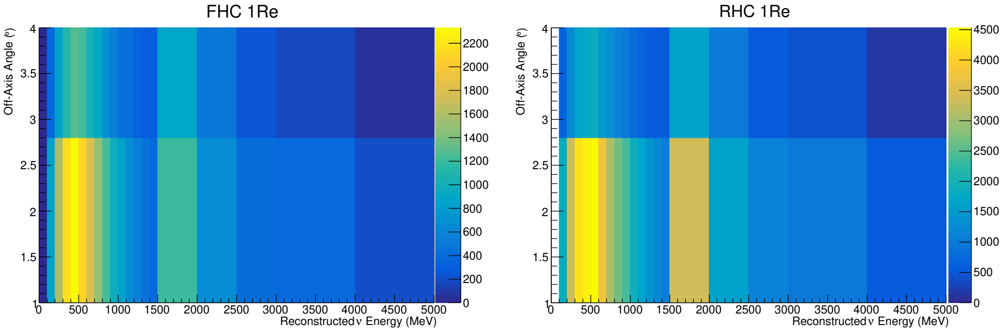

FIGURE 7.13: The one ring electron-like samples in FHC (left) and RHC (right) in the binning used in the fit. The exposure is 7×10^{21} POT in FHC and 20×10^{21} POT in RHC.

7.5.2 Systematic Model

Due to the similarities between the two experiments, the systematic model used for the IWCD fit is derived from the model used by T2K.

Flux

As with the flux systematics used in MaCh3, the IWCD fit makes use of a series of normalisation parameters controlling a specific neutrino flavour in a given horn mode and in a given true energy range. Due to the variable fluxes observed at the different off-axis positions of the IWCD, an additional freedom is required to vary the flux in the different off-axis regions.

The IWCD flux model therefore consists of a series of normalisation parameters, each controlling a single neutrino flavour in a single horn current mode in a specific energy range and range of off-axis angles. This includes five off-axis regions 1-1.86°, 1.86-2.71°, 2.71-3.14°, 3.14-3.57° and 3.57-4°.

A prior uncertainty on these parameters is then included, this is based on the T2K flux model, including the improvements in flux uncertainty from the NA61/SHINE replica target data [44][45], bringing the ν_μ flux uncertainty at the 600MeV flux peak to 5%.

Cross-Section

The HK cross-section model is heavily derived from the 2018 T2K model [90], as described in Appendix A. Parameters specific to ND280 have been disabled, as has the nucleon binding energy uncertainty. The application of these parameters is the same as that described in §5.5.2. The 2018 T2K prior constraint on these parameters is also included. In addition, a parameter is included to control the overall normalisation of entering gamma events from interactions in the OD and surrounding sand.

Pileup

Due to the large neutrino flux and large detector mass, many beam bunches will have two or more corresponding interaction events in the ID or OD. Simultaneously reconstructing two interaction events in a water Chererenkov detector is extremely challenging. It may be possible to use positional information to separate independent ID and OD events. However, as this has not yet been demonstrated, this analysis will focus on what can be measured using only bunches with a single event in the ID and OD.

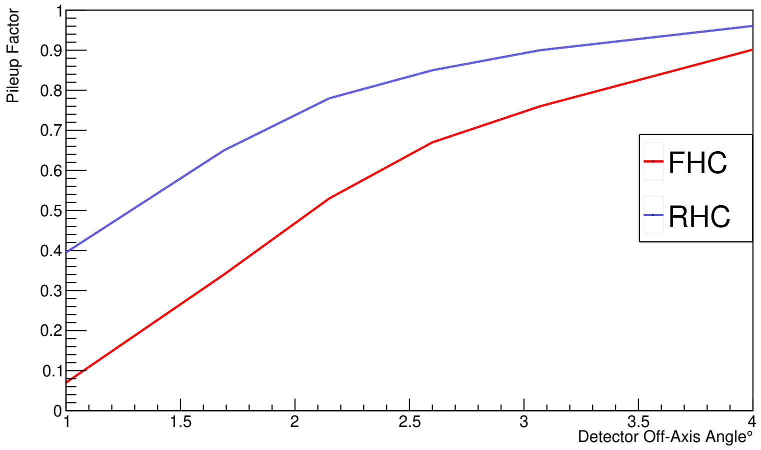

FIGURE 7.14: The proportion of events that occur within the detector and are not coincident with any other ID or OD light as a function of the off-axis position of the detector at the 750m position. At low off-axis angles the high incident flux results in only a small proportion of beam bunches having a single interaction, thus the efficiency for selecting events here is low. At large off-axis angles most bunches have no associated ID or OD events therefore a large proportion of all events that do occur are not co-incident with other events. Due to the lower cross-section of antineutrinos, the effect of pileup is reduced in RHC operation.

The probability of multiple interaction events occurring in a single beam bunch is heavily dependant on detector position; at low off-axis angles the increased neutrino flux results in a greater proportion of bunches with multiple interaction events. Conversely, at high off-axis angles the reduced neutrino flux and therefore event rate, reduces the proportion of bunches with multiple events. Fig 7.14 shows the probability for any given event to have occurred as part of a single event bunch, as a function of detector off-axis angle.

Due to the lower antineutrino cross-section, the number of events in IWCD per beam bunch is lower in RHC operation than in FHC. The probability of multiple interactions is therefore reduced, reducing the pileup induced efficiency loss.

All MC events were weighted down by their corresponding factor to give the expected event rate of true single interaction events. As the intrinsic ν_e flux proportion is greatest at high off-axis angles, the ν_e cross-section measurement is not too adversely affected by this.

The pileup efficiency for each detector position will be measured, however, some uncertainty will remain. This can be accounted for in the fitter by including a parameter to control overall event rate at each detector position. This parameter is weighted by 1− nominal pileup efficiency. This is to account for the increased uncertainty in overall event rate at more on-axis positions which has a non-linear relationship with pileup. Depending on the prior given, the parameters therefore have freedom to vary the number of events at each detector position independently.

Energy Scale

There are two detector parameters controlling energy scale in electron and muon events, these parameters act to shift the reconstructed energy of events by as much as 5% and 3% of their nominal values respectively. This is a conservative approximation of the difference in the energy reconstruction difference between the MC prediction and the final detector performance. By comparison, a single uncertainty for both event types of 2.4% is used at SK.

Electron Neutrino Cross-section Parameterisation

As the selection of ν_e events at IWCD and HK have different efficiencies and the ν_e/ν_μ CC cross-section is expected to be dependant on kinematics, a single parameter controlling the ν_e/ν_μ CC cross-section is not sufficient to accurately encompass the uncertainty on the prediction of event rate at HK.

In order to improve on this, a series of normalisation parameters are used, each parameter controls the ν_e/ν_μ CC cross-section ratio in a given range of true neutrino energy. Five parameters are used for ν_e/ν_μ and five for $\bar{\nu}_e/\bar{\nu}_\mu$, an uncorrelated 100% prior uncertainty is included on all of these parameters. This allows for a significant amount of normalisation and energy dependant freedom in these ratios.

7.6 Fit Results

In order to estimate the precision to which IWCD can measure these fit parameters over its lifetime, it is possible to perform a fit to the nominal MC. The six samples are generated taking the MC, weighting all events to correspond to a given exposure in POT, weighting to account for pileup and finally applying selection criteria to each event.

These samples may then be treated as if they were real data from IWCD and a set of nominal MC may be fitted to the selected samples. Here, to save on regenerating new MC, the same nominal MC may be used. This is then weighted in a similar manner, including a total exposure weighting and a pileup weighting. This fitting MC is however also weighted in accordance with the values of the parameters of the fit. A Hessian evaluator is then used at the best-fit point in order to obtain a post-fit covariance matrix over all parameters.

As the ν_e/ν_μ and $\bar{\nu}_e/\bar{\nu}_\mu$ parameters are considered the signal parameters in this IWCD fit and all others are nuisance parameters, only these parameters are investigated in detail here. The uncertainty on the ν_e/ν_μ and $\bar{\nu}_e/\bar{\nu}_\mu$ cross-section ratio as a function of true neutrino energy can be seen in Fig 7.15 (top). The parameters controlling the 0-300MeV energy range are only constrained to approximately the 30% level, this is due to the very low ν_e and $\bar{\nu}_e$ event rate in this energy range. The ν_e/ν_μ parameters are in general more tightly constrained than the $\bar{\nu}_e/\bar{\nu}_\mu$ parameters. This is a result of the large wrong-sign background in the RHC 1Re sample, Fig 7.10, reducing the $\bar{\nu}_e$ purity in this sample, hence limiting the available sensitivity.

The correlation between these parameters can be seen in Fig 7.15 (bottom). Due to detector energy resolution, each true energy parameter affects multiple reconstructed neutrino energy bins, hence two adjacent parameters in true energy can affect the event rate in each other's fit bins. This results in the slight anticorrelations seen between parameters with similar energy ranges.

7.7 Physics Impact

In order to assess the impact of the IWCD ν_e cross-section constraint on HK's δ_{CP} sensitivity, a separate near-detector and far-detector fit approach was used. An Asimov near-detector fit was performed to the 750m IWCD design, the resulting covariance matrix for the true energy ν_e and $\bar{\nu}_e$ parameters was then used as a prior constraint in the official HK oscillation fitting framework VALOR [122].

All other parameters used the HK 'improved systematics' constraint which aims to anticipate the improvement in systematic uncertainty that will be achieved during HK. The only IWCD constraint included at present is therefore the ν_e/ν_μ and $\bar{\nu}_e/\bar{\nu}_\mu$

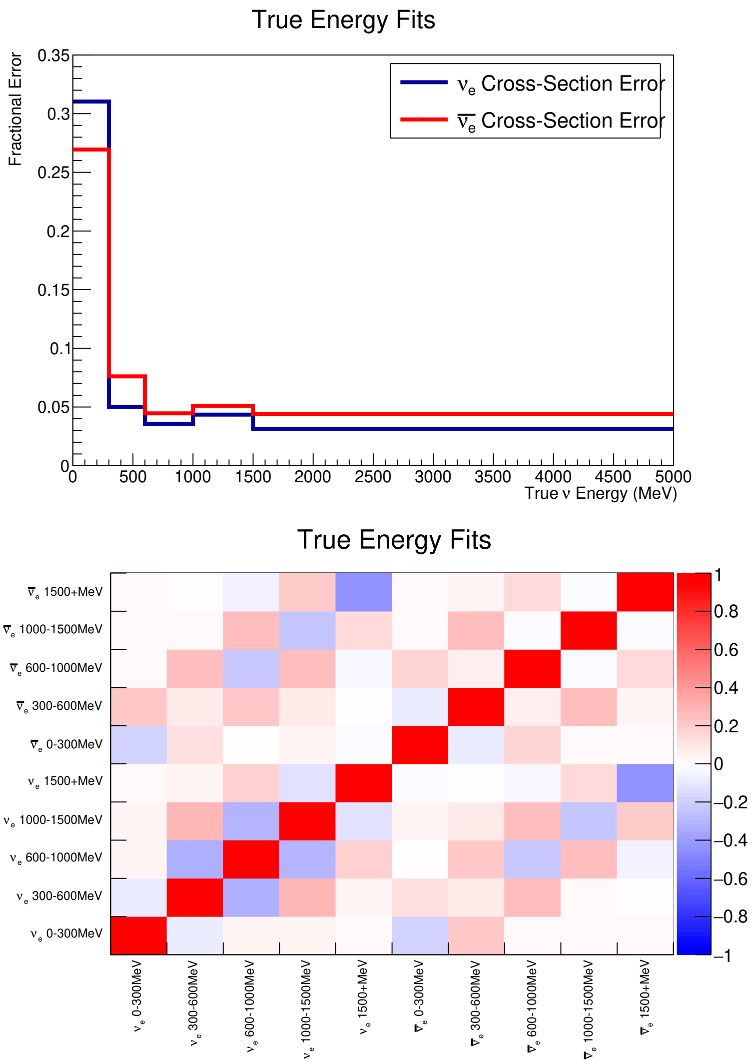

FIGURE 7.15: The post-fit error on ν_e and $\bar{\nu}_e$ cross-sections when fitting in true neutrino energy (top) and the correlations between these parameters (bottom). Due to the reduced purity in the RHC sample, the uncertainty on $\bar{\nu}_e$ is greater than on ν_e for energies greater than 300MeV.

parameters. The resulting sensitivity to exclude CP conservation is shown in Fig 7.16, the use of the IWCD constraint results in a slight improvement over the current, theory-driven uncertainty used by T2K.

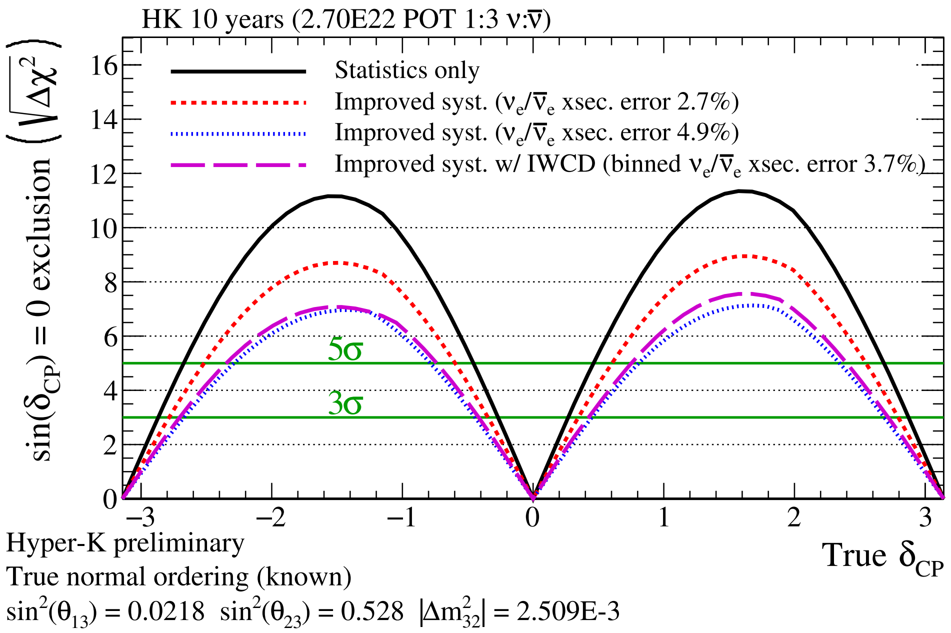

FIGURE 7.16: The ability of HK to exclude CP conservation as a function of the true value of δ_{CP}. With the energy dependant IWCD constraint. There is a small improvement over the current $\nu_e/\bar{\nu}_e$ cross-section used by T2K, this is more significant for the positive values of δ_{CP}. Additional improvement is however necessary to approach the desired sensitivity in red.

Of note is the fact that the IWCD constrained sensitivity to CP violation does not scale as would be expected from a naive calculation of the effect on the ν_e to $\bar{\nu}_e$ signal event rate ratio. The IWCD constraint, despite limiting this signal event rate ratio to 3.7% results in a sensitivity much closer to the theoretical 4.9% curve than that of the 2.7% goal. This may be a result of the energy-dependant binning adopted here giving more freedom to the fit to vary the cross-section in place of the δ_{CP} parameter. Alternatively, it may be that the fit obtains a significant portion of its CP sensitivity from the lower energy region of the ν_e appearance spectrum, below 600MeV. Hence the looser IWCD constraint in this region, Fig 7.15, may result in a more degraded CP sensitivity than would be expected from the constraint on total event rate alone. Finally the correlation between these parameters may play a role. The precise relationship between the choice of this parameterisation and CP sensitivity is a topic of further study and will need to be understood when designing the complete IWCD analysis.

While the improvement observed here is modest, any measurement of ν_e cross-section at GeV scale is extremely challenging with current ν_μ dominated pion decay beams. Despite this, the IWCD is capable of making an improvement over theory and any other experiment, with a relatively unoptimised, early stage analysis.

7.8 NCπ Cross-section Constraining Power

As discussed in Chapter 6, there is a growing interest in constraining the backgrounds to the physics sensitive samples in LBL experiments. In the case of NC1π backgrounds, this can be constrained at T2K with a far-detector NCπ^0 sample.

Such a sample does however have limits to its power, owing to the lower event rates available at a far-detector compared to a near-detector. Unlike ND280, the IWCD is capable of selecting a large number of NCπ^0 events, it is therefore in principle possible to make a direct measurement of NC1π cross-section with the high statistics available at IWCD.

The fit was therefore run with separate NC1π and CC1π parameters as in Chapter 6. The resulting constraint on the CC1π and NC1π cross-section parameters can be seen in Table 7.4 and Fig 7.17. Overall the NC1π cross-section can be constrained to the sub 5% level, this is however subject to the caveat that detector systematics are not present on these samples.

The IWCD has the potential to measure NCπ^0 event rate and cross-section precisely, this may prove useful as a cross-check between the IWCD and the HK detector. With an NCπ^0 sample implemented in both detectors, both experiencing the same effective neutrino flux, it is possible to make direct comparisons between the performance of each detector.

	CC C_5^A	NC C_5^A	CC M_{Res}^A	NC M_{Res}^A	CC $I_{1/2}$	NC $I_{1/2}$
Error	0.79%	3.1%	1.2%	3.4%	1.5%	11%

TABLE 7.4: The post-fit errors on the CC and NC pion cross-section parameters.

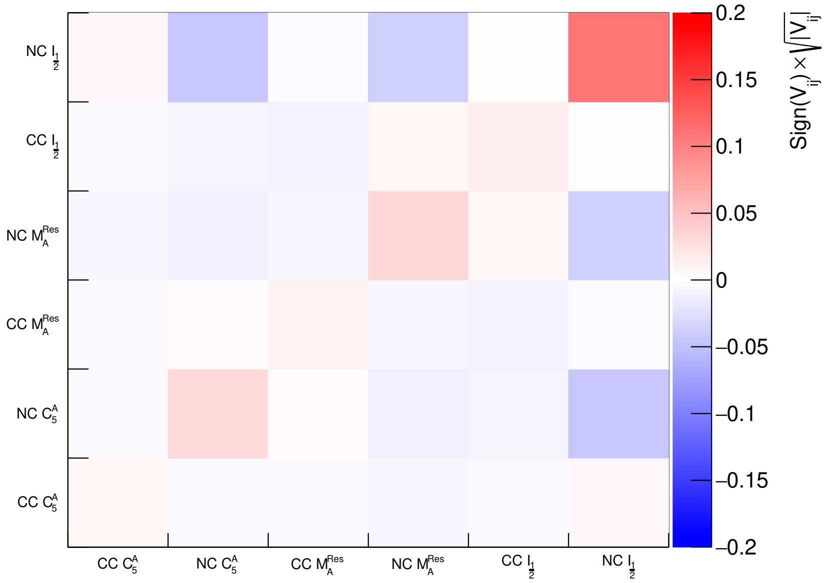

FIGURE 7.17: The post-fit constraint on the separate NC and CC pion cross-section parameters.

7.9 Outlook

The unprecedented event rates made available by HK will require tight constraints on systematic parameters in order to obtain the desired physics sensitivity. As shown here, the IWCD has the ability to constrain the most significant systematic for δ_{CP} sensitivity, the ν_e and $\bar{\nu}_e$ CC interaction cross-section.

The design of the IWCD is not yet fixed, these fits can therefore be used as a guide towards optimisation of the sensitivity to these cross-sections within the available resources and budget. Under current consideration is the detector diameter and off-axis span. The results of the fits with slight variations in these values are discussed in Appendix D. Overall sensitivity is negatively affected with changes that reduce the fiducial volume, however reduction of the off-axis span at low off-axis angles has a comparatively small effect due to the low ν_e purity closer to the beam axis.

Improvements to this constraint are possible, an improved selection of ν_e and $\bar{\nu}_e$ events is likely to have the most significant impact. Due to the small fraction of electron flavour in the beam, small changes to cut points can have a large impact on the resulting sample, the impact of which on the resulting cross-section constraint has not been well explored. Improvements in event reconstruction have great potential here, such as machine learning approaches which can offer improved $e - \mu$ and $e - \pi^0$ separation [123].

The ν_e cross-section measurement is only one part of the full analyses made possible by the IWCD, construction of new flux spectra through linear combination of the events at different off-axis angles is one of the key features of the IWCD, which will allow for improved differentiation of flux and cross-section effects. The use of a more data-driven cross-section parameterisation is of interest to HK due to the challenges posed by neutrino interaction modelling, the large number of events available at IWCD will enable such a model to be constrained directly with data from within the same experiment.

Chapter 8

Conclusions and Outlook

As the available statistics in LBL experiments increases, the impact of systematic uncertainties on the resulting oscillation sensitivity will become more apparent. This thesis has focused on improvements to the leading systematic uncertainty for both current and next-generation neutrino LBL experiments; the neutrino-nucleus interaction cross-section.

For T2K, the goal has been to provide a more expansive approach to the treatment of NC1π interactions within the oscillation analysis. This event type makes a significant contribution to the background component of the T2K oscillation-sensitive SK samples, this contribution is currently predicted via an interaction model constrained by CC1π data at ND280. Differences in cross-section for NC and CC interaction types, or differences in the kinematic regions probed at the two detectors, may result in this model prediction being incorrect for the NC1π background events at SK. Hence additional verification or replacement of this extrapolation is desirable.

In order to provide this verification, two SK NCπ^0 samples have been used, in conjunction with a significant increase in NC1π cross-section model freedom. This allows for fitting of NC1π event rate using the same interaction type and detector as the oscillation sensitive samples, along with allowing a direct comparison of the cross-section constraint provided by the ND280 CC1π and the SK NCπ^0 samples.

These samples have been included in the Bayesian Markov Chain Monte Carlo fitter, MaCh3. This provides simultaneous fitting of the near and far-detector data without the assumption of a Gaussian constraint at ND280. Due to the detector systematic uncertainties and low purity of the NC component in the ND280 samples, this ND280 NC1π cross-section constraint is not known to be Gaussian a-priori. As this analysis marks the first time a far-detector sample has been included with the intention of constraining an interaction cross-section, the ability of MaCh3 to separately probe the constraint provided by the ND280 and SK samples is valuable.

The resulting fit shows a NC1π constraint on event rate half as strong as the corresponding CC1π constraint, with a slight preference towards higher NC1π event rate than the CC model. Due to the small difference between the NC and CC cross-sections, the effect on recovered oscillation parameters is minimal. This should however give confidence in the robustness of the current pion cross-section constraint, given the general agreement achieved from differing final states in two different detectors.

In the future, we should look to leverage the specific advantages of the NCπ^0 sample to constrain more theoretically motivated differences between the NC and CC pion cross-section, such as the impact of the different intermediate resonant mass distributions present for these events. The purity of the NCπ^0 selection can be improved through the use of PID requirements on the pion decay rings that were omitted in this analysis. With the resulting increase in purity, such a sample could then be binned in a variable with more sensitivity to the expected kinematic differences between models, such as reconstructed π^0 momentum. A momentum binning is of particular interest, as this would be the only T2K sample directly binned in pion kinematics, the spectra of which current generators struggle to recreate [101].

Finally, with a data constrained cross-section for NC1π events, it may be possible to include signal ν_e CC events from π^0-like regions that were cut from the existing 1Re samples. With the current statistics limited ν_e and $\bar{\nu}_e$ appearance channels, such an increase in signal statistics of up to 6% should provide additional CP sensitivity for a given beam period.

Further in the future, HK will depend on precise determination of systematic uncertainties to achieve its sensitivity goals, the IWCD aims to provide constraint for a number of these. This work has investigated the potential of replacing the existing, theoretically-motivated uncertainty on the ν_e and $\bar{\nu}_e$ CC cross-sections, with a measured value from the IWCD detector. This cross-section uncertainty is expected to be the leading systematic limiting HK's CP violation sensitivity. In order to assess the ability of the IWCD to constrain this cross-section, a series of MC selections have been made and included in a near-detector fitting framework. This includes one-ring muon, electron, and two-ring π^0 samples, with both neutrino and antineutrino samples.

The resulting fits show that the IWCD is capable of measuring these ν_e and $\bar{\nu}_e$ CC cross-sections to a precision equal to, or greater than, existing theoretical uncertainties, furthermore, the fits demonstrate the ability for this constraint to be provided as a function of kinematics such as incident neutrino energy. The resulting IWCD ν_e and $\bar{\nu}_e$ cross-section constraint has been included in a HK oscillation fit, and yields an improvement in CP violation sensitivity over the theoretical constraint.

The IWCD analysis will require a number of improvements before the start of HK data collection, one such improvement will be the expansion of the existing cross-section model, for this, the ongoing cross-section model development within T2K will be useful. Due to the higher statistics available at HK, additional HK specific parameters will also be required. The current IWCD analysis does not include the detector systematic uncertainty on event selection, given the large number of events in the IWCD samples, such systematics may have a strong interplay with the attainable physics sensitivity and should be properly considered. Finally, robustness studies into the convergence of these fits will be needed, given the complexity of the model being fit and the dominance of the data term in the likelihood, multiple local minima may be possible, and a strategy to identify the global minimum will be needed.

In the future, the two analyses discussed here may be combinable. An NCπ^0 sample in the HK far-detector could be compared to the IWCD NCπ^0 sample from the 2.5° position, such samples would represent the same interaction mode in the same effective flux but in two different detectors at different baselines to the beam production point. These would allow for comparison of the reconstruction properties of the detectors, or potentially be used in a sterile neutrino search, with the IWCD providing a prediction for NCπ^0 event rate at the far detector, which could then be compared to the HK NCπ^0 sample to identify a deficit due to sterile oscillation.

Overall, LBL neutrino oscillation experiments have yielded excellent measurements of neutrino oscillation parameters with a limited number of interaction events.

To date, these low statistics have been the dominant uncertainty on the recovered oscillation parameters, however, as additional data is collected during T2K-II and with the data available at HK, systematic uncertainties currently considered unimportant to the physics results will become limiting. It is therefore essential that these uncertainties be properly considered and mitigation against their effects be made wherever possible, either through better use of existing data or with the construction of new detectors.

Bibliography

[1] J. Chadwick. "Intensitätsverteilung im magnetischen Spektrum der β-Strahlen von Radium B+C". In: *Verh. d Phys. Ges.* (16 1914), pp. 383–391.

[2] Wolfgang Pauli. "Dear radioactive ladies and gentlemen". Typed copy. URL: http://cds.cern.ch/record/83282.

[3] Fred L. Wilson. "Fermi's Theory of Beta Decay". In: *American Journal of Physics* 36.12 (1968), pp. 1150–1160. DOI: 10.1119/1.1974382. eprint: https://doi.org/10.1119/1.1974382. URL: https://doi.org/10.1119/1.1974382.

[4] G. Gamow and E. Teller. "Selection Rules for the β-Disintegration". In: *Phys. Rev.* 49 (12 June 1936), pp. 895–899. DOI: 10.1103/PhysRev.49.895. URL: https://link.aps.org/doi/10.1103/PhysRev.49.895.

[5] Frederick Reines and Clyde L. Cowan. "The neutrino". In: *Nature* 178 (1956), pp. 446–449. DOI: 10.1038/178446a0.

[6] L. M. Langer and R. J. D. Moffat. "The Beta-Spectrum of Tritium and the Mass of the Neutrino". In: *Phys. Rev.* 88 (4 Nov. 1952), pp. 689–694. DOI: 10.1103/PhysRev.88.689. URL: https://link.aps.org/doi/10.1103/PhysRev.88.689.

[7] Seth H. Neddermeyer and Carl D. Anderson. "Note on the Nature of Cosmic-Ray Particles". In: *Phys. Rev.* 51 (10 May 1937), pp. 884–886. DOI: 10.1103/PhysRev.51.884. URL: https://link.aps.org/doi/10.1103/PhysRev.51.884.

[8] G. Danby et al. "Observation of High-Energy Neutrino Reactions and the Existence of Two Kinds of Neutrinos". In: *Phys. Rev. Lett.* 9 (1 July 1962), pp. 36–44. DOI: 10.1103/PhysRevLett.9.36. URL: https://link.aps.org/doi/10.1103/PhysRevLett.9.36.

[9] Martin L. Perl et al. “Evidence for Anomalous Lepton Production in e+ - e- Annihilation”. In: *Phys. Rev. Lett.* 35 (1975), pp. 1489–1492. DOI: `10.1103/PhysRevLett.35.1489`.

[10] G. J. Feldman et al. “Inclusive Anomalous Muon Production in e^+e^- Annihilation”. In: *Phys. Rev. Lett.* 38 (3 Jan. 1977), pp. 117–120. DOI: `10.1103/PhysRevLett.38.117`. URL: `https://link.aps.org/doi/10.1103/PhysRevLett.38.117`.

[11] J. Burmester et al. “Anomalous Muon Production in e+ e- Annihilation as Evidence for Heavy Leptons”. In: *Phys. Lett. B* 68 (1977), p. 297. DOI: `10.1016/0370-2693(77)90292-1`.

[12] K. Kodama et al. “Observation of tau neutrino interactions”. In: *Physics Letters B* 504.3 (Apr. 2001), pp. 218–224. DOI: `10.1016/s0370-2693(01)00307-0`. URL: `https://doi.org/10.1016%2Fs0370-2693%2801%2900307-0`.

[13] “Precision electroweak measurements on the Z resonance”. In: *Physics Reports* 427.5 (2006), pp. 257–454. ISSN: 0370-1573. DOI: `https://doi.org/10.1016/j.physrep.2005.12.006`. URL: `https://www.sciencedirect.com/science/article/pii/S0370157305005119`.

[14] Carsten Burgard. *Standard model of physics*. Dec. 2016. URL: `https://texample.net/tikz/examples/model-physics/`.

[15] P.A. Zyla et al. “Review of Particle Physics”. In: *PTEP* 2020.8 (2020), p. 083C01. DOI: `10.1093/ptep/ptaa104`.

[16] M. Aker et al. “Direct neutrino-mass measurement with sub-electronvolt sensitivity”. In: *Nature Phys.* 18.2 (2022), pp. 160–166. DOI: `10.1038/s41567-021-01463-1`. arXiv: `2105.08533 [hep-ex]`.

[17] Carlo Giunti and Kim Chung Wook. *Fundamentals of Neutrino Physics and Astrophysics*. Oxford: Oxford Univ., 2007. DOI: `10.1093/acprof:oso/9780198508717.001.0001`. URL: `https://cds.cern.ch/record/1053706`.

[18] Ettore Majorana. “Teoria simmetrica dell’elettrone e del positrone”. In: *Nuovo Cim.* 14 (1937), pp. 171–184. DOI: `10.1007/BF02961314`.

[19] D. Q. Adams et al. “Search for Majorana neutrinos exploiting millikelvin cryogenics with CUORE”. In: *Nature* 604.7904 (2022), pp. 53–58. DOI: `10.1038/s41586-022-04497-4`. arXiv: `2104.06906 [nucl-ex]`.

[20] S. Abe et al. “First Search for the Majorana Nature of Neutrinos in the Inverted Mass Ordering Region with KamLAND-Zen”. In: (Mar. 2022). arXiv: `2203.02139 [hep-ex]`.

[21] J. Schechter and J. W. F. Valle. “Neutrino masses in SU(2) $\otimes$ U(1) theories”. In: *Phys. Rev. D* 22 (9 Nov. 1980), pp. 2227–2235. DOI: `10.1103/PhysRevD.22.2227`. URL: `https://link.aps.org/doi/10.1103/PhysRevD.22.2227`.

[22] Raymond Davis, Don S. Harmer, and Kenneth C. Hoffman. “Search for Neutrinos from the Sun”. In: *Phys. Rev. Lett.* 20 (21 May 1968), pp. 1205–1209. DOI: `10.1103/PhysRevLett.20.1205`. URL: `https://link.aps.org/doi/10.1103/PhysRevLett.20.1205`.

[23] J. N. Bahcall et al. “Solar neutrino flux”. In: *Astrophys. J.* 137 (1963), pp. 344–346. DOI: `10.1086/147513`.

[24] J. N. Abdurashitov et at. “Measurement of the Solar Neutrino Capture Rate by SAGE and Implications for Neutrino Oscillations in Vacuum”. In: *Physical Review Letters* 83.23 (Dec. 1999), pp. 4686–4689. DOI: `10.1103/physrevlett.83.4686`. URL: `https://doi.org/10.1103\%2Fphysrevlett.83.4686`.

[25] W. Hampel et al. “GALLEX solar neutrino observations: Results for GALLEX IV”. In: *Phys. Lett. B* 447 (1999), pp. 127–133. DOI: `10.1016/S0370-2693(98)01579-2`.

[26] Y. Fukuda et al. “Solar neutrino data covering solar cycle 22”. In: *Phys. Rev. Lett.* 77 (1996), pp. 1683–1686. DOI: `10.1103/PhysRevLett.77.1683`.

[27] Y. et al. Fukuda. “Evidence for Oscillation of Atmospheric Neutrinos”. In: *Phys. Rev. Lett.* 81 (8 Aug. 1998), pp. 1562–1567. DOI: `10.1103/PhysRevLett.81.1562`. URL: `https://link.aps.org/doi/10.1103/PhysRevLett.81.1562`.

[28] Q. R. et al. Ahmad. “Measurement of the rate of $\nu_e + d \to p + p + e^-$ interactions produced by ^{8}B solar neutrinos at the Sudbury Neutrino Observatory”. In: *Phys. Rev. Lett.* 87 (2001), p. 071301. DOI: 10.1103/PhysRevLett.87.071301. arXiv: nucl-ex/0106015.

[29] Q. R. Ahmad et al. “Direct evidence for neutrino flavor transformation from neutral current interactions in the Sudbury Neutrino Observatory”. In: *Phys. Rev. Lett.* 89 (2002), p. 011301. DOI: 10.1103/PhysRevLett.89.011301. arXiv: nucl-ex/0204008.

[30] Ling-Lie Chau and Wai-Yee Keung. “Comments on the Parametrization of the Kobayashi-Maskawa Matrix”. In: *Phys. Rev. Lett.* 53 (19 Nov. 1984), pp. 1802–1805. DOI: 10.1103/PhysRevLett.53.1802. URL: https://link.aps.org/doi/10.1103/PhysRevLett.53.1802.

[31] Ivan Esteban et al. “The fate of hints: updated global analysis of three-flavor neutrino oscillations”. In: *Journal of High Energy Physics* 2020.9 (Sept. 2020). DOI: 10.1007/jhep09(2020)178. URL: https://doi.org/10.1007%2Fjhep09%282020%29178.

[32] *NuFIT 5.1*. 2021. URL: http://www.nu-fit.org/.

[33] Boris Kayser. *Neutrino Oscillation Phenomenology*. 2008. DOI: 10.48550/ARXIV.0804.1121. URL: https://arxiv.org/abs/0804.1121.

[34] Claudio Giganti, Stéphane Lavignac, and Marco Zito. “Neutrino oscillations: The rise of the PMNS paradigm”. In: *Prog. Part. Nucl. Phys.* 98 (2018), pp. 1–54. DOI: 10.1016/j.ppnp.2017.10.001. arXiv: 1710.00715 [hep-ex].

[35] The NOvA Collaboration. *An Improved Measurement of Neutrino Oscillation Parameters by the NOvA Experiment*. 2021. arXiv: 2108.08219v1 [[hep-ex]].

[36] Naotoshi Okamura. “Effect of the Smaller Mass-Squared Difference for the Long Base-Line Neutrino Experiments”. In: *Progress of Theoretical Physics* 114.5 (Nov. 2005), pp. 1045–1056. ISSN: 0033-068X. DOI: 10.1143/PTP.114.1045. eprint: https://academic.oup.com/ptp/article-pdf/114/5/1045/5259974/114-5-1045.pdf. URL: https://doi.org/10.1143/PTP.114.1045.

[37] D. Adey et al. "Measurement of the Electron Antineutrino Oscillation with 1958 Days of Operation at Daya Bay". In: *Phys. Rev. Lett.* 121.24 (2018), p. 241805. DOI: `10.1103/PhysRevLett.121.241805`. arXiv: `1809.02261 [hep-ex]`.

[38] C. Andreopoulos et al. *T2K Neutrino and Anti-Neutrino 3-Flavour Joint Analysis of Run 1-10 (1.4938 × 1021-POT nu 1.6346 × 1021-POT nubar) data sets*. 2020. URL: `https://t2k.org/docs/technotes/394`.

[39] Yoshinari Hayato and Luke Pickering. "The NEUT neutrino interaction simulation program library". In: *The European Physical Journal Special Topics* 230.24 (Oct. 2021), pp. 4469–4481. DOI: `10.1140/epjs/s11734-021-00287-7`. URL: `https://doi.org/10.1140%2Fepjs%2Fs11734-021-00287-7`.

[40] Dieter Rein and Lalit M. Sehgal. "Neutrino Excitation of Baryon Resonances and Single Pion Production". In: *Annals Phys.* 133 (1981), pp. 79–153. DOI: `10.1016/0003-4916(81)90242-6`.

[41] K. Abe et al. (The T2K experiment). "The T2K experiment". In: *Nuclear Instruments and Methods in Physics Research Section A: Accelerators, Spectrometers, Detectors and Associated Equipment* 659.1 (2011), pp. 106–135. ISSN: 0168-9002. DOI: `https://doi.org/10.1016/j.nima.2011.06.067`. URL: `https://www.sciencedirect.com/science/article/pii/S0168900211011910`.

[42] K. Matsuoka et al. "Design and performance of the muon monitor for the T2K neutrino oscillation experiment". In: *Nuclear Instruments and Methods in Physics Research Section A: Accelerators, Spectrometers, Detectors and Associated Equipment* 624.3 (2010), pp. 591–600. ISSN: 0168-9002. DOI: `https://doi.org/10.1016/j.nima.2010.09.074`. URL: `https://www.sciencedirect.com/science/article/pii/S016890021002098X`.

[43] K. et al. Suzuki. "Measurement of the muon beam direction and muon flux for the T2K neutrino experiment". In: *Progress of Theoretical and Experimental Physics* 2015.5 (May 2015). 053C01. ISSN: 2050-3911. DOI: `10.1093/ptep/ptv054`. eprint: `https://academic.oup.com/ptep/article-pdf/2015/5/053C01/7696856/ptv054.pdf`. URL: `https://doi.org/10.1093/ptep/ptv054`.

[44] N. et al. Abgrall. "Measurements of π ˆ± differential yields from the surface of the T2K replica target for incoming 31 GeV/ c protons with the NA61/SHINE spectrometer at the CERN SPS". In: *European Physical Journal C* 76.11, 617 (Nov. 2016), p. 617. DOI: 10.1140/epjc/s10052-016-4440-y.

[45] T. Vladisavljevic et al. *Flux Prediction and Uncertainty with NA61/sHINE 2009 Replica-Target Data (Update for runs 1-10)*. 2020. URL: https://t2k.org/docs/technotes/354.

[46] K. Abe et al. "T2K neutrino flux prediction". In: *Physical Review D* 87.1 (Jan. 2013). ISSN: 1550-2368. DOI: 10.1103/physrevd.87.012001. URL: http://dx.doi.org/10.1103/PhysRevD.87.012001.

[47] T T Böhlen et al. "The FLUKA Code: Developments and Challenges for High Energy and Medical Applications". In: *Nucl. Data Sheets* 120 (2014), 211–214. 4 p. DOI: 10.1016/j.nds.2014.07.049. URL: https://cds.cern.ch/record/2109973.

[48] René Brun et al. *GEANT: Detector Description and Simulation Tool; Oct 1994*. CERN Program Library. Long Writeup W5013. Geneva: CERN, 1993. DOI: 10.17181/CERN.MUHF.DMJ1. URL: https://cds.cern.ch/record/1082634.

[49] C. Zeitnitz and T.A. Gabriel. "The GEANT-CALOR interface and benchmark calculations of ZEUS test calorimeters". In: *Nuclear Instruments and Methods in Physics Research Section A: Accelerators, Spectrometers, Detectors and Associated Equipment* 349.1 (1994), pp. 106–111. ISSN: 0168-9002. DOI: https://doi.org/10.1016/0168-9002(94)90613-0. URL: https://www.sciencedirect.com/science/article/pii/0168900294906130.

[50] A. Blondel et al. "The WAGASCI experiment at JPARC to measure neutrino cross-sections on water". In: *PoS* EPS-HEP2015 (2015), p. 292. DOI: 10.22323/1.234.0292.

[51] M. Antonova et al. "Baby MIND: A Magnetised Spectrometer for the WAGASCI Experiment". In: *Prospects in Neutrino Physics*. Apr. 2017. arXiv: 1704.08079 [physics.ins-det].

[52] A. Hiramoto et al. “First measurement of $\overline{\nu}_\mu$ and ν_μ charged-current inclusive interactions on water using a nuclear emulsion detector”. In: *Phys. Rev. D* 102.7 (2020), p. 072006. DOI: `10.1103/PhysRevD.102.072006`. arXiv: `2008.03895 [hep-ex]`.

[53] K. Abe et al. “Measurements of the T2K neutrino beam properties using the INGRID on-axis near detector”. In: *Nuclear Instruments and Methods in Physics Research Section A: Accelerators, Spectrometers, Detectors and Associated Equipment* 694 (Dec. 2012), 211–223. ISSN: 0168-9002. DOI: `10.1016/j.nima.2012.03.023`. URL: `http://dx.doi.org/10.1016/j.nima.2012.03.023`.

[54] Tatsuya Kikawa et al. *INGRID neutrino beam measurements with new analysis method*. 2013. URL: `https://t2k.org/docs/technotes/132`.

[55] Tatsuya Hayashino et al. *INGRID measurement in the anti-neutrino beam mode*. 2016. URL: `https://t2k.org/docs/technotes/226`.

[56] P.-A. et al Amaudruz. “The T2K fine-grained detectors”. In: *Nuclear Instruments and Methods in Physics Research Section A: Accelerators, Spectrometers, Detectors and Associated Equipment* 696 (Dec. 2012), 1–31. ISSN: 0168-9002. DOI: `10.1016/j.nima.2012.08.020`. URL: `http://dx.doi.org/10.1016/j.nima.2012.08.020`.

[57] K. Abe et al. “Characterization of nuclear effects in muon-neutrino scattering on hydrocarbon with a measurement of final-state kinematics and correlations in charged-current pionless interactions at T2K”. In: *Physical Review D* 98.3 (Aug. 2018). DOI: `10.1103/physrevd.98.032003`. URL: `https://doi.org/10.1103%2Fphysrevd.98.032003`.

[58] N. Abgrall et al. “Time Projection Chambers for the T2K Near Detectors”. In: *Nucl. Instrum. Meth. A* 637 (2011), pp. 25–46. DOI: `10.1016/j.nima.2011.02.036`. arXiv: `1012.0865 [physics.ins-det]`.

[59] Y. Giomataris et al. “MICROMEGAS: a high-granularity position-sensitive gaseous detector for high particle-flux environments”. In: *Nuclear Instruments and Methods in Physics Research Section A: Accelerators, Spectrometers, Detectors and Associated Equipment* 376.1 (1996), pp. 29–35. ISSN: 0168-9002. DOI:

https://doi.org/10.1016/0168-9002(96)00175-1. URL: https://www.sciencedirect.com/science/article/pii/0168900296001751.

[60] I. Giomataris et al. “Micromegas in a bulk”. In: *Nuclear Instruments and Methods in Physics Research Section A: Accelerators, Spectrometers, Detectors and Associated Equipment* 560.2 (May 2006), 405–408. ISSN: 0168-9002. DOI: 10.1016/j.nima.2005.12.222. URL: http://dx.doi.org/10.1016/j.nima.2005.12.222.

[61] S. Assylbekov et al. “The T2K ND280 Off-Axis Pi-Zero Detector”. In: *Nucl. Instrum. Meth. A* 686 (2012), pp. 48–63. DOI: 10.1016/j.nima.2012.05.028. arXiv: 1111.5030 [physics.ins-det].

[62] S. Fukuda et al. “The Super-Kamiokande detector”. In: *Nuclear Instruments and Methods in Physics Research Section A: Accelerators, Spectrometers, Detectors and Associated Equipment* 501.2 (2003), pp. 418–462. ISSN: 0168-9002. DOI: https://doi.org/10.1016/S0168-9002(03)00425-X. URL: https://www.sciencedirect.com/science/article/pii/S016890020300425X.

[63] S. Tobayama. *An analysis of the oscillation of atmospheric neutrinos*. 2016. URL: https://open.library.ubc.ca/soa/cIRcle/collections/ubctheses/24/items/1.0340615.

[64] Andrew D. Missert (on behalf of the T2K experiment). “Improving the T2K Oscillation Analysis With fiTQun: A New Maximum-Likelihood Event Reconstruction for Super-Kamiokande”. In: *Journal of Physics: Conference Series* 888 (Sept. 2017), p. 012066. DOI: 10.1088/1742-6596/888/1/012066. URL: https://doi.org/10.1088/1742-6596/888/1/012066.

[65] A. et al. Takenaka. “Search for proton decay via $p \to e + \pi^0$ and $p \to \mu + \pi^0$ with an enlarged fiducial volume in Super-Kamiokande I-IV”. In: *Physical Review D* 102.11 (Dec. 2020). ISSN: 2470-0029. DOI: 10.1103/physrevd.102.112011. URL: http://dx.doi.org/10.1103/PhysRevD.102.112011.

[66] Hyper-Kamiokande Proto-Collaboration. *Hyper-Kamiokande Design Report*. 2018. arXiv: 1805.04163 [physics.ins-det].

[67] K. Abe et al. “J-PARC Neutrino Beamline Upgrade Technical Design Report”. In: (Aug. 2019). arXiv: `1908.05141 [physics.ins-det]`.

[68] K. Abe et al. *T2K ND280 Upgrade – Technical Design Report*. 2020. arXiv: `1901.03750 [physics.ins-det]`.

[69] P. et al. Abratenko. “Measurement of the flux-averaged inclusive charged-current electron neutrino and antineutrino cross section on argon using the NuMI beam and the MicroBooNE detector”. In: *Phys. Rev. D* 104 (5 Sept. 2021), p. 052002. DOI: `10.1103/PhysRevD.104.052002`. URL: `https://link.aps.org/doi/10.1103/PhysRevD.104.052002`.

[70] J. et al. Wolcott. “Measurement of Electron Neutrino Quasielastic and Quasielasticlike Scattering on Hydrocarbon at $<E_\nu> = 3.6$ GeV”. In: *Phys. Rev. Lett.* 116 (8 Feb. 2016), p. 081802. DOI: `10.1103/PhysRevLett.116.081802`. URL: `https://link.aps.org/doi/10.1103/PhysRevLett.116.081802`.

[71] J. Blietschau et al. “Total cross sections for ve and ve interactions and search for neutrino oscillations and decay”. In: *Nuclear Physics B* 133.2 (1978), pp. 205–219. ISSN: 0550-3213. DOI: `https://doi.org/10.1016/0550-3213(78)90299-7`. URL: `https://www.sciencedirect.com/science/article/pii/0550321378902997`.

[72] K. Abe et al. “Measurement of the charged-current electron (anti-)neutrino inclusive cross-sections at the T2K off-axis near detector ND280”. In: *Journal of High Energy Physics* 2020.10 (Oct. 2020). DOI: `10.1007/jhep10(2020)114`. URL: `https://doi.org/10.1007%2Fjhep10%282020%29114`.

[73] E. Atkin et al. *Measuring PMNS parameters in a joint ND280-SK analysis using MCMC*. 2020. URL: `https://t2k.org/docs/technotes/393`.

[74] S. Bhadra et al. *Letter of Intent to Construct a nuPRISM Detector in the J-PARC Neutrino Beamline*. 2014. arXiv: `1412.3086 [physics.ins-det]`.

[75] Yoshitaka Itow. “Construction status and prospects of the Hyper-Kamiokande project”. In: *PoS* ICRC2021 (2021), p. 1192. DOI: `10.22323/1.395.1192`.

[76] Gianfranca De Rosa. “A multi-PMT photodetector system for the Hyper-Kamiokande experiment”. In: *PoS* ICHEP2020 (2021), p. 831. DOI: `10.22323/1.390.0831`.

[77] Stephane Zsoldos. “The Outer Detector (OD) system for Hyper-Kamiokande experiment”. In: *PoS* ICHEP2020 (2021), p. 886. DOI: `10.22323/1.390.0886`.

[78] A. Gelman et al. *Bayesian Data Analysis (3rd ed.)* Chapman and Hall, 2013. DOI: `10.1201/b16018`.

[79] K. Duffy. *Measurement of the neutrino oscillation parameters sin2theta23, Delta m232, sin2theta13, and delta CP in neutrino and antineutrino oscillation at T2K*. 2016. URL: `https://t2k.org/docs/thesis/078`.

[80] Spiegelhalter D. (Eds.). Gilks W.R. Richardson S. *Markov Chain Monte Carlo in Practice*. 1995. ISBN: 9780412055515.

[81] W. K. Hastings. “Monte Carlo sampling methods using Markov chains and their applications”. In: *Biometrika* 57.1 (Apr. 1970), pp. 97–109. ISSN: 0006-3444. DOI: `10.1093/biomet/57.1.97`. eprint: `https://academic.oup.com/biomet/article-pdf/57/1/97/23940249/57-1-97.pdf`. URL: `https://doi.org/10.1093/biomet/57.1.97`.

[82] Josef Dick, Frances Y Kuo, and Ian H Sloan. “High-dimensional integration: the quasi-Monte Carlo way”. In: *Acta Numerica* 22 (2013), pp. 133–288.

[83] Sergey Dolgov et al. “Approximation and sampling of multivariate probability distributions in the tensor train decomposition”. In: *Statistics and Computing* 30 (May 2020). DOI: `10.1007/s11222-019-09910-z`.

[84] Nicholas Metropolis et al. “Equation of state calculations by fast computing machines”. In: *The journal of chemical physics* 21.6 (1953), pp. 1087–1092.

[85] Robert E. Kass et al. “Markov Chain Monte Carlo in Practice: A Roundtable Discussion”. In: *The American Statistician* 52.2 (1998), pp. 93–100. ISSN: 00031305. URL: `http://www.jstor.org/stable/2685466` (visited on 05/12/2022).

[86] K. Abe et al. “Improved constraints on neutrino mixing from the T2K experiment with 3.13e21 protons on target”. In: *Physical Review D* 103.11 (June

2021). DOI: 10.1103/physrevd.103.112008. URL: https://doi.org/10.1103%2Fphysrevd.103.112008.

[87] L. Munteanu et al. *Constraining the Flux and Cross Section Models with Data from ND280 using FGD1 and FGD2 for the 2020 Oscillation Analysis*. (Under internal review). 2022. URL: https://t2k.org/docs/technotes/395.

[88] P. Bartet et al. *NuMu CC event selections in the ND280 tracker using Run 2+3+4 data*. 2015. URL: https://t2k.org/docs/technotes/212.

[89] X. Li and M. Wilking. *FiTQun Event Selection Optimization*. 2017. URL: https://t2k.org/docs/technotes/319.

[90] S. Bolognesi et al. *NIWG model and uncertainties for 2017 oscillation analysis*. 2017. URL: https://t2k.org/docs/technotes/315.

[91] E.T. Atkin et al. *NIWG model and uncertainties for 2019-2020 oscillation analysis*. (Under internal review). 2019. URL: https://t2k.org/docs/technotes/344.

[92] Krzysztof M. Graczyk and Jan T. Sobczyk. "Form factors in the quark resonance model". In: *Phys. Rev. D* 77 (5 Mar. 2008), p. 053001. DOI: 10.1103/PhysRevD.77.053001. URL: https://link.aps.org/doi/10.1103/PhysRevD.77.053001.

[93] P. Bartet et al. *NuMu CC event selections in the ND280 tracker using Run 2+3+4 data*. 2015. URL: https://t2k.org/docs/technotes/212.

[94] C. Bojechko et al. *CC multiple pion nu-mu event selections in the ND280 tracker using Run 1+2+3+4 data*. 2013. URL: https://t2k.org/docs/technotes/152.

[95] J. Imber et al. *T2K-SK Systematic Error Summary for the 2017 Oscillation Analysis*. 2017. URL: https://t2k.org/docs/technotes/326.

[96] G. Bak et al. "Measurement of Reactor Antineutrino Oscillation Amplitude and Frequency at RENO". In: *Phys. Rev. Lett.* 121.20 (2018), p. 201801. DOI: 10.1103/PhysRevLett.121.201801. arXiv: 1806.00248 [hep-ex].

[97] Patrick Dunne on behalf of the T2K experiment. *Latest Neutrino Oscillation Results from T2K*. July 2020. DOI: 10.5281/zenodo.3959558. URL: https://doi.org/10.5281/zenodo.3959558.

[98] T. Leitner, L. Alvarez-Ruso, and U. Mosel. "Neutral current neutrino-nucleus interactions at intermediate energies". In: *Phys. Rev. C* 74 (6 Dec. 2006), p. 065502. DOI: 10.1103/PhysRevC.74.065502. URL: https://link.aps.org/doi/10.1103/PhysRevC.74.065502.

[99] A. A. Aguilar-Arevalo et al. "Measurement of numu and numu bar induced neutral current single pi0 production cross sections on muneral oil at Enu O(1 GeV)". In: *Physical Review D* 81.1 (Jan. 2010). DOI: 10.1103/physrevd.81.013005. URL: https://doi.org/10.1103%2Fphysrevd.81.013005.

[100] E. Hernández, J. Nieves, and M. J. Vicente Vacas. "Single π production in neutrino-nucleus scattering". In: *Phys. Rev. D* 87 (11 June 2013), p. 113009. DOI: 10.1103/PhysRevD.87.113009. URL: https://link.aps.org/doi/10.1103/PhysRevD.87.113009.

[101] P. A. Rodrigues. "Comparing pion production models to MiniBooNE data". In: *AIP Conference Proceedings*. AIP Publishing LLC, 2015. DOI: 10.1063/1.4919470. URL: https://doi.org/10.1063%2F1.4919470.

[102] Hyper-K collaboration. *Hyper-K near-detector CDR*. 2022.

[103] C. Licciardi and M. Barbi. *Measurement of Single pi+ Production Induced by NuMu NC Interactions Using the ND280 Tracker*. 2012. URL: https://www.t2k.org/docs/technotes/129/.

[104] K. et al. Abe. "Measurement of the single π^0 production rate in neutral current neutrino interactions on water". In: *Phys. Rev. D* 97 (3 Feb. 2018), p. 032002. DOI: 10.1103/PhysRevD.97.032002. URL: https://link.aps.org/doi/10.1103/PhysRevD.97.032002.

[105] L. Anthony. *A model independent determination of the pi0 background in Super-Kamiokande in the T2K nue appearance measurement*. 2020. DOI: 10.17638/03076633. URL: https://livrepository.liverpool.ac.uk/3076633/.

[106] K. Iyogi et al. *T2K data acquisition and FC event selection at Super-Kamiokande*. 2011. URL: https://t2k.org/docs/technotes/027.

[107] A.A. Aguilar-Arevalo et al. "First observation of coherent pi0 Production in Neutrino Nucleus Interactions with E nu < 2 GeV". In: *Physics Letters B* 664.1-2 (June 2008), pp. 41–46. DOI: `10.1016/j.physletb.2008.05.006`. URL: `https://doi.org/10.1016%2Fj.physletb.2008.05.006`.

[108] R Castillo and F. Sanchez. *Measurement of the numu CC1pi+ Cross Section on CH using the near detector*. 2016. URL: `https://t2k.org/docs/technotes/199`.

[109] M. et al. Derrick. "Study of single-pion production by weak neutral currents in low-energy νd interactions". In: *Phys. Rev. D* 23 (3 Feb. 1981), pp. 569–575. DOI: `10.1103/PhysRevD.23.569`. URL: `https://link.aps.org/doi/10.1103/PhysRevD.23.569`.

[110] G.L. Fogli and G. Nardulli. "Neutral current induced one-pion production: A new model and its comparison with experiment". In: *Nuclear Physics B* 165.1 (1980), pp. 162–184. ISSN: 0550-3213. DOI: `https://doi.org/10.1016/0550-3213(80)90312-0`. URL: `https://www.sciencedirect.com/science/article/pii/0550321380903120`.

[111] W. Krenz et al. "Experimental study of exclusive one-pion production in all neutrino-induced neutral current channels". In: *Nuclear Physics B* 135.1 (1978), pp. 45–65. ISSN: 0550-3213. DOI: `https://doi.org/10.1016/0550-3213(78)90213-4`. URL: `https://www.sciencedirect.com/science/article/pii/0550321378902134`.

[112] P. J. Nienaber. *Single Neutral Pion Production in Charged Current and Neutral Current Neutrino Interactions, PhD. Thesis*. 1988. URL: `http://hdl.handle.net/2142/77420`.

[113] G. P. Zeller. *Low Energy Neutrino Cross Sections: Comparison of Various Monte Carlo Predictions to Experimental Data*. 2003. DOI: `10.48550/ARXIV.HEP-EX/0312061`. URL: `https://arxiv.org/abs/hep-ex/0312061`.

[114] A. Missert. *Fit to Super-K Atmospheric Neutrino Data for Optimization of the fiTQun Fiducial Volume Cuts and Estimation of Detector Uncertainties*. 2017. URL: `https://t2k.org/docs/technotes/318`.

[115] T. Mueller and S. Mine. *SK pi0 systematic errors for the nue analysis with T2K 6.4×1020 POT (RUN1-4) data*. 2013. URL: https://t2k.org/docs/technotes/156.

[116] C. Bronner et al. *Update of SK nue systematic error for 2012a oscillation analysis*. 2012. URL: https://t2k.org/docs/technotes/107.

[117] S. Lakshmi et al. *Super-Kamiokande detector systematic uncertainty including the multi-ring 1mu 1pi+ sample*. 2022. URL: https://t2k.org/docs/technotes/448.

[118] K. M. Tsui et al. *Sterile neutrino oscillation studies with the T2K far detector Super-Kamiokande*. 2018. URL: https://t2k.org/docs/technotes/343.

[119] Melanie Day and Kevin S. McFarland. "Differences in quasielastic cross sections of muon and electron neutrinos". In: *Phys. Rev. D* 86 (5 Sept. 2012), p. 053003. DOI: 10.1103/PhysRevD.86.053003. URL: https://link.aps.org/doi/10.1103/PhysRevD.86.053003.

[120] S. Agostinelli et al. "Geant4—a simulation toolkit". In: *Nuclear Instruments and Methods in Physics Research Section A: Accelerators, Spectrometers, Detectors and Associated Equipment* 506.3 (2003), pp. 250–303. ISSN: 0168-9002. DOI: https://doi.org/10.1016/S0168-9002(03)01368-8. URL: https://www.sciencedirect.com/science/article/pii/S0168900203013688.

[121] *Water Cherenkov Simulator*. URL: https://github.com/WCSim.

[122] *The VALOR neutrino fit*. URL: https://valor.pp.rl.ac.uk.

[123] N. Prouse. "Machine Learning Techniques to Enhance Event Reconstruction in Water Cherenkov Detectors". NuFact. 2022. URL: https://indico.fnal.gov/event/53004/contributions/244477/.

[124] Arie Bodek. "A Unified Model for inelastic e - N and v - N cross sections at all Q2". In: *AIP Conference Proceedings*. AIP, 2005. DOI: 10.1063/1.2122031. URL: https://doi.org/10.1063%2F1.2122031.

[125] T. Yang et al. "A hadronization model for few-GeV neutrino interactions". In: *The European Physical Journal C* 63.1 (Aug. 2009), pp. 1–10. DOI: 10.1140/epjc/

s10052-009-1094-z. URL: https://doi.org/10.1140%2Fepjc%2Fs10052-009-1094-z.

[126] A. Bercellie et al. *Cross section parameters for 2014 oscillation analysis*. 2014. URL: https://t2k.org/docs/technotes/192.

[127] P. de Perio et al. *Cross section parameters for the 2012a oscillation analysis*. 2012. URL: https://t2k.org/docs/technotes/108.

[128] T Feuseles et al. *Tuning of the NEUT Cascade Model using pi+–A Scattering External Data to Improve Final State Interaction and Secondary Interaction Systematic Uncertainties*. (Under internal review). 2017. URL: https://t2k.org/docs/technotes/325.

Appendix A

The T2K Cross-section Model

The T2K neutrino cross-section model has been developed to provide the necessary theoretically motivated freedom in the oscillation analysis to fit the generated MC to the data observed at ND280 and SK. When implemented in the oscillation analysis this model consists of 47 parameters, controlling certain event types and interactions at either ND280, SK or both. These are summarised in Table A.1.

- MaQE— The axial mass of the axial vector dipole form factor for CCQE interactions, adjusts Q^2 shape of the CCQE interaction cross-section. Prior derived from bubble chamber data [90].
- 2p-2h— The 2p-2h interaction involves a neutrino interaction resulting in two nucleons escaping the nucleus. This can occur via two mechanisms, meson exchange, dominated by a pionless Δ decay or via nucleon-nucleon correlations. As this is highly dependant on the nuclear environment, separate uncertainties are included for carbon and oxygen targets. The shape refers to the relative contribution from the meson exchange mechanism compared to nucleon-nucleon correlation. As the struck nucleon will be different for ν and $\bar{\nu}$ interactions separate uncertainties are included. In order to account for the different cross-section from different models of 2p-2h interactions, additional energy-dependant parameters are included. These affect the shape of the 2p-2h cross-section as a function of incident neutrino energy. The low energy parameters control events with neutrino energy below 600MeV, with high energy being above 600MeV [91]. Priors are very loose due to a lack of experimental 2p-2h data, the carbon-to-oxygen prior is based on electron scattering data [90].

Parameter Name	ND280	SK	Spline	Pre-fit Error	Interaction Types
MaQE	yes	yes	yes	6%	CCQE
2p-2h norm ν	yes	yes	no	100%	ν 2p-2h
2p-2h norm $\bar{\nu}$	yes	yes	no	100%	$\bar{\nu}$ 2p-2h
2p-2h norm C to O	yes	yes	no	20%	2p-2h
2p-2h shape C	yes	no	yes	flat	2p-2h on carbon
2p-2h shape O	yes	yes	yes	flat	2p-2h on oxygen
2p-2h Edep low E_ν	yes	yes	yes	100%	ν 2p-2h
2p-2h Edep high E_ν	yes	yes	yes	100%	ν 2p-2h
2p-2h Edep low $E_{\bar{\nu}}$	yes	yes	yes	100%	$\bar{\nu}$ 2p-2h
2p-2h Edep high $E_{\bar{\nu}}$	yes	yes	yes	100%	$\bar{\nu}$ 2p-2h
Q^2 0	yes	yes	no	33%	CCQE
Q^2 1	yes	yes	no	21%	CCQE
Q^2 2	yes	yes	no	17%	CCQE
Q^2 3	yes	yes	no	17%	CCQE
Q^2 4	yes	yes	no	17%	CCQE
Q^2 5	yes	yes	no	11%	CCQE
Q^2 6	yes	yes	no	18%	CCQE
Q^2 7	yes	yes	no	40%	CCQE
E_b C ν	yes	no	no	6MeV	ν on carbon
E_b C $\bar{\nu}$	yes	no	no	6MeV	$\bar{\nu}$ on carbon
E_b O ν	yes	yes	no	6MeV	ν on oxygen
E_b O $\bar{\nu}$	yes	yes	no	6MeV	$\bar{\nu}$ on oxygen
C_5^A	yes	yes	yes	16%	CC1π and NC1π
M_{Res}^A	yes	yes	yes	14%	CC1π and NC1π
$I_{1/2}$ low P_π	no	yes	yes	135%	$\bar{\nu}$ CC1π and NC1π
$I_{1/2}$	yes	yes	yes	42%	CC1π and NC1π
CC norm ν	yes	yes	no	2%	ν CC
CC norm $\bar{\nu}$	yes	yes	no	1%	$\bar{\nu}$ CC
CC ν_e/ν_μ	yes	yes	no	2.8%	ν_e CC
CC $\bar{\nu}_e/\bar{\nu}_\mu$	yes	yes	no	2.8%	$\bar{\nu}_e$ CC
CC BY DIS	yes	yes	yes	100%	CC DIS
CC BY Multiπ	yes	yes	yes	100%	CC Multi π
CC AGKY Multiπ	yes	yes	yes	100%	CC Multi π
CC Misc	yes	yes	no	100%	CC Miscellaneous
CC DIS Multiπ norm ν	yes	yes	no	3.5%	CC ν DIS and Multi π
CC DIS Multiπ norm $\bar{\nu}$	yes	yes	no	6.5%	CC $\bar{\nu}$ DIS and Multi π
CC Coh C	yes	no	no	30%	CC Coherent on carbon
CC Coh O	yes	yes	no	30%	CC Coherent on oxygen

Parameter Name	ND280	SK	Spline	Pre-fit Error	Interaction Types
NC coherent	yes	yes	no	30%	NC Coherent
NC 1γ	yes	yes	no	100%	NC 1γ
NC Other near	yes	no	no	30%	NC Other at ND280
NC Other far	no	yes	no	30%	NC Other at SK
FEFQE low	yes	yes	yes	30%	Events with pions
FEFQE high	yes	yes	yes	47%	Events with pions
FEFINEL	yes	yes	yes	110%	Events with pions
FEFABS	yes	yes	yes	31%	Events with pions
FEFCX	yes	yes	yes	44%	Events with pions

TABLE A.1: The individual parameters of the T2K cross-section model.

- Q^2 normalisation — External experiments have consistently shown a reduction in CCQE cross-section at low Q^2 relative to that predicted by the spectral function model of the nuclear environment as used by the T2K CCQE model. In order to account for this, explicit normalisation parameters are included for specific regions of Q^2. A total of five such parameters are included to suppress the low Q^2 region covering 0 to 0.25GeV^2 with prior based on MINERνA data [91]. At high Q^2 is it believed that the dipole form factor does not adequately describe the Q^2 shape of the CCQE cross-section, hence three further normalisation parameters are included covering the region above 0.25GeV^2 the prior on this is based upon the difference between the dipole form factor prediction and the Z-expansion form-factor [90][91].

- E_b — The spectral function model of the nuclear environment includes shell structure, hence there is no single nucleon binding energy. A full model of the uncertainty on the energy required to remove a struck nucleon would necessitate separate uncertainties depending on the shell. Instead a conservative uncertainty of 6MeV is assumed based on the uncertainty on p shell binding energy from electron scattering experiments. Freedom for neutron binding energy relative to the proton binding energy is provided with different parameters for ν and $\bar{\nu}$ interaction. As the nuclear environment in carbon and oxygen are different separate freedom is provided for each nucleus [91]. The effect of these parameters is to alter the energy of the outgoing charged lepton.

- C_5^A and M_{Res}^A— The normalisation and Q^2 shape of the dipole form factor in resonant pion production, described in more detail in §5.5.2.

- $I_{1/2}$ low P_π and $I_{1/2}$— The non-resonant pion production contribution, described in more detail in §5.5.2.

- CC normalisation — An outgoing charged lepton from a neutrino interaction will gain or lose energy as it escapes the charged nucleus as a result of the Coulomb potential, as this effect is not directly included in NEUT it is added as a post-hoc uncertainty on interaction cross-section in the region in which this effect is greatest. These apply to neutrino interactions with true energy in the range of 400 to 600MeV [91].

- CC ν_e/ν_μ and $\bar{\nu}_e/\bar{\nu}_\mu$— Due to the uncertainty on radiative corrections that are not modelled in NEUT there is a theoretical uncertainty on the ratio of ν_e to ν_μ and $\bar{\nu}_e$ to $\bar{\nu}_\mu$ cross-section, this is included in T2K as a single normalisation parameter.

- CC Bodek-Yang DIS and Multi π — In deep inelastic scattering the neutrino interaction occurs on a single quark within a nucleon, a parton PDF is required to model the interaction cross-section. The QCD models upon which these parton PDFs are based can break down at low Q^2, Bodek and Yang [124] modifications allow for the use of these PDFs at low Q^2. These corrections are however subject to additional uncertainties, in order to include these the ratio between the predicted cross-section with and without Bodek-Yang corrections is used as a weighting on CC DIS and CC multiple π events separately as a function of neutrino energy and Q^2.

- CC AGKY Multi π — By comparing the prediction of CC multiple π cross-section from NEUT to a prediction made with the AGKY model [125], a measure of model uncertainty is obtained. This parameter acts to weight the MC from NEUT towards the AGKY prediction as a function of neutrino energy.

- CC Miscellaneous — A conservative uncertainty on the cross-section for all CC events not covered by other components of the model, such as CC 1γ and CC 1η.

- CC DIS Multi π normalisation — Normalisation uncertainty on CC DIS and multiple π events, motivated by the difference in cross-section seen between NEUT at high energy and PDG CC inclusive cross-section [91].

- CC coherent — Normalisation uncertainty on CC coherent interactions with the whole nucleus. Two parameters are used, one for oxygen and one for carbon with the water in FGD2 at ND280 able to provide the some constraint relevant to the water target at SK [126].

- NC coherent — Normalisation uncertainty on NC interactions upon the entire nucleus, uncertainty derived from comparison to SciBooNE data [127].

- NC 1γ— A normalisation uncertainty on NC 1γ events, prior uncertainty motivated by a lack of experimental evidence of the existence of NC 1γ events.

- NC other — A normalisation parameter on all other NC interactions at ND280 and SK separately, the expected selected interaction types being sufficiently different at the two detectors that correlation is not made between them.

- FEFQE — Uncertainty on the quasi-elastic scattering of pions off nuclei within the nucleus in which it is created. This is split into a low and high energy regime. Prior is derived from fits to pion-nucleus scattering [128].

- FEFINEL — Uncertainty on production of pions from in-nucleus interactions.

- FEFABS — Uncertainty on pion absorption probability in the nucleus.

- FEFCX — Uncertainty on pion charge exchange within the nucleus, in which a charged pion becomes an uncharged π^0 (single charge exchange) or becomes a charged pion of opposite charge (double charge exchange). Prior uncertainty derived from fits to pion-nucleus scattering [128].

Appendix B

The Super-K Multi-Ring Atmospheric Fit

A fit to SK atmospheric data is used to estimate the impact of the detector reconstruction uncertainty on the NCπ^0 samples. This fit consists of dividing the SK MC and data into eight samples by the number of reconstructed rings, decay electrons and, in the one-ring samples by e-like or μ-like ring as shown in Table B.1.

Sample Number	Description
1	1 e-like ring, 0 decay electrons
2	1 e-like ring, 1 decay electrons
3	1 μ-like ring, 0 decay electrons
4	1 μ-like ring, 1 decay electrons
5	1 μ-like ring, 2 decay electrons
6	Multiple rings, 0 decay electrons
7	Multiple rings, 1 decay electrons
8	Multiple rings, 2 decay electrons

TABLE B.1: The samples used in the multi-ring atmospheric fit to constrain the ring counting and PID uncertainties.

These samples are then binned in chosen reconstructed likelihood ratios e.g. the e/π^0 PID ratio. For each of these ratios a set of 'shift and smear' parameters are used for each final state topology, Table B.2, and visible energy range, Table B.3. These modify the likelihood ratio of a given event according to:

$$L^i_{jk} \rightarrow \alpha^i_{jk} L^i_{jk} + \beta^i_{jk}, \tag{B.1}$$

Topology index j	Final State Topology
0	$1e$
1	1μ
2	$1e$ + Other
3	$1\mu + 1\pi^{+}$
4	1μ + Other
5	$1\pi^{0}$
6	$1\pi^{\pm}$
7	Other

TABLE B.2: The true final-state topologies used in the SK detector systematic uncertainty fit [117].

Bin index k	Visible Energy Range (GeV)
0	0.1—0.3
1	0.3—0.7
2	0.7—1.33
3	1.33—3.0
4	3.0—5.0

TABLE B.3: The visible energy ranges used in the definition of the shift and smear parameters eqn. B.1 for the SK detector uncertainty [117].

where L^{i}_{jk} is the modified likelihood ratio for a given fiTQun selection variable 'i' for an event with true final-state topology 'j' and visible energy bin 'k'. α is the 'smear' parameter spreading or compressing the fiTQun variable likelihood distribution while β is the 'shift' parameter, which uniformly moves the distribution.

In total there are eight final-state topologies in five visible energy ranges for the seven fiTQun variables. This results in 280 shift and 280 smear parameters in the fit, parameters being shared between events with the same topology and visible energy range but from different samples.

In order to constrain the shift and smear parameters, an MCMC fit is performed to SK atmospheric data with these as free parameters. This fit includes atmospheric flux, cross-section and oscillation nuisance parameters.

Each step in this fit entails applying the shift and smear parameters on an event-by event basis, applying the weights from the flux, cross-section and oscillation parameters and applying the event selection criteria to the resulting likelihood ratios.

The resulting selections are binned in the PID likelihood ratios for each range of visible energies and a shape-only comparison between data and this MC prediction is made:

$$-\ln(P(\mathbf{Data}|\mathbf{MC}(\mathbf{x}))) = -\sum_{i,k,l,m}\left[N^{Data}_{i,k,l,m}\ln\left(\frac{N^{MC}_{i,k,l,m}}{\sum_n N^{MC}_{i,k,l,n}}\right)\right] \tag{B.2}$$

Where **x** are the values of the model parameters. The summation runs over the seven fiTQun variables i, the five visible energy bins k, the eight samples l and the bins in the fiTQun variables m and n. This is therefore a shape comparison between the MC and data.

Additional constraint on the shift and smear parameters is included through 'hybrid' samples. There are two such samples, $1\pi^0$ and 1μ+$1\pi^+$. The $1\pi^0$ sample takes a true π^0 MC event and substitutes one of the π^0 decay photons for a SK atmospheric 1Re event of the same reconstructed energy, the second photon is then simulated and the MC detector response overlaid on the data response from the first ring. The overall event is then reconstructed by fiTQun as is the corresponding pure MC event.

These MC events are then binned in the same way as the atmospheric samples above, with the same shift and smear parameters applied. A two dimensional χ^2 map in the (α, β) space is made for each fiTQun variable and visible energy range by comparing the MC to the hybrid data:

$$\chi^2 = \sum_{bins}\frac{(N_{data} - N_{MC})^2}{\sigma^2_{data} + \sigma^2_{MC}} \tag{B.3}$$

Where the summation runs over the bins in the fiTQun variable for a given visible energy range. These maps are then used as a prior constraint on the shift and smear parameters for the $1\pi^0$ and 1μ + $1\pi^+$ final state topologies.

The combination of these χ^2 maps and the atmospheric likelihoods are used as the likelihood in the MCMC fit.

Appendix C

Simulated Data Distributions

The event distributions used in the simulated data study of §6.1.1. Here the contribution of NC1π events in all samples has been increased by 30%. The resulting distributions are shown along with the fractional change relative to the unmodified MC prediction.

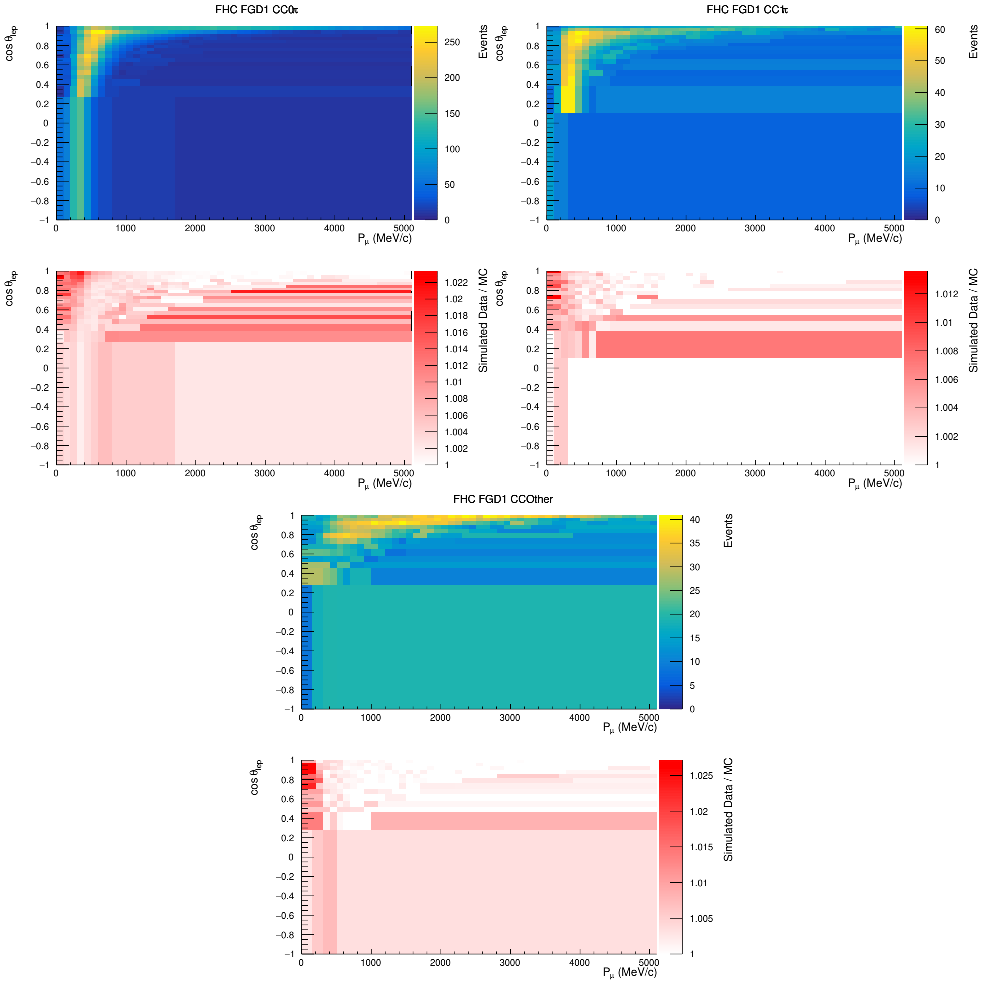

FIGURE C.1: The effect of the 30% increase in NC1π cross-section on the FHC FGD1 ND280 samples.

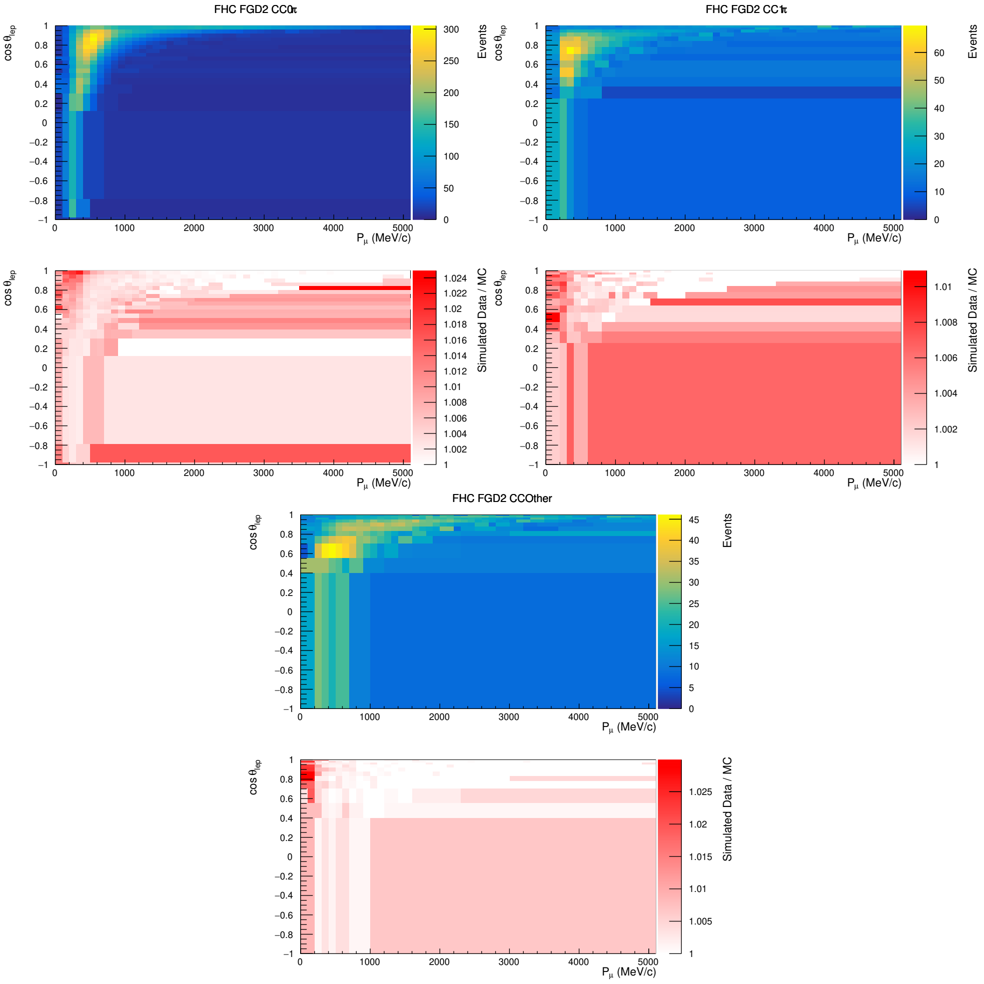

FIGURE C.2: The effect of the 30% increase in NC1π cross-section on the FHC FGD2 ND280 samples.

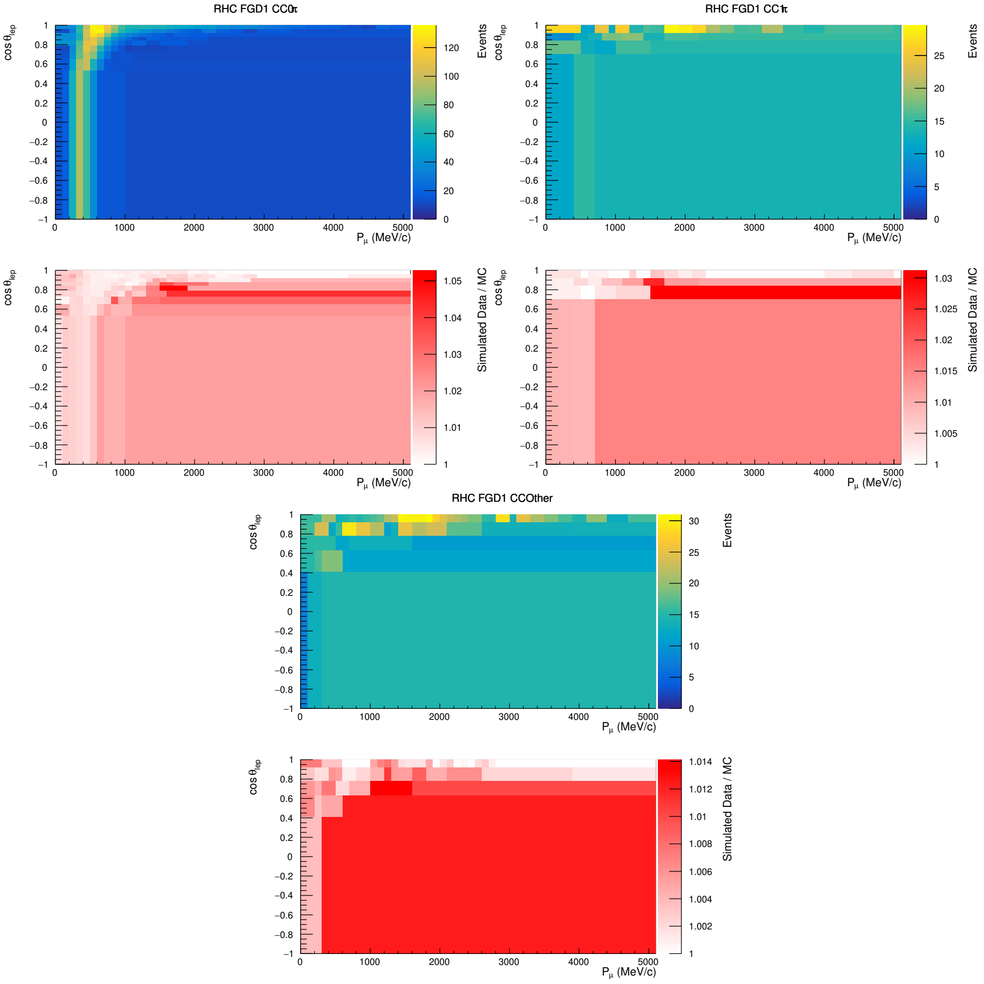

FIGURE C.3: The effect of the 30% increase in NC1π cross-section on the RHC FGD1 ND280 samples.

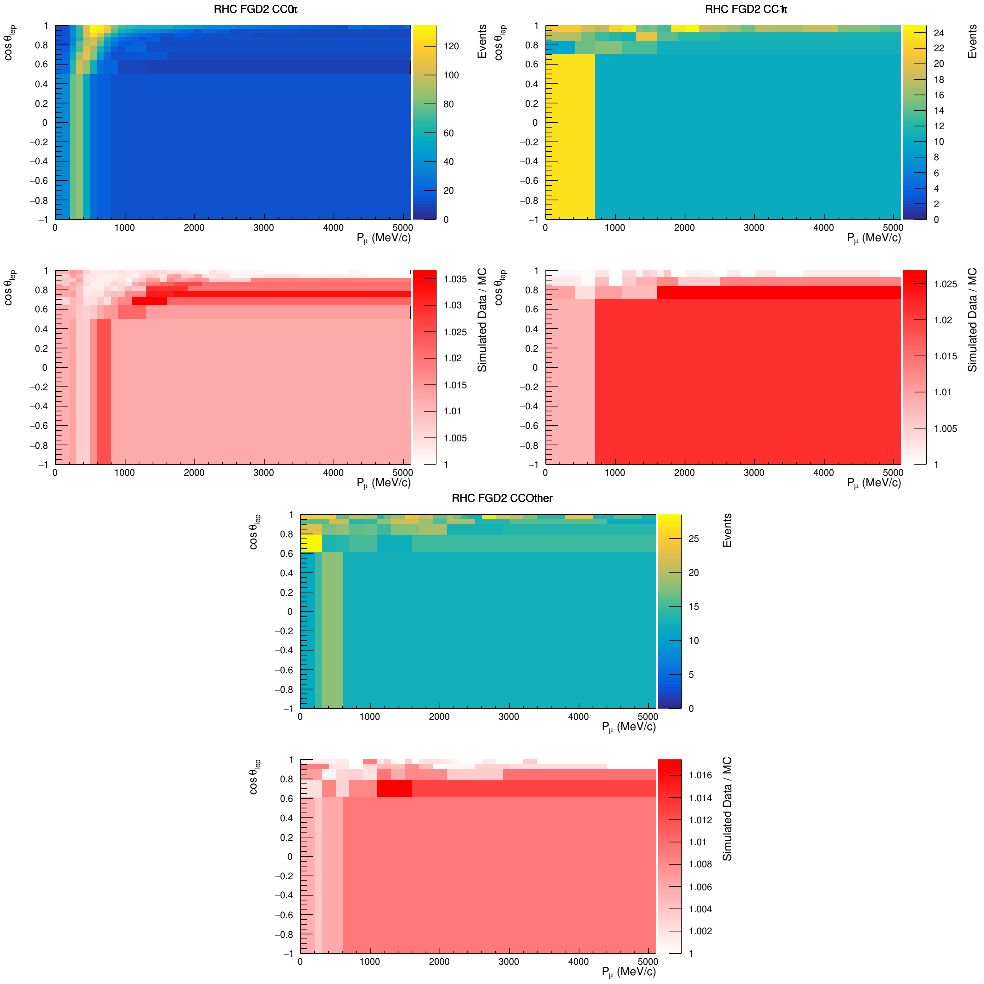

FIGURE C.4: The effect of the 30% increase in NC1π cross-section on the RHC FGD2 ND280 samples.

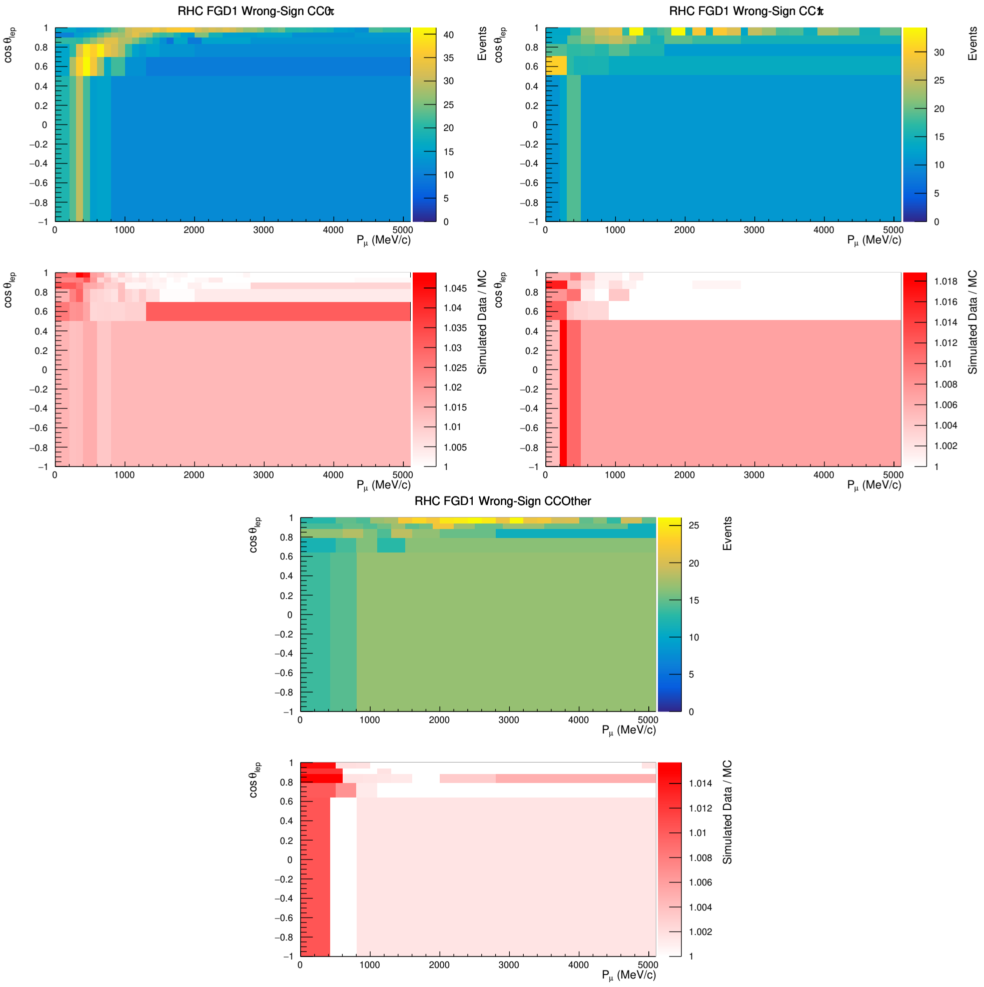

FIGURE C.5: The effect of the 30% increase in NC1π cross-section on the wrong-sign RHC FGD1 ND280 samples.

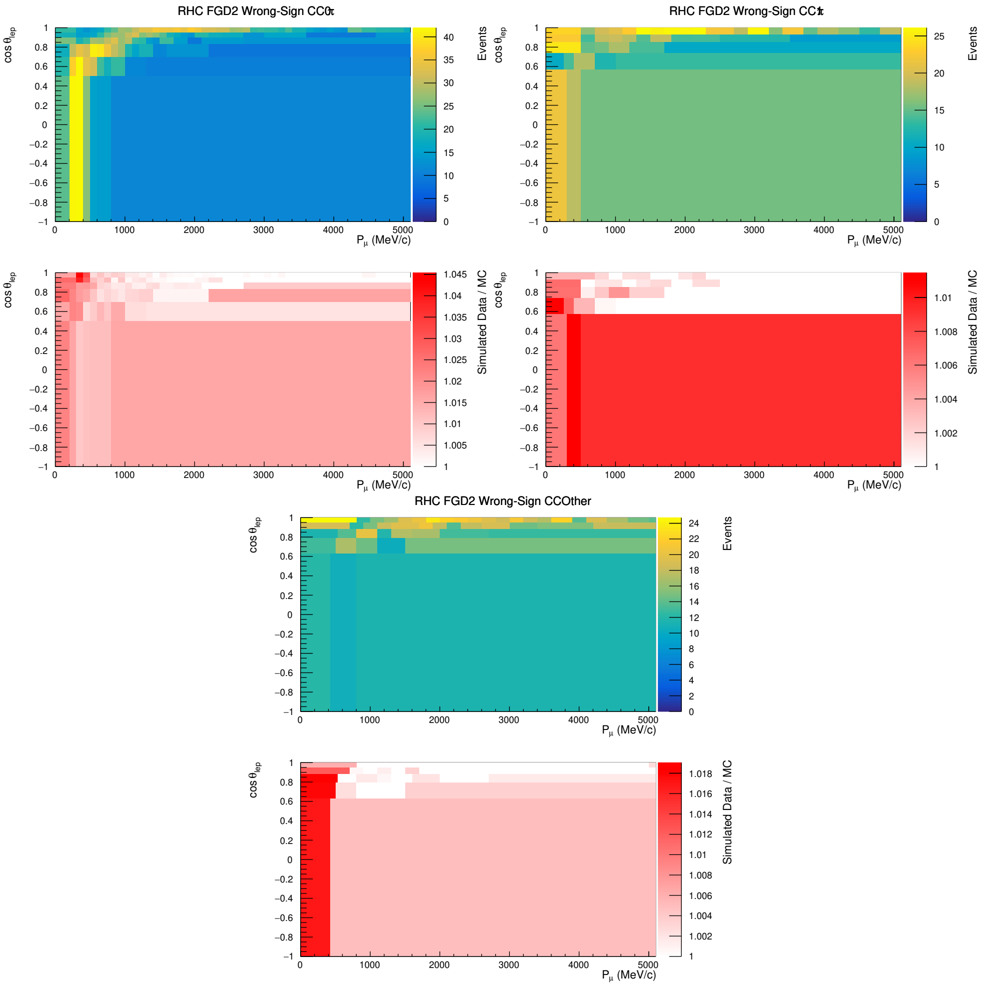

FIGURE C.6: The effect of the 30% increase in NC1π cross-section on the wrong-sign RHC FGD2 ND280 samples.

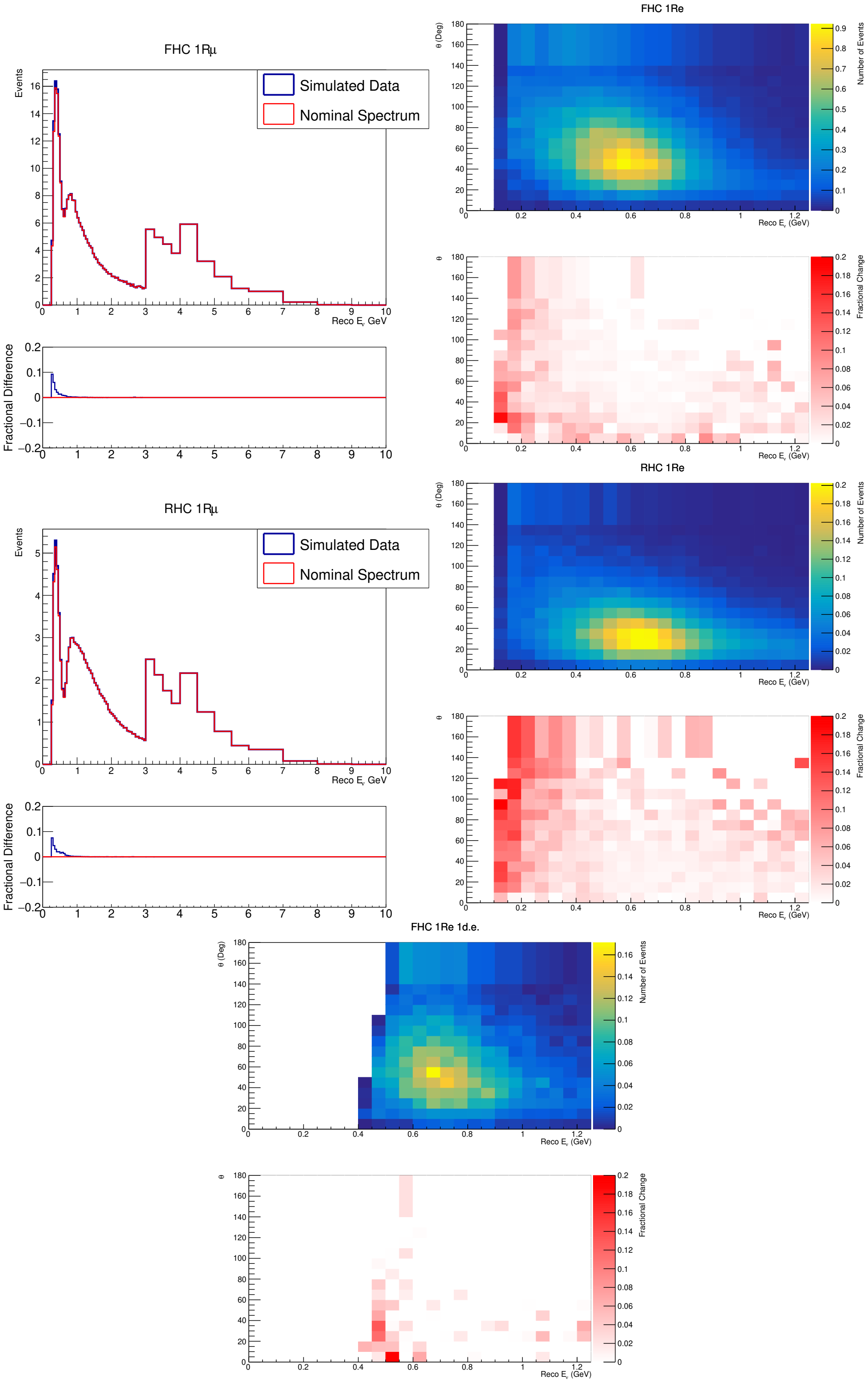

FIGURE C.7: The effect of the 30% increase in NC1π cross-section on the SK samples.

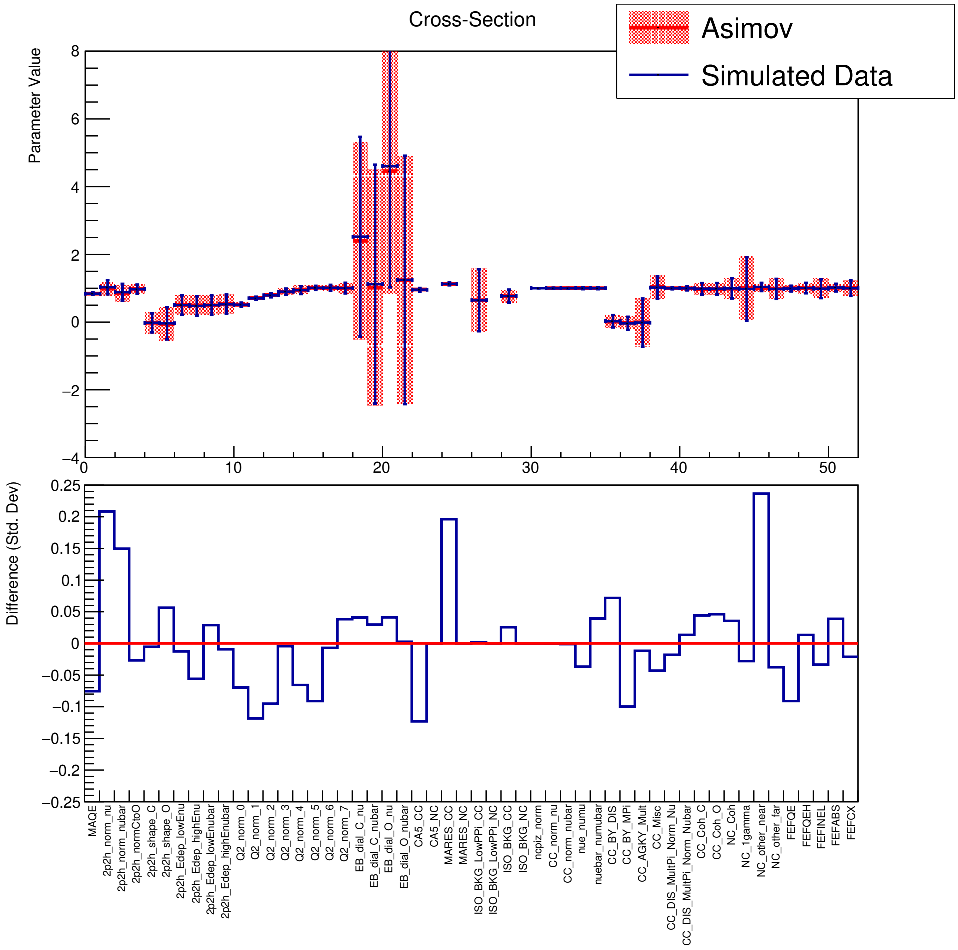

FIGURE C.8: The postfit constraint on the T2K cross-section parameters when fitting to the simulated NC1π data described in §6.1.1.

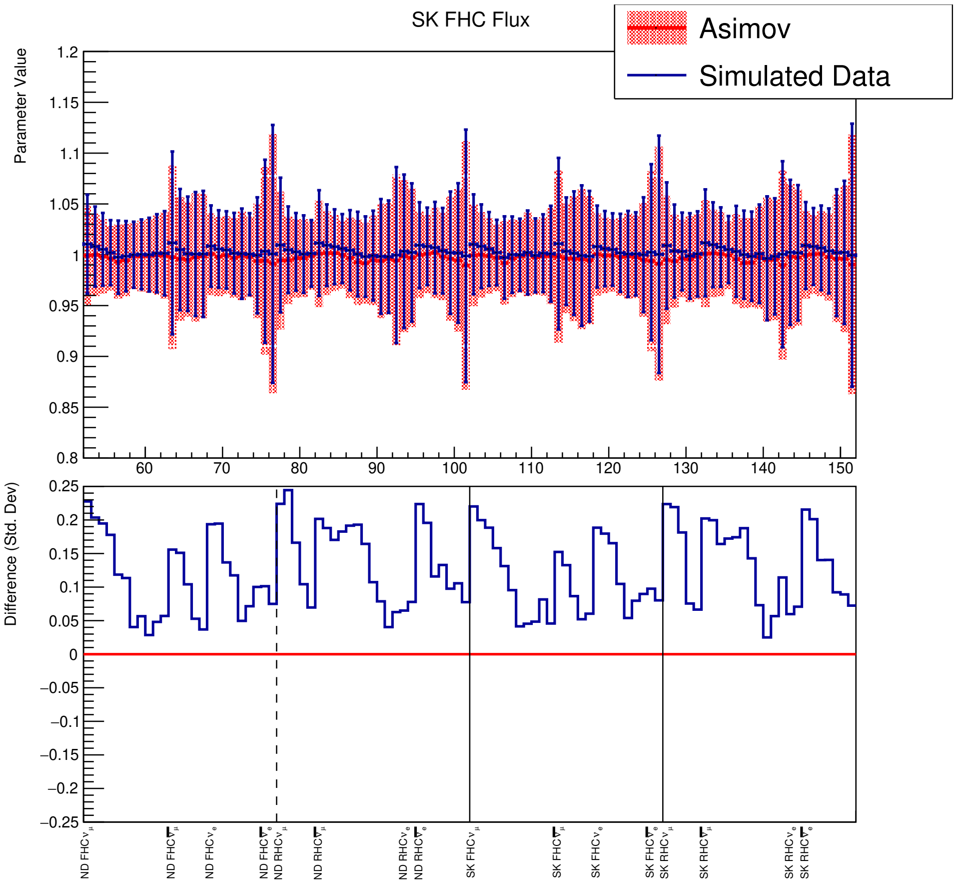

FIGURE C.9: The postfit constraint on the T2K flux parameters when fitting to the simulated NC1π data described in §6.1.1.

Appendix D

Additional IWCD Studies

D.1 Further Studies

To investigate the impact of different detector diameters and off-axis spans on the cross-section results, some investigations were performed varying these properties and investigating the impact on FHC only fits. These fits used a looser flux prior based on the thin target tuned T2K flux model with a 10% error on ν_μ flux at the flux peak. The impact of pileup on the event rates was included but uncertainties on this were not included. Additionally these fits were performed with the ν_e cross-section parameterised as a function of reconstructed neutrino energy.

D.2 Fit Parameters

As the cross-section fit is performed in reconstructed ν_e energy the correspondence between each fit parameter and the true energy distribution of ν_e events is of interest. The selected event breakdown as a function of reconstructed ν_e energy over all off-axis angles is shown in Fig D.1 (left).

The true energy distribution of selected events with reconstructed energies between 0 and 300MeV is shown in Fig D.1 (right). Many selected ν_e CC events have energies above 300MeV and are mis-reconstructed to be at low energy. However the majority of backgrounds in this reconstructed energy range backgrounds in this 0-300MeV region come from high incident energy NC interactions.

The distributions for the remaining four signal parameters are shown in Figs D.2, D.3. These show good agreement between the true energy distributions of ν_e

events and the reconstructed energy parameters to which they correspond, with sharp boundaries in event rate at the parameter edges.

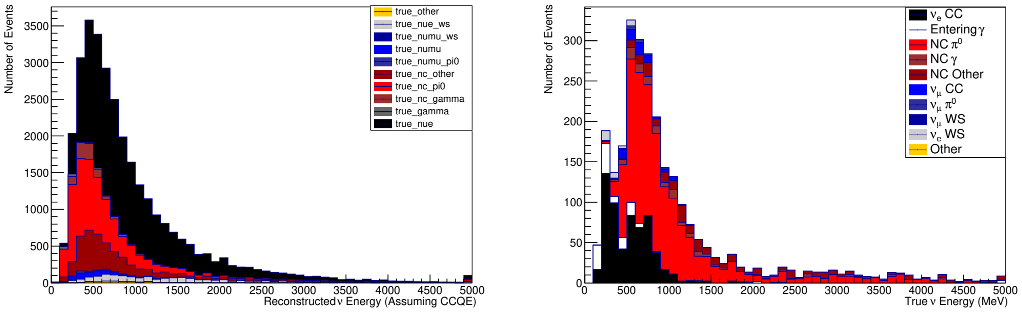

FIGURE D.1: The reconstructed energy distribution and interaction breakdown of all selected ν_e like events at all angles (left). The distribution and breakdown by mode of those selected events with reconstructed energies below 300MeV corresponding to the first signal parameter, as a function of true incident neutrino energy (right).

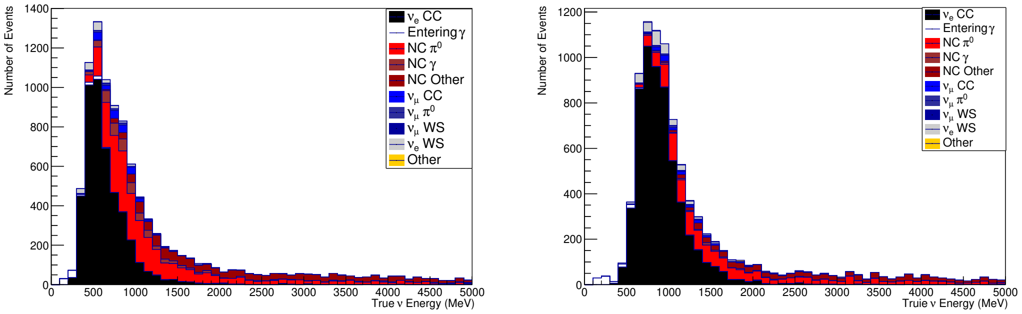

FIGURE D.2: The breakdown by true incident neutrino energy and interaction mode for selected events with reconstructed energies between 300-600MeV (left) and 600-1000MeV (right).

D.2.1 Neutron Tagging

In order to investigate the impact of neutron tagging at IWCD on the electron neutrino cross-section measurement, a toy neutron generation model was added to the fitter. This model uses the number and momentum of outgoing post FSI (final state interactions) hadrons to generate post secondary interaction (SI) neutrons. For each outgoing post FSI hadron as generated by NEUT, a momentum dependant particle gun based neutron multiplicity probability distribution function is used. This randomly assigns a number of post SI Neutrons generated by that outgoing hadron. The PDFs used for this calculation are shown in Fig D.4.

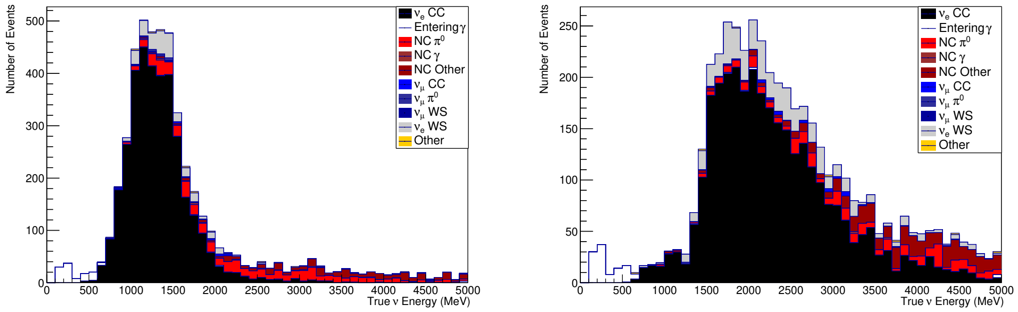

FIGURE D.3: The breakdown by true incident neutrino energy and interaction mode for selected events with reconstructed energies between 1000-1500MeV (left) and greater than 1500MeV (right).

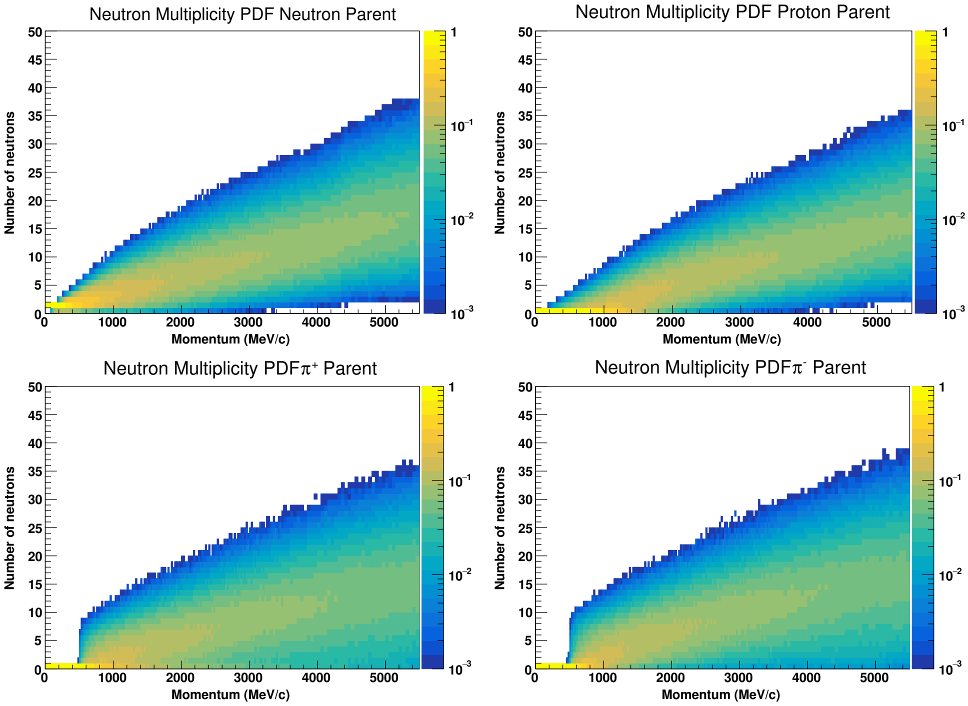

FIGURE D.4: The particle gun MC based neutron multiplicity probability distribution functions as a function of true hadron momentum for the four hadrons responsible for the majority of SI neutron production.

Summing all of the neutrons generated by the outgoing hadrons from an event yields the total neutron multiplicity of the event. The neutron multiplicity event distribution is shown in Fig D.5. This shows the generated multiplicity for true $\bar{\nu}_\mu$ events in FHC operation and includes both NC and CC events.

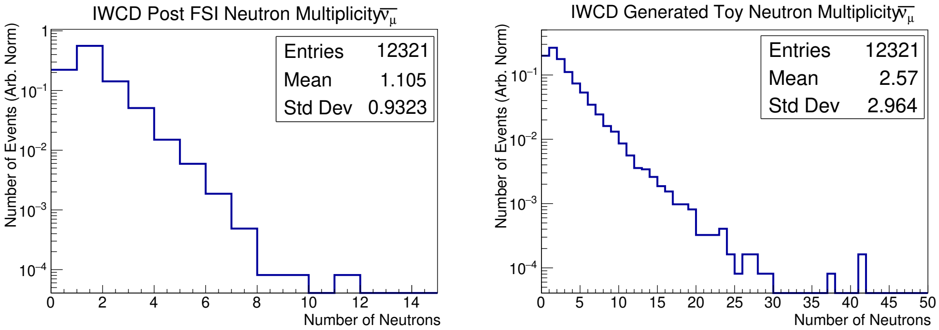

FIGURE D.5: The NEUT generated neutron multiplicity after FSI (left) and after FSI and SI (right) for true $\bar{\nu}_\mu$ events in FHC operation in the 2.4 - 2.6 ° off-axis range of IWCD. The post FSI neutron multiplicity is dominated by the outgoing neutron expected in the CC $\bar{\nu}_\mu$ interaction proces. The post FSI and SI distribution is skewed to higher neutron multiplicities due to the addition of multiple neutron generation from high momentum outgoing hadrons.

This toy generation model does not account for the spatial distribution of the final captured neutrons. The majority of these neutrons are however expected to be captured less than 1m from the primary vertex. With the 1m dwall cut used in this analysis it is expected that the majority of these neutrons will not escape the inner detector volume. Accounting for detector efficiency, a conservative estimate of 70% tagging efficiency for each generated neutron was assumed, independent of other neutrons generated by the event.

The cross-section fitter was expanded to account for this tagging information, the 1 ring e-like and 1 ring-μ like samples were split into two, one for events with one or more tagged neutrons and one for events without tagged neutrons, as shown for the 1Re samples in Fig D.6.

The addition of neutron tagging allows for neutrino sign selection, this is most clearly seen in the RHC samples in Fig D.6. Here the ν_e background to this $\bar{\nu}_e$ sample is primarily contained in the untagged sample, furthermore, few NCπ^0 events generate neutrons, hence the majority of this large background is present in the untagged sample. The overall result is that the tagged RHC 1Re sample has greater $\bar{\nu}_e$ CC sample purity than the no neutron tagging sample Fig 7.10.

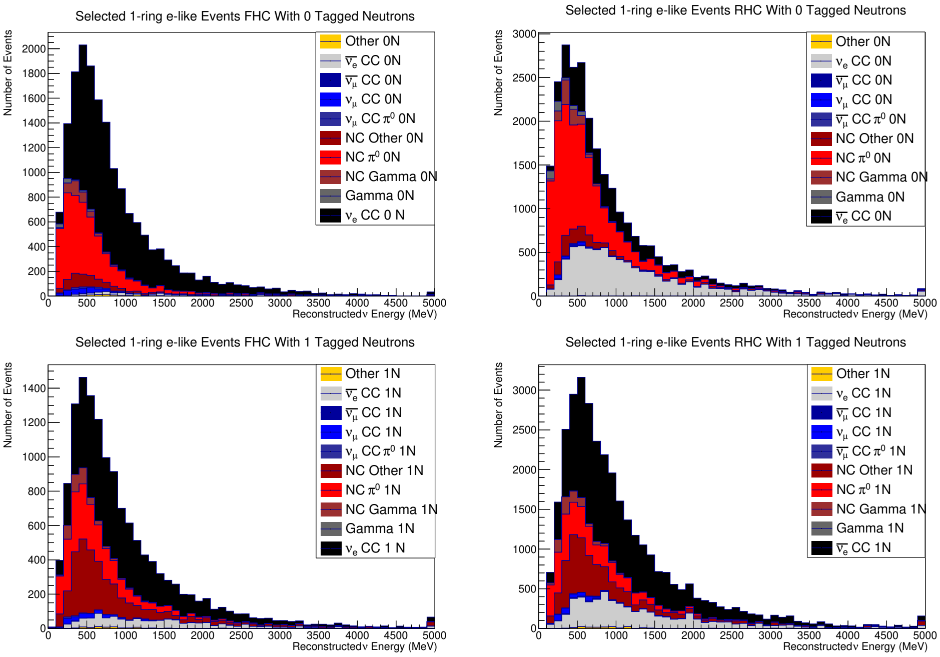

Selected 1-ring e-like Events FHC With 0 Tagged Neutrons

Selected 1-ring e-like Events RHC With 0 Tagged Neutrons

Selected 1-ring e-like Events FHC With 1 Tagged Neutrons

Selected 1-ring e-like Events RHC With 1 Tagged Neutrons

FIGURE D.6: The selected 1 ring electron-like samples broken down by true neutrino and interaction mode. The top row shows the FHC sample (left) and the RHC sample (right) for events without tagged neutrons in the final state. The bottom row shows the breakdown in the neutron tagged sample.

Tagging Uncertainty

Uncertainty in neutron tagging comes from two sources; uncertainty in neutron production rate and uncertainty in tagging efficiency. Uncertainty on production rate is complex and depends heavily on post FSI neutron multiplicity which is currently poorly constrained. As this uncertainty is not included in the fitter, these results are representative of a best-case scenario in which neutron production uncertainty is well constrained.

Uncertainty in tagging efficiency is included in both the electron and muon samples. This is included in the fitter as a single parameter that varies the tagging efficiency applied to each true neutron. For each fit bin in each sample the MC predicted event rate for three different neutron tagging efficiencies is evaluated. These three points are normalised to the event rate at the nominal 70% tagging efficiency and a quadratic spline is fitted to these three values. This yields a spline that can be used to continuously reweight each fit bin according to the neutron tagging parameter value. This prevents discontinuities in predicted event rate as MC events are moved between the tagged and untagged samples. A conservative 10% prior uncertainty on neutron tagging is included.

The results of this fit are shown in Fig D.7. There is a percent level improvement in the precision of the $\bar{\nu}_e$ cross-section measurement when neutron tagging information is added. This can be explained as a result of the reduced background contamination in the most signal rich regions as seen in Fig D.6.

Here, in the RHC sample, the majority of the signal $\bar{\nu}_e$ events are associated with a tagged neutron, while the background NCπ^0 events are associated with very few tagged neutrons. Thus the resulting tagged sample has higher purity, allowing for an improved constraint on the cross-section.

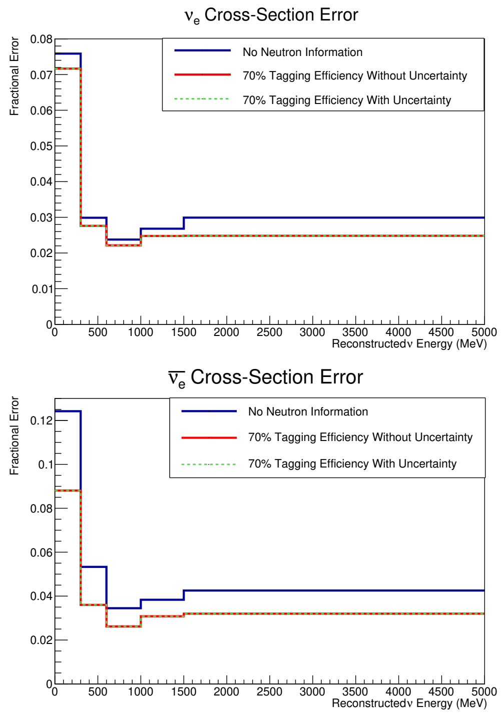

FIGURE D.7: The post-fit cross-section ratio uncertainty for ν_e/ν_μ (left) and $\bar{\nu}_e/\ \bar{\nu}_\mu$ (right) when fitting in true incident neutrino energy. The addition of neutron information yields a significant decrease in cross-section uncertainty. Due to the lack of neutron production multiplicity uncertainty, the tagging efficiency parameter is tightly constrained to 0.14% uncertainty and so has very little effect on the cross-section measurement.

Due to the lack of uncertainty in neutron multiplicity the fit tightly constrains the tagging efficiency parameter to 0.14%. This is a result of the large numbers of ν_μ events constraining this tagging efficiency, hence this cross-section is an upper bound on the potential impact of neutron tagging in IWCD, with appropriate neutron generation uncertainty the cross-section errors would increase.

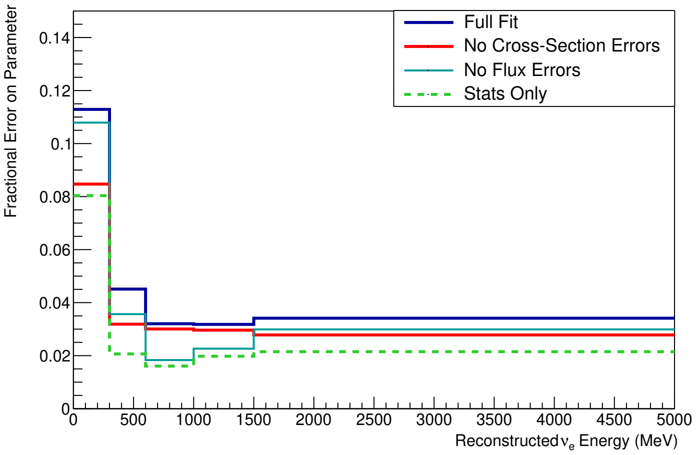

FIGURE D.8: The effect on the cross-section measurement of fixing various sources of systematic error in the fit. Cross-section uncertainty plays a significant role at energies below 600MeV while flux uncertainty is limiting at energies between this and 1500MeV.

D.2.2 Sources of Error

In order to identify which systematic uncertainties affect the signal parameters most strongly, fits are run with the parameters of interest set at their nominal values and not varied. This eliminates the freedom provided by these and allows for understanding the fit performance if these parameters were a priori perfectly known. The fixed parameters investigated include the flux uncertainty, all non-ν_e cross-section parameters, and finally, the case of all parameters fixed except the ν_e cross-section. This latter case represents the maximum sensitivity achievable with the 1Re sample described in §7.4.1.

The resulting constraint on the ν_e signal parameters of these fits is shown in Fig D.8, it can be seen that the removal of flux uncertainty has a significant effect on the measurement precision of the ν_e event rate in the 600 — 1500MeV region, reducing the overall error to a level comparable to a statistics only fit. This indicates that with this 10% flux prior, the uncertainty in the ν_e cross-section measurement in this energy range is dominated by flux errors. Furthermore, the flux error is also a significant contributor to the overall error in the 300 — 600MeV region, the removal of the flux uncertainty decreases this measurement error from 4.5% to 3.5%.

Uncertainty in the cross-section parameters drive the signal parameter error in the 0 — 300 MeV energy range and are the largest systematic contributor in the

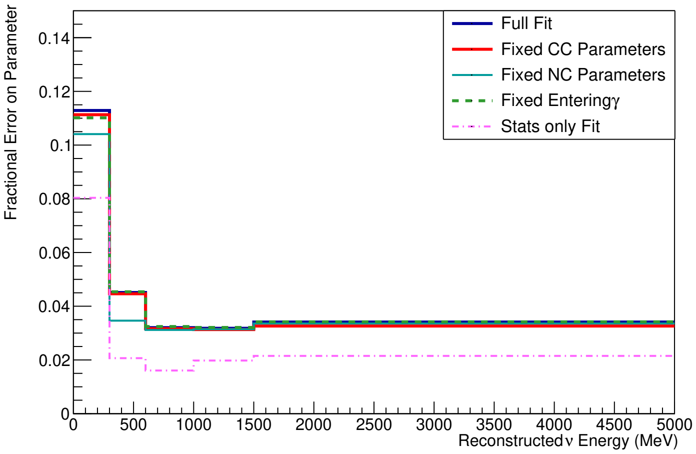

FIGURE D.9: The effect on the ν_e cross-section measurement error of fixing all charged current cross-section parameters, all neutral current cross-section parameters and the entering γ parameter.

300 — 600MeV and 1500+MeV signal regions. Further breaking down these cross-section parameters into CC and NC components as seen in Fig D.9, it can be seen that the NC parameters have a greater impact on the ν_e cross-section parameters at energies below 600MeV. The CC parameters have a slight impact at reconstructed ν_e energies above 1500 MeV. The impact of entering γ events is quite small and is limited to the lowest energy bins, this is due to the low entering γ event rate, as a result of the effective removal by the fiducial volume cut.

Fig D.10 shows that NC γ uncertainty is a significant source of error in the ν_e cross-section measurement in the 300 — 600MeV reconstructed energy range. This is corroborated by the distribution of NC γ events seen in Fig 7.9 peaking at this energy range. As these events have a 100% prior uncertainty applied, a small contamination of the sample with NC γ events can significantly adversely affect the resulting measurement.

D.2.3 Off-Axis Span

In order to assess the impact of a reduced off-axis span of IWCD, the fit can be run excluding events from certain off-axis ranges. The current proposed design includes an off-axis span of 1 - 4°, however other ranges may be of interest.

The results of excluding parts of this span from the analysis are shown in Fig D.11, these are shown for the 6m tall, 8m diameter ID design placed at 750m. When

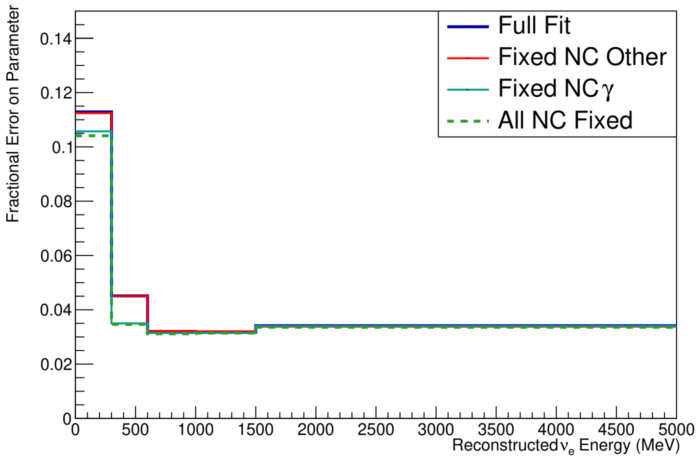

FIGURE D.10: The effect on the ν_e cross-section of fixing different NC cross-section parameters in the fit. Due to the large 100% prior uncertainty given to NC γ events and the lack of an NC γ control sample in the fit this parameter can be seen to be the dominant NC cross-section parameter in terms of the effect on ν_e cross-section.

excluding off-axis ranges, the exposure in the remaining span is equally weighted up to ensure total exposure remains the same, as would be the case with a run plan consisting of uniform sampling over the off-axis range.

At high off-axis angles an increasing proportion of incident flux is ν_e. Hence, additional data taking at these high off-axis angles would benefit this measurement as these positions have an increased signal to background ratio. This is the cause of the slight improvement seen in Fig D.11 when the off-axis span is reduced from 1 - 4° to 1.5 - 4° and to 2 - 4°.

D.2.4 Michel Electron Cut

Due to the high event rate environment of IWCD, and the long decay time of muons relative to beam bunch intervals, identifying which event from a given spill is responsible for a detected Michel electron may be challenging. Therefore, the impact of an imperfect or entirely absent Michel electron tag on the ν_e fit is of interest. Fig D.12 (left) and Table D.1 show the effect of removing the Michel cut on the event selection in the most signal rich 2.7-4.0° off-axis angles. Overall there is a significant increase in ν_e CC Other events when compared to Fig 7.9 as a result of a lower sensitivity to pion decays when the Michel tag is removed. Additionally there is an

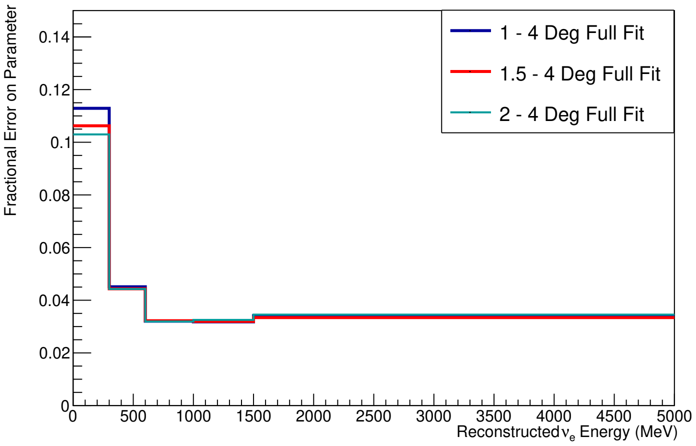

FIGURE D.11: The effect on ν_e cross-section of changing the off-axis span of IWCD. The total exposure is set to 7×10^{21} POT in FHC operation. There is a slight improvement in measurement precision when using the more restricted off-axis ranges, this is a result of redistributing the 1-2 degree exposure over the remaining off-axis angles. This results in a greater exposure at the more off-axis detector positions where the intrinsic signal to background ratio is greatest. The difference is however very slight at reconstructed energies above 300MeV.

increased number of selected pion events and a significant increase in the number of selected ν_μ CC events.

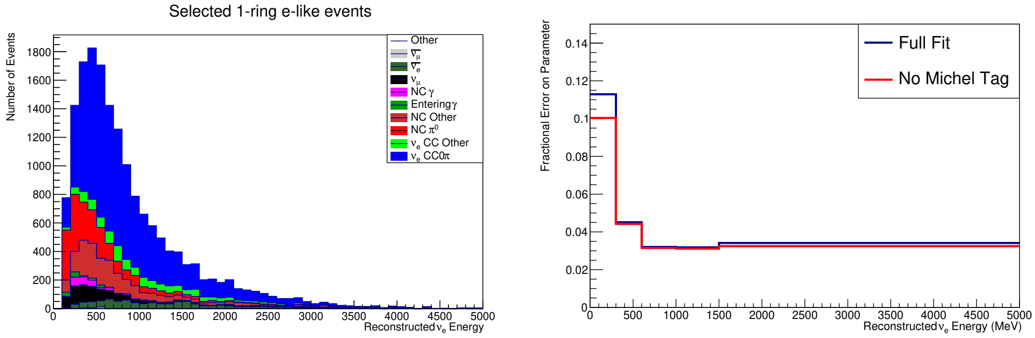

FIGURE D.12: The ν_e selection breakdown by mode and reconstructed energy without Michel electron tagging (left). There is a significant population of events with pions in the final state as a result of the removal of this tag. The effect of this on the cross-section measurement (right) relative to the with Michel tag case. There is a slight improvement in the ν_e CC inclusive cross-section measurement due to an increase in overall ν_e CC event rate.

The effect of the removal of the Michel tag on the resulting cross-section measurement can be seen in Fig D.12 (right), due to the increase in ν_e CC event rate the constraint improves slightly with the removal of the Michel electron tag. This is a result of the definition of signal used, here a CC-inclusive measurement is being made, hence an increase in ν_e CC pion events in the selection improves the sensitivity.

	FHC With Michel Tag		FHC Without Michel Tag	
Off-Axis Angle	1-2.7°	2.7-4°	1-2.7°	2.7-4°
ν_e CCQE	6 108	6 364	6 160	6 416
ν_e 2p2h	1 268	1 065	1 280	1 080
ν_e CC1π	1 573	1 410	3 064	2 696
ν_e CC Multi π	137	129	340	319
ν_e CC Other	28	33	68	53
ν_μ CC	435	144	2 622	746
$\bar{\nu}_\mu$ CC	2	4	23	21
$\bar{\nu}_e$	635	816	658	854
NC 1 γ	590	209	593	209
NC 1 π^0	5 035	1 790	5 135	1 843
NC Other	2 661	1 159	4 025	1 828
Total ν_e CC	9 114	9 001	10 912	10 564
Total Backgrounds	9 358	4 122	13 056	5 501
Total	18 472	13 123	23 968	16 065
ν_e CC Purity	49.3%	68.6%	45.5%	65.8%
$\nu_e + \bar{\nu}_e$ CC Purity	52.8%	74.8%	48.3%	71.1%

TABLE D.1: The number of events in the electron-like selection broken down by incident neutrino and interaction mode after applying an off-axis angle dependant pileup induced efficiency Fig 7.14. The exposure in FHC is 7×10^{21} POT. The removal of the Michel electron tag significantly increases both ν_e CC1π and ν_μ CC contributions to the sample. Overall there is a slight decrease in selection purity relative to the Michel electron tag sample.

D.2.5 Pileup

As shown in Fig 7.14, pileup in the detector will have a significant impact on the number of events selected in each bin of the fit. Uncertainty in this pileup therefore has the potential to significantly affect the results of a fit if not properly considered. As the pileup efficiency depends only on the central position of the detector it is natural to include one parameter per detector position in the fit. Each of these parameters controls a normalisation weight for all events that occurred at the corresponding detector position. As the samples used in the fit are binned in off-axis angle, these pileup parameters will be constrained by the fitting process. The action of each parameter is however equivalent to an increase in total flux at that detector position. These pileup parameters will therefore be highly correlated with flux parameters, and so the constraint offered by this fit alone may be quite poor. At IWCD independent, high precision measurements of pileup will be desirable, these can then be included into the fitter as a prior uncertainty on pileup.

For each detector position, the corresponding pileup parameter is weighted by 1

- the nominal pileup at that position. This is then used to scale the overall event rate at this position. The weighting is used to account for the greater uncertainty in the measurement of pileup in positions with high intrinsic pileup.

Including these parameters into the fitter and using the 750m weighted fit, the post-fit errors on these pileup parameters are shown in Fig D.13 (top) with a range of uncorrelated priors placed on the pileup parameters. At the most on-axis positions, the fitter is able to constrain the pileup beyond that provided by the prior due to the high event rate at these positions. At the higher off-axis angle positions however there is little data constraint and the prior plays a more significant role. Due to the significant anti-correlation between these pileup parameters and the incident flux, as seen in Fig D.14, the resulting error on the pileup parameters is significantly greater than that possible from the statistics of the samples alone. The effect of the inclusion of these parameters on the resulting ν_e cross-section measurement is shown in Fig D.13 (bottom). Overall, pileup does have an effect on the measurement precision, however this is quite small, even for relatively large given prior uncertainties.

D.2.6 Integrated Flux

As IWCD measures the intrinsic, unoscillated ν_e flux near the production point, electron neutrinos from kaon decay parents play a significant role. IWCD therefore experiences a ν_e flux with a longer high energy tail than that seen in the oscillated spectrum at the far detector.

To compare the fluxes seen at IWCD to that seen at HK, the integrated ν_e flux at IWCD must be evaluated. Taking off-axis slices of the IWCD ν_e flux distribution and weighting by pileup efficiency at the corresponding detector positions yields the effective flux used by the IWCD ν_e cross-section fit, as shown in Fig 7.2. IWCD has a significantly broader distribution however a significant proportion of flux overlaps with the HK oscillation maximum energy range, which provides sufficient statistics in the ν_e sample in the energy range of interest, between 300—1000MeV.

The measured flux at IWCD with a reduced off-axis span of 2-4 degrees is shown in Fig D.15. In contrast to Fig 7.2 the 2-4 degree flux is peaked slightly more sharply at lower energies with a slightly reduced overall spread.

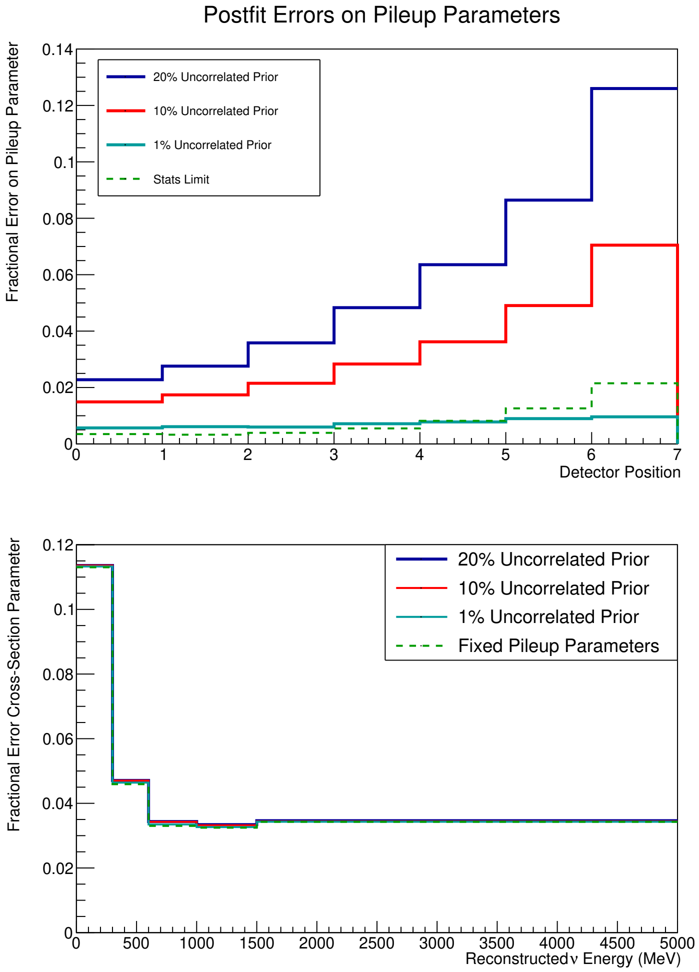

FIGURE D.13: The post-fit errors on the pileup parameters (top) for a range of uncorrelated prior uncertainties on these parameters. The uncertainty is greatest at the most off-axis positions due to lower event rate in these regions. The resulting impact on the ν_e cross-section parameters (bottom) is small however.

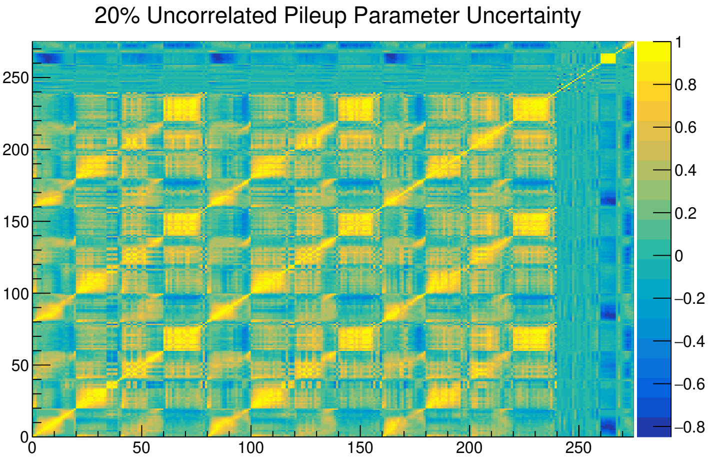

FIGURE D.14: The post-fit correlations between parameters. Parameters 0 to 239 are flux, 240-259 are cross-section parameters, 260-266 are pileup parameters, 267 & 268 are detector energy scale uncertainties for electrons and muons events respectively, parameter 269 corresponds to entering γ normalisation and parameters 270-274 are the ν_e signal parameters. There is strong anti-correlation between the pileup parameters and the ν_μ flux parameters (0-19, 80-99, 160-179).

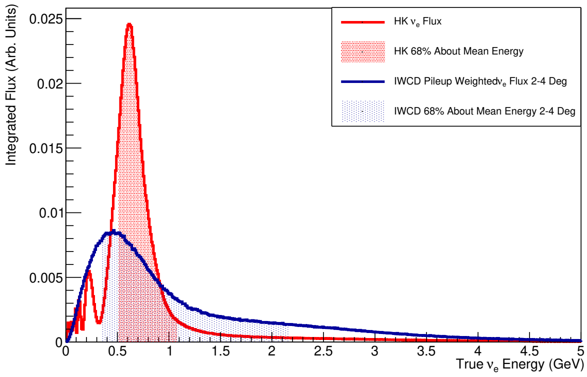

FIGURE D.15: The total ν_e flux measured by IWCD over a reduced 2-4° off-axis range and that present at HK. The highlighted regions show 68% of the incident flux symmetrically about the mean. The IWCD Flux has a significantly broader distribution than the oscillated HK spectrum. Both fluxes are normalised to a total integral of one with oscillation parameters $\sin^2\theta_{23} = 0.51$, $\Delta m^2_{23} = 2.51 \times 10^{-3}$ eV^2 and $\delta_{CP} = 0$.

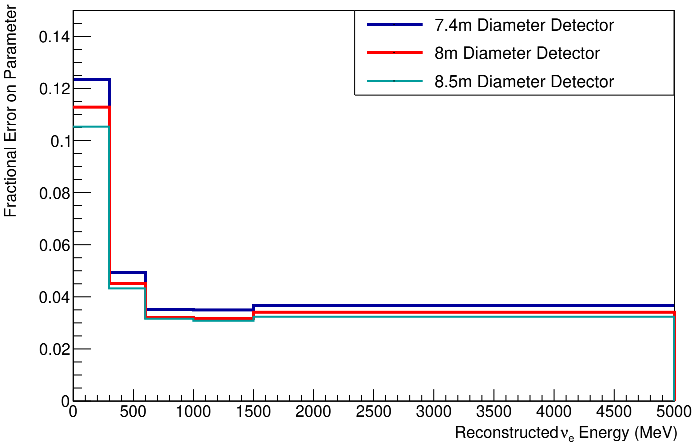

FIGURE D.16: The errors on the signal parameters for the different detector sizes. In all cases the detector height is 6m and a 100cm wall cut is used. The same cuts are used to select events in all three cases. Due to the limited statistics, the precision of the ν_e cross-section measurement is quite sensitive to changes in the number of events detected.

D.3 Detector Size & Position

The precision in the measurement of the ν_e CC inclusive cross-section will depend on the total number of these events detected. This is affected by the size of the detector and its distance from the beam production point. It is possible to investigate this effect using MC from a single detector size and position by re-weighting events to account for the changes in expected event rate. Three detector sizes at 750m are investigated for their impact on the ν_e cross-section constraint, these are summarised in Table D.2;

	Height (m)	Diameter (m)	ν_e Fiducial Volume (m^3)
990m MC Design	10.42	7.42	194
750m Reduced	6.0	7.4	91.6
750m Nominal	6.0	8.0	113
750m Enlarged	6.0	8.5	132

TABLE D.2: The detector sizes considered for this comparison.

Fig D.16 shows the effect of these different detector designs on the resulting error on the ν_e cross-section parameters. The same cuts were used in all cases. From this it can be seen that changes in detector size can have a large impact on IWCD's ν_e cross-section sensitivity, with reductions in diameter yielding significant reductions in sensitivity while enlargements show a smaller effect.